The Pennsylvania State University

The Graduate School

College of Engineering

IN-SITU MONITORING OF REMOTE SPECIMENS USING ULTRASONIC GUIDED WAVES

A Dissertation in

Engineering Science and Mechanics

by

Manton John Guers

Submitted in Partial Fulfillment
of the Requirements
for the Degree of

Doctor of Philosophy

August 2011

The dissertation of Manton John Guers was reviewed and approved* by the following:

Bernhard R. Tittmann
Schell Professor of Engineering Science and Mechanics
Dissertation Advisor
Chair of Committee

Joseph L. Rose
Paul Morrow Professor of Engineering Science and Mechanics

Clifford J. Lissenden
Professor of Engineering Science and Mechanics

Albert E. Segall
Professor of Engineering Science and Mechanics

Karl M. Reichard
Assistant Professor of Acoustics

Judith A. Todd
P.B. Breneman Department Head Chair and Professor of
Engineering Science and Mechanics

*Signatures are on file in the Graduate School.

ABSTRACT

There are a wide variety of engineering applications where it can be advantageous to perform real time ultrasonic measurements. In structural health monitoring (SHM) applications (aircraft, bridges, etc.), real time data can be used to improve safety and reduce maintenance costs. In other applications (such as carbon-carbon production and ceramic sintering) in-situ ultrasonic measurements can be used to study how a material is affected by different manufacturing conditions. Ultrasonic measurements can also be used in place of convention temperature, pressure, fluid flow, or level sensors.

The work presented in this dissertation focused on studying an ultrasonic guided waves based system for performing in-situ measurements on specimens which are commonly used in the accelerated life tests conducted in materials and test reactors (MTRs). Using this system, ultrasonic waves could be sent down a thirty foot long waveguide to a specimen while locating the transducer outside of the hostile environment. Both the theoretical and experimental results demonstrated how individual components of the system influenced the monitoring capabilities.

As one example, the in-situ monitoring system was studied for use in measuring the change in length of creep specimens. Successful measurements of creep elongation were demonstrated using a pulse-echo configuration of the in-situ monitoring system. In addition, the temperature dependence of the in-situ creep measurement was also studied. Both theoretical calculations and experiments showed that the temperature dependence of group velocity was approximately linear for the creep specimen geometry.

'Blister' specimens having a rectangular cross-section were also considered in this work. Theoretically driven semi-analytical finite element (SAFE) calculations, time-domain finite element calculations, and experimental measurements were performed to investigate guided wave propagation in this specimen. The SAFE calculations, finite element predictions, and experimental results all demonstrated good agreement. In general, the guided wave mode with the fastest group velocity appeared to be the most prominent in both the simulated and experimentally measured waveforms. Several types of defects were considered. Defects can sometimes produce temperature anomalies in the

specimen. The models indicated that detection of a defect induced temperature gradient in the rectangular ‘blister’ specimen was possible.

In the design and operation of an in-situ monitoring system based on guided ultrasonic waves, the transducer design plays an important roll in the performance of the system. In this work, a magnetostrictive sleeve design was tested as an alternative to a wire-wire joint configuration. Results showed that the sleeve design was effective for generating ultrasonic guided waves in the wire waveguide. In addition, the sleeve design simplifies specimen fabrication, minimizes the amount of magnetostrictive material required, and eliminates the artifacts associated with the wire-wire joint.

TABLE OF CONTENTS

LIST OF FIGURES

LIST OF TABLES

LIST OF ABBREVIATIONS

ALT	Accelerated Life Test(ing)
AlN	Aluminum Nitride (high temperature piezoelectric material)
AWG	Arbitrary Waveform Generator
BiT	Bismuth Titinate (high temperature piezoelectric material)
DSP	Digital Signal Processing
FEA	Finite Element Analysis
FEM	Finite Element Method
FFT	Fast Fourier Transform
LDV	Laser Doppler Vibrometer
LVDT	Linear Variable Differential Transducer
MTR	Materials and Test Reactor
NDE	Nondestructive Evaluation
PSU	Pennsylvania State University
PWR	Pressurized Water Reactor
PZT	Lead-Zirconate-Titinate (conventional piezoelectric material)
SAFE	Semi-Analytical Finite Element
SHM	Structural Health Monitoring
ZnO	Zinc Oxide (high temperature piezoelectric material)

LIST OF SYMBOLS

ω	Angular Frequency
J_n	Bessel Function of n^{th} Order
ρ	Density
u	Displacement
E	Elastic (Young's) Modulus
f	Frequency
C_g	Group Velocity
d	Half-thickness
λ_{Lame}	Lame's Constant
L	Length
C_L	Longitudinal Wave Velocity
C_p	Phase Velocity
v	Poisson's Ratio
a	Radius
G	Shear Modulus
C_T	Shear (or Transverse) Wave Velocity
h	Thickness
t	Time
k	Wave number
λ	Wavelength

ACKNOWLEDGEMENTS

I would like to thank Ray and Ben for starting the in-situ monitoring program and for being strong advocates for the continued study of in-situ techniques.

I would like to thank my advisor, Dr. Bernhard Tittmann, for giving me the opportunity to work on this project and for his support during my time working with him.

I would like to thank my committee for their time and valuable advice throughout the course of my project.

I would like to thank Dr. Bakis and his Ph.D. student Anurag for their time and very generous use of their equipment for performing the creep experiment.

I would like to thank Dr. Joy Rempe, Steven Taylor, Curt Wilkins, and Gerald Posakony for their valuable insight and suggestions.

I would like to thank all of my friends and family for the support and encouragement. Eric, Jason, Jon, and Brian were especially helpful.

DEDICATON

In loving memory of my mother.

CHAPTER 1: INTRODUCTION

There are a wide variety of engineering applications where it can be advantageous to perform real time ultrasonic measurements. In structural health monitoring (SHM) applications (aircraft, bridges, etc.), real time data can be used to improve safety and reduce maintenance costs. In other applications (such as carbon-carbon production and ceramic sintering) in-situ ultrasonic measurements can be used to study how a material is affected by different manufacturing conditions. Ultrasonic measurements can also be used in place of convention temperature, pressure, fluid flow, or level sensors.

The work presented in this dissertation focused on studying an ultrasonic guided waves based system for performing in-situ measurements on specimens which are commonly used in the accelerated life tests conducted in materials and test reactors (MTRs). Using this system, ultrasonic waves could be sent down a thirty foot long waveguide to a specimen while locating the transducer outside of the hostile environment. The work was primarily motivated by the desire to detect defects or dimensional changes in the MTR specimens. However, the scope of the work also had to encompass a system level perspective to understand how the various components interact. In doing so, the magnetostrictive transducer design was also studied to improve system performance.

1.1 In Reactor Measurements

When designing commercial nuclear power plants, careful consideration must be given to selecting appropriate structural and fuel materials. High operating temperatures, radiation effects, and corrosion can all lead to significant degradation of reactor components. Typically, this degradation results in altered material properties, geometric changes, and defect formation. [1-5]. Therefore, all materials must be tested to verify how the material responds to radiation exposure. Typically, the evaluation of materials is studied by performing accelerated life testing (ALT) in a MTR [6-9].

Following irradiation in an MTR, a “Post Irradiation Examination” (PIE) is often used to characterize the degradation in a given material. In order to perform PIE on a specimen, the MTR must be shut down, the specimen must be removed from the MTR,

and then the specimen must be transported to a special facility where the PIE is performed. This process can be very costly and there is a strong desire to develop technologies which are more economical [6-9]. Additional major short comings of the PIE process are that data collection is limited by the reactor schedule and data are not collected under prototypical conditions. There is simply no way to know if changes occur in a specimen during the time it takes to remove and transport the specimen to the PIE facility. Furthermore, each cycle (6 to 8 weeks) of the ALT may correspond to a year or more of commercial conditions. It is highly desirable to develop technologies which allow more frequent data collection in order to better understand how the materials age. Therefore, continuous monitoring techniques are of significant interest for MTR applications [6-11].

Linear Variable Differential Transducers (LVDTs) are one candidate technology for continuously monitoring for the occurrence of dimensional changes in MTR specimens. However, LVDTs have inherent limitations. LVDTs can only detect external dimensional changes and are not capable of detecting changes inside the volume of a specimen. In addition, some LVDT designs suffer from a Curie temperature effect [12,13]. The ultrasonic based system studied in this work has the potential to address many of the short coming found in competing technologies.

1.2 Additional Engineering Considerations

The in-situ monitoring technique studied in this work was primarily intended for monitoring specimens in a MTR. However, the ultrasonic monitoring technique may also be applicable to use in a commercial nuclear power plant.

Most commercial nuclear power plants are Pressurized Water Reactors (PWRs). In PWRs, temperatures in the reactor core are approximately 330°C (635°F). The reactor core is pressurized to approximately 15.5 MPa (2250 psi) to prevent boiling of the water cooling the core. The hot, high pressure core coolant is circulated to a steam generator unit where a separate water supply is converted into steam. The steam formed in the steam generator is then sent through a turbine to generate electricity [1-5].

In developing a continuous monitoring system for in-core use, the ideal scenario would be to have piezoelectric transducers mounted directly to the test specimens.

However, core temperatures are well above the Curie temperature of most piezoelectric materials [14]. In addition, many piezoelectric materials contain elements such as lead and lithium which are not allowed inside reactor cores because of radiation effects [1-5].

1.3 Wire Waveguides for Remote Inspection

As an alternative to directly mounting transducers on the test specimens, a remote monitoring technique can be used. By transmitting ultrasonic guided waves down a wire waveguide, the transducer can be located outside the radiation environment while still performing measurements on the specimen. In order to implement a remote monitoring technique, the waveguide between the transducer and specimen must conform to existing capabilities. This means a 1.5875 mm (1/16 inch) diameter stainless steel waveguide must be used to match fittings in the head of the reactor.[1]

The essence of remote inspection is to perform nondestructive evaluation (NDE) measurements on a specimen while isolating the transducers from the environmental conditions experienced by the specimen. In many cases, researchers seek to protect transducers from high temperatures which would damage the transducer. In other cases, the presence of radiation or other experimental conditions can restrict placing the transducers directly in the hostile environment.

1.4 Previous Work

Cegla and Cawley [15,16] reported on sending shear horizontal (SH) waves down square waveguides for locating cracking in specimens inside a 500°C oven. A proprietary transducer was used to send the SH waves down one waveguide, SH and surface waves propagated through the specimen, and were received via a second waveguide. Amplitude drop was used for crack sizing. Time-of-flight diffraction was also discussed, but it is unclear if temperature effects could be separated from damage effects.

Grossmann [17] used guided waves in wires to study the corrosion behavior of the waveguide material. Oxide formation on the wire waveguide produced a change in the

[1] This allows the use of the same fittings used for standard stainless steel encased thermocouples.

guided wave velocity, and Grossmann was able to correlate the associated change in time-of-flight to oxide thickness.

Royer and Rose [18,19] reported on a system for the in-situ monitoring of crystal growth. By positioning the waveguide in the molten material, a change in time-of-flight indicated the position of the solidified crystal surface relative to the end of the waveguide.

Vogt et al. [20] placed a wire waveguide in un-cured epoxy. As the epoxy cured, a change in time of flight was used to characterize the quality of the epoxy.

Tittmann and Yen [21] demonstrated that passive measurements could also be performed with wire waveguide techniques. In their work, wire waveguides were used to monitor the acoustic emissions produced during the manufacturing of carbon-carbon.

In many of the remote monitoring examples discussed, only the wire is used as the sensing mechanism. In some cases, liquid coupling is used between the wire and the specimen of interest. It is rare to fine examples where a remote specimen with a complex geometry is permanently attached to a wire waveguide system for in-situ measurements.

Previous Work with Attached Specimens

Pedrick [22] and Heckman [23] previously demonstrated that ultrasonic guided waves could be transmitted to a specimen at the end of a 30 ft waveguide. Although their early proof-of-concept work provided a valuable staring point for this investigation, there were several aspects of their design which could be improved. In particular, Pedrick [22] and Heckman [23] assumed that Lamb waves were generated in their specimen. As discussed in Chapter 5, the true boundary conditions of the specimen are not compatible with a Rayleigh-Lamb solution. A new theoretical analysis was required to correctly describe the guided wave propagation under appropriate boundary conditions. In addition, the manner in which the magnetostrictive material was attached to the waveguide produced artifacts in the recorded signal. Thus, a new transducer configuration was desired to eliminate the signal artifacts.

1.5 Dissertation Objectives

The primary objective of this dissertation was to examine three aspects of the in-situ monitoring system. First, the design of the magnetostrictive transducer was examined to find an alternative design that eliminated the signal artifacts and simplified fabrication. Second, this work set out to accurately describe the guided wave propagation in rectangular bar specimens using valid boundary conditions. Third, this work also set out to demonstrate that the deformation of creep specimens could be monitored with the proposed in-situ monitoring system.

The bar and creep specimens are test cases which are most closely associated with the MTR applications which inspired this work. However, the tools and methods studied in this work are applicable to virtually any guided wave analysis. Through the selected test cases, valuable information about the system behavior can be obtained and lay the ground work for future generalizations of in-situ system.

1.6 Organization

Chapter 2 provides a brief review of guided wave inspections. Chapter 3 discusses the various analysis techniques used in the course of this work. Chapter 4 discusses magnetostriction and the improvements made compared to the original transducer configuration. Chapter 5 discusses the analysis of guided wave propagation in specimens with rectangular cross sections. Dispersion curves were derived and experimental validations performed. Chapter 6 discusses the analysis of using the in-situ monitoring technique for monitoring creep specimens. Once again, dispersion curves were derived and experimental validations performed. Chapter 7 summarizes the results of this investigation and gives suggestions for future work.

CHAPTER 2: GUIDED WAVES

Nondestructive evaluation (NDE) is a broad field where certain techniques are used to examine objects without altering their current state or future usefulness. Examples of NDE techniques include: liquid penetrant, magnetic particles, eddy currents, acoustic emission, x-rays, thermography, and ultrasonic inspection [24]. The work in this dissertation is based on ultrasonic NDE principles.

Ultrasonic NDE is also a broad field encompassing many different techniques. At the heart of any ultrasonic NDE is the ultrasonic A-scan. The A-scan is simply a record of signal amplitude received by an ultrasonic transducer versus time. Many basic NDE measurements can be made using only the A-scan information. More sophisticated scans (B-scan, C-scan, phased array scans) utilize multiple A-scans to form images of a small area in an object [24,25]. The main disadvantage to traditional ultrasonic NDE techniques is that the transducer must be moved repeatedly to inspect large structures.[2] In some cases, such as nuclear reactors, it may be impossible to place transducers in the appropriate locations for traditional ultrasonic NDE techniques to be effective.

Guided wave ultrasonic NDE is an attractive option to address some of the limitations associated with traditional inspection methods. In guided wave ultrasonic NDE, the surfaces or boundaries of a structure can be used to achieve constructive interference phenomena which allow ultrasonic waves to travel over large distances. Popular examples of guided wave inspection application include plates, pipes, and railroad tracks [26-33]. Because guided waves can travel over long distances, it becomes reasonable to develop structural health monitoring (SHM) systems where sensors are placed permanently on a structure for continuous monitoring.

2.1 Classic Examples

If a homogeneous, isotropic medium is assumed, the Navier-Cauchy equations for waves in solid media take the form given in Equation 2.1 where λ_{Lame} is Lame's constant, E is elastic modulus, G is shear modulus, ρ is density, $\bar{u}$ is the displacement vector, and t is time [34-36].

[2] For example, inspecting the entire fuselage of an airplane.

$$\left(\lambda_{Lame}+G\right)\nabla\nabla\bullet\overline{u}+G\nabla^2\overline{u}=\rho\frac{\partial^2\overline{u}}{\partial t^2} \tag{2.1}$$

$$\lambda_{Lame}=\frac{G\left(2G-E\right)}{E-3G}$$

From Equation 2.1, it is clear that the ultrasonic wave propagation is influenced by the fundamental material properties of the specimen. In addition, the wave propagation is influenced by the boundaries (surfaces) of the specimen. As the waves reflect off the boundaries of the specimen, interference phenomena lead to waves propagating in modes unique to the specific geometry. This is called guided wave propagation. The accurate mathematical description of guided wave propagation in a homogeneous, isotropic medium entails solving Equation 2.1 with appropriate boundary conditions [34-36].

With the appropriate boundary conditions, Equation 2.1 is used to determine the dispersion curves for a given geometry. Solving for the correct dispersion curves is critically important because the dispersion curves provide valuable insight into the expected wave propagation behavior. First and foremost, the dispersion curve solutions dictate what are real propagating wave modes for a given geometry. Secondly, the dispersion curves indicate whether a particular wave mode is dispersive or non-dispersive at a particular frequency. Third, the dispersion curves indicate how fast a wave mode travels at a given frequency (group velocity).

Plates

One of the most widely studied examples of guided wave propagation is Lamb wave propagation in plates. For the Lamb wave solution, the plate is assumed to have a finite thickness and infinite width. Under these boundary conditions, the solution of the Equation 2.1 is the Rayleigh-Lamb equations (Equations 2.2 and 2.3). Here, C_L is bulk longitudinal velocity, C_T is bulk shear velocity, C_p is phase velocity, k is wave number, h is thickness, and ω is angular frequency [34-36]. For practical applications, the Rayleigh-Lamb solution remains a valid approximation as long as the width of the plate is much larger than the wavelength of the guided waves (width >> wavelength). Further discussion of Lamb waves is given in Appendix D.

$$\frac{\tan(qh)}{q}+\frac{4k^2p\cdot\tan(ph)}{(q^2-k^2)^2}=0 \quad \text{symmetric} \tag{2.2}$$

$$q\cdot\tan(qh)+\frac{(q^2-k^2)^2\cdot\tan(ph)}{4k^2p}=0 \quad \text{anti-symmetric} \tag{2.3}$$

$$\text{where: } p^2=\left(\frac{\omega}{C_L}\right)^2-k^2=\left(\frac{\omega}{C_L}\right)^2-\left(\frac{\omega}{C_p}\right)^2$$

$$\text{and } q^2=\left(\frac{\omega}{C_T}\right)^2-k^2=\left(\frac{\omega}{C_T}\right)^2-\left(\frac{\omega}{C_p}\right)^2$$

Circular Rods

Another common example of guided wave propagation is wave propagation in a circular rod. To solve for the propagation in a circular waveguide, the governing equations are converted to cylindrical coordinates.[3] Under these boundary conditions, the solution is the Pochhammer equations (Equations 2.4 and 2.5). Here, C_L is bulk longitudinal velocity, C_T is bulk shear velocity, C_p is phase velocity, k is wave number, a is radius, and ω is angular frequency. J_n are Bessel equations [34-36].

$$\frac{2\alpha}{a}(\beta^2+k^2)J_1(\alpha a)J_1(\beta a)-(\beta^2-k^2)J_0(\alpha a)J_1(\beta a)-4k^2\alpha\beta J_1(\alpha a)J_0(\beta a)=0 \text{ axial} \tag{2.4}$$

$$(\beta a)J_0(\beta a)-2J_1(\beta a)=0 \quad \text{torsional} \tag{2.5}$$

$$\text{where: } \alpha^2=\left(\frac{\omega}{C_L}\right)^2-k^2=\left(\frac{\omega}{C_L}\right)^2-\left(\frac{\omega}{C_p}\right)^2$$

$$\text{and } \beta^2=\left(\frac{\omega}{C_T}\right)^2-k^2==\left(\frac{\omega}{C_T}\right)^2-\left(\frac{\omega}{C_p}\right)^2$$

Numerical Solutions

The roots of Equations 2.2 through 2.5 describe phase velocity dispersion curves which indicate the guided wave modes and if a selected guided wave mode is dispersive or non-dispersive. Typically, numerical methods are employed to find the roots. Once phase velocity curves are determined, the phase velocity results can be used to derive group velocity dispersion curves. Group velocity curves are used to interpret the group velocities observed in experiments.

[3] See Chapter 6.

Comments

The Rayleigh-Lamb equations (Equation 2.2 and 2.3) and the Pochhammer equations (Equations 2.4 and 2.5) show that the solution of the Navier-Cauchy equations is significantly different depending on the boundary condition. Thus, dispersion curves for one geometry cannot be used to approximate the dispersion curves of another geometry. The Navier-Cauchy equations must always be solved with the appropriate boundary conditions for each unique geometry in order to obtain valid dispersion curves.

For the bar of rectangular cross-section being studied in this research (Chapter 5), it may be tempting to approximate it as a plate and use Rayleigh-Lamb equations. However, the width of the bar specimen is approximately equal to one wavelength of the bulk shear wave in Zircaloy at the 150 kHz operating frequency. Thus, the necessary condition for a valid Rayleigh-Lamb solution (width >> wavelength) is not satisfied [34-36]. There will be simultaneous interference effects produced by all boundaries.

2.2 Other Examples

Guided waves have been studied extensively for pipe inspection. The guided waves have the unique capability to inspect buried pipes and also inspecting under pipe coatings. In addition, time delays can be used to focus energy at a point or steer the guided waves around bends in the pipe [30,31]. Despite their complex shape, railroad tracks can also be inspected using guided waves. By selecting different wave modes and frequencies, energy can be concentrated in different portions of the rail [32,33].

It is well known that temperature affects both the material properties and geometry of the specimen being considered, and there are several papers in the scientific literature that deal with the temperature dependence of guided wave propagation. However, the available literature appears to be limited in two respects. First, the available literature only deals with limited temperature ranges (i.e. ± 65°C). Second, the best papers only report maximum operating temperatures of 150°C (302°F) [37,38]. The works in the literature also appear to be limited in application. Most papers focus on thin plates (Rayleigh-Lamb solutions) at frequencies where only the A0 and S0 modes are present [37-41].

For this research, the specified operating temperature range of 21-427°C (70-800°F) is significantly higher than what has been previously reported in literature. In addition, the guided wave modes for a rectangular bar specimen are significantly different than the guided wave modes in plates.

CHAPTER 3: ANALYSIS METHODS

Within the course of this work, several methods were used to analyze the theoretical predictions and experimental measurements of guided wave propagations. This chapter provides background information on each of these methods.

3.1 Semi-Analytic Analysis

The Rayleigh-Lamb equations (Equations 2.2 and 2.3) fully describe the guided wave modes in a plate. Similarly, the Pochhammer equations (Equations 2.4 and 2.5) fully describe the guided wave modes in a circular rod [34-36]. Although these are exact equations, there is no closed form solution. Instead, a numerical solution must be found. The use of a numerical solution to solve the exact governing equations is sometimes referred to as a semi-analytic analysis.

For Rayleigh-Lamb equations (Equations 2.2 and 2.3) and Pochhammer equations (Equations 2.4 and 2.5) the numerical solution can be easily found using a 'root finding' algorithm [34,42,43]. The root finding procedure is summarized as follows:

1. Select a frequency.
2. Select a starting phase velocity.
3. Evaluate the left had side of the selected equation and determine the sign.
4. Increment phase velocity, and reevaluate the sign of the result.
5. Repeat steps 3 and 4 until the sign changes. A root of the selected equation must exist in the interval $(C_p)_n < x < (C_p)_{n+1}$.
6. Iteratively search the interval $(C_p)_n < x < (C_p)_{n+1}$ (i.e. bisection) to find the precise phase velocity of that root.
7. After finding a root, continue searching the selected frequency for additional roots using steps 2 through 6.
8. Select a new frequency and repeat steps 2 through 7.

This method was used to determine the dispersion curves of the circular creep specimens discussed in Chapter 6. Morse and Feshbach [44] present a partial simplification of the Navier-Cauchy equation for the rectangular cross-section considered

in Chapter 5. However, Morse and Feshbach's [44] representation is not in a mathematical form that permits a straight forward iterative root finding approach for determining the dispersion curves. Thus, an alternative technique, the semi-analytical finite element (SAFE) method, was required for analyzing the rectangular specimen.

3.2 Semi-Analytic Finite Element Analysis

In the literature [45,46] the semi-analytical finite element (SAFE) technique is reported to be a versatile and powerful technique for determining the dispersion curves for arbitrary cross-sections. The basic idea is to assume a harmonic wave solution, and then derive an Eigen value equation which is then solved numerically via the finite element method.

As described by Hayashi et al [46], the first step is to discretize the arbitrary two-dimensional cross-section. The orthogonal function $e^{(i\xi z)}$ is then assumed to describe wave propagation in the z-direction. The displacement vector can then be written as Equation 3.1, where $N(x,y)$ is the interpolation function, and $U^j(z)$ is the nodal displacement vector of the j^{th} element.

$$u = [N(x,y)][U^j(z)]e^{(-i\omega t)} \tag{3.1}$$

Following the derivation given by Hayashi et al [46], the equations can be formulated into the Eigen value problem given in Equation 3.2 where ξ is the wave number.

$$([A] - \xi[B])\{Q\} = 0 \tag{3.2}$$

Equation 3.2 has the same basic form as a typical Eigen value problem in finite element analysis [47]. However, the SAFE formulation is such that the harmonic wave solution is included in the Eigen vector Q. Once the Eigen value problem is correctly formulated, standard numerical techniques in the finite element method can be used to solve for the wave number ξ at varying frequencies. The resulting set of Eigen values will contain solutions of both real propagating waves and imaginary results (solutions which are not physically possible). A root sorting is then used to remove non-real results.

From the wave number solution, phase velocity (C_p) and group velocity (C_g) results are derived according to Equations 3.3 and 3.4, respectively.

$$C_p = \frac{\omega}{\xi} \tag{3.3}$$

$$C_g = \frac{\partial \omega}{\partial \xi} \tag{3.4}$$

Figure 3.1 shows a comparison of both numerical methods for a circular waveguide. The SAFE solution is in good agreement with the results determined by the semi-analytical solution of the Pochhammer equation.

3.3 Finite Element Analysis

Finite element modeling is a valuable tool which is used in a wide variety of engineering disciplines [47,48]. With respect to modeling ultrasonic wave propagation, finite element modeling provides the capability to predict the ultrasonic waveforms which would be recorded in experimental measurements [49,50]. This is particularly useful in cases where there are complex geometries (such as the trapezoidal horn) and the time-of-flight associated with guided wave propagation must be determined. Finite element modeling also permits parametric design optimization to identify ways to improve ultrasonic measurement techniques.

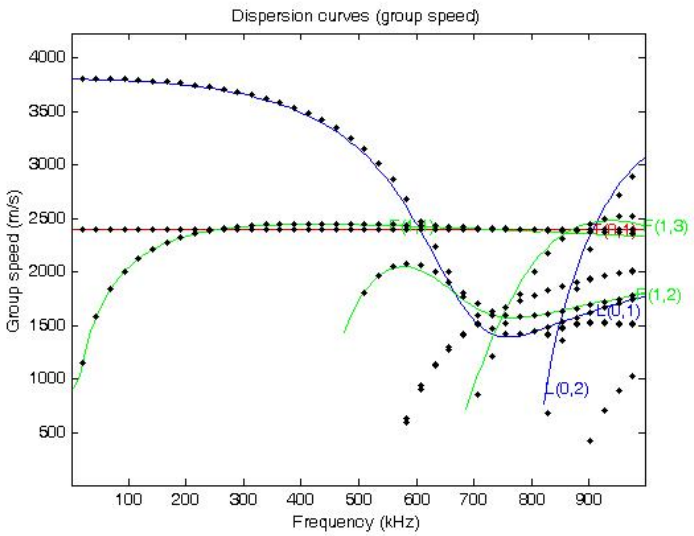

Figure 3.1: Comparison of numerical results for a waveguide of circular cross-section. Solid lines were obtained via a semi-analytic analysis to determine to roots of the Pochhammer equations [43]. Dotted lines were obtained via a SAFE analysis [46].

In order to simulate the ultrasonic waveforms, a transient analysis of the stress wave propagation must be solved. First, a time dependent form of the nodal displacement must be used. In Equation 3.5, M is the mass matrix, K is the stiffness matrix, C is the damping matrix, and F is applied force [47,48].

$$[M]\{\ddot{u}\}+[C]\{\dot{u}\}+[K]\{u\}=[F] \tag{3.5}$$

In addition to the spatial discretization, the transient analysis must also be discretized in the time-domain so that the time dependent behavior can be solved for by numerical methods. As time is incremented, the nodal displacements u, nodal velocities $\dot{u}$, and nodal accelerations $\ddot{u}$ must be liked in time. Equation 3.6 shows how displacement must be related to velocity, and equation 3.7 shows how velocity must be related to acceleration. In Equations 3.6 and 3.7, i indicates the time index in the discretized calculation

$$u^{i+1}=u^{i}+\Delta t\cdot\dot{u}^{i} \tag{3.6}$$

$$\dot{u}^{i+1}=\dot{u}^{i}+\Delta t\cdot\ddot{u}^{i} \tag{3.7}$$

3.4 Time-of-Flight Analysis

In guided wave propagation, the group velocity determines how long it takes for the guided ultrasonic waves to travel through a specimen. By simply determining the difference in arrival time of reflections in the signal, the time-of-flight measurement can be used to confirm group velocity values.

Figure 3.2 shows an example waveform and an envelope of the signal.[4] The envelope of the signal is commonly used to determine time-of-flight in guided wave signals because the phase and group velocities are not equal. However, the results shown in Chapter 6 indicated that the use of a signal envelope is not always accurate.

[4] See Appendix C for additional information on the signal envelope.

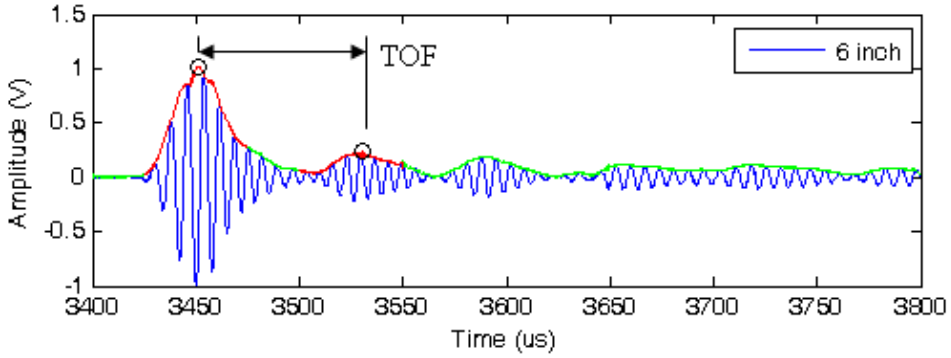

Figure 3.2: Example waveform and analytic envelope with time-of-flight (TOF) between reflections shown.

3.5 Frequency Spectrum Analysis

In the transducer study presented in Chapter 4, it was of interest to know what frequency content was produced for different transducer designs and pulse excitations. In order to determine the frequency content of a signal, a Fourier transform is performed. The discrete-time Fourier transform is symmetric, so the useful range of the Fourier frequency spectrum is limited to half of the sampling frequency. In practice, longer length signals (having more total sample points) produce discrete-time Fourier transforms with smaller frequency steps.

CHAPTER 4: REMOTE MAGNETOSTRICTIVE TRANSDUCERS

Magnetostriction has been studied for a wide variety of ultrasonic sensor applications [51]. In particular, several members of Southwest Research Institute (including Kwan) have published multiple papers on the subject [52-62]. In some examples, the magnetostrictive material is simply used as a substitute for the piezoelectric material inside a commercial style transducer [63]. In other cases, a highly magnetostrictive material is attached directly to the specimen of interest [17,64-68].

Many examples of magnetostriction are based on the Joule effect. In the Joule effect, an applied longitudinal magnetic field[5] produces strain in a magnetostrictive material because the applied magnetic field is exerting a small force on the magnetic domains of the material. The observed strain is parallel to the applied magnetic field because the small force induced by the magnetic field works to try and align the magnetic domain with the field. By alternating the magnetic field, compressional ultrasonic waves can be transmitted parallel to the magnetic field [69].

Detection of ultrasonic wave propagation occurs via the inverse effect known as the Villari effect. In the Villari effect, transient strains in the magnetostrictive material disrupt the magnetic domains and produce a 'stray flux.' This flux in the magnetic field induces a current in a receiving coil (via Faraday's Law) [69].

A second type of magnetostriction is based on the Wiedemann effect. In the Wiedemann effect, a circular magnetic field and longitudinal magnetic field are combined to form a helical magnetic field. This induces a torsional force in the magnetostrictive material. Thus, the Wiedemann effect can be used to transmit torsional ultrasonic waves [69-72].

Detection of the torsional ultrasonic waves occurs via a combination of the inverse Wiedemann effect and the Matteuci effect. The magnetic fluxes induced by these two effects induce a current in a receiving coil (via Faraday's Law) [69-72].

All magnetic materials exhibit some amount of magnetostriction. However, most engineering materials typically have low magnetostrictive coefficients and produce virtually no useful strain under an applied magnetic field. Therefore, it is common for

[5] The applied field is often generated by a coil of wire with an alternating current.

researchers to attach highly magnetostrictive material (such as Terfenol and Galfenol) to a specimen for stronger signals as described in papers by Kannan et al. [64] and I.K. Kim et al. [65,66]. Y.Y. Kim [67], Kulczyk et al. [68], and Grossmann [17] attached magnetostrictive stubs to the ends of wires or shafts.

The highly magnetostrictive materials (such as Terfenol-D) are often brittle and may be unsuitable for certain applications. As an alternative, there are several metal alloys available which are capable of producing sufficient magnetostrictive strain for ultrasonic sensor applications. Common examples include 50Ni-50Fe ("50 Permalloy"), 95Ni-5Co, 51Fe-49Co ("Permendur"), 49Co-49Fe-2V ("Remendur"), and 87Fe-13Al ("Alfer") [73-77]. In the work for this dissertation, a few tests were conducted with Permendur and Remendur. However, much of the transducer development tests were carried out with a newer alloy called Arnokrome 3 (a proprietarily Fe-Cr-Co alloy) [78].

4.1 Older Wire-Wire Design

Figure 4.1 shows the older remote magnetostrictive transducer configuration first used by Pedrick [22] and Heckman [23]. This older set up is based on the work first reported by Bell [79] and is similar in concept to that used by Y.Y. Kim [67], Kulczyk et al. [68], and Grossmann [17]. In this design, the wire of magnetostrictive material was coupled to a long stainless steel waveguide through a brass coupling. The brass coupling was included because explosion bonds (as used by Grossmann [17]) where mechanically weak. By using the long stainless steel waveguide, the magnetostrictive material remains outside the reactor environment while allowing the ultrasonic guided waves to travel to and from the specimen.

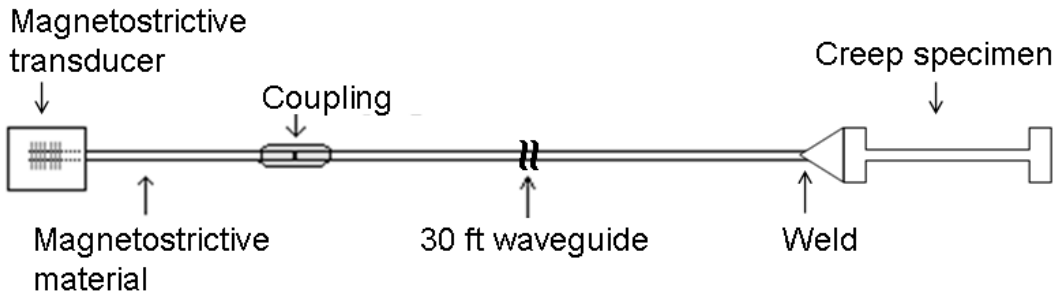

Figure 4.1: Older design for the in-situ monitoring of creep specimens. The magnetostrictive wire is coupled to the stainless steel waveguide using a brass coupling. The coupling produces unwanted artifacts in the received signals.

Although this design is effective, there are drawbacks. First, the inline joints are difficult to manufacture. Special soldering tools are required, and several attempts are often required to achieve a joint with acceptable ultrasonic transmission. Second, even the best inline joints reflect a portion of the ultrasonic waves. As Figure 4.2 illustrates, the energy reflected from the joint (R1) will reflect off of the free end of the magnetostrictive stub and travel back towards the specimen. This in turn leads to unwanted artifacts in the received signals as illustrated in Figure 4.3. The joint artifacts are problematic because they can masks slower modes. Also, the artifacts can interfere with time-of-flight measurements as temperature increases because the modes in the specimen slow down. In order to prevent the artifacts from corrupting the received signals, relatively long lengths of the magnetostrictive wire are required. This is undesirable because of both the costs and the difficulty associated with obtaining the magnetostrictive material.

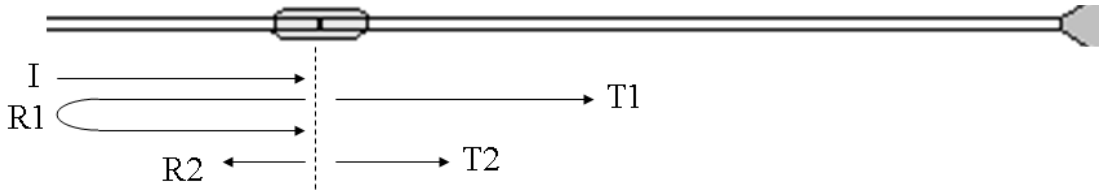

Figure 4.2: Illustration indicated the transmission and reflection of ultrasound form the wire-wire joint. When the incident ultrasonic wave (I) reaches the wire-wire joint, both transmission (T1) and reflection (R1) occurs. Reflected wave R1 can then reflect off the free end of the magnetostrictive wire and return to the wire-wire joint. When R1 returns to the wire-wire joint, there is once again transmission (T2) and reflection (R2). The round-trip time-of-flight for wave R1 determines the time spacing of T1 and T2. Thus, the round-trip time-of-flight in the magnetostrictive wire must be greater than the time-of flight in the specimen so that T2 does not over lap with the first reflection from the end of the specimen.

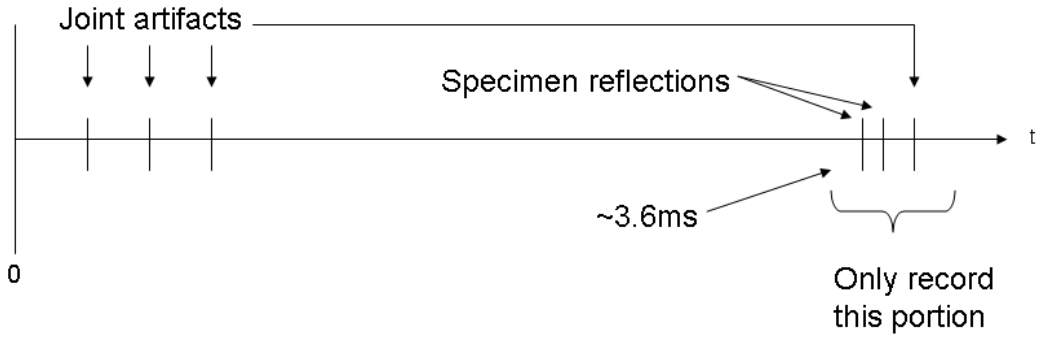

Figure 4.3: Illustration showing the feature expected in the data collected using the setup shown in Figure 4.2. The brass joint produces artifacts in the signal. The time-of-flight between the artifacts (as dictated by the length of magnetostrictive stub used) must be sufficiently long so that an artifact does not coincide with the reflection from the end of the specimen. Typically only the data of interest (at ~ 3.6 ms) is recorded to reduce the amount of data which must be recorded.

4.2 Sleeve Design

As an alternative to the wire-wire coupling, a design based on a sleeve of magnetostrictive material was developed in the course of this work. As shown in Figure 4.4, the stainless steel waveguide simply fits inside the magnetostrictive sleeve. The sleeve assembly then slides inside the excitation coil in a transducer housing.

In developing the sleeve design three prototypes were tested. The first prototype consisted of wrapping magnetostrictive foil around the end of a stainless steel wire. The second and third prototypes were fabricated by drilling an approximately 0.063 inch diameter hole in the center of a 0.102 inch diameter piece of magnetostrictive material. One of these sleeves was press-fit onto the wire waveguide, and the other sleeve was glued on.

Figure 4.5 shows a comparison of waveforms for the three prototypes attached to a short piece of wire with no specimen attached. The glued sleeve had the best performance. The prototype involving the press-fit did not perform as well as the glued joint. The most likely explanation for the press-fit having a lower amplitude is that the crimping process to form the press-fit resulted in residual stresses. Such a degradation of magnetostriction dues to stress is consistent with the theory presented by Tremolet [69].

Steve Taylor [80] suggested using a friction fitting. However, the results shown in Figure 4.6 indicated that the signal amplitude varied based on the tightness of the friction fit. Thus, the glued joint is expected to be more reliable.

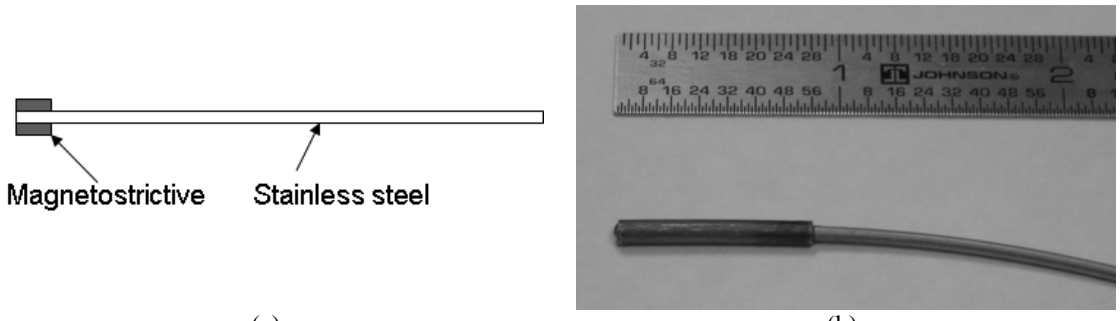

(a) (b)

Figure 4.4: New magnetostrictive sleeve design. (a) Illustration of the concept. (b) Photo of a prototype tested in this work. In this work, the outer diameter of the magnetostrictive sleeve was such that the sleeve could still fit into the housing of an existing magnetostrictive transducer coil. As an alternative, the coil can be wound directly onto the sleeve. This design eliminated the coupling joint used in the original design and removes unwanted artifacts from the received signals.

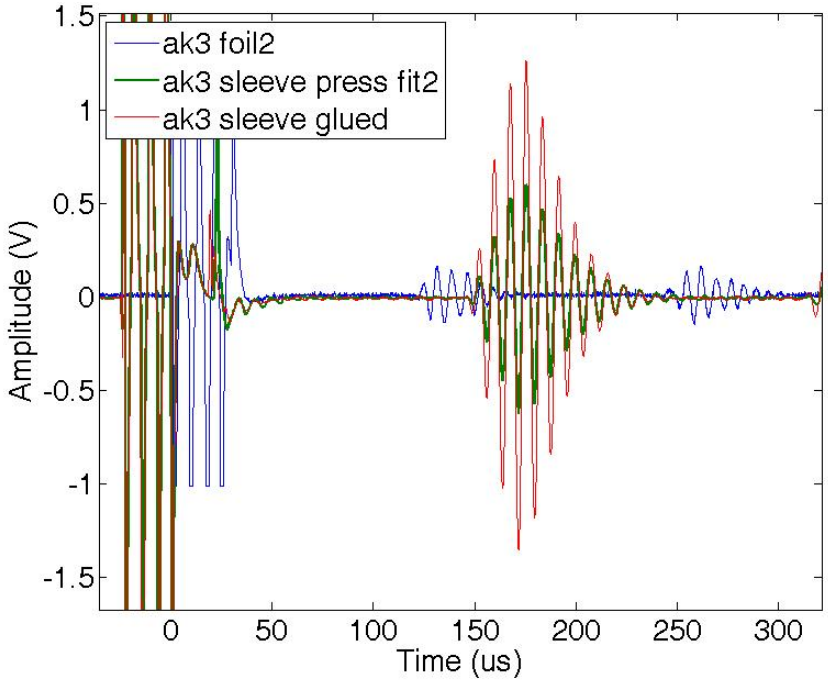

Figure 4.5: Experimental results for three prototypes tested in the development of the magnetostrictive sleeve transducer approach. The glued joint produced the highest amplitude signal.

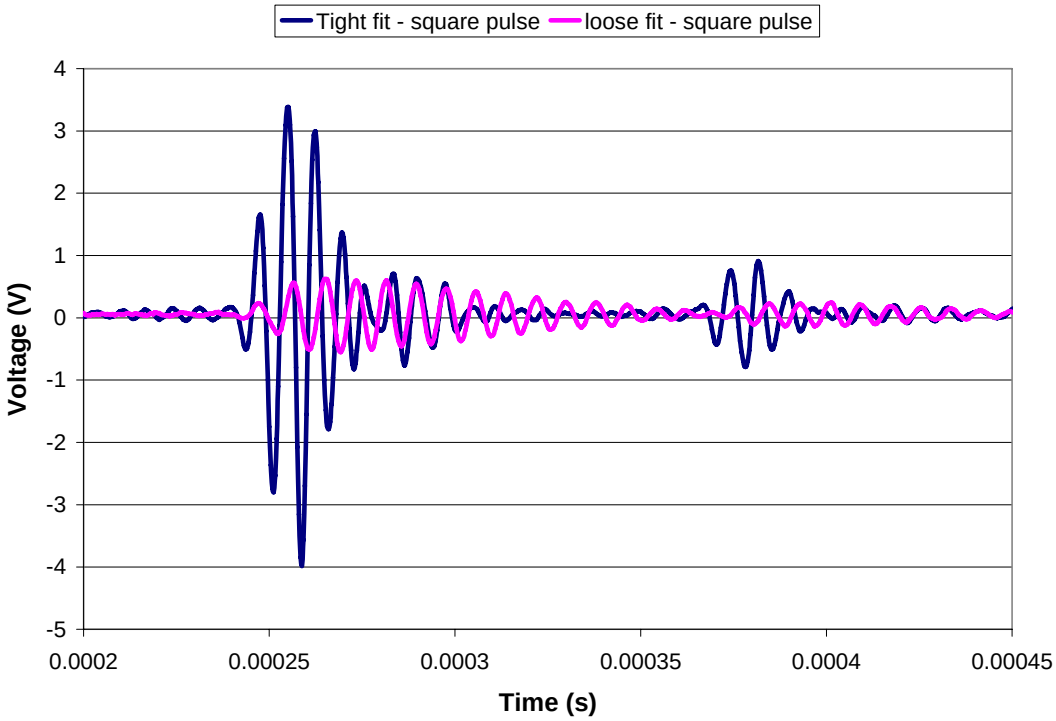

Figure 4.6: Experimental results for a friction fit sleeve transducer. A tighter fit produces a higher amplitude ultrasonic signal compared to a loose fit.

4.3 Test Parameters

In earlier work by Kropf and Tittmann [81], it was proposed to use a swept continuous wave for studying the performance of magnetostrictive wire transducers. Although this approach can yield insightful facts about the magnetostrictive transduction, it does not represent the tone burst excitation used in guided wave applications. In this work, tone burst excitation was used to examine the amplitude and frequency content of the sleeve transducer.

Both a MATEC tone burst card (TB1000) and a National Instruments arbitrary waveform generator (AWG) were used. The settings for the MATEC card were held constant during testing and are summarized as follows: 200 V peak-to-peak ("low" volts) at 80% output, pulse-echo mode, 33 dB gain, pulse width of 20 μs, no filters, no rectification, and positive internal trigger. The AWG was programmed with custom waveforms to supply tone burst excitation at maximum voltage (approximately 8 V peak-to-peak) with an enveloped pulse width of 20 μs. All measurements were performed over a frequency sweep of 50 kHz to 250 kHz with 32 signal averages per frequency. Voltage data (MATEC experiments only) were collected after gain by the MATEC card. Displacement data (both MATEC and AWG) were collected based on the output voltage of a Polytec Laser Doppler Vibrometer (LDV). The LDV was used to measure displacement at the end of the wire waveguide.

4.4 Comparison of Wave Excitation

In order to evaluate the performance of the sleeve transducer, baseline data was needed. As a first step, a series of frequency sweeps were performed on a solid Remendur wire. The analytic envelope of the waveform at each driving frequency was calculated via the Hilbert transform.[6] The color scale in Figure 4.7 plots the amplitude of the analytic envelope versus driving frequency. Figure 4.7a shows that excitation by the MATEC card produced distinct artifacts near 90 kHz and 150 kHz where the output voltage abruptly changes. A second MATEC card was obtained for comparison. The results shown in 4.7b contain the same artifacts and also more noise because the

[6] See Appendix C for additional information on the analytic envelope.

transducer was held by hand. Figure 4.7c shows LDV data for MATEC excitation with the same artifacts. Since the artifacts appear in the LDV data, the source of the artifacts is on the transmit side of the MATEC card. Figure 4.7d shows LDV data for excitation by the AWG. The results for the AWG excitation have lower amplitudes because the AWG has a significantly lower excitation voltage. There is an artifact near 130 kHz in the AWG, but this is caused by triggering off of the excitation voltage. The amplitude of the AWG artifact was relatively small, so it is not as problematic compared to the MATEC artifacts. Therefore, subsequent measurements relied on the AWG.

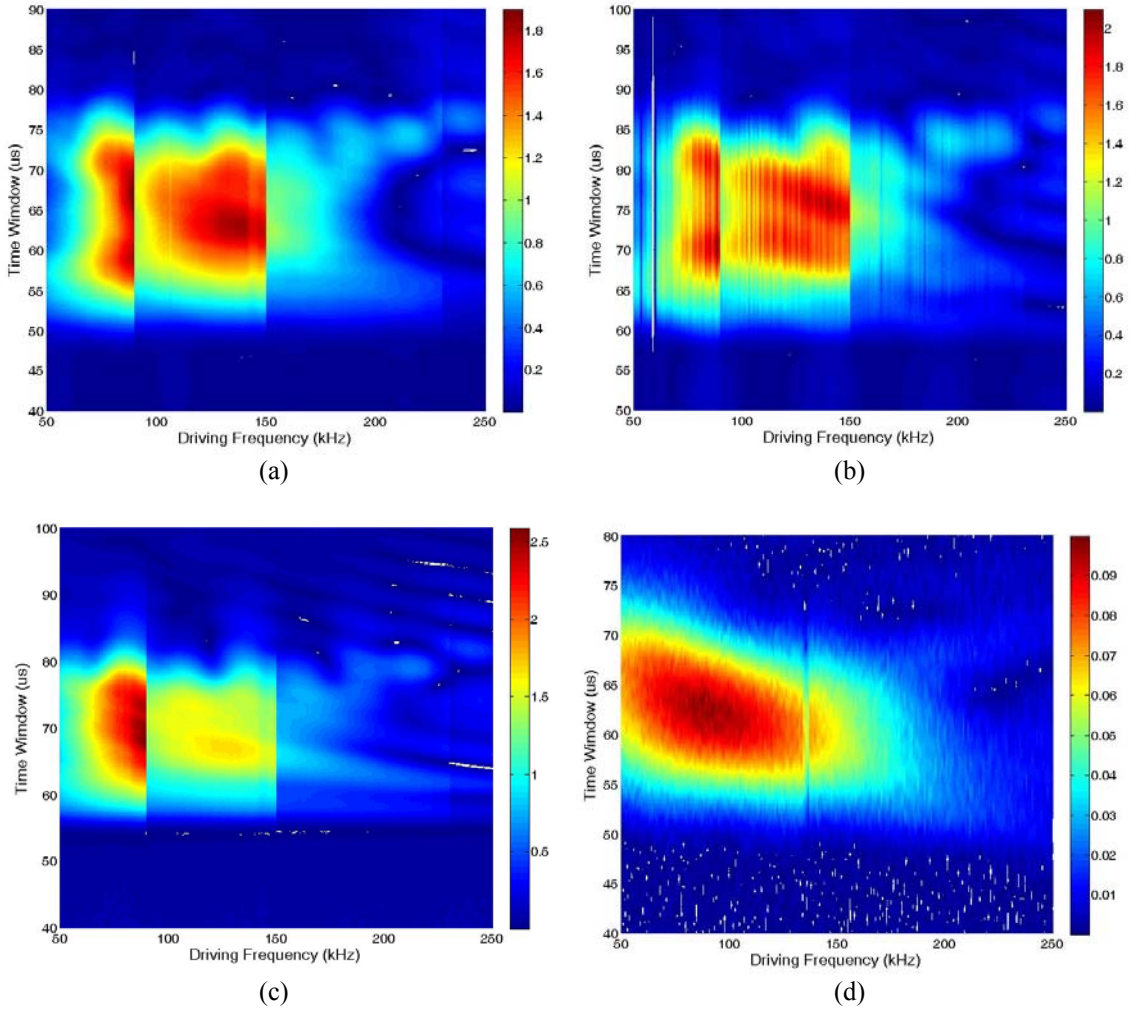

Figure 4.7: Base line data obtained using a solid 0.0625 inch diameter Remendur wire. The color scale depicts the magnitude of the analytic envelope based on the voltage received from: (a) MATEC #1, (b) MATEC #2, (c) LDV output for excitation by MATEC #1, and (d) LDV output for excitation by the AWG. The MATEC cards exhibit distinct voltage jumps near 90 kHz and 150 kHz. The artifact in the AWG results (d) is a by-product of triggering off of the excitation pulse.

A second set of frequency sweeps was performed on four specimens using AWG excitation. The color scale in Figure 4.8 plots the amplitude of the analytic envelope (obtained via the Hilbert transform) versus driving frequency. In Figure 4.8, it is important to note that the amplitude of the LDV voltage data can be affected by factors other than the strength of the magnetostrictive strain. For example, poor alignment on the laser and specimen wire can decrease LDV signal amplitude. However, the general trend of Remendur amplitude (Figure 4.8a) being greater than Arnokrome 3 amplitude (Figure 4.8b) being slightly greater than sleeve transducer amplitude (Figure 4.8d) is consistent with pulse-echo coil voltages recorded using the MATEC.

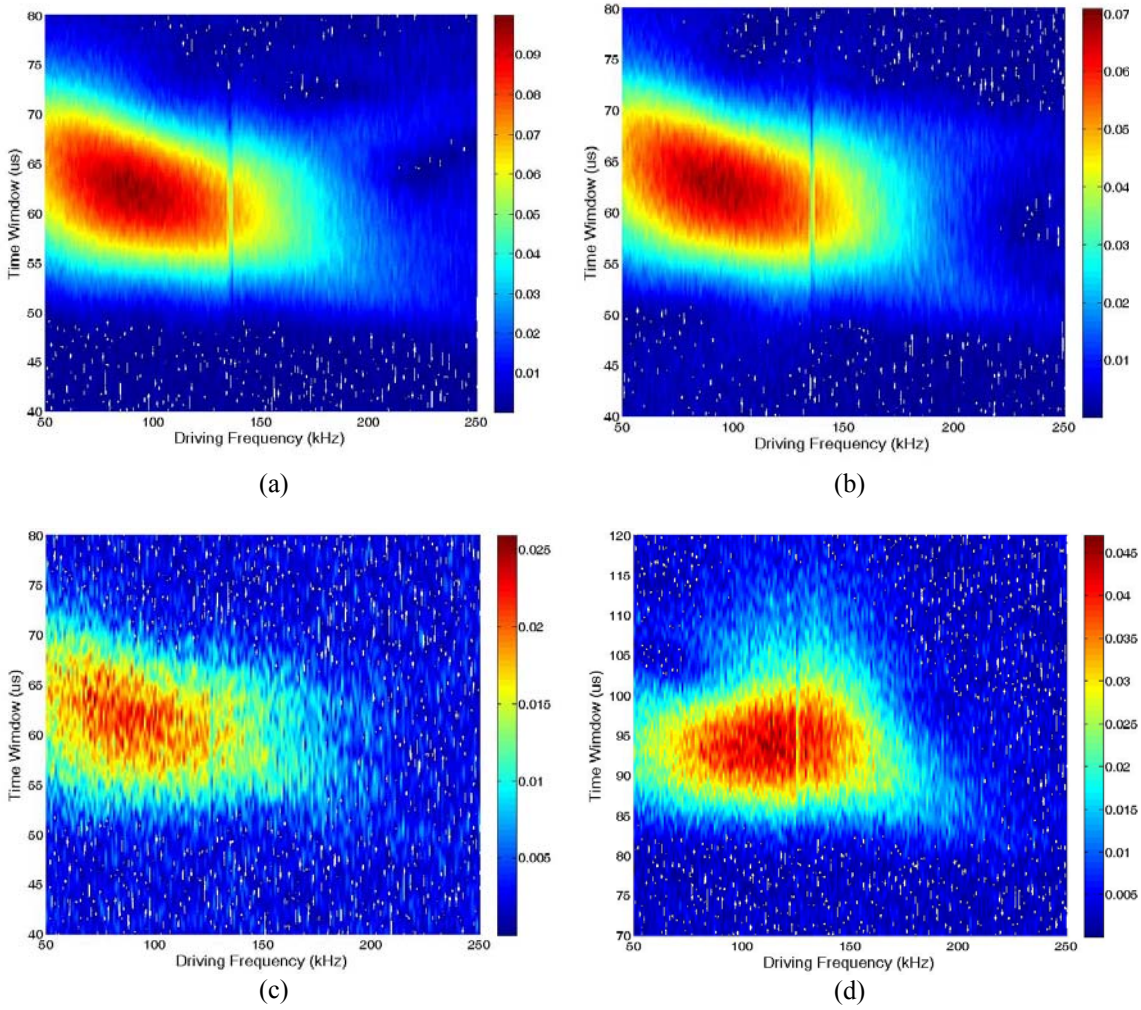

Figure 4.8: Time-domain comparison of four specimens using AWG excitation. The color scale depicts the magnitude of the analytic envelope based on the LDV output voltage for: (a) 0.0625 inch diameter Remendur wire, (b) 0.0625 inch diameter Arnokrome 3 wire, (c) 0.102 inch diameter Arnokrome 3 wire, and (d) a solid sleeve prototype. The artifact near 130 kHz is a result of triggering off of the driving voltage.

When interpreting the results in Figure 4.8, the trends of the analytic envelope data versus driving frequency are the more significant results. The 0.0635 inch diameter Remendur (Figure 4.8a) and the 0.0635 inch diameter Arnokrome 3 (Figure 4.8b) wires both performed well over the same frequency range (50 kHz to 200 kHz). The sleeve transducer (Figure 4.8d) demonstrated reduced signal strength near 50 kHz. Thus, the sleeve design has unique response to driving frequency.

As an alternative to analyzing the magnitude of the analytic envelope, a Fourier Transform can be performed on the received signals in order to analyze the frequency content produced for each driving frequency. The color scale in Figure 4.9 plots the amplitude of the Fourier transform versus driving frequency. Since Figure 4.9 is also based on LDV data, the peak frequencies and the trends of the Fourier transform versus driving frequency have the most significance.

Figure 4.9a shows that the 0.0625 inch diameter Remendur wire has a peak output frequency of approximately 85 kHz. Figure 4.9b shows that the 0.0625 inch diameter Arnokrome 3 had peak frequencies near 100 kHz and 120 kHz. The results for the sleeve transducer (Figure 4.9d) indicated a significantly narrower frequency spectrum with a peak frequency near 120 kHz. Based on the simple calculation in Equation 4.1 (where the sleeve length L corresponds to half a wavelength) it is reasonable to conclude that the sleeve length controls the optimal frequency.

$$f = \frac{c}{\lambda} = \frac{c}{2L} \approx \frac{5.5\,\text{mm}/\mu s}{2*0.875*25.4\text{mm}} = 123\text{kHz} \tag{4.1}$$

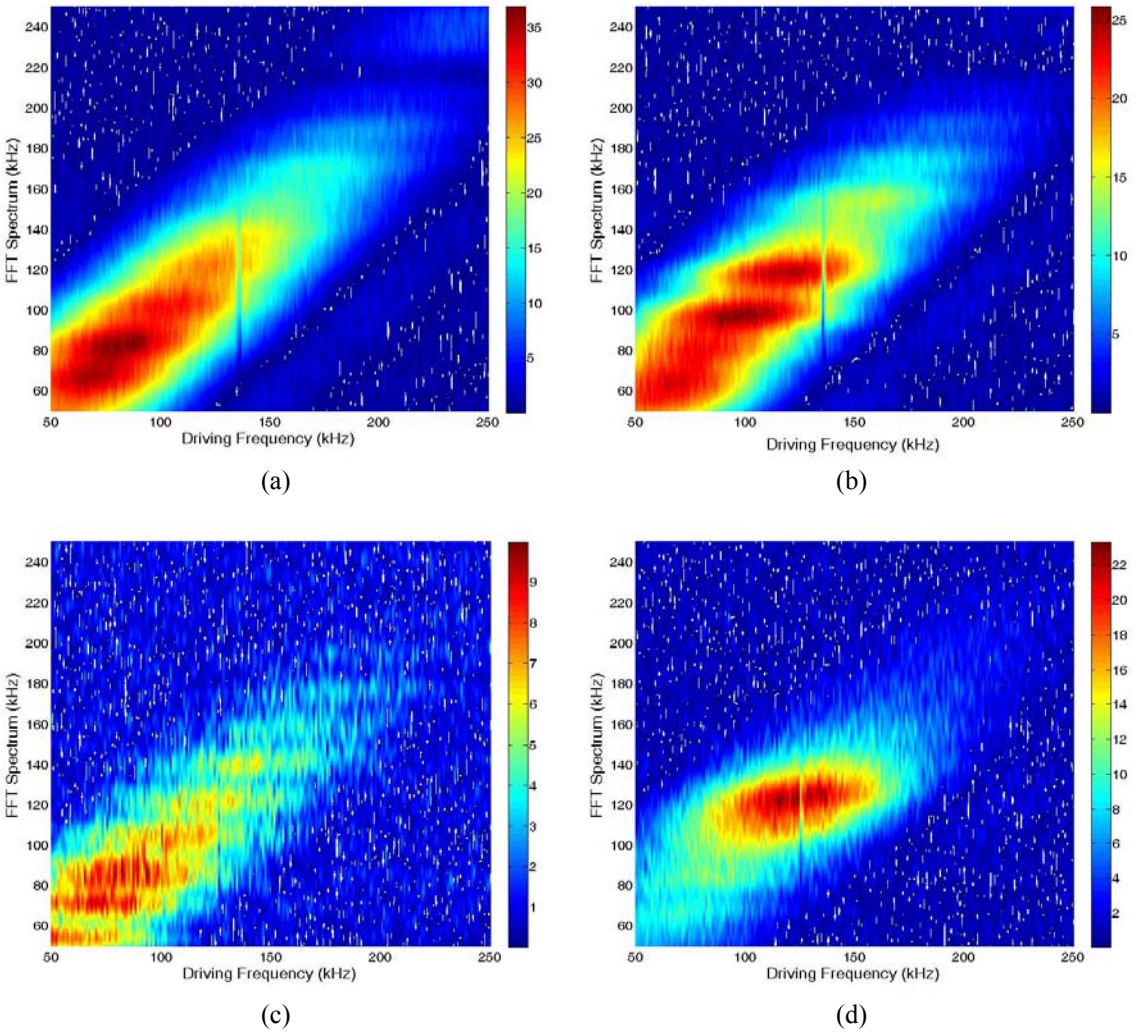

Figure 4.9: Frequency-domain comparison of four specimens using AWG excitation. The color scale depicts the amplitude of the Fourier transform spectrum based on the LDV output voltage for: (a) 0.0625 inch diameter Remendur wire, (b) 0.0625 inch diameter Arnokrome 3 wire, (c) 0.102 inch diameter Arnokrome 3 wire, and (d) a solid sleeve prototype. The artifact near 130 kHz is a result of triggering off of the driving voltage. The sleeve transducer design (d) exhibited less spectral content compared to standard magnetostrictive wires.

4.5 Comparison of Long Waveguides (With and Without Joints)

In section 4.4, the experimental tests focused on comparing the displacements produced by the sleeve design and a simple magnetostrictive wire. However, it was also important to characterize the effect of the wire-wire joint as well as different types of pulse excitation.

To study the effect of the pulse excitation, Laser Doppler Vibrometer (LDV) displacement measurements were performed on two specimens. One specimen consisted

of a magnetostrictive wire connected to a ~ 15 foot long stainless steel waveguide via the older wire-wire joint and brass coupling. The second specimen consisted of a magnetostrictive sleeve glued to a ~ 15 foot long stainless steel waveguide. The LDV was used to record the displacement amplitudes of the ultrasonic wave after the ultrasonic wave had traveled to the end of the 15 foot waveguide. A Fourier Transform was also calculated to determine the frequency content of each displacement measurement.

During these experiments, three different pulse excitations were used: a 20μs tone-burst, a 10μs tone-burst, and a 'quarter square' pulse.[7] The objective of testing the different pulse types was to determine if the pulse excitation could be tailored to achieve high bandwidth pulses with minimal width in time-of-flight.

Results are summarized in Figures 4.10 through 4.21. Because the LDV was used to perform displacement measurements on a 1/16 inch diameter wire and perfect alignment cannot be guaranteed, an accurate comparison of absolute displacement amplitude cannot be made. However, a comparison of pulse width and frequency content can be made.

Throughout the results (Figures 4.10 through 4.21), the magnetostrictive sleeve design consistently has a peak in the Fourier Transform results near 125 kHz when excited by the 'quarter square' pulse. This makes sense because the length of the magnetostrictive sleeve is approximately equal to one half of a wavelength at 125 kHz (as discussed in Section 4.4). Tone-burst excitation of the sleeve is more effective at generating frequency content above and below 125 kHz, but the sleeve naturally wants to vibrate at the frequency corresponding to the length of the sleeve.

The results for the wire-wire joint indicate that the wire-wire design is better at generating sub-125kHz frequency content. This also makes sense because the longer piece of magnetostrictive wire is better able to support the generation of lower frequencies (longer wavelengths). However, the wire-wire coupling adds noise and artifacts to the received signals. Also note that the natural hysteresis of magnetostrictive materials prevents higher frequency (> 250 kHz) content [69].

[7] A 'quarter square' pulse is a square pulse with a time width corresponding to ¼ of the period associated with the center driving frequency.

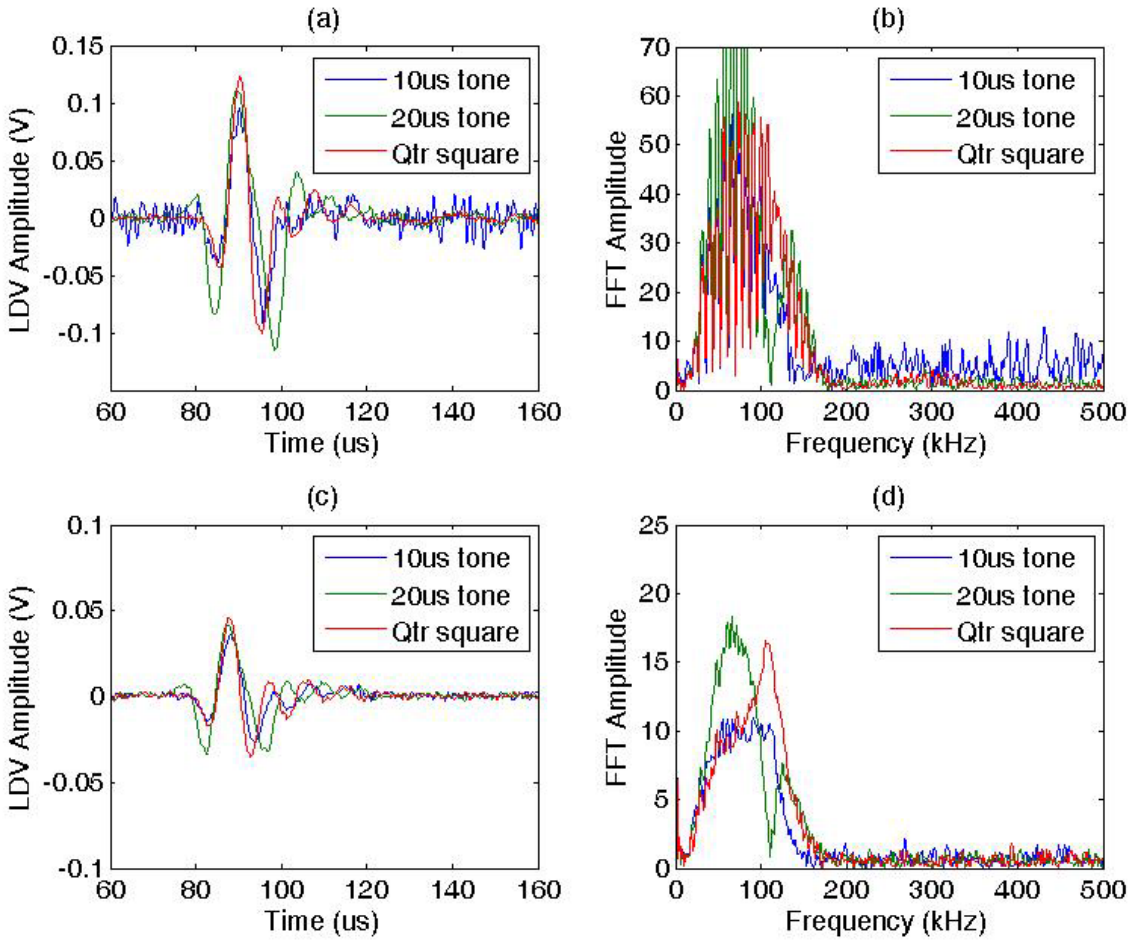

Figure 4.10: Comparison of wire-wire joint design and sleeve transducer design performance at 50 kHz. (a) LDV displacement measurements and (b) FFT results for the wire-wire joint design. (c) LDV displacement measurements and (d) FFT results for the sleeve design. In (d), note that the quarter period square pulse consistently produces a peak near 125 kHz which is the center frequency associated with the length of the magnetostrictive sleeve. The wire-wire joint design (b) appears to have more bandwidth compared to the sleeve design (d). However, the wire-wire joint suffers from signal noise and unwanted artifacts.

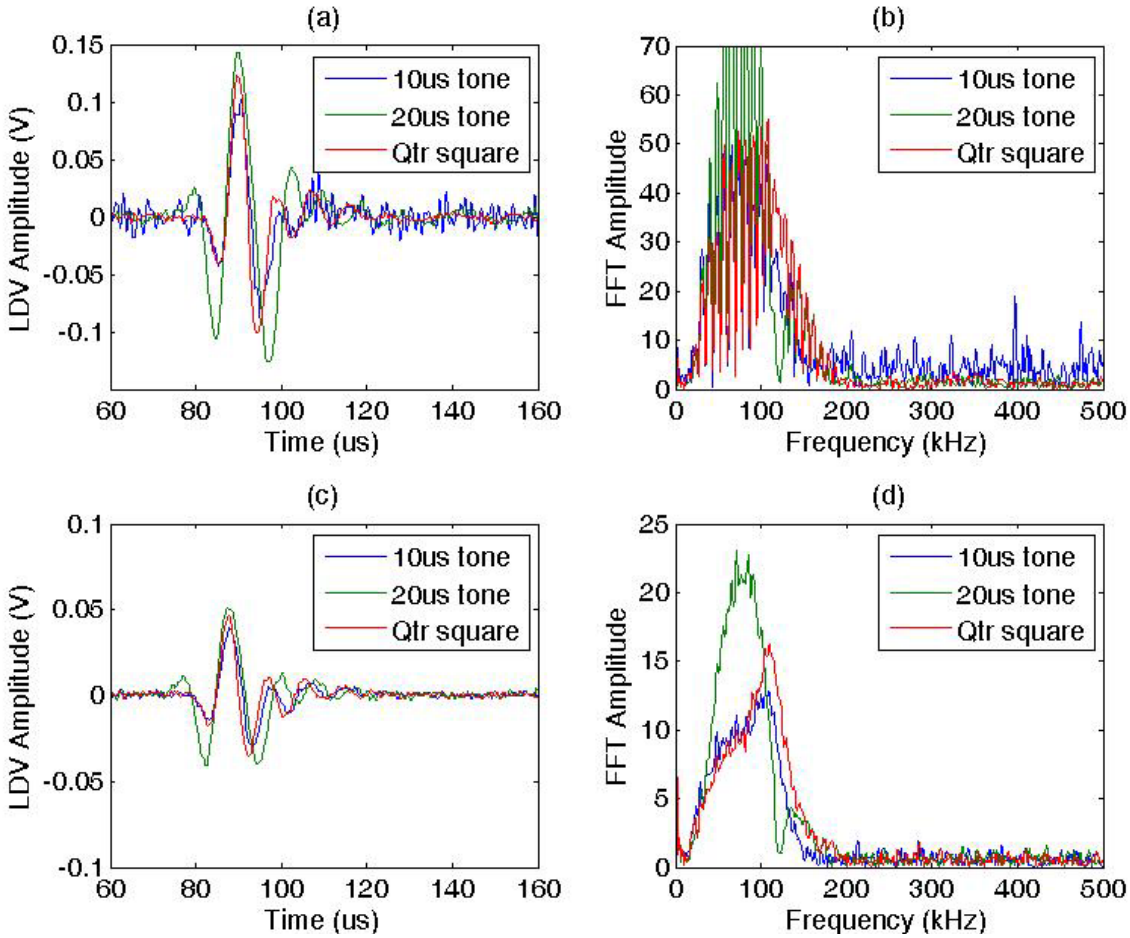

Figure 4.11: Comparison of wire-wire joint design and sleeve transducer design performance at 60 kHz. (a) LDV displacement measurements and (b) FFT results for the wire-wire joint design. (c) LDV displacement measurements and (d) FFT results for the sleeve design. In (d), note that the quarter period square pulse consistently produces a peak near 125 kHz which is the center frequency associated with the length of the magnetostrictive sleeve. The wire-wire joint design (b) appears to have more bandwidth compared to the sleeve design (d). However, the wire-wire joint suffers from signal noise and unwanted artifacts.

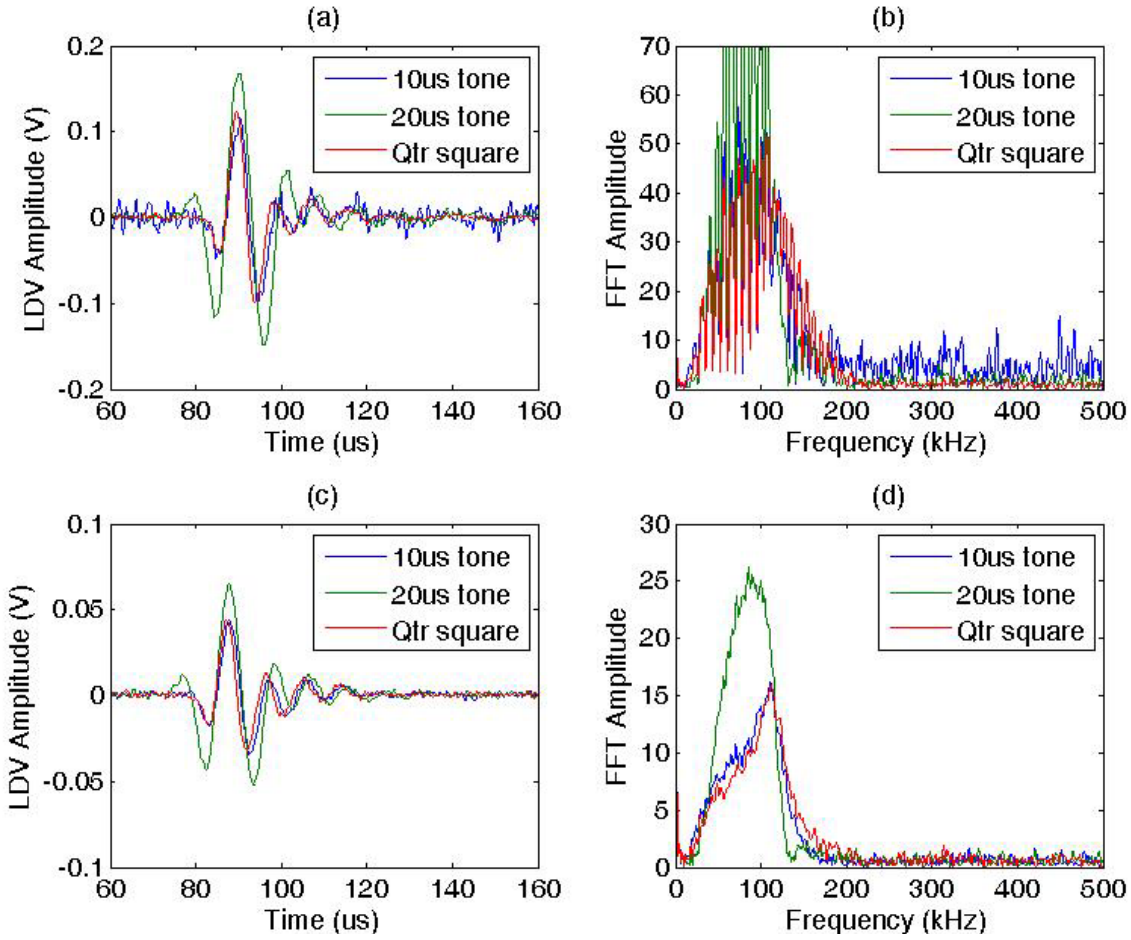

Figure 4.12: Comparison of wire-wire joint design and sleeve transducer design performance at 71 kHz. (a) LDV displacement measurements and (b) FFT results for the wire-wire joint design. (c) LDV displacement measurements and (d) FFT results for the sleeve design. In (d), note that the quarter period square pulse consistently produces a peak near 125 kHz which is the center frequency associated with the length of the magnetostrictive sleeve. The wire-wire joint design (b) appears to have more bandwidth compared to the sleeve design (d). However, the wire-wire joint suffers from signal noise and unwanted artifacts.

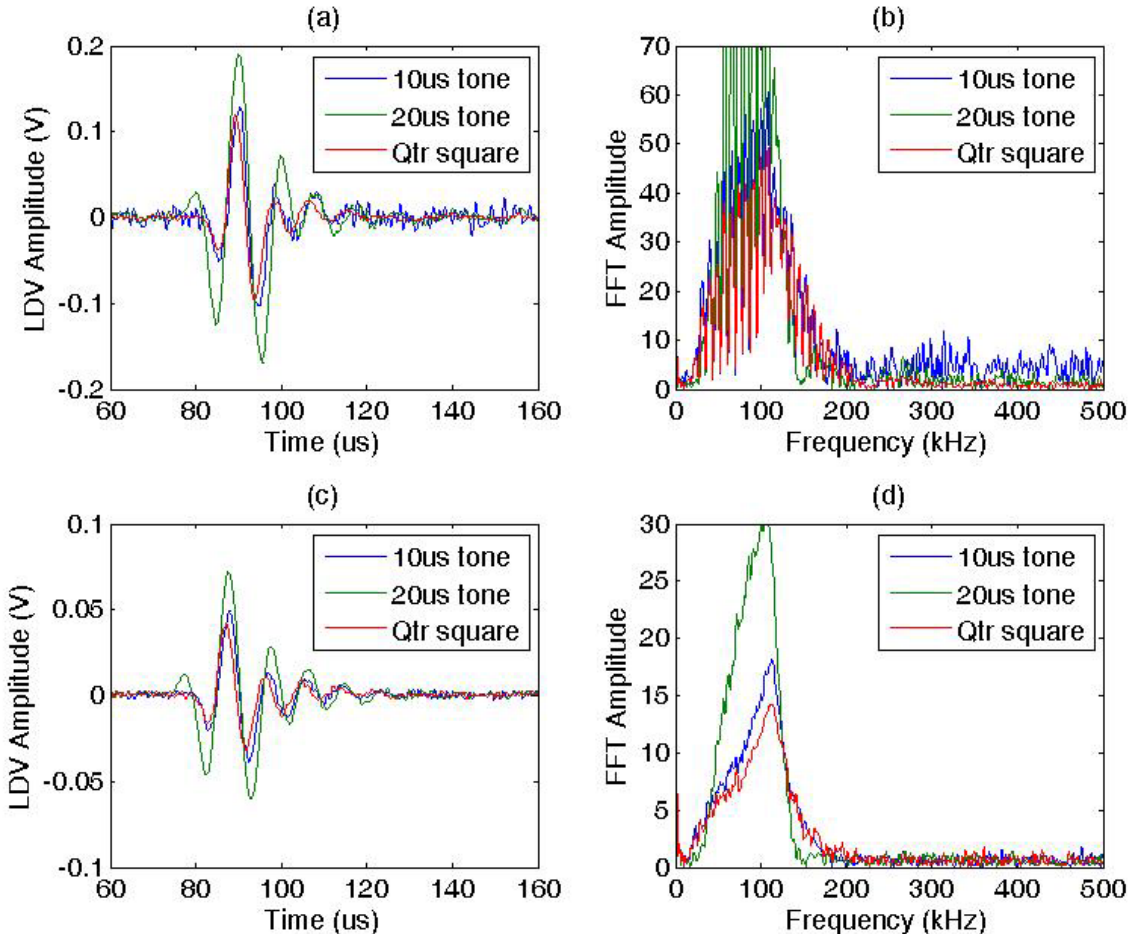

Figure 4.13: Comparison of wire-wire joint design and sleeve transducer design performance at 81 kHz. (a) LDV displacement measurements and (b) FFT results for the wire-wire joint design. (c) LDV displacement measurements and (d) FFT results for the sleeve design. In (d), note that the quarter period square pulse consistently produces a peak near 125 kHz which is the center frequency associated with the length of the magnetostrictive sleeve. The wire-wire joint design (b) appears to have more bandwidth compared to the sleeve design (d). However, the wire-wire joint suffers from signal noise and unwanted artifacts.

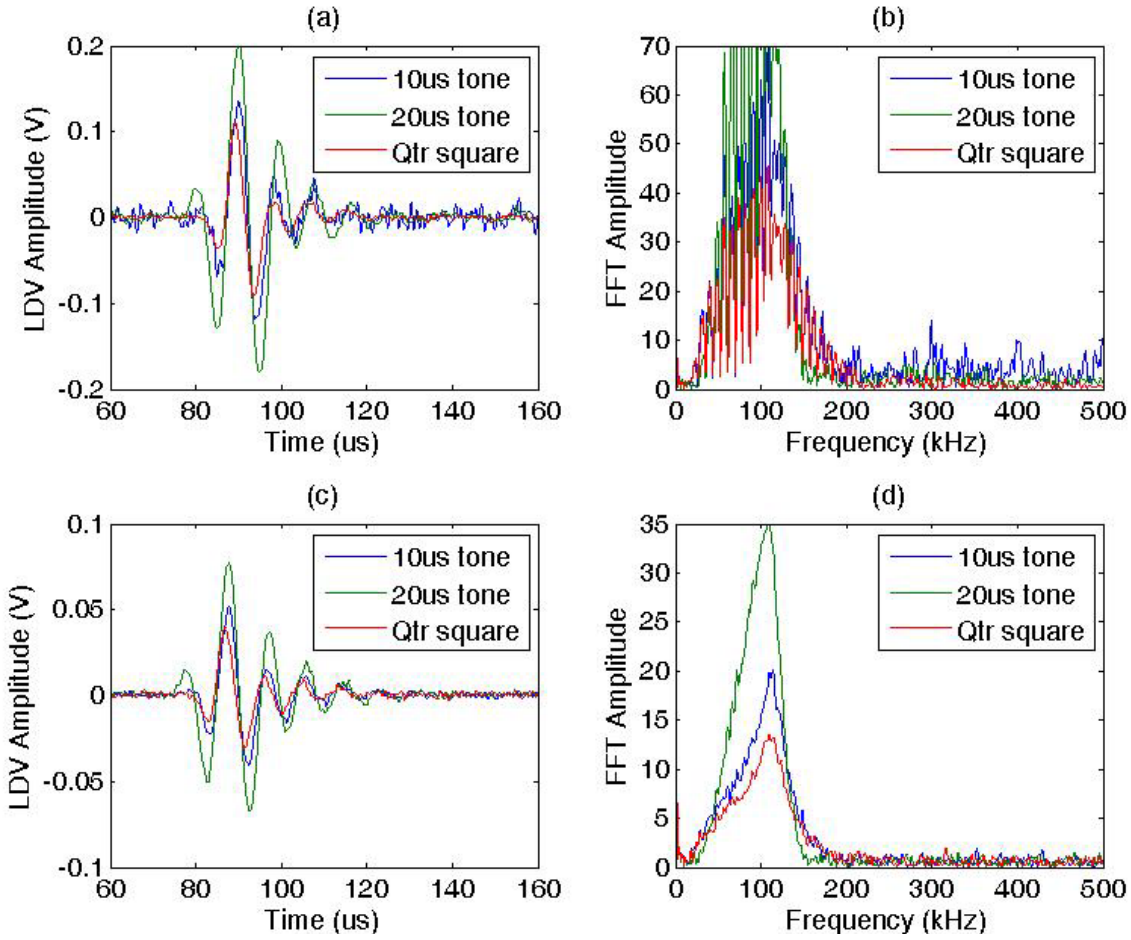

Figure 4.14: Comparison of wire-wire joint design and sleeve transducer design performance at 89 kHz. (a) LDV displacement measurements and (b) FFT results for the wire-wire joint design. (c) LDV displacement measurements and (d) FFT results for the sleeve design. In (d), note that the quarter period square pulse consistently produces a peak near 125 kHz which is the center frequency associated with the length of the magnetostrictive sleeve. The wire-wire joint design (b) appears to have more bandwidth compared to the sleeve design (d). However, the wire-wire joint suffers from signal noise and unwanted artifacts.

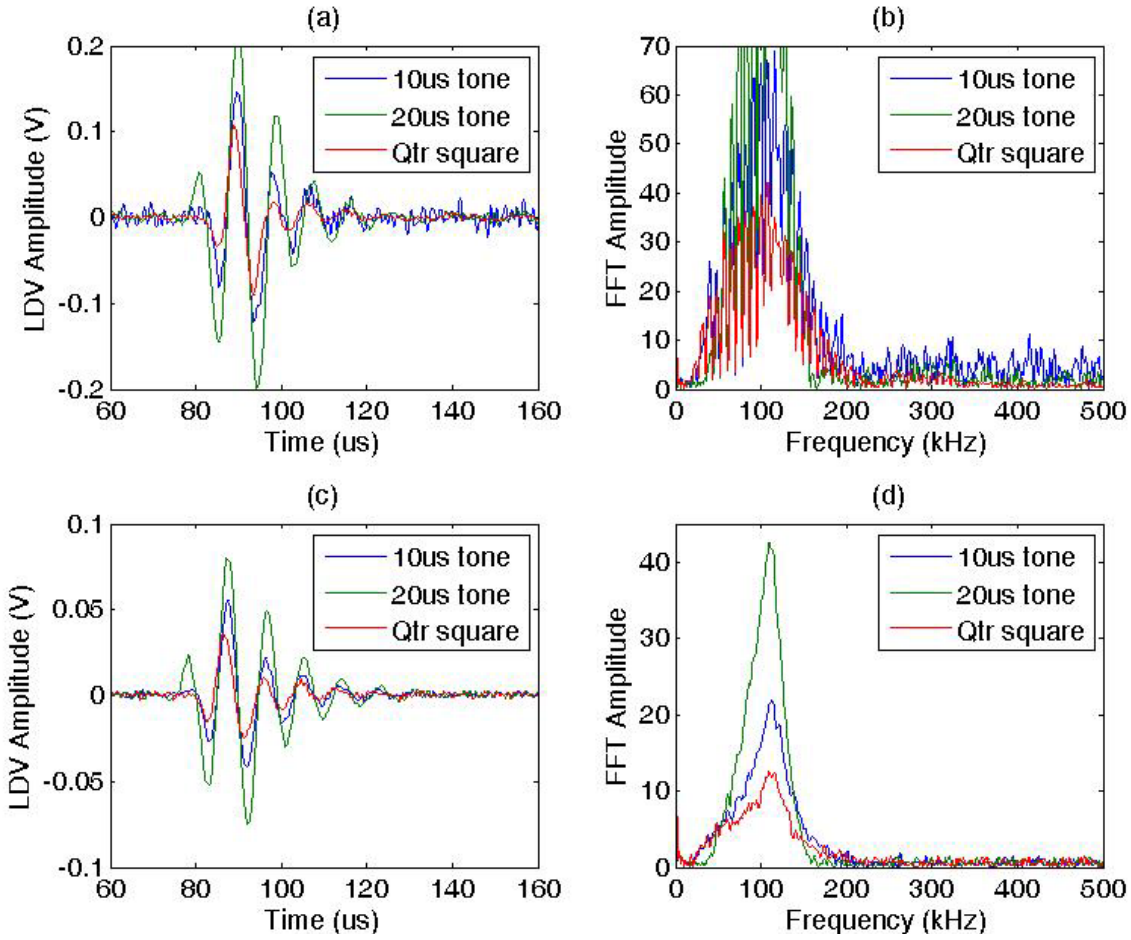

Figure 4.15: Comparison of wire-wire joint design and sleeve transducer design performance at 100 kHz. (a) LDV displacement measurements and (b) FFT results for the wire-wire joint design. (c) LDV displacement measurements and (d) FFT results for the sleeve design. In (d), note that the quarter period square pulse consistently produces a peak near 125 kHz which is the center frequency associated with the length of the magnetostrictive sleeve. The wire-wire joint design (b) appears to have more bandwidth compared to the sleeve design (d). However, the wire-wire joint suffers from signal noise and unwanted artifacts.

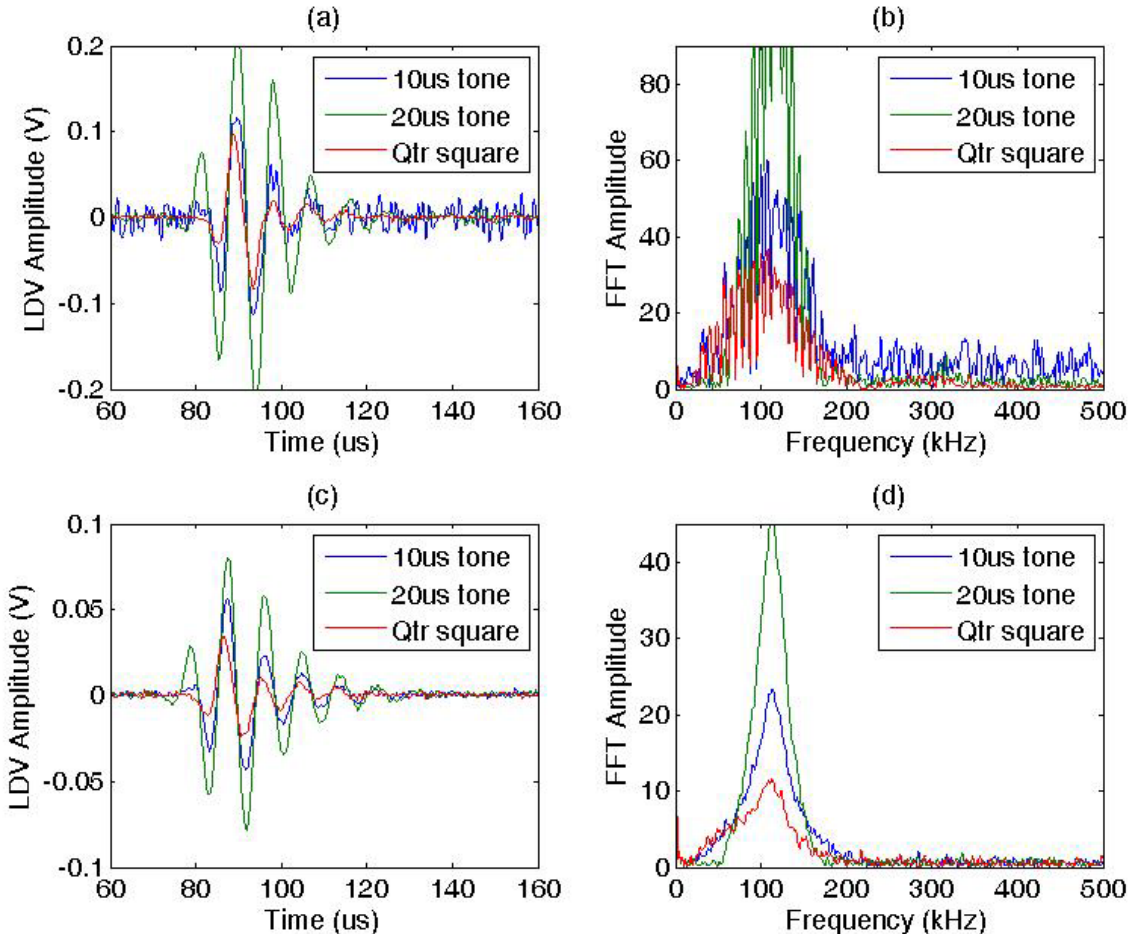

Figure 4.16: Comparison of wire-wire joint design and sleeve transducer design performance at 114 kHz. (a) LDV displacement measurements and (b) FFT results for the wire-wire joint design. (c) LDV displacement measurements and (d) FFT results for the sleeve design. In (d), note that the quarter period square pulse consistently produces a peak near 125 kHz which is the center frequency associated with the length of the magnetostrictive sleeve. The wire-wire joint design (b) appears to have more bandwidth compared to the sleeve design (d). However, the wire-wire joint suffers from signal noise and unwanted artifacts.

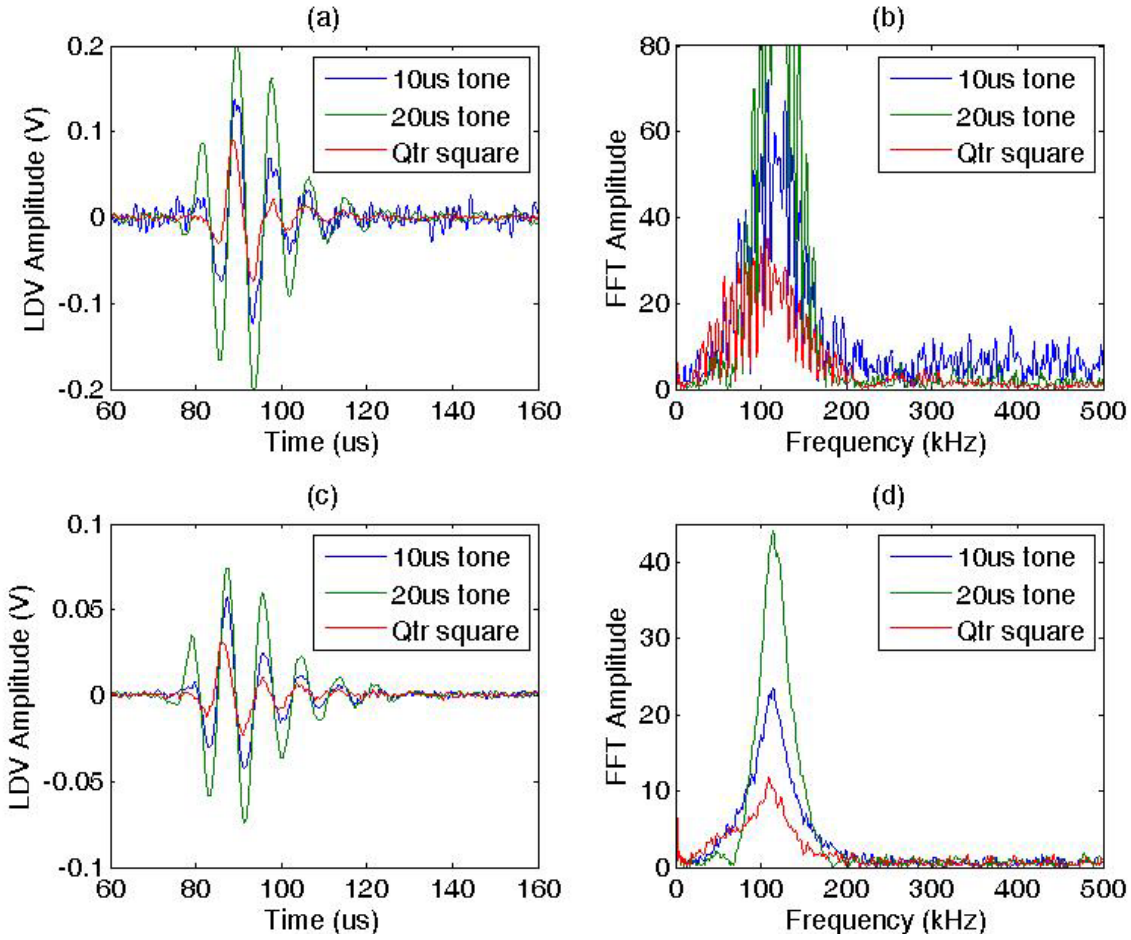

Figure 4.17: Comparison of wire-wire joint design and sleeve transducer design performance at 125 kHz. (a) LDV displacement measurements and (b) FFT results for the wire-wire joint design. (c) LDV displacement measurements and (d) FFT results for the sleeve design. In (d), note that the quarter period square pulse consistently produces a peak near 125 kHz which is the center frequency associated with the length of the magnetostrictive sleeve. The wire-wire joint design (b) appears to have more bandwidth compared to the sleeve design (d). However, the wire-wire joint suffers from signal noise and unwanted artifacts.

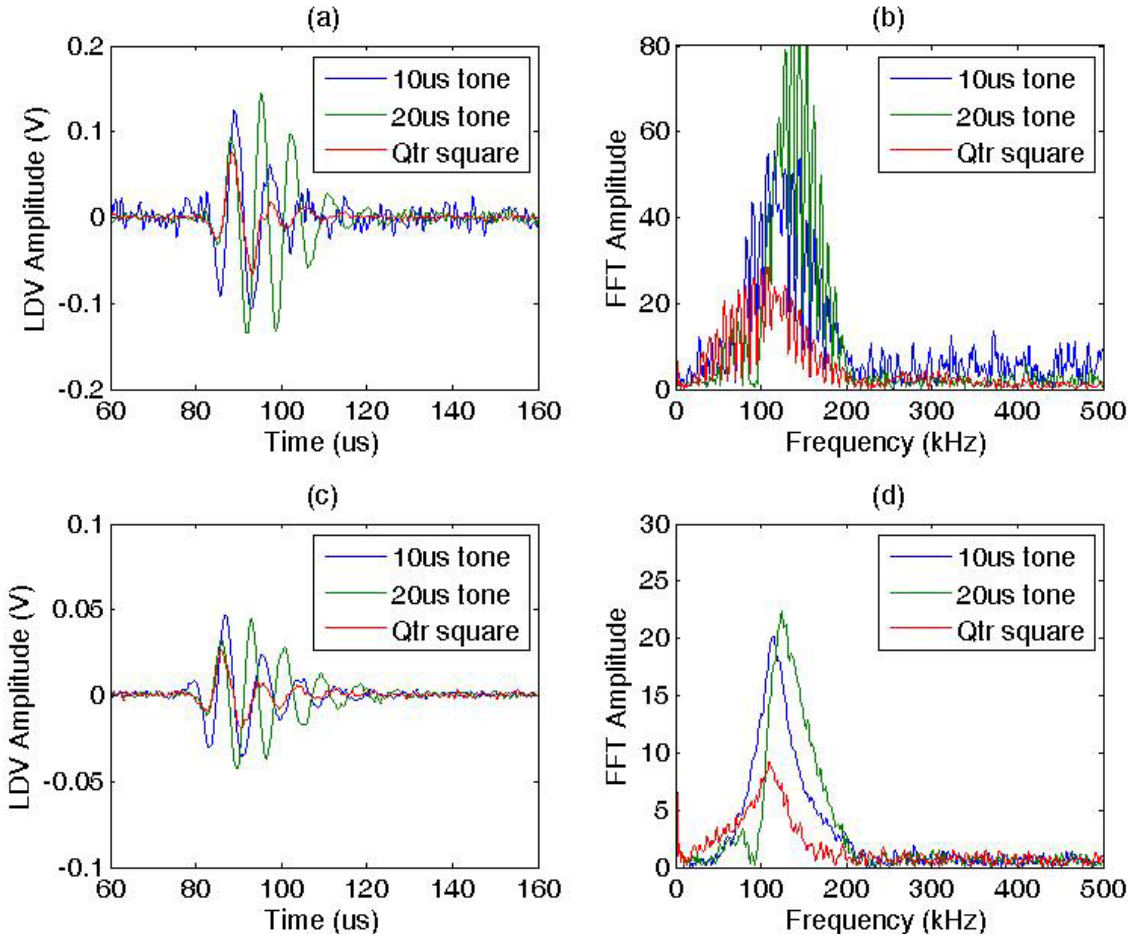

Figure 4.18: Comparison of wire-wire joint design and sleeve transducer design performance at 156 kHz. (a) LDV displacement measurements and (b) FFT results for the wire-wire joint design. (c) LDV displacement measurements and (d) FFT results for the sleeve design. In (d), note that the quarter period square pulse consistently produces a peak near 125 kHz which is the center frequency associated with the length of the magnetostrictive sleeve. The wire-wire joint design (b) appears to have more bandwidth compared to the sleeve design (d). However, the wire-wire joint suffers from signal noise and unwanted artifacts.

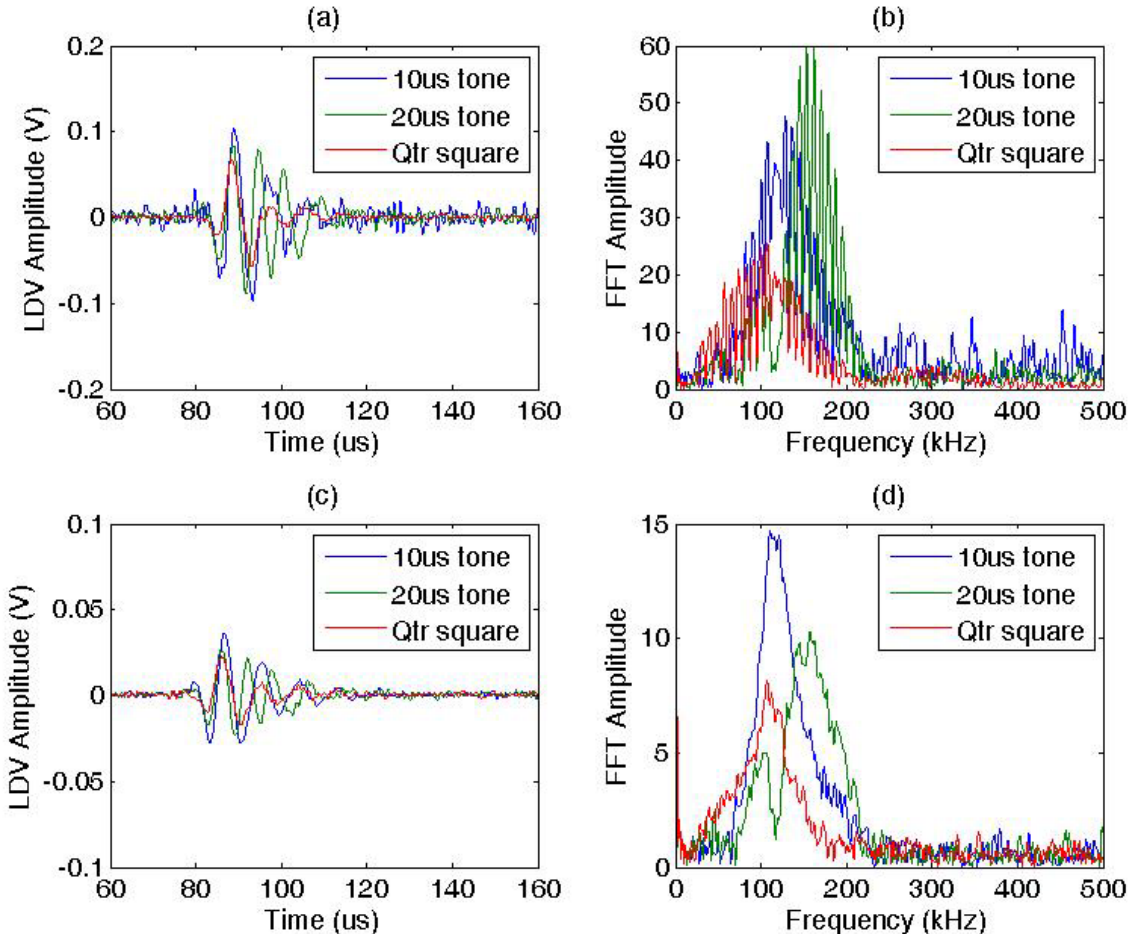

Figure 4.19: Comparison of wire-wire joint design and sleeve transducer design performance at 179 kHz. (a) LDV displacement measurements and (b) FFT results for the wire-wire joint design. (c) LDV displacement measurements and (d) FFT results for the sleeve design. In (d), note that the quarter period square pulse consistently produces a peak near 125 kHz which is the center frequency associated with the length of the magnetostrictive sleeve. The wire-wire joint design (b) appears to have more bandwidth compared to the sleeve design (d). However, the wire-wire joint suffers from signal noise and unwanted artifacts.

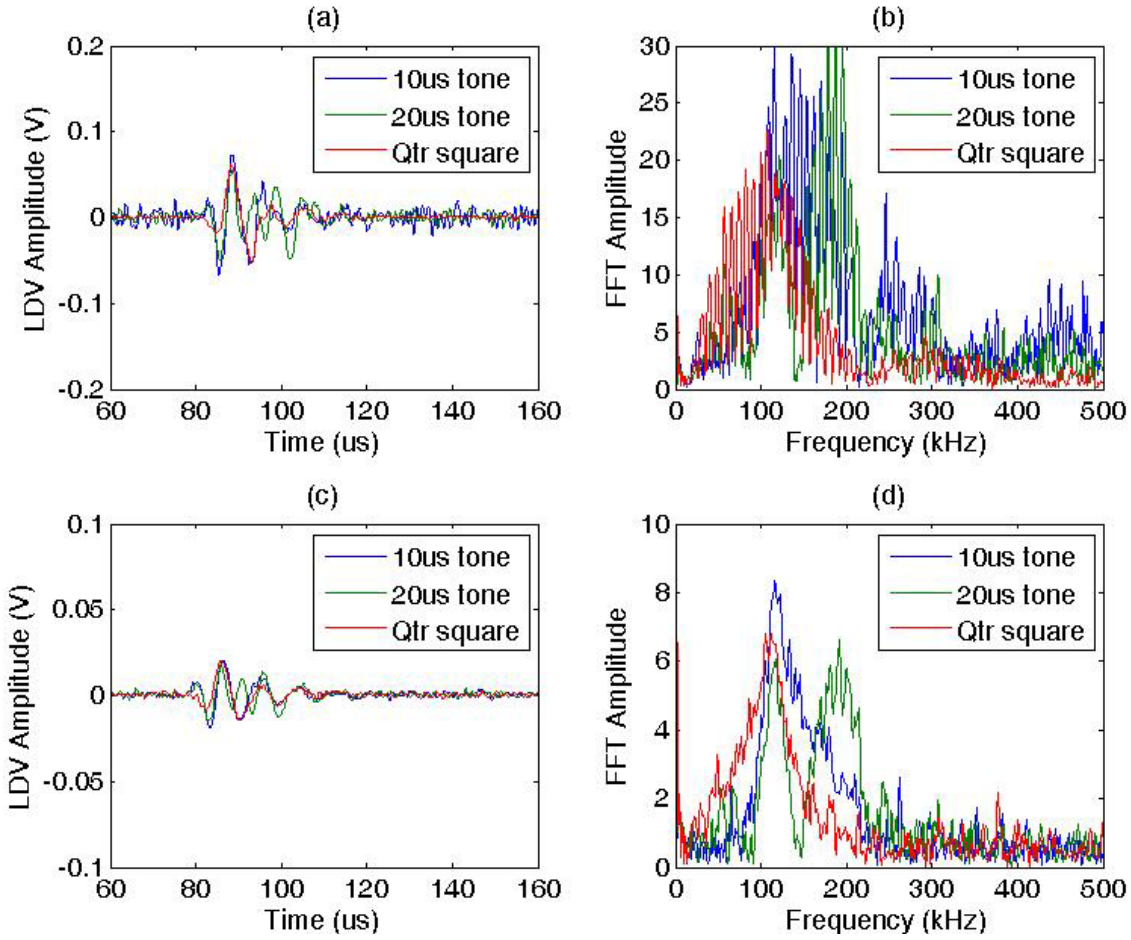

Figure 4.20: Comparison of wire-wire joint design and sleeve transducer design performance at 208 kHz. (a) LDV displacement measurements and (b) FFT results for the wire-wire joint design. (c) LDV displacement measurements and (d) FFT results for the sleeve design. In (d), note that the quarter period square pulse consistently produces a peak near 125 kHz which is the center frequency associated with the length of the magnetostrictive sleeve. The wire-wire joint design (b) appears to have more bandwidth compared to the sleeve design (d). However, the wire-wire joint suffers from signal noise and unwanted artifacts.

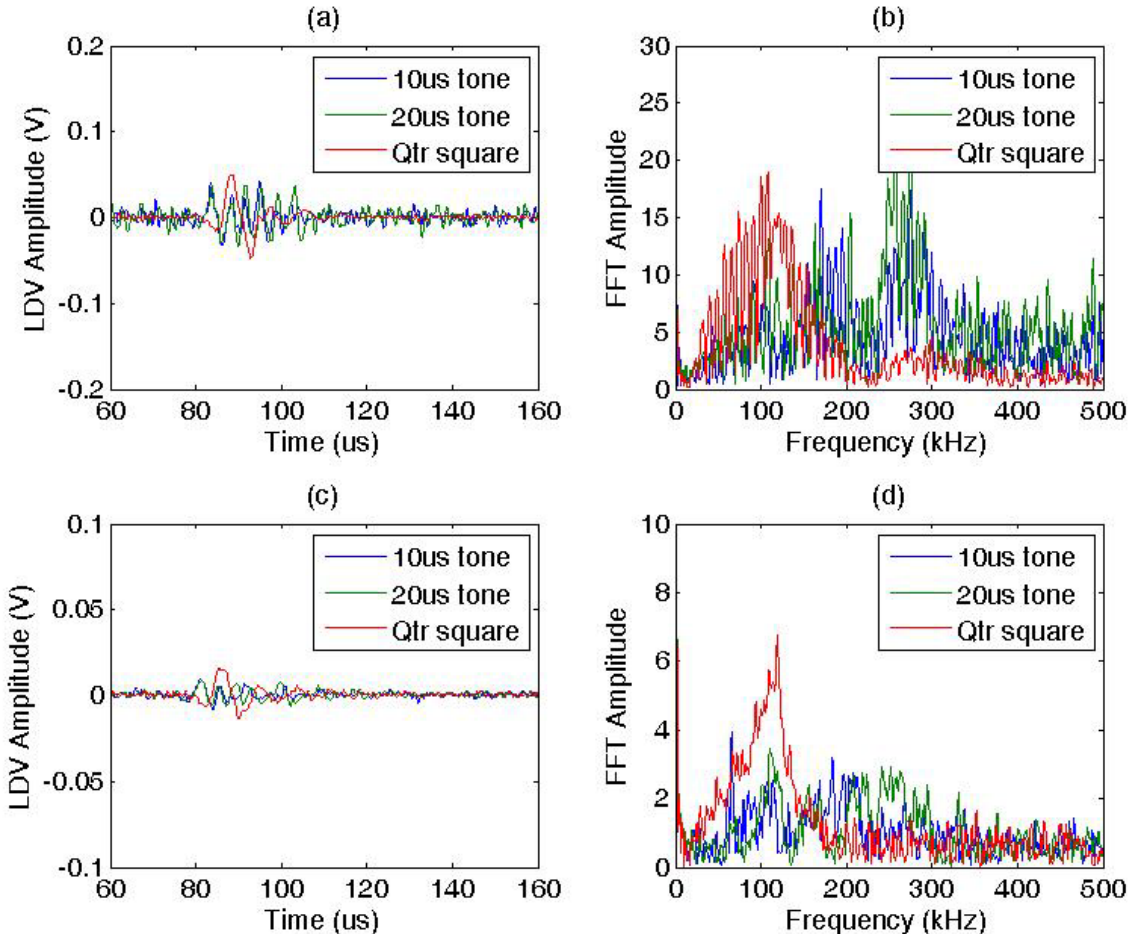

Figure 4.21: Comparison of wire-wire joint design and sleeve transducer design performance at 250 kHz. (a) LDV displacement measurements and (b) FFT results for the wire-wire joint design. (c) LDV displacement measurements and (d) FFT results for the sleeve design. In (d), note that the quarter period square pulse consistently produces a peak near 125 kHz which is the center frequency associated with the length of the magnetostrictive sleeve. The wire-wire joint design (b) appears to have more bandwidth compared to the sleeve design (d). However, the wire-wire joint suffers from signal noise and unwanted artifacts.

The results shown in Figures 4.10 through 4.21 indicate that a 20 μs tone-burst pulse width generates a wider pulse compared to the 10 μs tone-burst pulse. However, there was not a significant difference between the 10 μs tone-burst pulse and the 'quarter square' pulse excitation. Figure 4.22 shows a comparison of a tone-burst excitation and a high voltage 'quarter square' pulse excitation. The high bandwidth square pulse does not appear to reduce the natural ringing of the sleeve transducer. Considering that the period of a 125 kHz signal is 8 μs, the total pulse width observed with the magnetostrictive excitation will always be significantly longer compared to MHz frequency signals.

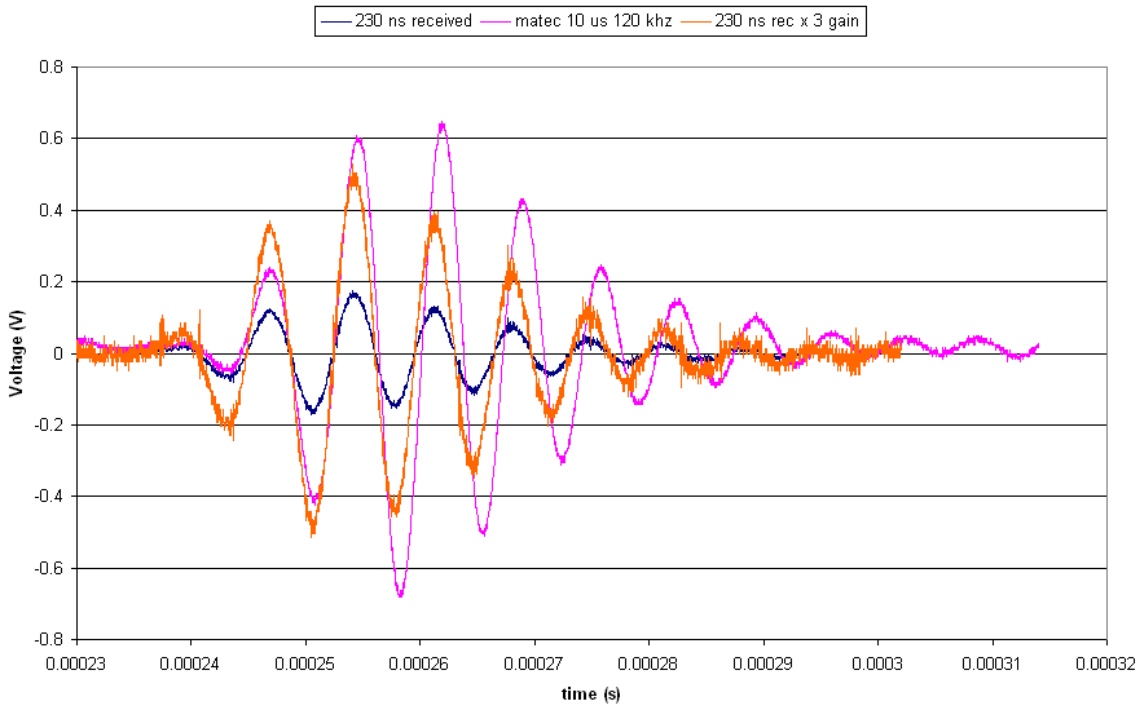

Figure 4.22: Comparison of waveforms produced with different pulse excitations. The approximately 4.5 MHz 'square pulse' does not produce a 'sharp,' high bandwidth pulse when using the magnetostrictive sleeve design.

4.6 Comparison of Different Sleeve Materials

In a separate set of experiments, Laser Doppler Vibrometer (LDV) displacement measurements were performed on three different sleeve specimens. One specimen consisted of an Arnokrome 3 sleeve glued to a 6 foot long stainless steel waveguide. The second specimen consisted of a Remendur sleeve glued to a 6 foot long stainless steel waveguide. The third sleeve was a piezoelectric cylinder which was attached to a 6 foot long stainless steel waveguide using the set screw in the transducer housing.[8] The LDV was used to record the displacement amplitudes of the ultrasonic wave after the ultrasonic wave had traveled to the end of the 6 foot waveguide. A Fourier Transform was also calculated to determine the frequency content of each displacement measurement. As before, three different pulse excitations (a 20μs tone-burst, a 10μs tone-burst, and a 'quarter square' pulse[9]) were used during these experiments.

[8] Piezoelectric cylinder transducer provided by Gerald Posakony, Pacific Northwest National Laboratory.
[9] A 'quarter square' pulse is a square pulse with a time width corresponding to ¼ of the period associated with the center driving frequency.

Figures 4.23 through 4.34 summarize the results from all cylinders for the frequency range 50 kHz to 250 kHz. Additional results for the piezoelectric sleeve are given in Figures 4.35 through 4.37 for measurements at 312 kHz, 417 kHz, and 500 kHz, respectively. Because the LDV was used to perform displacement measurements on a 1/16 inch diameter wire and perfect alignment cannot be guaranteed, an accurate comparison of absolute displacement amplitude cannot be made. However, a comparison of pulse width and frequency content can be made.

Once again, the magnetostrictive sleeves (both Arnokrome 3 and Remendur) produced peaks in the frequency spectrum near 125 kHz. The frequency spectra obtained for the Arnokrome 3 sleeve were not as sharp or smooth as the frequency spectra obtained for Remendur sleeve. This could potentially be an indication of a poor glue bond for this Arnokrome 3 specimen.

In the frequency sweep of the piezoelectric sleeve, the highest displacement amplitudes were recorded for the tests at 312 kHz, 417 kHz, and 500 kHz (Figures 4.35 through 4.37). This was expected because the piezoelectric sleeve was designed to have a 400 kHz central frequency. At certain driving frequencies (71 kHz to 125 kHz) (Figures 4.25 through 4.30), the data from the piezoelectric sleeve measurements also produced a peak near 125 kHz. This was somewhat unexpected since the piezoelectric sleeve was rated for a 400 kHz central frequency and had a much shorter length than the magnetostrictive sleeves. This suggests that the 1/16 inch diameter wire waveguide is particularly susceptible to guided waves propagation at approximately 125 kHz.

The results shown in Figures 4.23 through 4.34 also indicate that a 20 μs tone-burst pulse width generates a wider pulse compared to the 10 μs tone-burst pulse. However, there was not a significant difference between the 10 μs tone-burst pulse and the ‘quarter square’ pulse excitation. This is in agreement with the results presented in Section 4.5.

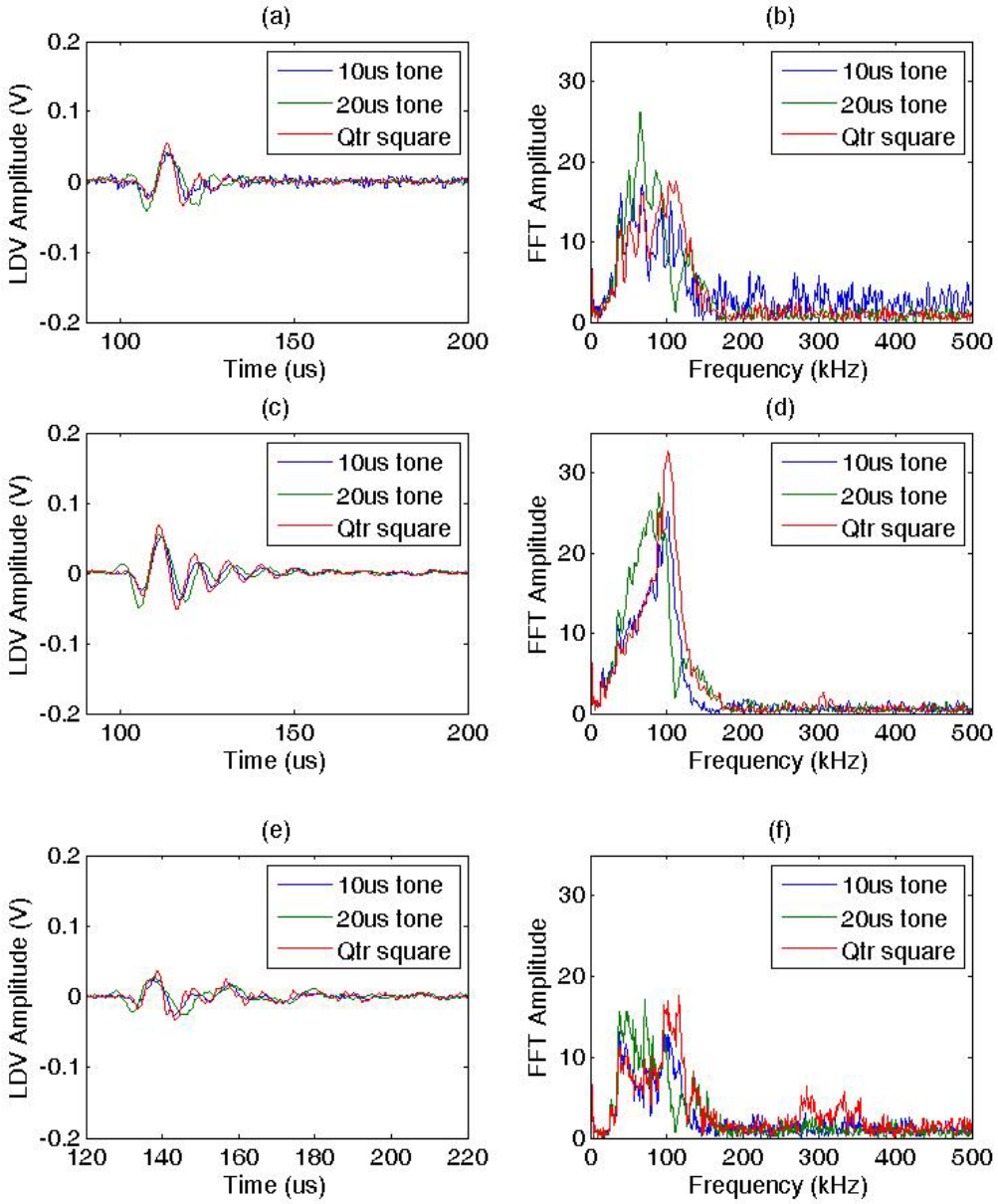

Figure 4.23: Comparison of an Arnokrome 3 sleeve, a Remendur sleeve, and a piezoelectric cylinder sleeve at 50 kHz. (a) LDV displacement measurements and (b) FFT results for the Arnokrome 3 sleeve. (c) LDV displacement measurements and (d) FFT results for the Remendur sleeve. (e) LDV displacement measurements and (f) FFT results for the piezoelectric cylinder sleeve transducer.

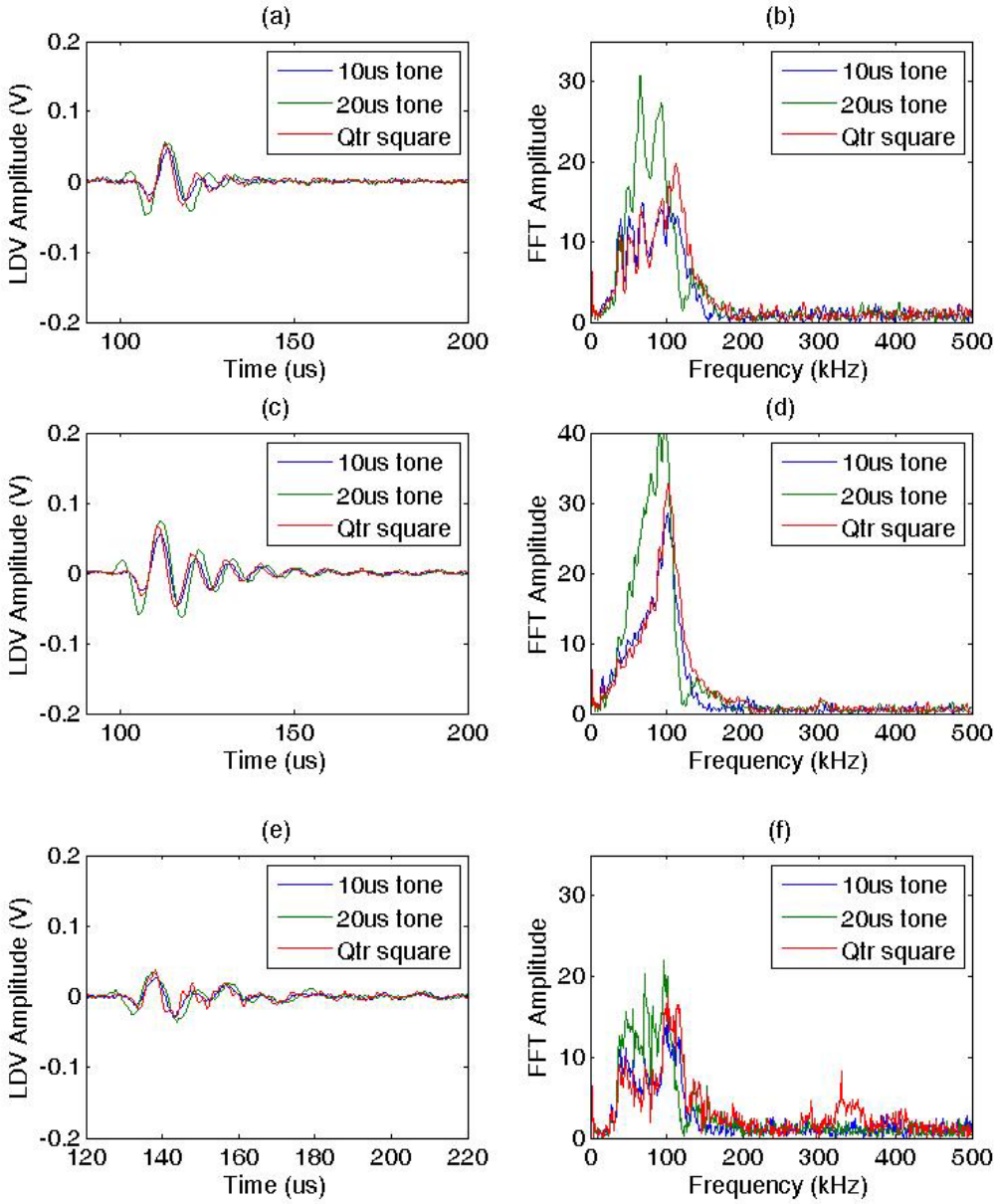

Figure 4.24: Comparison of an Arnokrome 3 sleeve, a Remendur sleeve, and a piezoelectric cylinder sleeve at 60 kHz. (a) LDV displacement measurements and (b) FFT results for the Arnokrome 3 sleeve. (c) LDV displacement measurements and (d) FFT results for the Remendur sleeve. (e) LDV displacement measurements and (f) FFT results for the piezoelectric cylinder sleeve transducer.

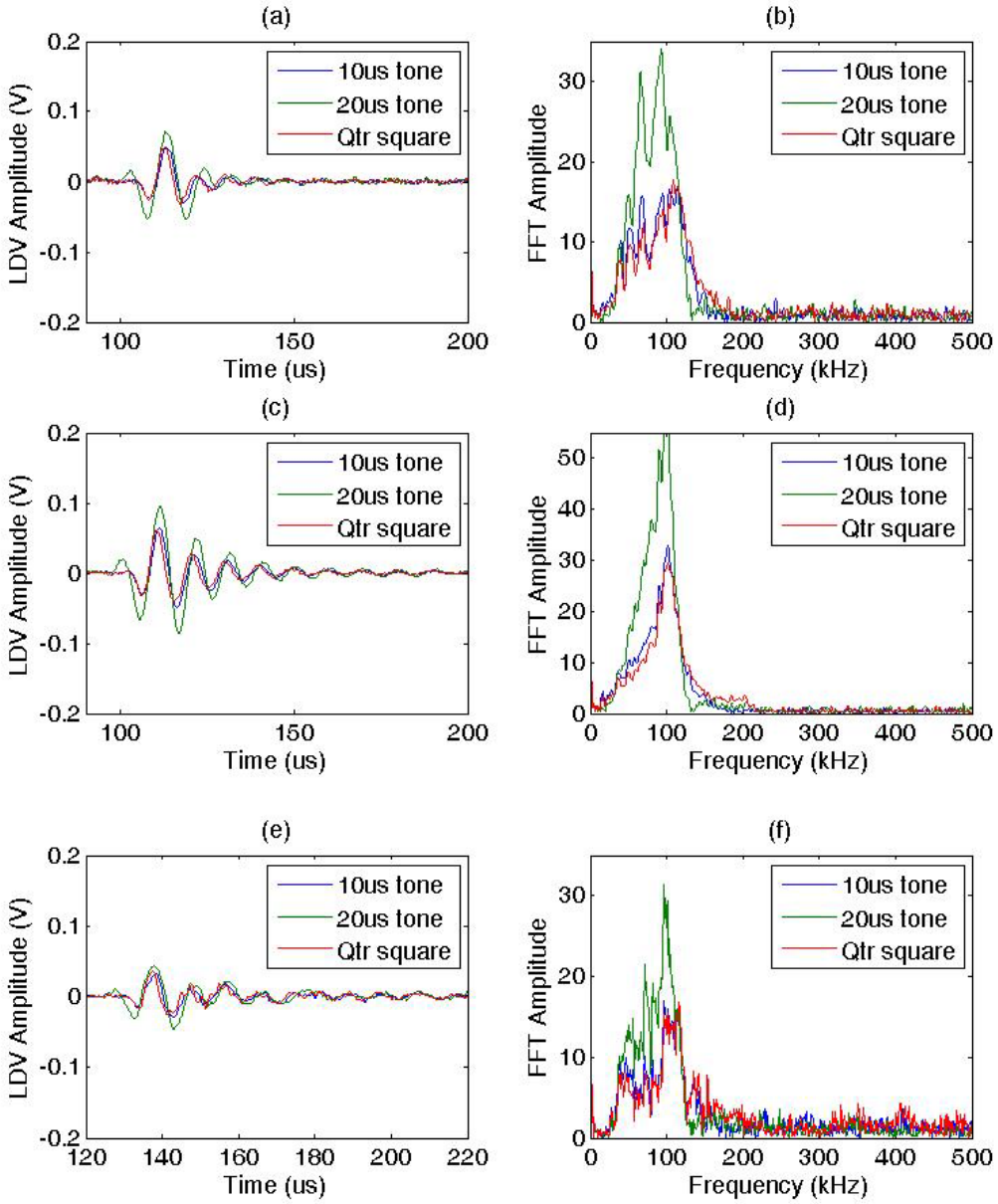

Figure 4.25: Comparison of an Arnokrome 3 sleeve, a Remendur sleeve, and a piezoelectric cylinder sleeve at 71 kHz. (a) LDV displacement measurements and (b) FFT results for the Arnokrome 3 sleeve. (c) LDV displacement measurements and (d) FFT results for the Remendur sleeve. (e) LDV displacement measurements and (f) FFT results for the piezoelectric cylinder sleeve transducer.

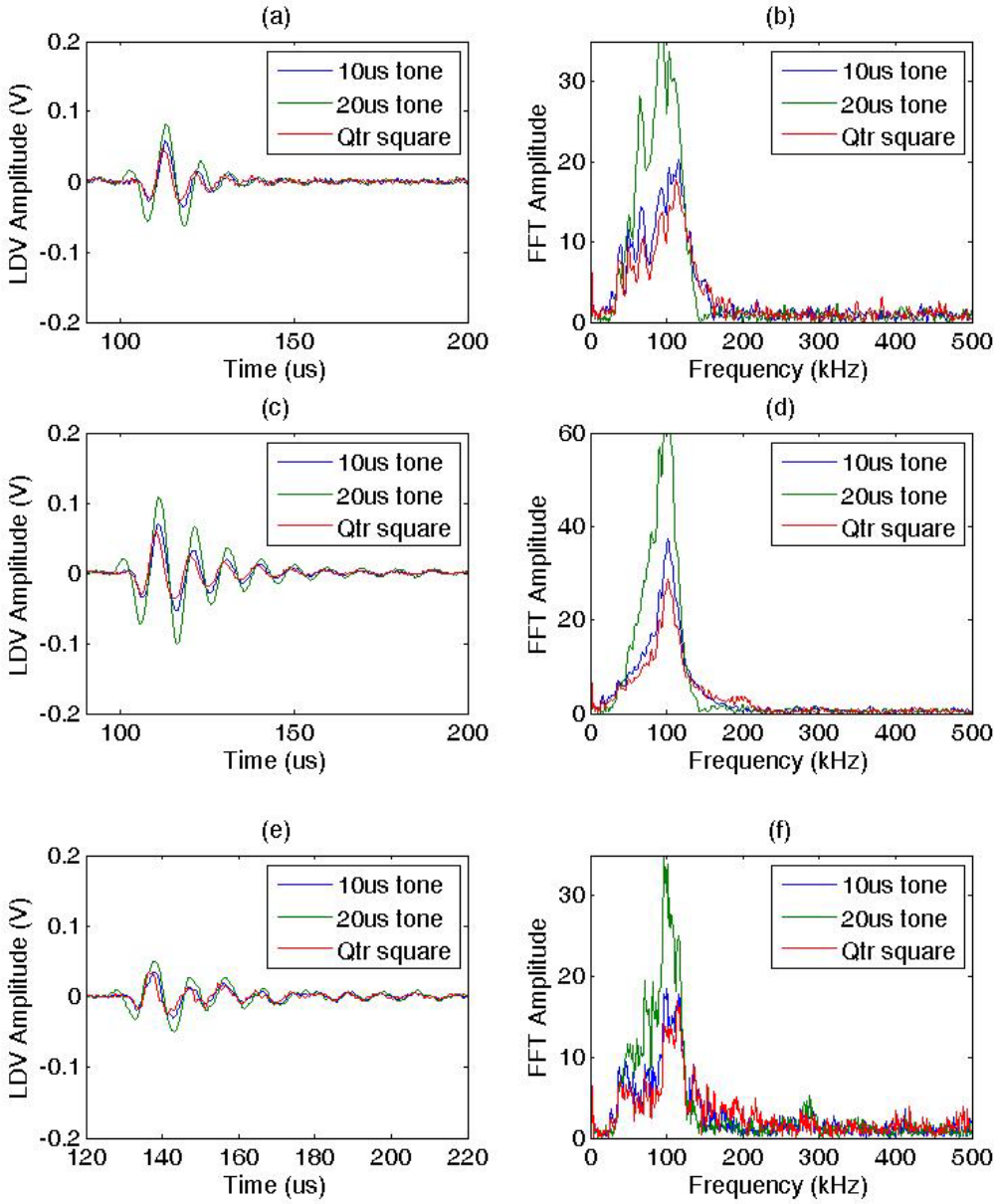

Figure 4.26: Comparison of an Arnokrome 3 sleeve, a Remendur sleeve, and a piezoelectric cylinder sleeve at 81 kHz. (a) LDV displacement measurements and (b) FFT results for the Arnokrome 3 sleeve. (c) LDV displacement measurements and (d) FFT results for the Remendur sleeve. (e) LDV displacement measurements and (f) FFT results for the piezoelectric cylinder sleeve transducer.

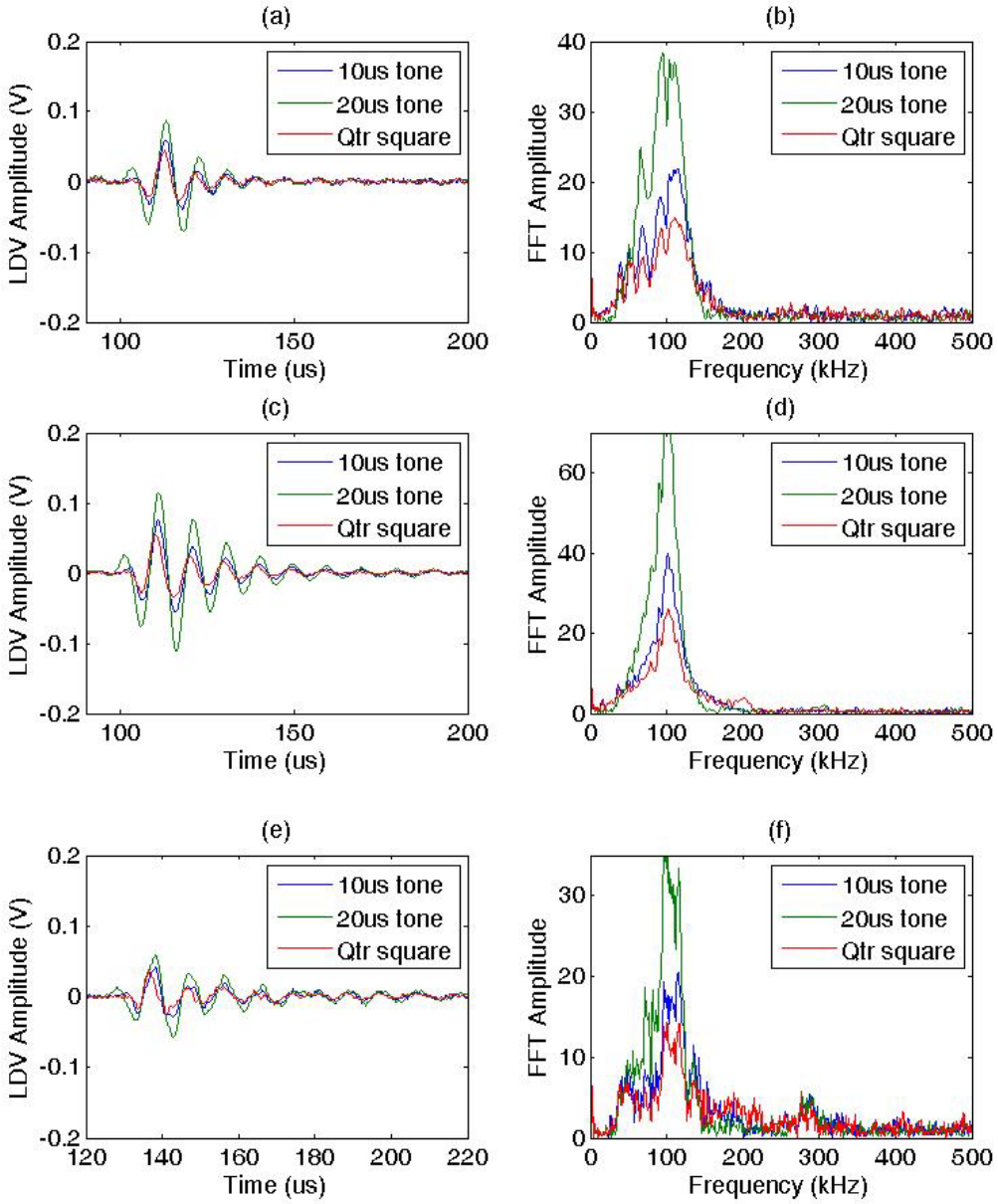

Figure 4.27: Comparison of an Arnokrome 3 sleeve, a Remendur sleeve, and a piezoelectric cylinder sleeve at 89 kHz. (a) LDV displacement measurements and (b) FFT results for the Arnokrome 3 sleeve. (c) LDV displacement measurements and (d) FFT results for the Remendur sleeve. (e) LDV displacement measurements and (f) FFT results for the piezoelectric cylinder sleeve transducer.

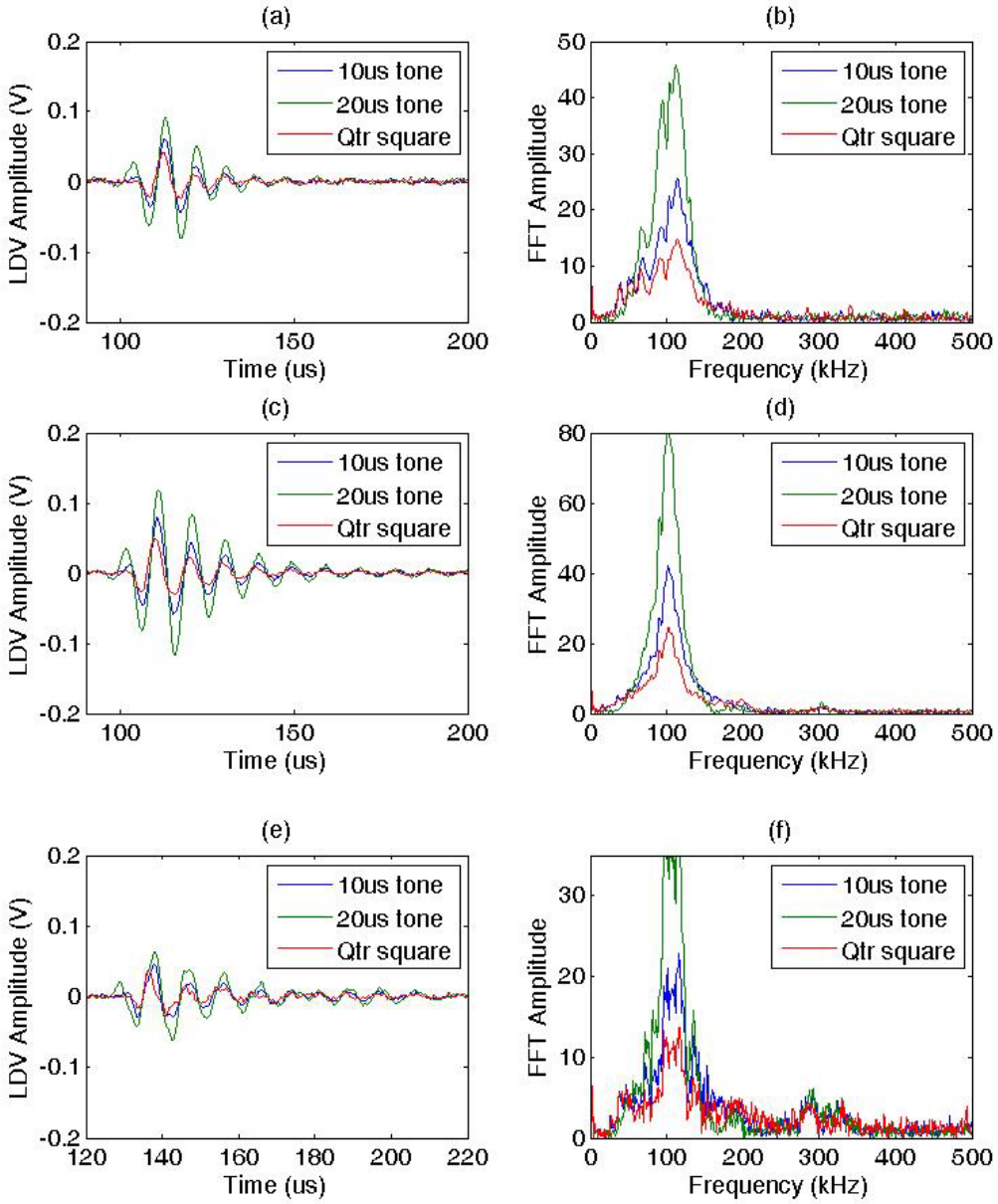

Figure 4.28: Comparison of an Arnokrome 3 sleeve, a Remendur sleeve, and a piezoelectric cylinder sleeve at 100 kHz. (a) LDV displacement measurements and (b) FFT results for the Arnokrome 3 sleeve. (c) LDV displacement measurements and (d) FFT results for the Remendur sleeve. (e) LDV displacement measurements and (f) FFT results for the piezoelectric cylinder sleeve transducer.

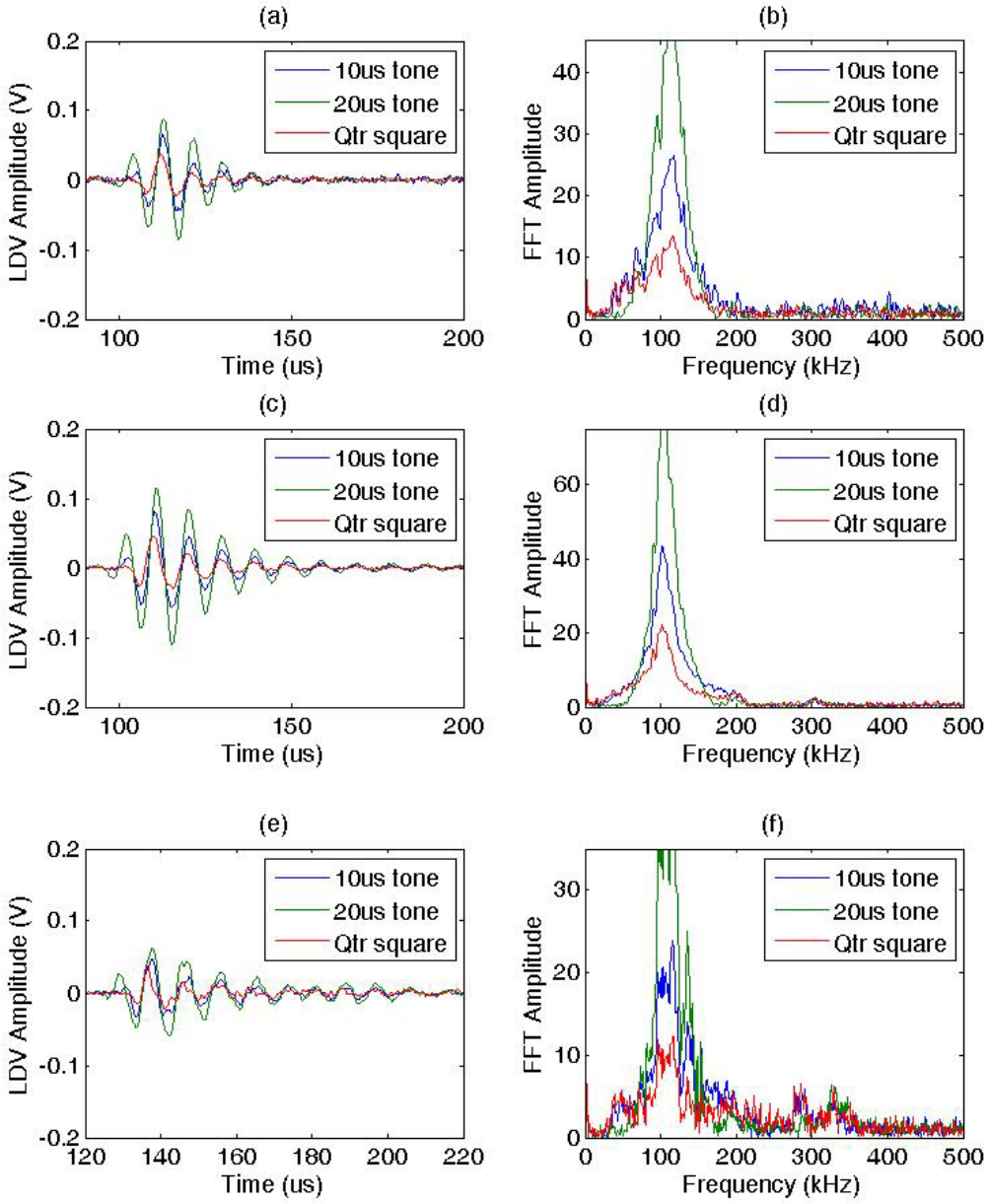

Figure 4.29: Comparison of an Arnokrome 3 sleeve, a Remendur sleeve, and a piezoelectric cylinder sleeve at 114 kHz. (a) LDV displacement measurements and (b) FFT results for the Arnokrome 3 sleeve. (c) LDV displacement measurements and (d) FFT results for the Remendur sleeve. (e) LDV displacement measurements and (f) FFT results for the piezoelectric cylinder sleeve transducer.

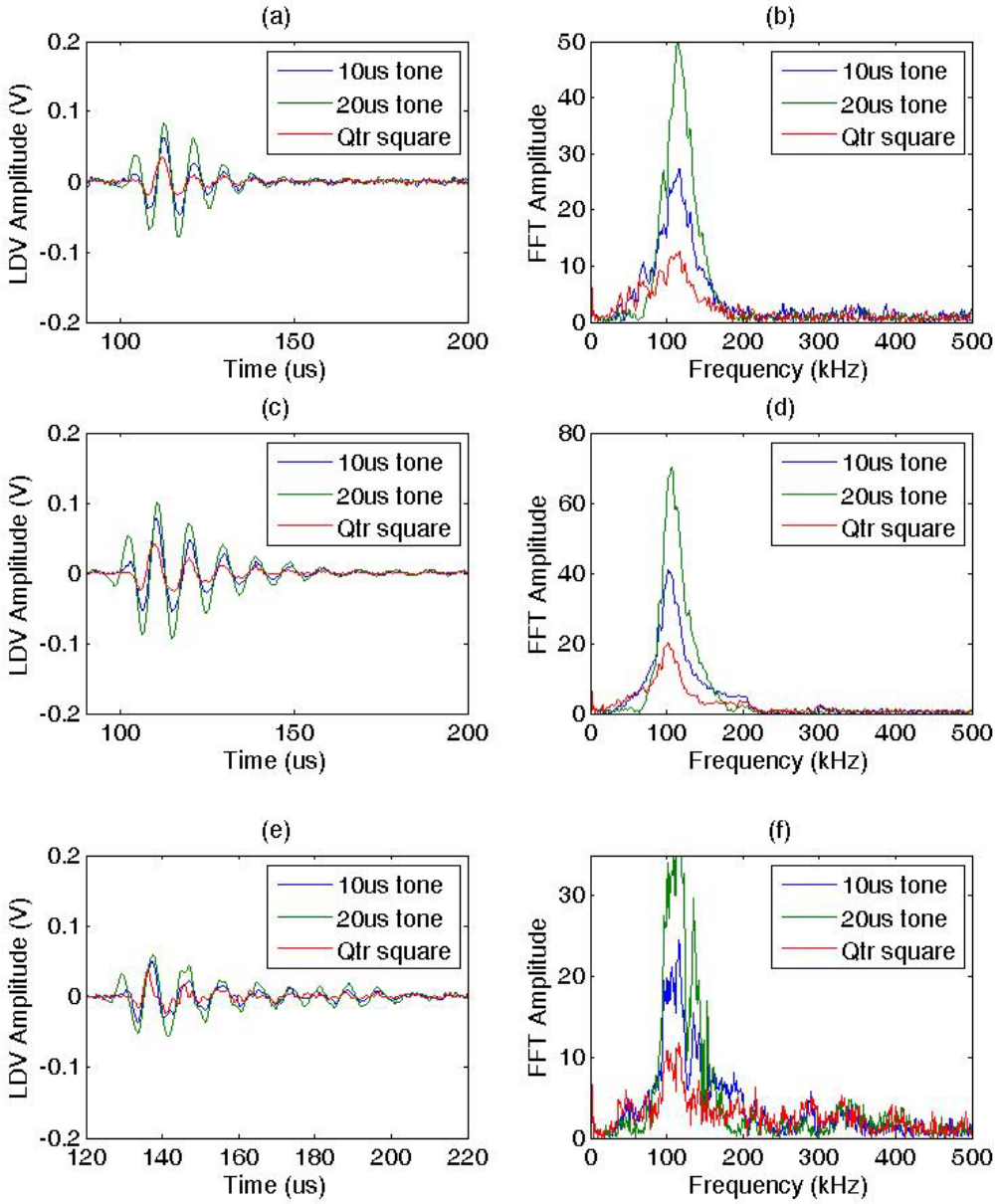

Figure 4.30: Comparison of an Arnokrome 3 sleeve, a Remendur sleeve, and a piezoelectric cylinder sleeve at 125 kHz. (a) LDV displacement measurements and (b) FFT results for the Arnokrome 3 sleeve. (c) LDV displacement measurements and (d) FFT results for the Remendur sleeve. (e) LDV displacement measurements and (f) FFT results for the piezoelectric cylinder sleeve transducer.

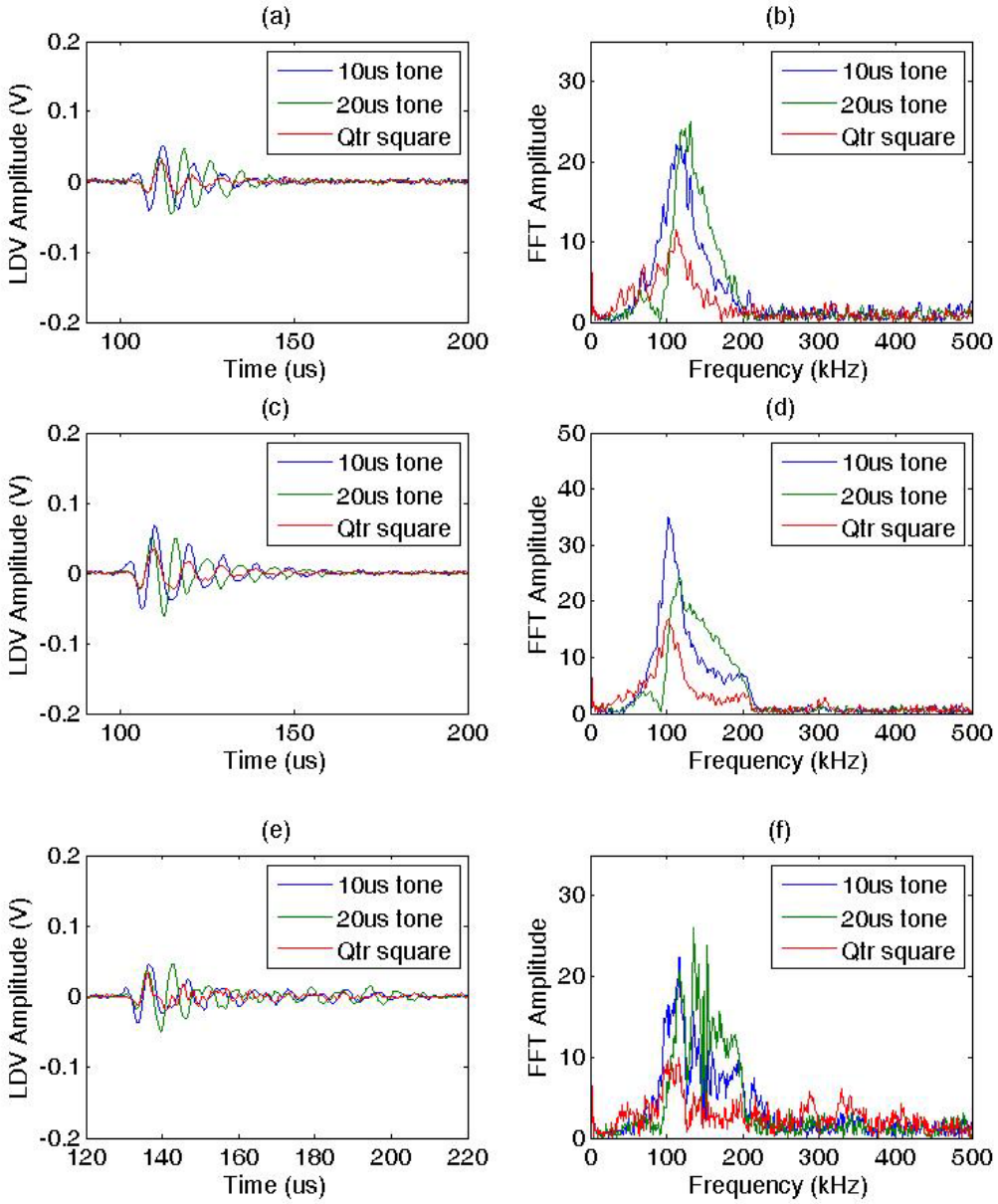

Figure 4.31: Comparison of an Arnokrome 3 sleeve, a Remendur sleeve, and a piezoelectric cylinder sleeve at 156 kHz. (a) LDV displacement measurements and (b) FFT results for the Arnokrome 3 sleeve. (c) LDV displacement measurements and (d) FFT results for the Remendur sleeve. (e) LDV displacement measurements and (f) FFT results for the piezoelectric cylinder sleeve transducer.

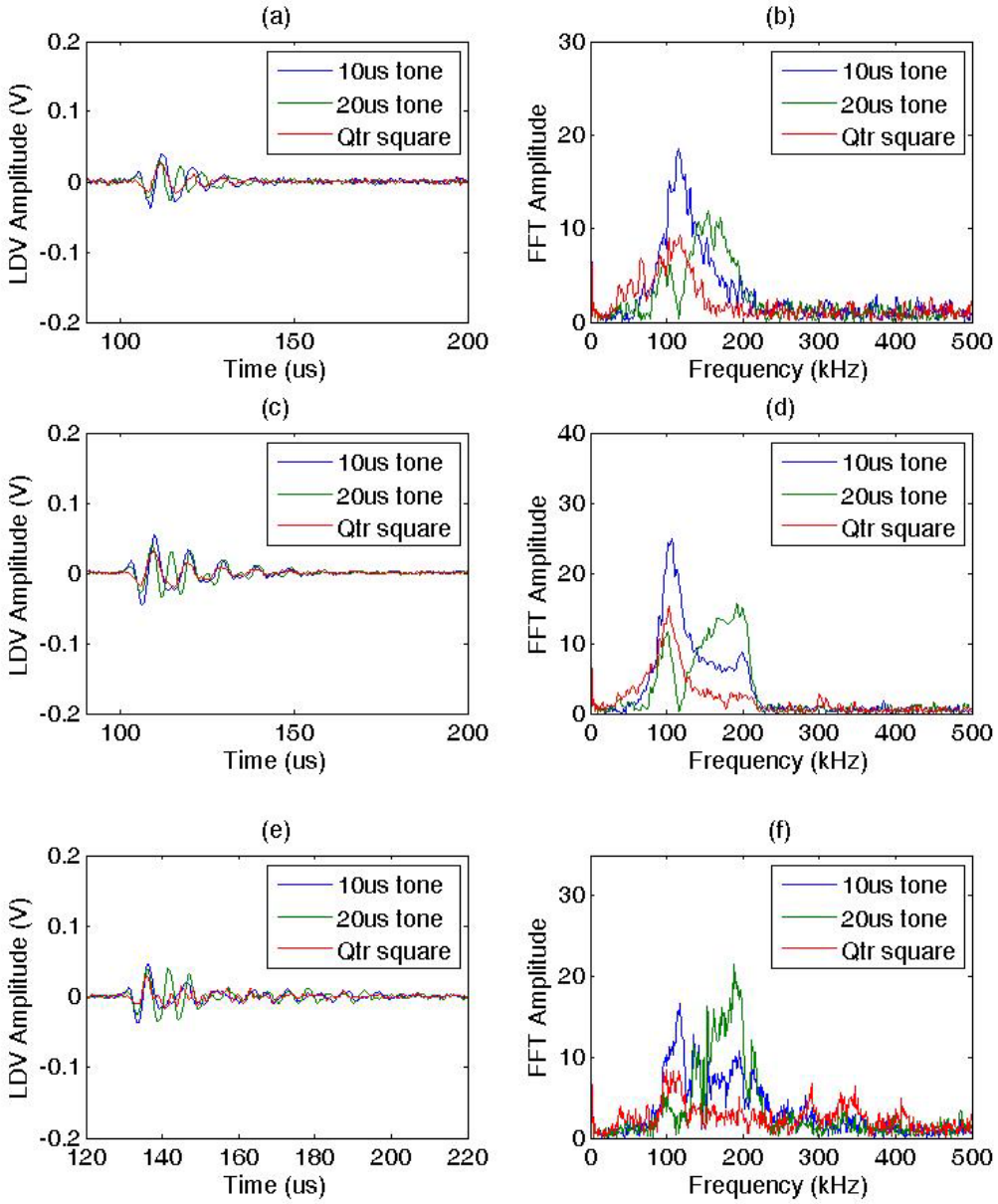

Figure 4.32: Comparison of an Arnokrome 3 sleeve, a Remendur sleeve, and a piezoelectric cylinder sleeve at 179 kHz. (a) LDV displacement measurements and (b) FFT results for the Arnokrome 3 sleeve. (c) LDV displacement measurements and (d) FFT results for the Remendur sleeve. (e) LDV displacement measurements and (f) FFT results for the piezoelectric cylinder sleeve transducer.

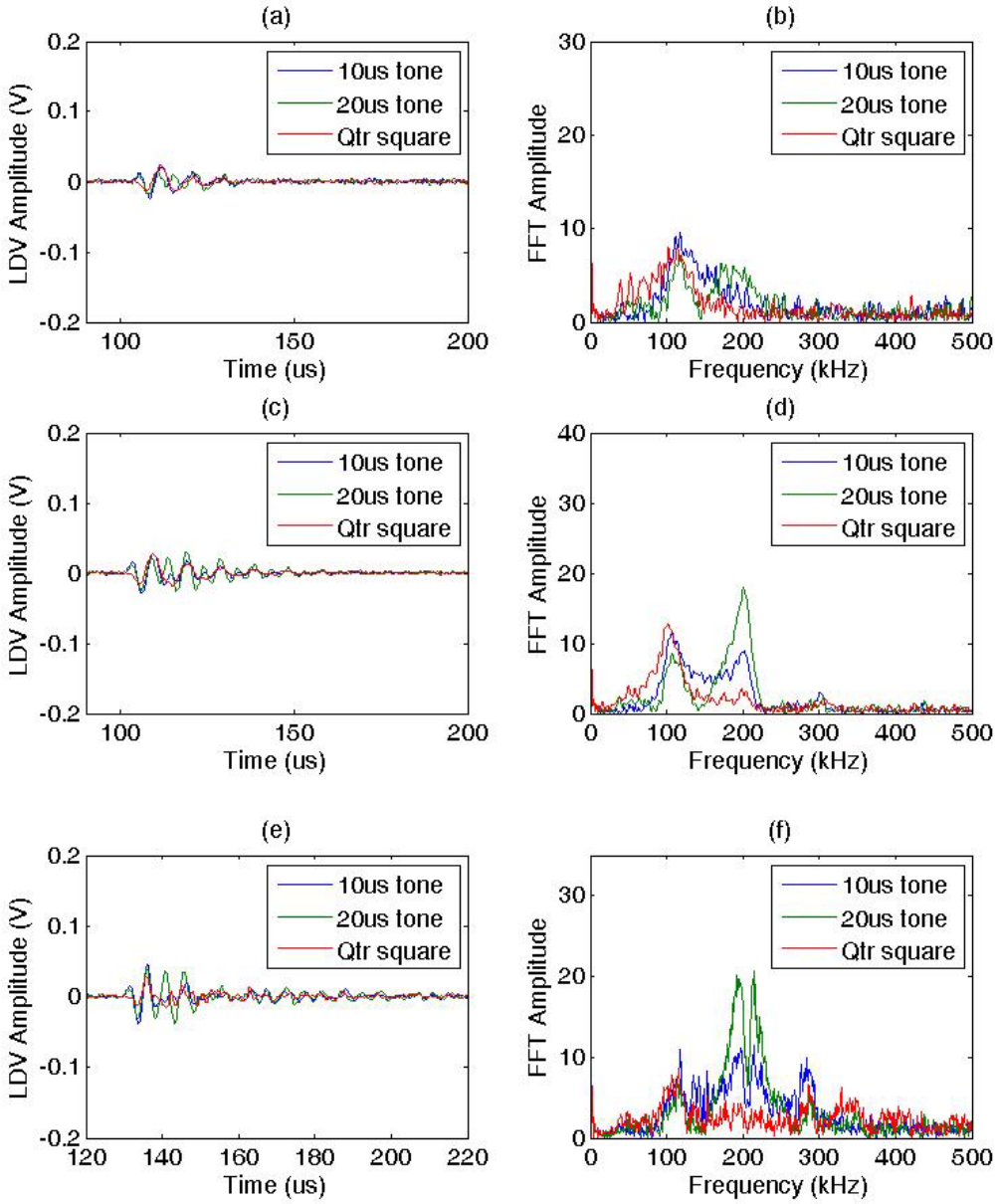

Figure 4.33: Comparison of an Arnokrome 3 sleeve, a Remendur sleeve, and a piezoelectric cylinder sleeve at 208 kHz. (a) LDV displacement measurements and (b) FFT results for the Arnokrome 3 sleeve. (c) LDV displacement measurements and (d) FFT results for the Remendur sleeve. (e) LDV displacement measurements and (f) FFT results for the piezoelectric cylinder sleeve transducer.

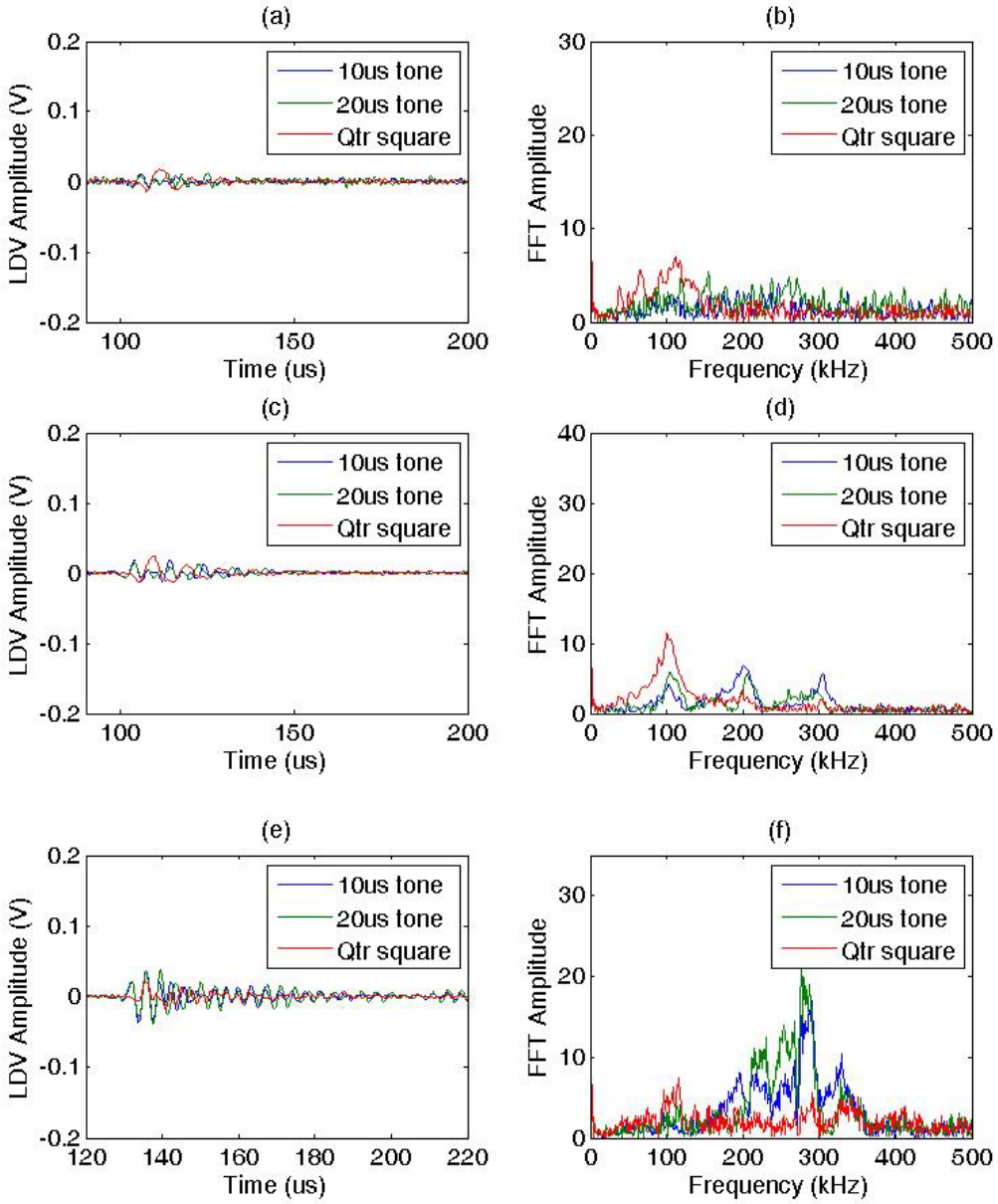

Figure 4.34: Comparison of an Arnokrome 3 sleeve, a Remendur sleeve, and a piezoelectric cylinder sleeve at 250 kHz. (a) LDV displacement measurements and (b) FFT results for the Arnokrome 3 sleeve. (c) LDV displacement measurements and (d) FFT results for the Remendur sleeve. (e) LDV displacement measurements and (f) FFT results for the piezoelectric cylinder sleeve transducer.

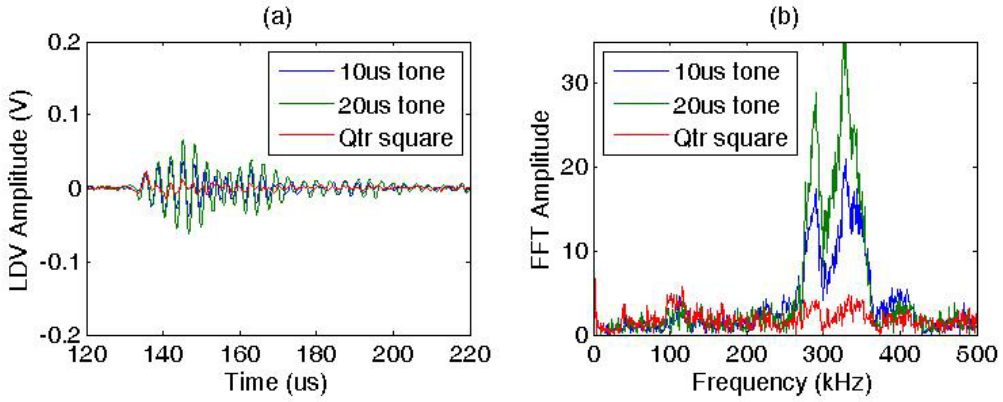

Figure 4.35: Piezoelectric cylinder sleeve results at 312 kHz. (a) LDV displacement measurements and (b) FFT results.

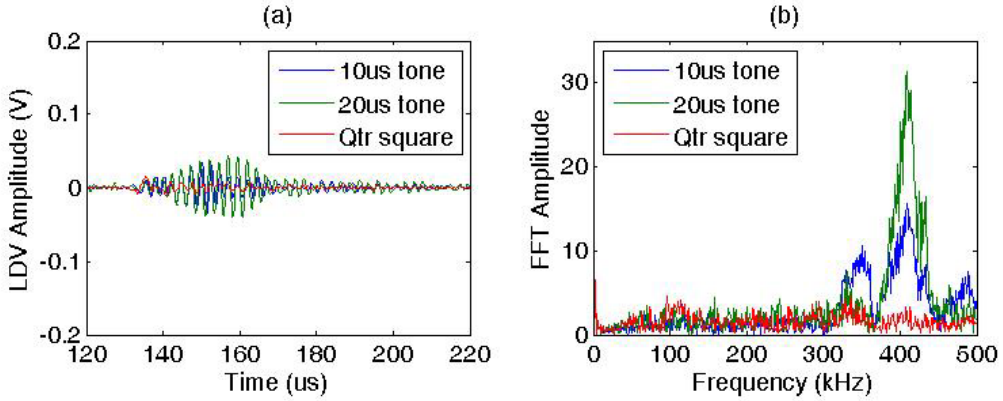

Figure 4.36: Piezoelectric cylinder sleeve results at 417 kHz. (a) LDV displacement measurements and (b) FFT results.

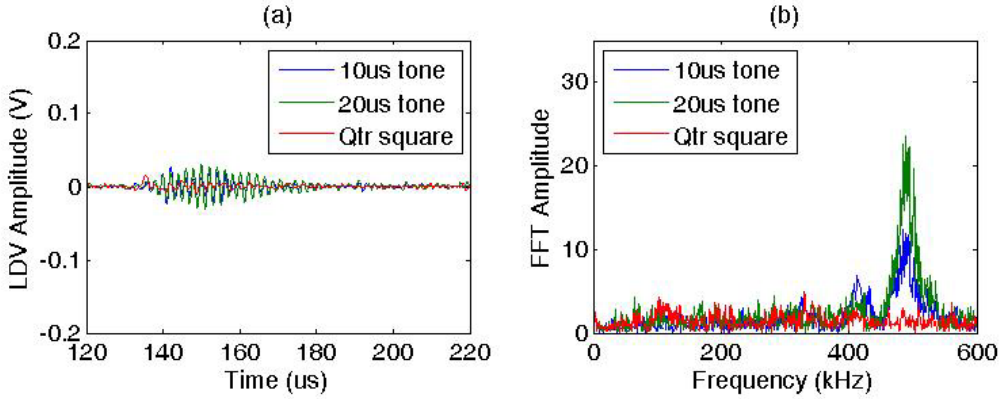

Figure 4.37: Piezoelectric cylinder sleeve results at 500 kHz. (a) LDV displacement measurements and (b) FFT results.

The color scale in Figure 4.38 plots the amplitude of the analytic envelope (obtained via the Hilbert transform) versus driving frequency for the frequency sweep performed with the piezoelectric sleeve transducer. The highest amplitudes were observed near 100-125 kHz and 300-400 kHz. Additional slower mode components were between 300 kHz and 500 kHz (Figure 4.38b). However, the scale bar indicates than the slower mode components had approximately 1/5 the amplitude compared to the faster mode (Figure 4.38a).

The color scale in Figure 4.39 plots the amplitude of the Fourier transform versus driving frequency. Peak amplitudes were observed at approximately 125 kHz and 330 kHz. There is also a weak peak near 400 kHz observed in the frequency domain results. However, the time domain results (Figure 4.38) indicate a poor signal at 400 kHz.

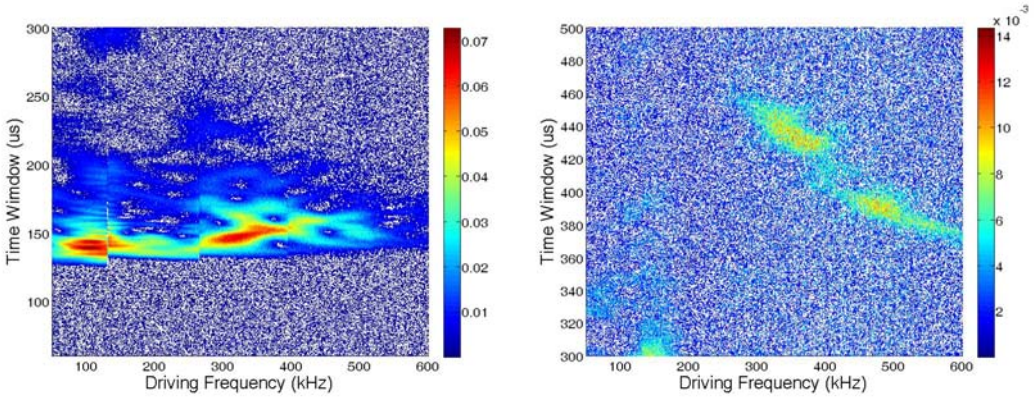

Figure 4.38: Time-domain results for the experiments with a piezoelectric sleeve transducer. The color scale depicts the magnitude of the analytic envelope based on the LDV output voltage for: (a) 50 to 300 μs time-of-flight window and (b) 300 to 500 μs time-of-flight window.

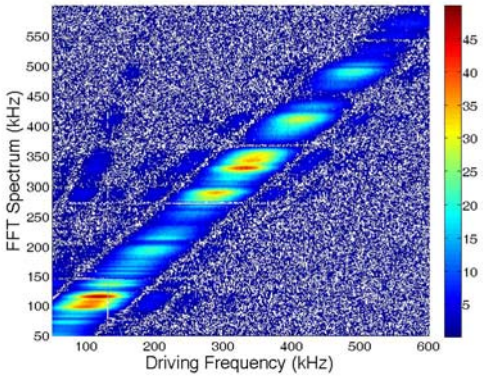

Figure 4.39: Frequency-domain results for the experiments with a piezoelectric sleeve transducer. The color scale depicts the magnitude of the Fourier transform based on the LDV output voltage. Peak amplitudes were observed at approximately 125 kHz and 330 kHz. The central frequency of an unloaded PZT sleeve was expected to be approximately 400 kHz. Downshift to 330 kHz is likely explained by the mechanical resistance of the wire waveguide inside the sleeve.

The central frequency of an unloaded PZT sleeve was expected to be approximately 400 kHz. However, the experiments consisted on a PZT sleeve attached to a stainless steel waveguide. The downshift to 330 kHz is likely explained by the mechanical resistance of the wire waveguide inside the PZT sleeve. The peak near 125 kHz may be related to the excitability of the guided waves in the wire.

4.7 Summary

In the design and operation of an in-situ monitoring system based on guided ultrasonic waves, the transducer design plays an important roll in the performance of the system. Earlier work [22,23] with a wire-wire coupling demonstrated that the wire-wire joint produced unwanted artifacts in the signal. In addition, the old wire-wire design was difficult to fabricate and often times provided poor transmission of the ultrasonic waves.

In this work, a magnetostrictive sleeve design was tested as an alternative to the old wire-wire joint configuration. Results showed that the sleeve design was effective for generating ultrasonic guided waves in the wire waveguide. In addition, the sleeve design simplifies specimen fabrication, minimizes the amount of magnetostrictive material required, and eliminates the artifacts associated with the wire-wire joint. By eliminating the wire-wire joint artifacts, some sources of error are removed and the data obtained with in-situ monitoring system is easier to interpret.

Experimental testing indicated that the optimal performance occurred at approximately 125 kHz. It appears that both the sleeve length and possibly the excitability of the guided waves lead to the strong performance at 125 kHz. However, additional calculations would be required to determine the excitability of the guided waves in the wire waveguide. Guided wave mode excitability calculations are beyond standard phase and group velocity calculations.

The experimental results also showed that the sleeve design generated a narrower bandwidth (less low frequency content). In guided wave applications, this can be advantageous because a more narrow-banded transducer excites a smaller region on the dispersion curves. In contrast, the wire-wire design is better suited for performing frequency sweeps if the intended measurement is not adversely effected by the wire-wire joint characteristics.

The hysteresis inherent to magnetostrictive materials limits the maximum frequency which can be generated. As an alternative, preliminary experiments with a piezoelectric sleeve were also performed. The results obtained with the piezoelectric sleeve were encouraging. A piezoelectric sleeve could be used to excite guided waves in the wire waveguide, but additional work would be required to optimize the design of the piezoelectric for better performance.

CHAPTER 5: BAR SPECIMENS

One potential application of the in-situ monitoring technique is to measure changes in "blister" specimens. An example of a "blister" specimen is shown in Figure 5.1. The "blister" specimens are essentially rectangular bars of material which are commonly used for accelerated life testing in test reactors [8,82]. A trapezoidal horn is used to transition between the specimen and the wire waveguide which leads to the remote magnetostrictive transducer.

In the nuclear industry, these "blister" specimens are commonly referred to as "plates." However, this can be misleading because the dimensions of the "blister" specimens are not compatible with the boundary conditions required for Lamb waves in a plate. The work presented in this chapter primarily focuses on characterizing solid rectangular bar specimens. However, composite bars containing two materials have also been considered.

5.1 Dispersion Curves

As discussed in Chapter 2, all wave propagation in solids is governed by the Navier-Cauchy equations. For a homogeneous, isotropic medium, Equation 5.1 shows the Navier-Cauchy equations in Cartesian coordinates using vector notation, where λ_{Lame} is Lame's constant, E is elastic modulus, G is shear modulus, ρ is density, $\bar{u}$ is the displacement vector, and t is time [34-36].

$$(\lambda_{Lame} + G)\nabla\nabla \bullet \bar{u} + G\nabla^2\bar{u} = \rho\frac{\partial^2\bar{u}}{\partial t^2} \tag{5.1}$$

$$\text{where: } \lambda_{Lame} = \frac{G(2G - E)}{E - 3G}$$

Figure 5.1: Photograph of a "blister" specimen used in this investigation.

Some authors [22,23] have suggested that the guided wave propagation in the rectangular bar specimen can be approximated via the Rayleigh-Lamb Equations.[10] However, such an approximation is invalid. The Rayleigh-Lamb solution assumes an infinitely wide plate. For practical applications, the Rayleigh-Lamb equations are still valid when the width of the plate is many times larger than the wavelength of the guided waves in the plate [34-36]. However, the width of the rectangular bar specimen is equal to only one wavelength of bulk shear waves in Zircaloy at 150 kHz operating frequency. Thus, the necessary condition for a valid Rayleigh-Lamb solution (width >> wavelength) is not satisfied by the boundary of the "blister" specimen.

Since there will be simultaneous interference effects produced by all boundaries, a solution for the correct boundary conditions is required. Morse and Feshbach [44] have presented a partial simplification based on the wave equation which is shown in Equations 5.2 through 5.4. L_{mn} is a longitudinal component. M_{mn} and N_{mn} are transverse components.

$$L_{mn} = \left(\frac{1}{ik_c}\right)\nabla[\varphi_{mn}(x,y)e^{ikz}]e^{-iwt} \tag{5.2}$$

$$M_{mn} = \left(\frac{1}{ik_s}\right)\nabla\times[a_z\psi_{mn}(x,y)e^{ikz}]e^{-iwt} \tag{5.3}$$

$$N_{mn} = \left(\frac{1}{ik_s^2}\right)\nabla\times(\nabla\times[a_z\chi_{mn}(x,y)e^{ikz}])e^{-iwt} \tag{5.4}$$

φ_{mn}, Ψ_{mn}, and χ_{mn} are functions which describe the cross-section and satisfy the boundary conditions. According to Morse and Feshbach [44], φ_{mn}, Ψ_{mn}, and χ_{mn} cannot be solved for independently in most cases. The wave propagation in a solid media must contain both longitudinal and transverse components.

The mathematical form given by Morse and Feshbach [44] does not allow for a straightforward iterative root finding approach for determining the dispersion curves of a rectangular cross-section. In addition, a composite cross-section was of interest. Thus, an alternative technique was required for calculating the dispersion curves associated with the "blister" specimens.

[10] See Appendix D for additional information on the Rayleigh-Lamb solution for plates.

In order to accurately address the "blister" specimen geometry, the semi-analytical finite element (SAFE) technique was used [45,46]. As described in Section 3.2, the SAFE technique assumes a wave solution in a manner similar to Morse and Feshbach [44]. However, the cross-section is discretized into finite elements as is done in a standard finite element analysis. The Eigen values and Eigen vectors of the resulting set of equations are then solved numerical [45,46].

For the sake of comparison, Figure 5.2 compares the SAFE results to the results obtained with the Rayleigh-Lamb equations[11] for infinitely wide plates with thicknesses corresponding to the dimensions of the rectangular bar specimen. Although there are certain areas of the dispersion curves where the SAFE solution matches the Rayleigh-Lamb solution, there are many regions of the dispersion curves where the SAFE solution and Rayleigh-lamb solution are different. There are modes in the bar (from the SAFE solution) which are not found in the Rayleigh-Lamb solution, and the Rayleigh-Lamb solution predicts modes which do not exist in the bar (based on SAFE solution). When analyzing guided wave propagation, the correct boundary conditions must be applied.

5.2 Initial Finite Element Analysis and Validation

The theoretical dispersion curves developed in the course of this research provide valuable insight into the guided wave propagation governing the in-situ monitoring of a rectangular bar specimen. However, the theoretical dispersion curves are only valid in the rectangular cross-section. In the experimental measurements, there is a trapezoidal horn which serves as a transition between the wire and bar specimen (Figure 5.3). To account for the effect of the horn, a finite element analysis must be performed.

The time domain finite element models consisted of a full 3D representation of the rectangular bar with trapezoidal horn and a long wire waveguide. The transducer excitation was approximated by using a displacement boundary condition on the end of the wire waveguide.[12] A-scan waveforms were then simulated for both a 6.25 inch long and a 10.0 inch long specimen.

[11] See Appendix D for additional information on the Rayleigh-Lamb solution for plates.
[12] See Appendix B for a detailed modeling procedure.

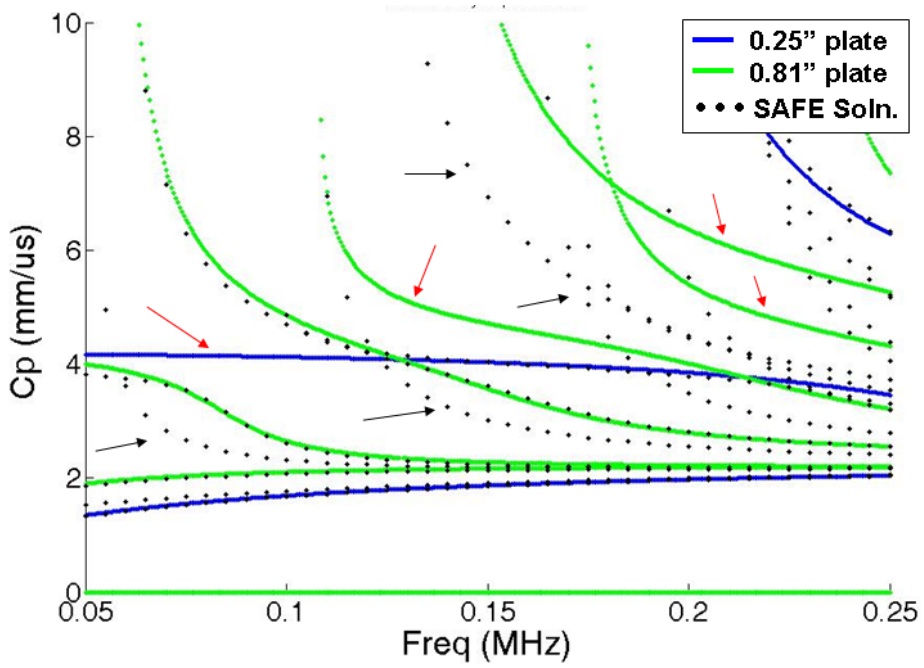

(a)

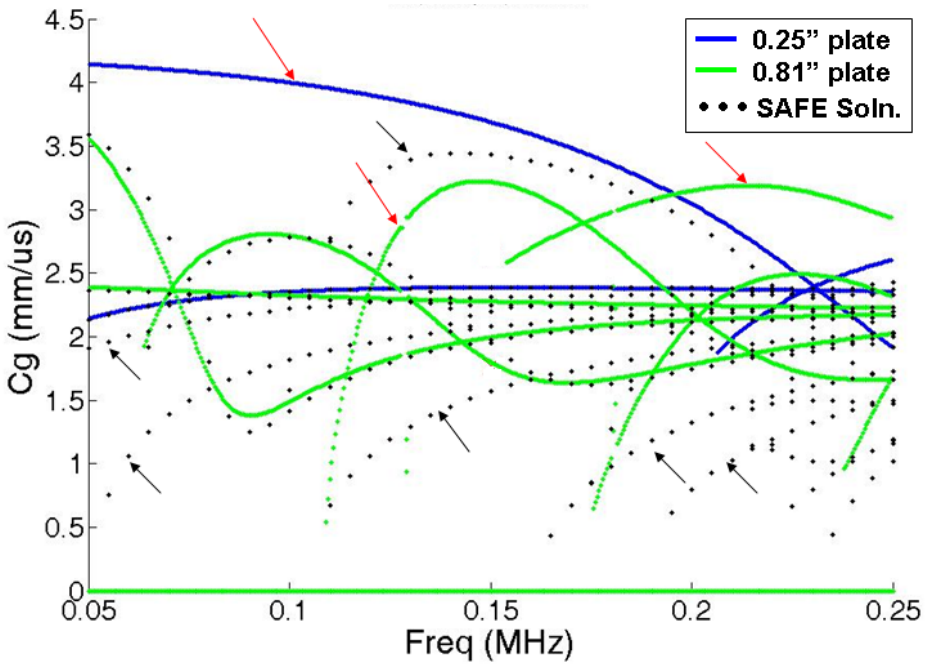

(b)

Figure 5.2: Comparison of dispersion curves: SAFE solution of a rectangular cross-section vs. Rayleigh-Lamb solution for an infinitely wide plate. (a) Phase velocity dispersion curves, (b) Group velocity dispersion curves. Blue lines represent the Rayleigh-Lamb solution for a 6.35 mm (0.25 inch) thick infinitely wide plate. Green lines represent the Rayleigh-Lamb solution for a 20.625 mm (0.812 inch) thick infinitely wide plate. Black dots indicate the SAFE solution for a 6.35 mm (0.25 inch) by 20.625 mm (0.812 inch) rectangular cross-section. The SAFE solution is plotted for fewer frequencies because it is more computationally demanding. Black arrows indicate where there are modes in the bar (from the SAFE solution) which are not found in the Rayleigh-Lamb solutions. Red arrows indicate where the Rayleigh-Lamb solutions predict modes which do not exist in the bar (based on the SAFE solution).

Figure 5.4 shows that the 3.75 inch difference in specimen length (7.5 inch or 190.5 mm round-trip travel distance), corresponds to a time-of-flight of approximately 55 µs in the time-domain models. In Figure 5.2, the guided wave mode with the fastest group velocity at 150 kHz has a group velocity of 3.37 mm/µs (at room temperature). This mode would have a time-of-flight of 56.5 µs for the same round-trip travel distance (7.5 inch or 190.5 mm) in a pure rectangular bar specimen. Therefore, the fastest mode observed in the time-domain finite element model is in excellent agreement with the theoretical velocity of the fastest mode determined in the SAFE analysis (at 150 kHz).

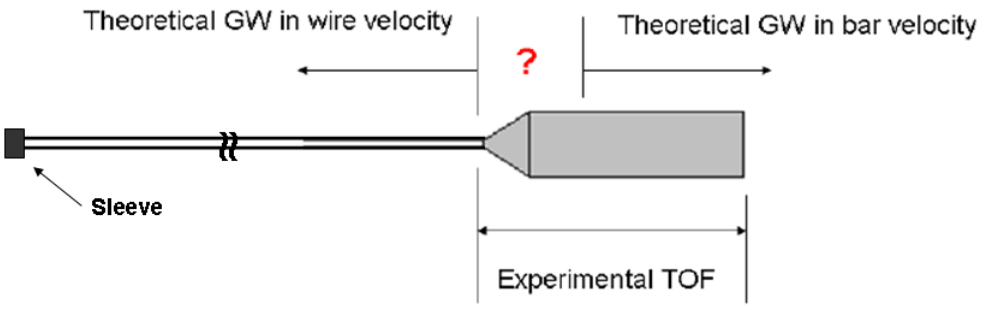

Figure 5.3: Illustration comparing the regions where theoretical guided wave solutions are known to apply. The theoretical guided wave (GW) in the bar is drawn intentionally to not start exactly where the horn meets the bar. This is done because the ultrasonic waves must travel a short distance in the bar before the correct wave structure of the guided wave mode(s) forms.

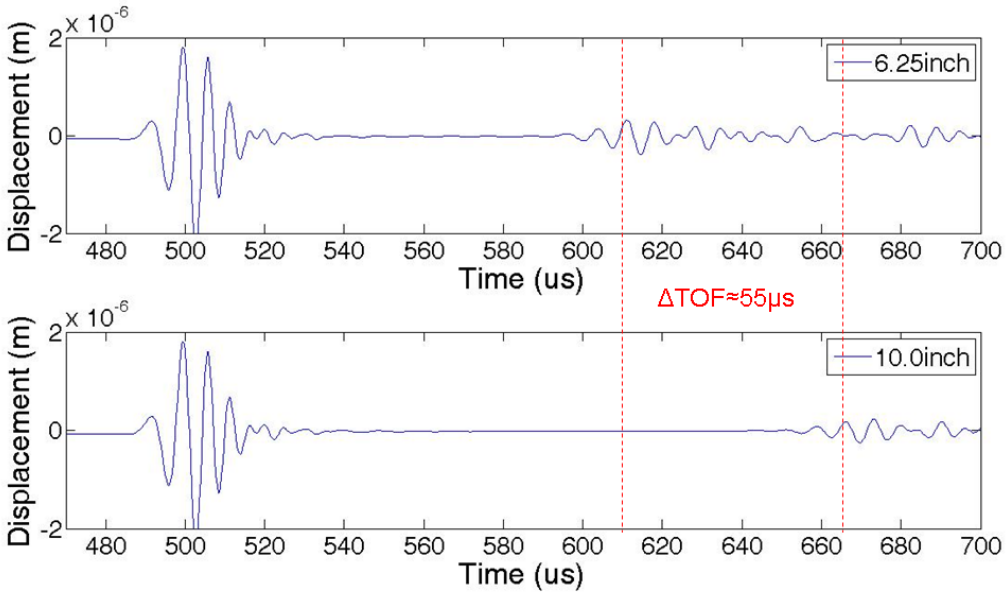

Figure 5.4: Simulated A-scan waveforms generated via the time-domain finite element modeling. Results show that the 3.75 inch difference in length corresponds to a time-of-flight of 55 µs. The time and amplitude axes shown here have been set to only show the region of interest.

The simulated waveforms generated by the time-domain finite element modeling (Figure 5.4) also indicate there are additional modes with lower group velocities. However, from Figure 5.2 it is clear that there are multiple modes possessing similar group velocities. A more sophisticated analysis would be required to analyze the overlapping wave modes.

In order to further validate the finite element results, the experimental time-of-flight in a 6.25 inch long specimen was measured. Figure 5.5 shows a comparison of the analytic envelopes for the simulated and experimental waveforms. In both the model and experiments, one round trip in the 6.25 inch long specimen corresponds to a total time-of-flight of approximately 100 μs. In the experimental results, a second round trip time-of-flight corresponds to a total time-of-flight of approximately 200 μs. The ultrasonic energy arriving between 100 and 200 μs time-of-flight may be related to modes with slower group velocities. However, these modes will be difficult to process because they begin to overlap with successive round trips of faster modes.

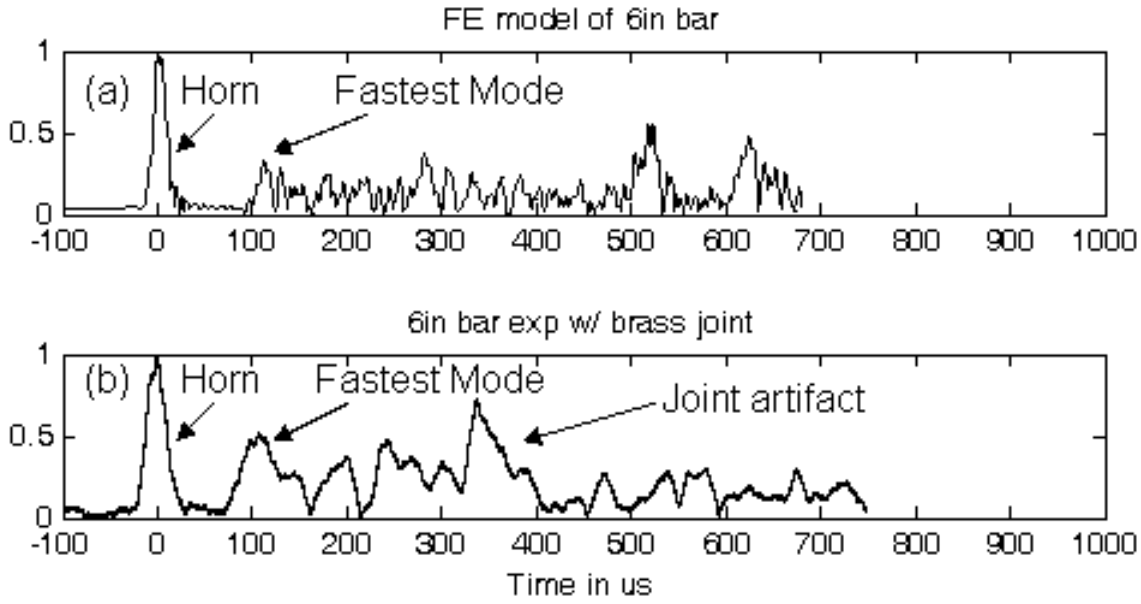

Figure 5.5: Comparison of simulated and experimental analytic envelopes. (a) the waveform predicted by time-domain finite element analysis, and (b) the experimental waveform obtained for a 6.25 inch rectangular bar specimen in air.

5.3 Frequency Sweep

In an attempt to examine the frequency dependency of the guided wave propagation, experimental waveforms were recorded at several frequencies at room temperature using a 6.25 inch long specimen. The wire-wire magnetostrictive transducer design (Figure 4.1) was used in order to have a wider transducer bandwidth. The results of the experimental frequency sweep are summarized in Figure 5.6. All of the results show a distinct reflection from the joint connecting the wire waveguide to the bar specimen arriving at approximately 175 μs time-of-flight.[13] Based on the dispersion curves and finite element calculations, the first reflection for the back of the specimens would then be expected at approximately 275 μs time-of-flight. The results at 105 kHz (Figure 5.6a) and 110 kHz (Figure 5.6b) do not have a clearly identifiable reflection corresponding to the back of the specimen. At higher frequencies (115 kHz to 150 kHz) the reflection arriving at approximately 275 μs time-of-flight is more prominent. This is most likely due to the guided wave mode being more dispersive in the 105 kHz to 110 kHz range.

The results indicated very little change in the time-of-flight between the joint reflection and the reflection from the end of the specimen in the 120 kHz to 150 kHz frequency range. This is consistent with the group velocity dispersion curve (Figure 5.2b) being relatively flat over this frequency range. The time-of-flight at 115 kHz was slightly higher, indicating a slightly slower group velocity.

When investigating the frequency dependence of the guided wave modes, it is valuable to recall the results for the magnetostrictive transducer presented in Chapter 4. As shown in Chapter 4, the magnetostrictive material and wire waveguide has an affinity for a certain frequencies. So, there is inherently some limit as to how much the actual frequency transmitted changes as the driving frequency changes.

Finite element models were also performed at several frequencies to further investigate the frequency dependence. In the finite element models, a 12 inch long specimen was modeled to increase the travel path of the guided waves and thereby increase the change in time-of-flight caused by a change in group velocity. Results of the finite element models are summarized in Figure 5.7. As in the experiments, there is not a

[13] Note that the time scale is relative to the segment of the signal saved by the data collection system.

distinct reflection from the back of the specimen at 105 kHz (Figure 5.7a) and 110 kHz (Figure 5.7b). The modeling results indicated no change in the time-of-flight between the joint reflection and the reflection from the end of the specimen in the 120 kHz to 150 kHz frequency range. The time-of-flight at 115 kHz was slightly higher, indicating a slightly slower group velocity.

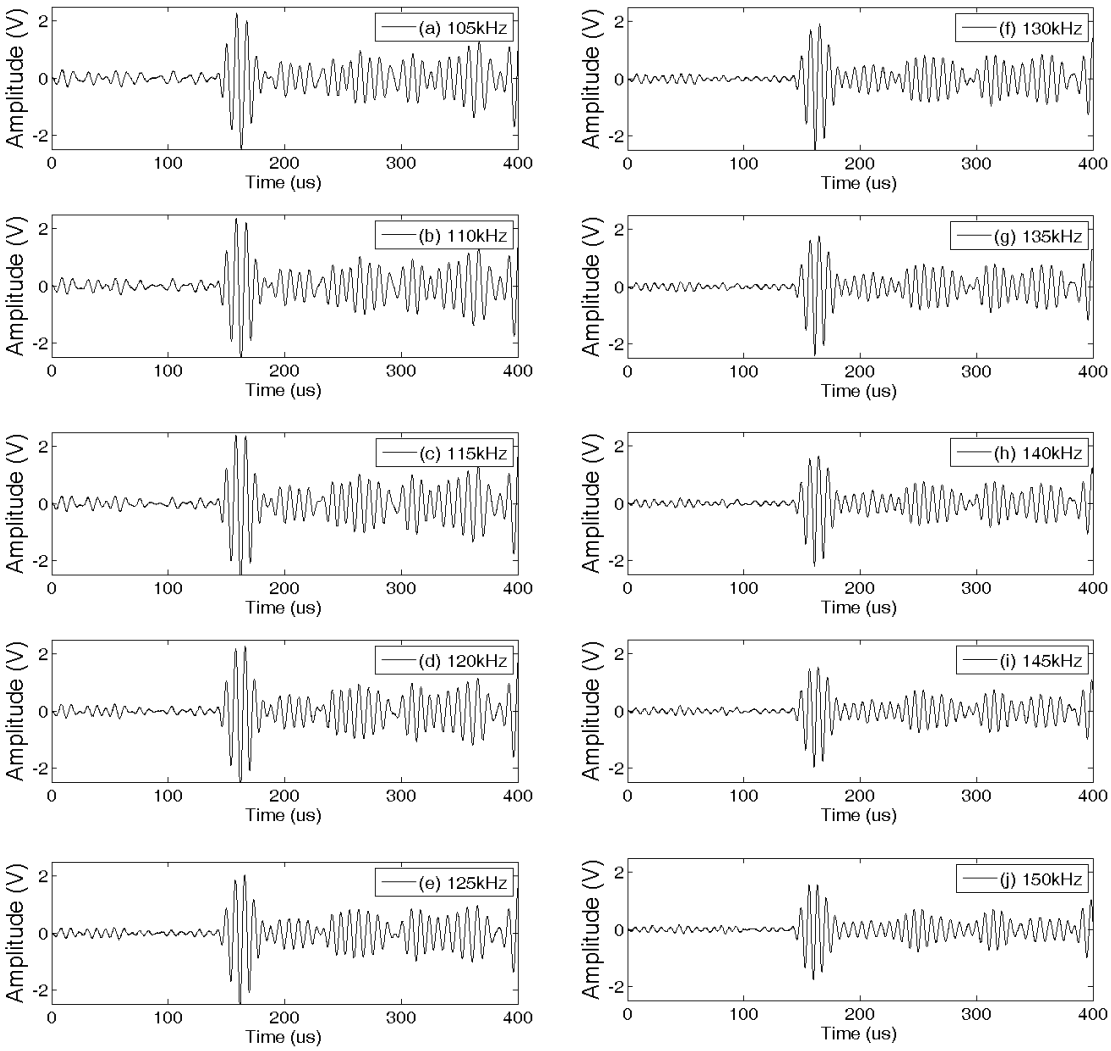

Figure 5.6: Results for the experimental frequency sweep performed with a 6.25 inch long bar specimen. (a) 105 kHz. (b) 110 kHz. (c) 115 kHz. (d) 120 kHz. (e) 125 kHz. (f) 130 kHz. (g) 135 kHz. (h) 140 kHz. (i) 145 kHz. (j) 150 kHz. Note that the time scale is relative to the segment of the signal saved by the data collection system.

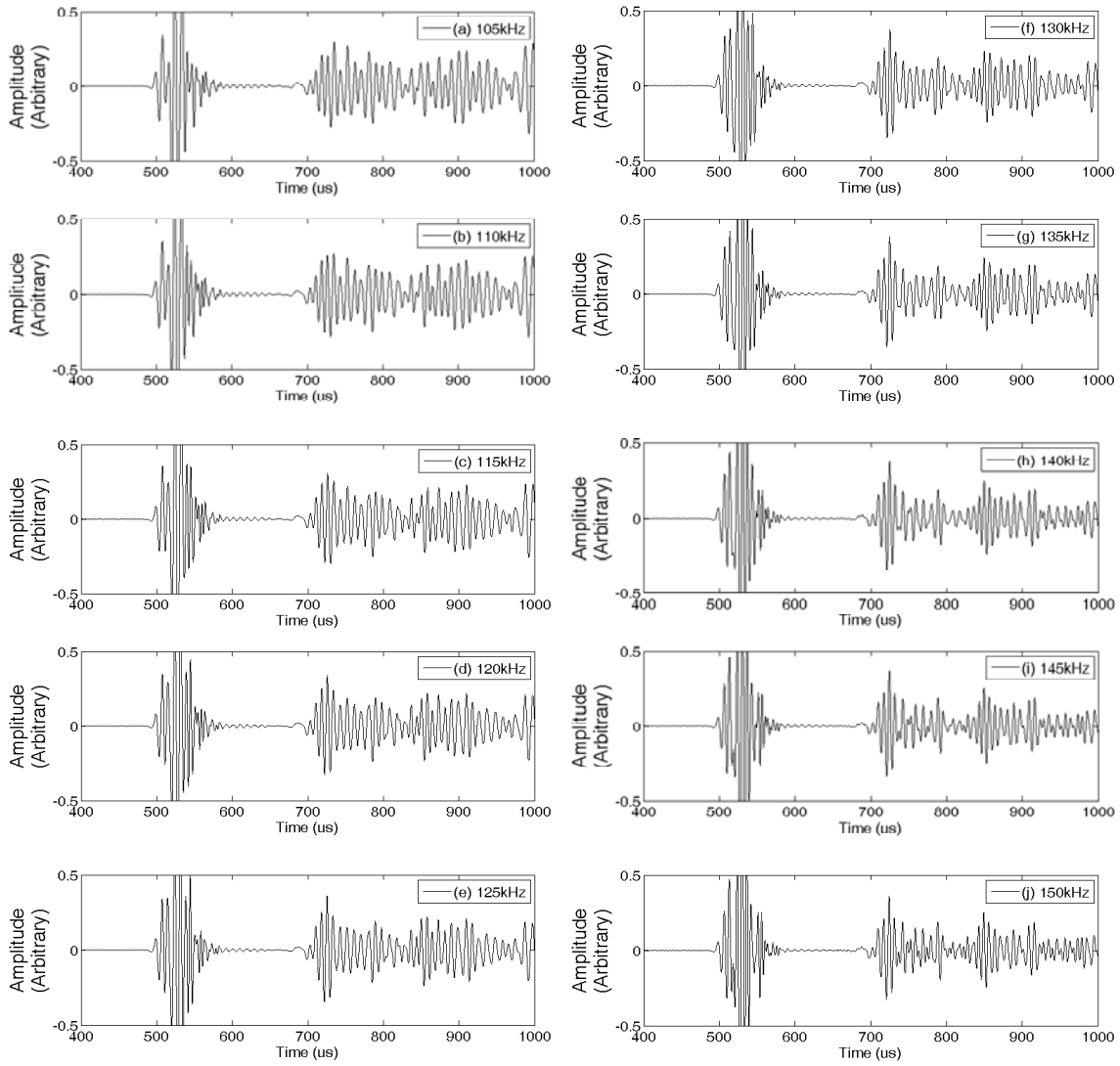

Figure 5.7: Results for the frequency sweep performed via time-domain finite element modeling for a 12 inch long bar specimen. (a) 105 kHz. (b) 110 kHz. (c) 115 kHz. (d) 120 kHz. (e) 125 kHz. (f) 130 kHz. (g) 135 kHz. (h) 140 kHz. (i) 145 kHz. (j) 150 kHz.

5.4 Temperature Dependence

In performing the guided wave analysis, temperature will have two effects. First, thermal expansion will cause some change in the cross-sectional and length dimensions (geometry) of the specimen. Second, temperature will change the basic material properties governing wave propagation.

The coefficient of thermal expansion for bulk Zircaloy was reported to be 6 u/K.[14] Increasing the temperature from 295°K (22°C / 70°F) to 700°K (427°C / 800°F) will yield a change in thickness of approximately 0.019 mm, and a change in width of approximately 0.06 mm. This should be negligible at operating frequencies of 150 kHz or less. Because the changes in cross-sectional dimensions due to thermal expansion were so small, it was decided that it was not necessary to account for this in the SAFE analysis and time-domain finite element studies.

For a 6.25 inch (159 mm) long bar, thermal expansion will result in a length change of 0.48 mm. For a 12 inch (305 mm) long bar, thermal expansion will results in a length change of 0.92 mm. Assuming a group velocity of 3.37 mm/μs, these length changes correspond to changes in time-of-flight of 0.29 μs and 0.55 μs, respectively. Although this is a non-trivial change in time-of-flight, the effect of thermal elongation is much smaller than the effect associated with the changes in material properties.[15]

The data shown in Appendix A demonstrates that the material properties of Zircaloy change significantly as a function of temperature. In order to determine how this affects the guided wave propagation, a parametric study was performed. The values of the material properties were calculated for each temperature point of interest. The resulting material properties were then used in the SAFE calculations to determine the corresponding dispersion curves for that temperature.

Figure 5.8a shows the raw group velocity results obtained from the SAFE calculations at two different temperatures. Figure 5.8b is obtained by manually sorting modes. Figure 5.8 shows that, in general, increasing temperature tends to shift the group velocity curves down (decreases velocity) and compresses the frequency axis towards the left. It is interesting to note that each mode has a unique response to temperature. In addition there appear to be certain combinations of frequency and mode where the group velocity is independent of temperature. At 145 kHz, there appears to be a mode with a constant 1.5 mm/μs group velocity. At 115 kHz, the mode with a group velocity of 3.0 mm/μs also appears to be minimally affected by temperature in theory.

[14] See Appendix A for reference.
[15] Further discussion of thermal elongation is included in Section 5.5.

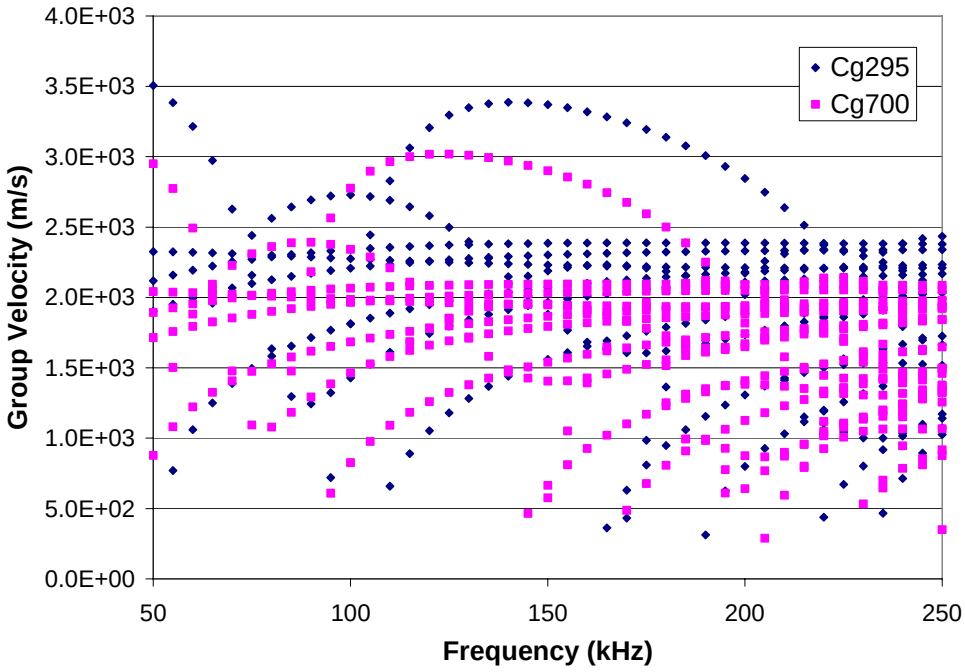

(a)

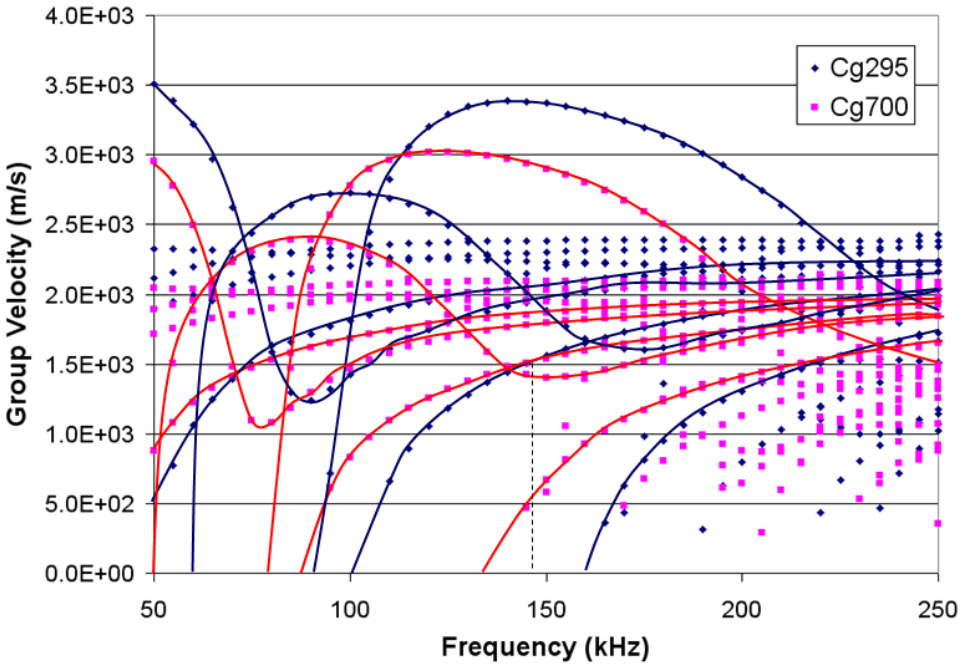

(b)

Figure 5.8: Group velocity dispersion curves for the rectangular bar specimen at selected temperatures. Temperature values are in °K. (a) Raw results from SAFE code. (b) After manual mode sorting. In general, increasing temperature tends to shift the group velocity curves down (decreases velocity) and compresses the frequency axis towards the left. It is interesting to note that each mode has a unique response to temperature, and there appears to be certain combinations of frequency and mode where the group velocity is independent of temperature. The dotted line in (b) identifies one such point in the dispersion curve. The quasi-SH modes (2.0-2.5 mm/us) were not processed in the manual mode sorting.

Figure 5.9 shows the calculated group velocity for each guided wave mode present at 150 kHz while temperature was parametrically stepped in 25°K increments. When appropriate, linear best fit lines were added to characterize the rate at which group velocity changed with changing temperature. Each mode with approximately linear dependence on temperature had a unique slope for the best fit line. One mode was nonlinear. The change in group velocity versus temperature (at 150 kHz) for 'Mode 6' is 95% less compared to change predicted for 'Mode 8.' Based on Figure 5.8, the slope of 'Mode 6' could in principal be reduced to zero by frequency tuning to approximately 145 kHz. However, it should be noted that other factors must be taken into account before it can be determined if it is practical to use such a special combination of mode and frequency. For example, there is an issue with generating and isolating 'Mode 6' at approximately 145 kHz because of source influence and the fact that another mode intersects the same point on the dispersion curve at 700°K (see Figure 5.8).

Figure 5.10 shows the calculated group velocity for each guided wave mode present at 115 kHz while temperature was parametrically stepped in 25°K increments. As before, linear best fit lines were added to characterize the rate at which group velocity changed with changing temperature when appropriate. In Figure 5.10, 'Mode 8' has a much smaller change in group velocity compared to the results at 150 kHz. Theoretically, the temperature dependence of 'Mode 8' can be minimized by tuning frequency. Figure 5.10 also shows that 'Mode 6' is much more sensitive to temperature at 115 kHz compared to the results at 150 kHz (Figure 5.9).

In theory, it may be advantageous to operate the in-situ monitoring techniques at 115 kHz to minimize the temperature dependence of the mode with the fastest group velocity. However, dispersion, transducer effects, and the effects of the trapezoidal horn also play a role in the final implementation.

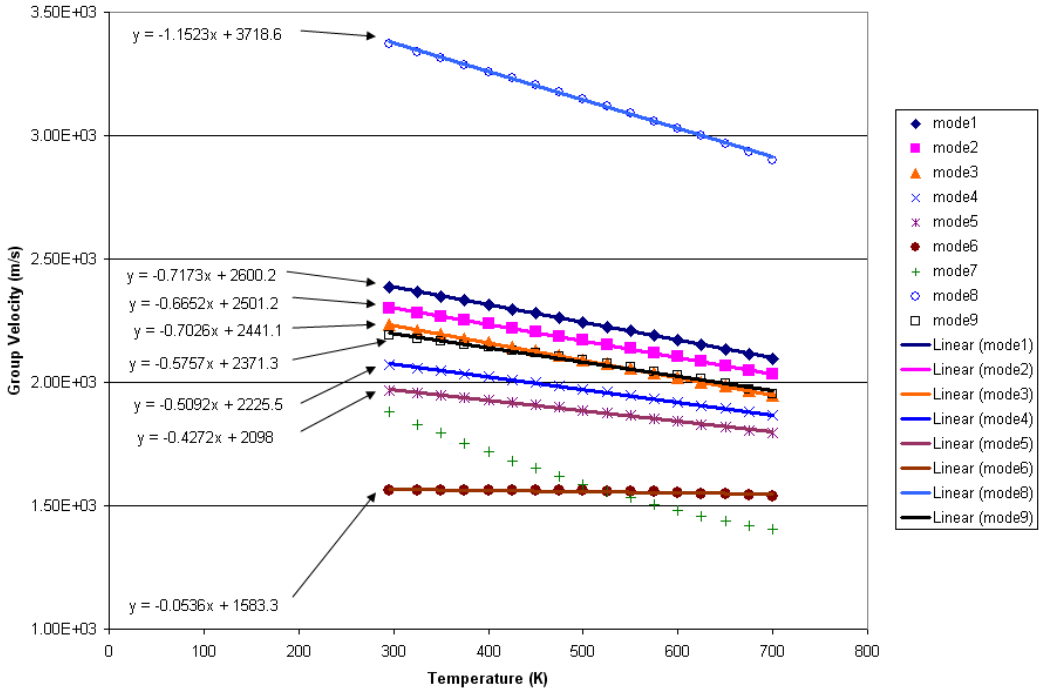

Figure 5.9: Group velocity of each wave mode at 150 kHz as a function of temperature (25°K increments). Solid lines are linear best-fits to the data obtained via the SAFE technique. Each wave mode has a unique response to temperature. There is a 95% difference in temperature dependence between 'mode 8' and 'mode 6' modes.

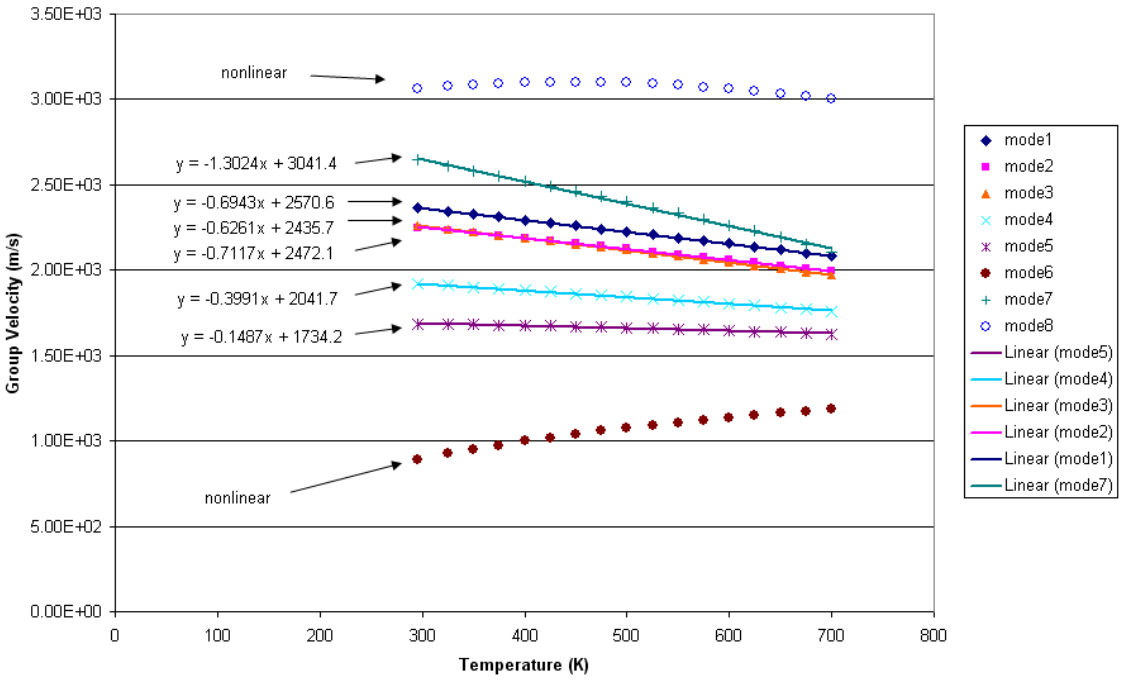

Figure 5.10: Group velocity of each wave mode at 115 kHz as a function of temperature (25°K increments). Solid lines are linear best-fits to the data obtained via the SAFE technique. Each wave mode has a unique response to temperature.

5.5 Temperature Models and Experiment

To further characterize the temperature dependence of the guided wave propagation, a series of time-domain finite element models of a 6.25 inch long Zircaloy specimen were run for varying temperatures. For each temperature selected, the material properties were adjusted according to the data given in Appendix A. Time-of-flight in the specimen was determined by calculating the difference in arrival time between the reflection from the trapezoidal horn and the reflection for the back of the specimen. Results are summarized in Figure 5.11.

For comparison, Figure 5.11 also shows the estimated time-of-flight values which were calculated based on the theoretical group velocities predicted by the SAFE analysis (Section 5.4). Since the SAFE group velocities are only valid for the rectangular cross-section, 22 μs was added to the estimated time-of-flight values to account for the time-of-flight in the trapezoidal horn.[16] The finite element results predicted a larger change in the time-of-flight versus temperature compared to the estimates based on the SAFE group velocities. However, this is expected because the estimates based on the SAFE group velocities only accounted for velocity changes in the rectangular cross-sections and did not account for velocity changes in the trapezoidal horn. The time-of-flight in the trapezoidal horn (i.e. the 22 μs shift) should also increase as temperature increases.

A series of experimental measurements were performed with a 6.25 inch long Zircaloy specimen. The specimen was heated in a tube furnace and allowed to cool. The tube furnace produced rapid temperature changes, so it was difficult to collect data at an equilibrium temperature. To reduce the rapid temperature swings, fiber glass insulation was used to wrap the specimen. A thermocouple was placed against the specimen inside the insulation to get the best estimate of the specimen temperature.[17] The results for the temperature experiments are also shown in Figure 5.11.

[16] The 22 μs shift sets the predicted time-of-flights approximately equal at room temperature. The 22 μs shift is also in agreement with information extracted from the finite element displacement data. Note that this 22 μs correction should increase as temperature increases.

[17] There was a large temperature differential between the furnace temperature and the temperature recorded by the thermocouple inside the insulation.

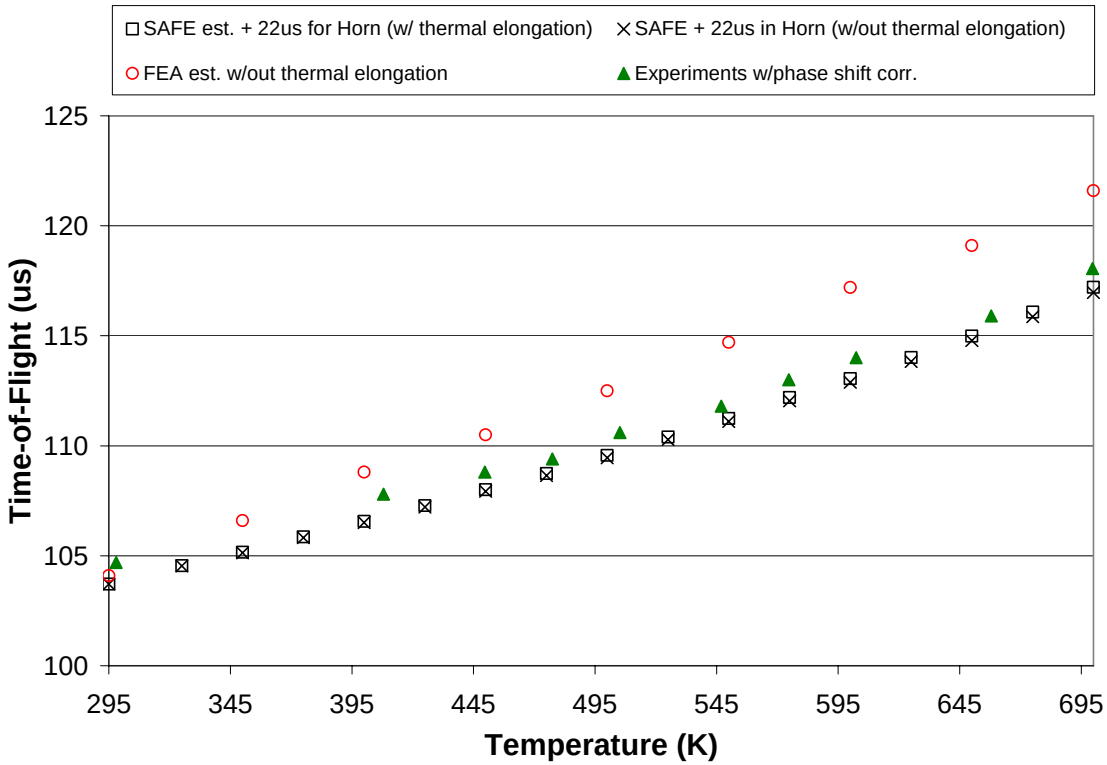

Figure 5.11: Comparison of the predicted and experimental guided wave time-of-flight versus temperature. The change in the experimental results was less than predicted by the finite element calculations. However, the temperature recorded in the experiments may be different than the average temperature of the bar specimen.

The experimental time-of-flight measurements turned out to be closer to the SAFE estimates. As previously discussed, the finite element results were expected to be more accurate because the SAFE estimates do not account for velocity changes in the trapezoidal horn. There was a small discrepancy in frequency between the model and experiments,[18] but it is unlikely that this explains the differential in time-of-flight values.

A more likely explanation is experimental error. Even with the fiber glass insulation, the temperatures recorded in the tube furnace still changed relatively quickly. It is likely that the surface of the specimen (and the thermocouple) were hotter than the inside volume of the specimen. Since the ultrasound propagates through the volume of the specimen, it is plausible that the 'average' temperature of the bar experienced by the ultrasonic waves was lower than the surface temperature recorded by the thermocouple.

[18] Finite element models performed at 150 kHz. The center frequency recorded in the experiments was approximately 137 kHz.

5.6 Displacement Profile

Within the course of this work, it was also of interest to predict what size defect in the bar specimen could potentially be identified using the in-situ monitoring system. In doing so, it is valuable to have knowledge of the displacement profiles for a selected wave mode. A plot of the displacement profile can be determined by plotting the displacements (Eigen vectors) at each node in the cross-section of the SAFE calculations.

Figure 5.12 shows the wave structures for the guided wave mode corresponding to the experimental observations. The profile for the Uz displacements (parallel to the length of the bar) shows that there is a lower displacement amplitude near the center of the cross-section.

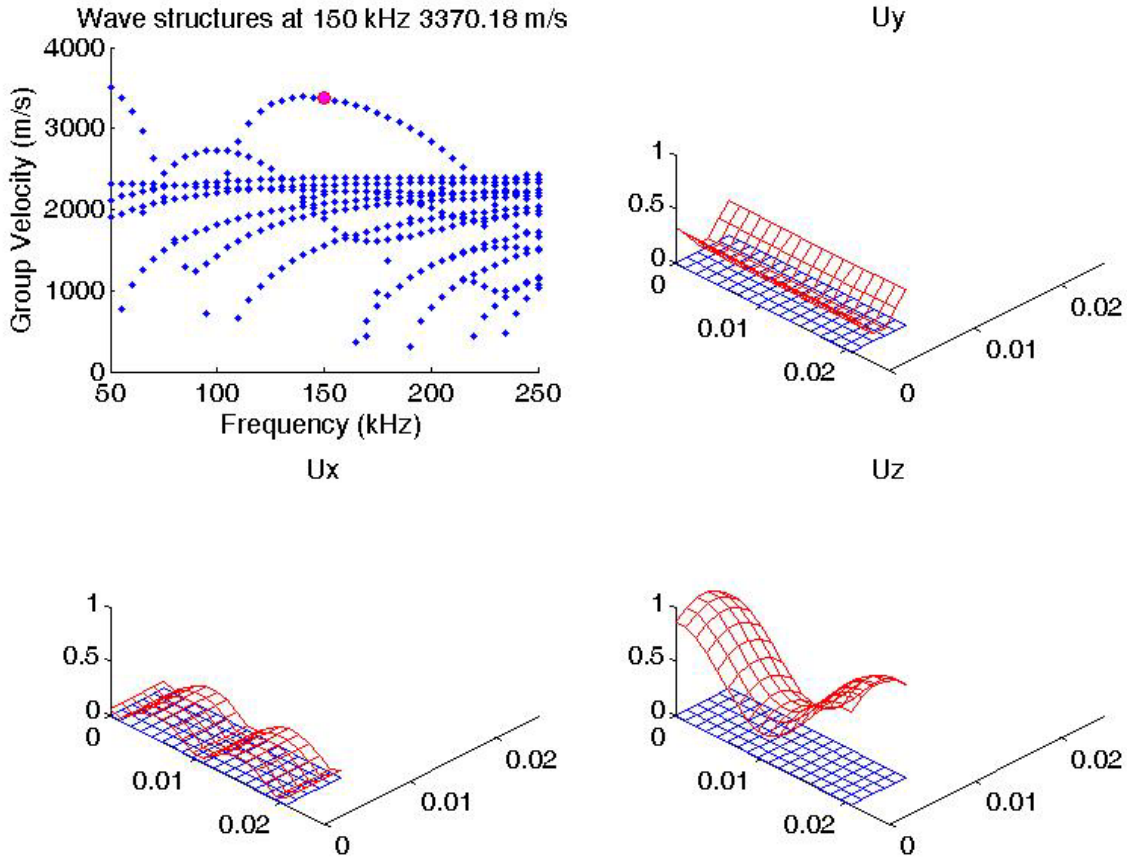

Figure 5.12: Wave structures at 150 kHz for the guided wave mode with highest group velocity. The Uz displacement field shown indicates that the displacement amplitude along the axis of the bar specimen is lower in the center of the bar.

5.7 Direct Detection of Defects

Several defects were modeled in the course of this work. Figure 5.13 illustrates Case 1 of a spherical air void located within the bar specimen volume. In Case 1, the defect was located in the center of the rectangular cross-section and in the center of the length of the specimen. Figure 5.14 shows the simulated signal for a 2.5 mm radius defect compared to the baseline signal for a specimen without defect. The defect reflection can be seen in the simulated signal. However, the defect reflection has a relatively low amplitude.

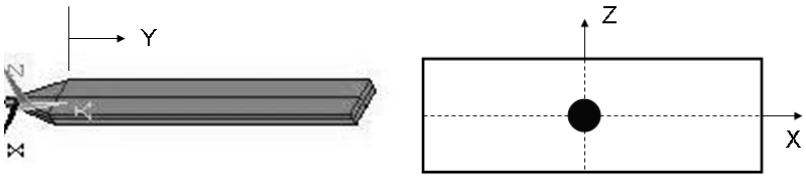

Figure 5.13: Case 1 of a spherical air void in the rectangular bar specimen. The defect was located at the center of the cross-section (X = 0 mm, Z = 0 mm) and at axial position Y = 63.5 mm. The defect radius was parametrically varied. Position Y = 0 is defined by where the horn meets the bar.

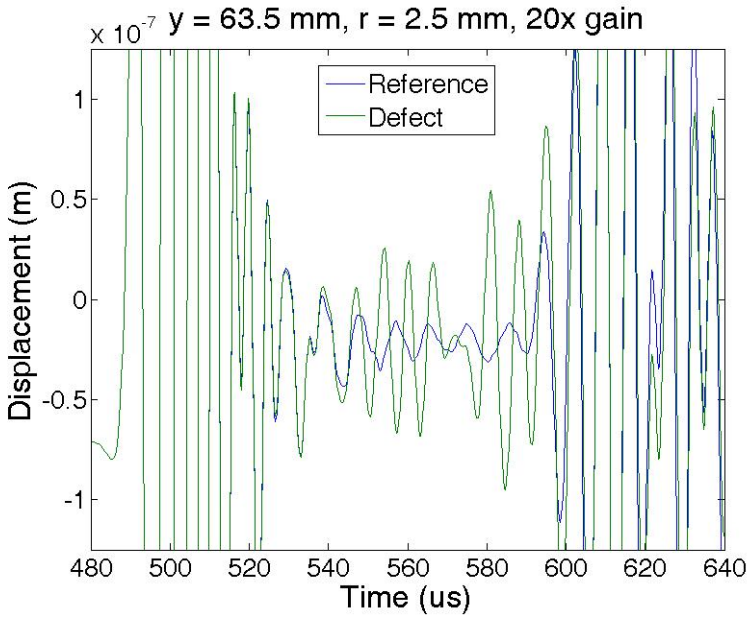

Figure 5.14: Example of simulated waveforms obtained in the parametric study of spherical air defect Case 1. The blue line is the reference signal (no defect) and the green line is the waveform for a 2.5 mm radius defect. The reflection at 500 μs is the horn reflection. The reflection at 600 μs is the reflection for the end of the specimen. The defect reflection is located at 555 μs.

Parametric Study

In Cases 2 and 3, off-center defects were studied as shown in Figure 5.15 (X = 3.5 mm) and Figure 5.16 (X = 7.0 mm), respectively. Then, the radii of the defects were parametrically varied to estimate what size defect was detectable.

Because the time-domain finite element analysis lacks the signal noise found in an experimental measurement, a 'signal-to-reference' ratio was calculated according to Equation 5.5. Using this equation, the relative change in the signal can be characterized as the defect size was parametrically varied in the finite element models.

$$\text{signal - to - reference ratio} = \frac{\text{amplitude of defect reflection}}{\text{amplitude of reference signal}} \tag{5.5}$$

By calculating the signal-to-reference ratio for each defect size studied in the parametric analysis, Figure 5.17 can be generated. For very small defects, the waveform was virtually identical to the reference waveform. As defect size increases, the defect reflections became easier to distinguish. In Figure 5.17a, the time-domain finite element results predict lower amplitudes in Case 2 (X = 3.5 mm) compared to Case 1 (X = 0 mm) for the same radius defect. In Figure 5.17b, the time-domain finite element results predict higher amplitudes in Case 3 (X = 7 mm) compared to Case 1 (X = 0 mm) for the same radius defect.

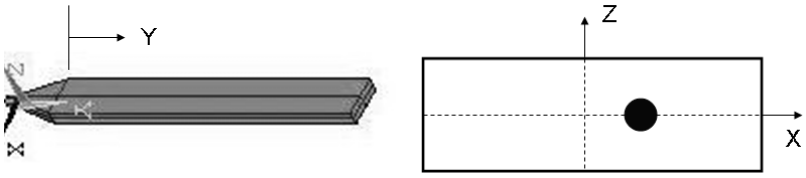

Figure 5.15: Case 2 of a spherical air void in the rectangular bar specimen. The defect was located at X = 3.5 mm, Z = 0 mm. The axial position was fixed at Y = 63.5 mm. The defect radius was parametrically varied. Position Y = 0 is defined by where the horn meets the bar.

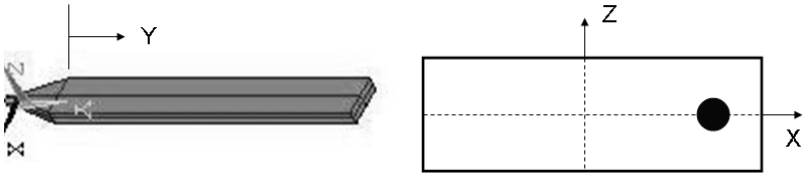

Figure 5.16: Case 3 of a spherical air void in the rectangular bar specimen. The defect was located at X = 7.0 mm, Z = 0 mm. The axial position was fixed at Y = 63.5 mm. The defect radius was parametrically varied. Position Y = 0 is defined by where the horn meets the bar.

The relative comparison of Cases 1, 2 and 3 presents a very interesting result. Not only does the signal amplitude vary with defect position in the cross-section of the bar, but this variation in amplitude does not appear to be systematic. It is not particularly clear why the 3.5 mm offset (Case 2) has slightly lower amplitudes compared to no offset (Case 1). One possible explanation is multi-path effects. The results for the 7 mm offset (Case 3) having a higher amplitude is consistent with the Uz displacement amplitude shown in Figure 5.12.

Figure 5.18 illustrated the off-center defects considered in Cases 4, 5 and 6 of the spherical defect investigation. Because the defects were closer to the surface of the bar, only defects up to 1.5 mm in radius could be modeled. In the results of the parametric study, there was no difference between the defect signals and the reference signal for Cases 4, 5 and 6.

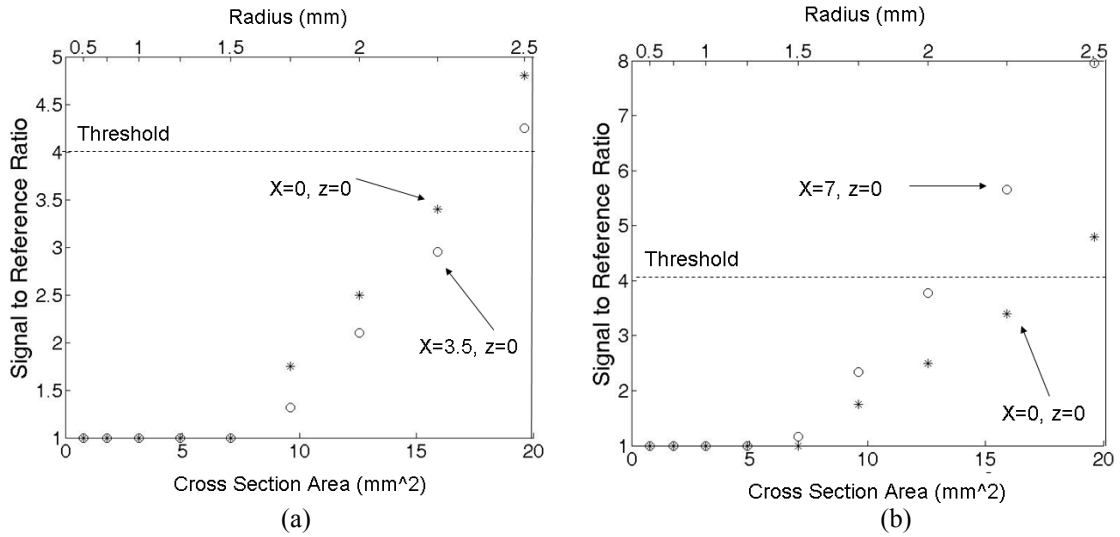

Figure 5.17: Comparison of signal amplitudes for spherical defects where the ratios of defect amplitude to reference signal amplitude are shown. (a) A 3.5 mm offset from center results in lower amplitude signals. (b) However, a 7 mm offset from center results in higher amplitude signals.

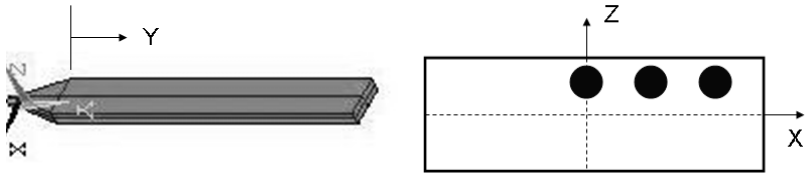

Figure 5.18: Cases 4, 5, and 6 of a spherical air void in the rectangular bar specimen. The defects were located at Z = 0 mm and the axial position was fixed at Y = 63.5 mm. Cases 4, 5, and 6 had X positions of 0 mm, 3.5 mm and 7.0 mm respectively. The defect radii were parametrically varied. Since these defects are closer to the surface of the bar, only defects up to 1.5 mm radius could be modeled. No change (defect signal vs. reference signal) was observed. Position Y = 0 is defined by where the horn meets the bar.

Axial Position Effect

In order to estimate the axial resolution of the in-situ monitoring technique, the axial position of the spherical defect described in Case 1 was parametrically varied. As the axial position of the defect was increased from Y = 63.5 mm (center of length), the arrival time of the defect increased in the simulated signal until the defect reflection became buried in the reflection from the end of the specimen. As the axial position of the defect was decreased from Y = 63.5 mm, the arrival time of the defect decreased. As the primary defect reflection merged with the horn reflection, a secondary reflection appears in the waveform.

Crack-like Defects

Figure 5.19 illustrated the position and orientation of the rectangular defects investigated in this work. The defects were all located in the center of the bar (Z = 63.5 mm), and all the defects were 5 mm in length (parallel to Y axis).[19] The height (parallel to Z axis) and width (parallel to X axis) were then varied parametrically. In this manner both defects parallel[20] to the bar axis and defects perpendicular[21] to the bar axis were simulated.

Figure 5.20 shows the results of the parametric analysis. The signal-to-reference ratio is calculated according to Equation 5.5. As before, the data has been plotted according to the defect surface area which is normal to the incident waves propagating along the axis of the bar. By plotting the results versus surface area, it was observed that a 5 mm high by 1 mm wide defect yields approximately the same reflection amplitude as a 1 mm high by 5 mm wide defect.

[19] The finite element code used in this investigation is only valid for open cracks (faces not touching). In the event of closed cracks (faces touching), a different modeling approach must be investigated.

[20] A defect with dimensions length = 5 mm, height = 5 mm, and width = 1mm would constitute a defect parallel to the bar axis. The approaching wave front will be incident on the thin edge of the defect.

[21] The approaching wave front will be normal to the crack faces.

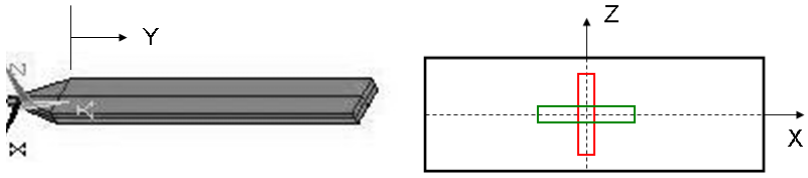

Figure 5.19: Position and orientation of the rectangular defects within the bar volume. The red rectangle indicates the orientation of a 'vertical' crack, and the green rectangle indicates the orientation of a 'horizontal' crack. The defects were centered in the cross-section (X = 0 mm and Z = 0 mm). The axial position was fixed at Y = 63.5 mm. The height and width of the defects were parametrically varied. Position Y = 0 is defined by where the horn meets the bar.

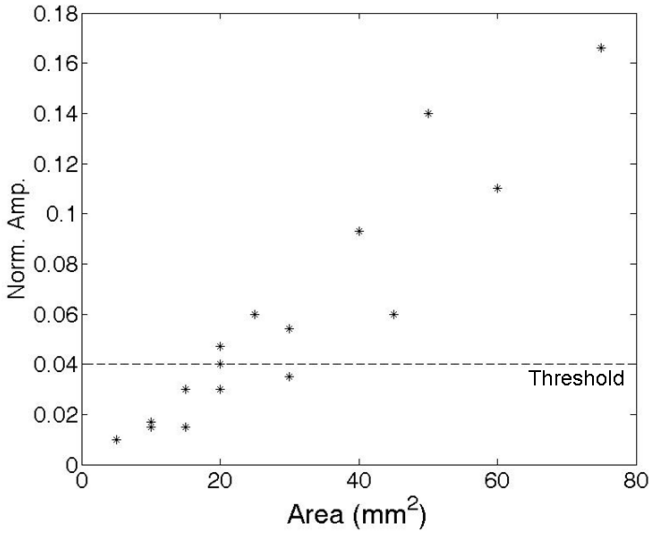

Figure 5.20: Comparison of signal amplitudes for rectangular defects where the ratios of defect amplitude to reference signal amplitude are shown.

Discussion

The magnetostrictive technique provides for an A-scan measurement of the rectangular bar specimen. Thus, the available data is amplitude versus time. As with all A-scan measurements, time information is very valuable because it can be used to determine the axial position of something producing a reflection. Utilization of amplitude information is somewhat difficult because it depends on many factors. The size, shape, and orientation of a defect will all affect reflection amplitude. For the rectangular bar specimen, results showed that amplitude will also vary due to the defect's position with respect to the cross-section of the specimen.

Other Defect Types

Several other defect geometries were investigated in the course of this work. Figure 5.21 illustrates a case where a hemispherical 'hole' defect on the surface on the bar specimen was considered in the modeling. This surface defect was considered at the center of the bar (Y = 63.5 mm) with X positions of 0 mm, 3.5 mm, and 7.0 mm. The defect radius was varied from 0 to 3 mm. None of the results had a signal-to-reference greater than 5. It was interesting to note that the received amplitudes for X = 7.0 mm were higher than the other X positions. This was consistent with the results observed for the internal spherical defects and the displacement amplitudes shown in Figure 5.12. Although surface defects are not of significant interest,[22] they would in principal permit experimental validation of the models.

Figure 5.22 and Figure 5.23 illustrate geometries with blister-like defects. Several parameters were varied in the analysis (blister radius, blister depth, and X position). Results showed virtually no change in the A-scan signal compared to the reference signal for all the cases studied.

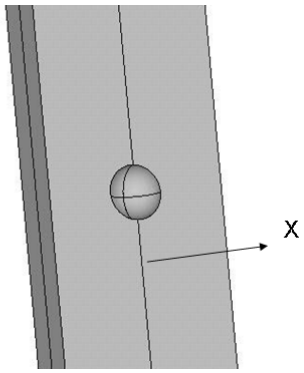

Figure 5.21: Hemispherical hole on the surface of the bar specimen. The axial position was fixed at Y = 63.5 mm. The radius of the defect was parametrically varied. Position Y = 0 is defined by where the horn meets the bar. X position of 0 mm, 3.5 mm, and 7.0 mm were considered.

[22] Surface defects are realistic analogs to defects common in MTR applications.

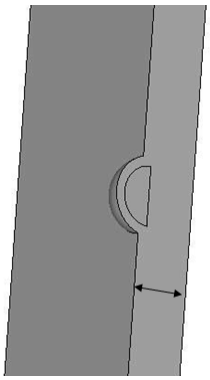

Figure 5.22: Hemispherical blister near the surface of the bar. The axial position was fixed at Y = 63.5 mm. The radius (0.5 to 1.5 mm), depth (0.5 to 1.5 mm) and X position (0 to 7 mm) were all varied parametrically in the investigation. Position Y = 0 is defined by where the horn meets the bar. The figure only shows one quadrant of the bar volume so that the internal defect can be seen. Thus, the dimension identified with black arrows is only half of the total specimen thickness.

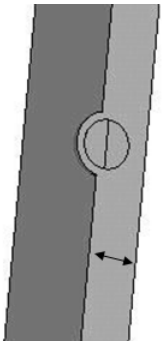

Figure 5.23: Spherical blister near the surface of the bar. The axial position was fixed at Y = 63.5 mm. The radius (0.5 to 1.5 mm), depth (0.5 to 1.5 mm) and X position (0 to 7 mm) were all varied parametrically in the investigation. Position Y = 0 is defined by where the horn meets the bar. The figure only shows one quadrant of the bar volume so that the internal defect can be seen. Thus, the dimension identified with black arrows is only half of the total specimen thickness.

5.8 Defect Induced Temperature Gradient

As previously mentioned, small defects are difficult to detect by observing a reflection in the A-scan measurement. However, there are other characteristics which can be considered. Ultimately, the in-situ monitoring technique is intended for monitoring specimens in a test reactor. For specimens of interest in reactor applications, it is possible that a defect will produce a temperature anomaly in the specimen. This temperature anomaly could be caused by radiation heating of the defect or by the defect affecting the heat transfer to the surrounding water [83].

As an example, a "blister" specimen containing a temperature gradient was modeling using the COMSOL finite element program.[23] To define the temperature gradient, one boundary was set to have a higher temperature compared to the surrounding environment. A steady state heat transfer solution was then calculated to solve for the temperature gradient across the volume of the "blister" specimen. Figure 5.24a shows the temperature gradient modeled for this test case. If temperature dependent material properties are used, the mechanical properties of the specimen will also vary as a function of temperature. Figure 5.24b shows the gradient in Young's modulus which corresponds to the temperature gradient in Figure 5.24a.

Using COMSOL, the steady state heat transfer solution can then be used as the initial condition to the transient analysis of guided wave propagation. Figure 5.25 shows a comparison of simulated waveforms with different temperature conditions. In the case of a temperature gradient, the end reflection has a reduced amplitude. The presence of the temperature gradient degrades the constructive interference needed for strong guided wave propagation.

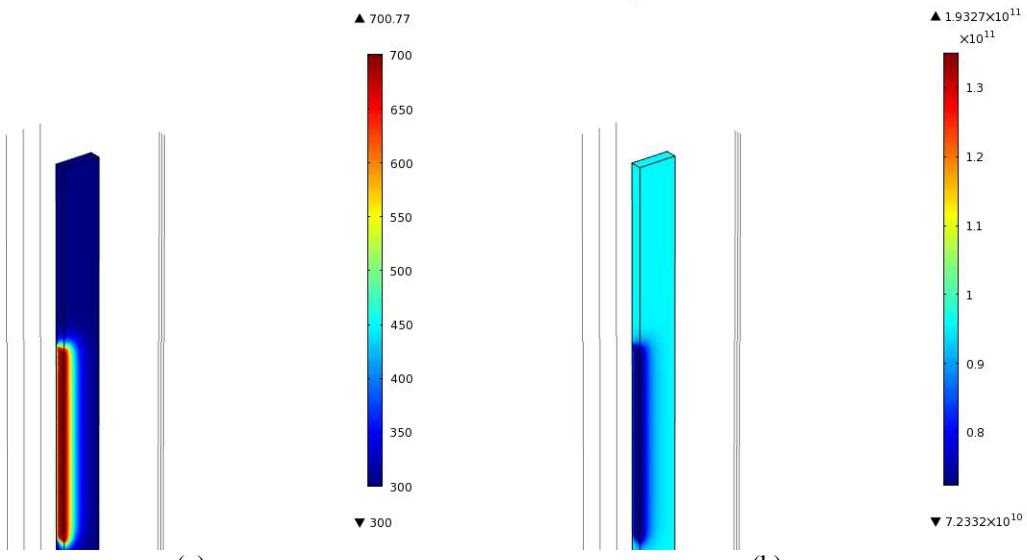

Figure 5.24: COMSOL model of "blister" specimen with a temperature gradient. (a) Temperature distribution. (b) Corresponding gradient in Young's modulus due to the temperature gradient.

[23] See Appendix B.

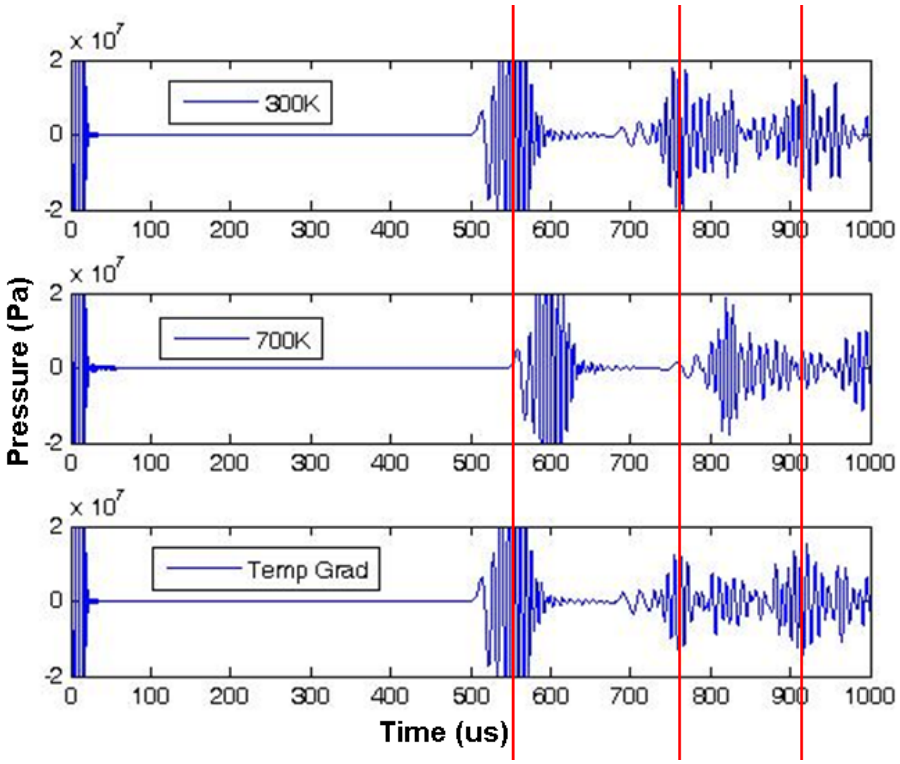

Figure 5.25: Comparison of simulated waveforms under different temperature conditions. The temperature gradient results in an end reflection with lower amplitude compared to a bar specimens with uniform temperature distributions.

5.9 Bar Specimen with Insert

In certain applications, the "blister" specimens utilized in test reactor experiments contain an insert of a second material [83]. At the outset of this work, there was an interest in determining how the ultrasonic signal from a composite specimen compared to the signals from a solid specimen.

5.9.1 Actual

Figure 5.26 shows experimental results for a bar specimen containing an insert. Unexpectedly, the experimental results did not show any significant reflections from the insert in the central region of the bar specimen. The results for the experiments with an insert were actually very similar to what would be expected for a solid specimen except for perhaps a lower amplitude reflection from the end of the specimen.

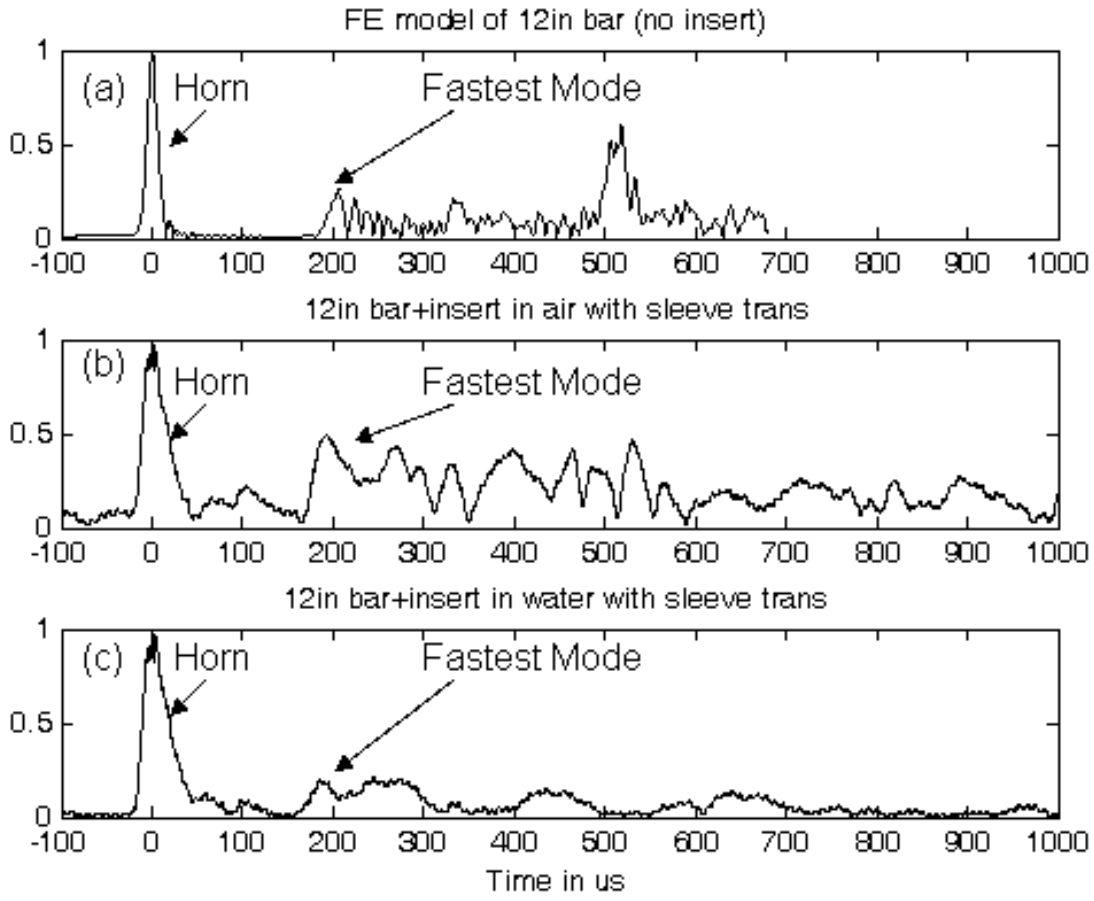

Figure 5.26: Comparison of results for specimens with and without inserts. Analytic envelopes of (a) the waveform predicted by time-domain finite element analysis of a specimen with no insert, (b) the experimental waveform of a specimen with an insert in air, and (c) the experimental waveform of a specimen with an insert in water for a 12 inch rectangular bar specimen. Actual insert has a negligible effect.

To further investigate the specimen with insert, pulse-echo measurements were carried out using 2.25 MHz contact transducers to measure the acoustic properties of the insert material. Results are summarized in Table 5.1. The recorded wave velocities for the insert were very similar to the velocities for bulk Zircaloy. However, the measured signals were highly attenuated in the insert region. The longitudinal waves appeared to be more attenuated compared to the shear waves.

Table 5.1: Velocity results from the specimen with insert material.

	Zircaloy reference values	Zircaloy section	Insert region
Long. waves	4.72 mm/μs	4.92 mm/μs	4.81 mm/μs
Shear waves	2.36 mm/μs	2.41 mm/μs	2.40 mm/μs

5.9.2 Hypothetical

The actual composition of the insert material is proprietary. Thus, the exact values of the mechanical properties of insert were not available. In an attempt to demonstrate how the insert composition could affect the ultrasonic signals, finite element models were performed with different insert materials.

Figure 5.27 shows the simulated waveform assuming the insert was composed of a Zirconium-Oxide found in the COMSOL material library. [24] The results shown in Figure 5.27 are similar to the experiments (Figure 5.26), but there is more noise present between the joint reflection (at ~550 μs) and the end reflection (at ~750 μs).

Figure 5.28 shows the simulated waveform assuming the insert was composed of Aluminum. The large differential between the acoustic properties of Aluminum and Zircaloy significantly alters the simulated waveform. There is much more reflected energy between the joint refection (at ~550 μs) and the end reflection (at ~750 μs).

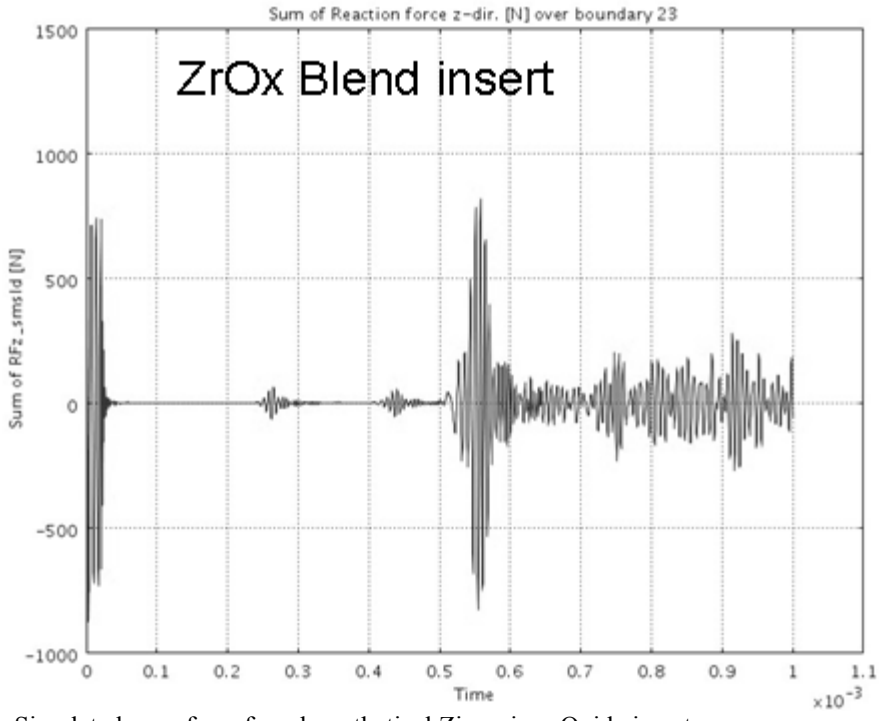

Figure 5.27: Simulated waveform for a hypothetical Zirconium-Oxide insert.

[24] See Appendix B.

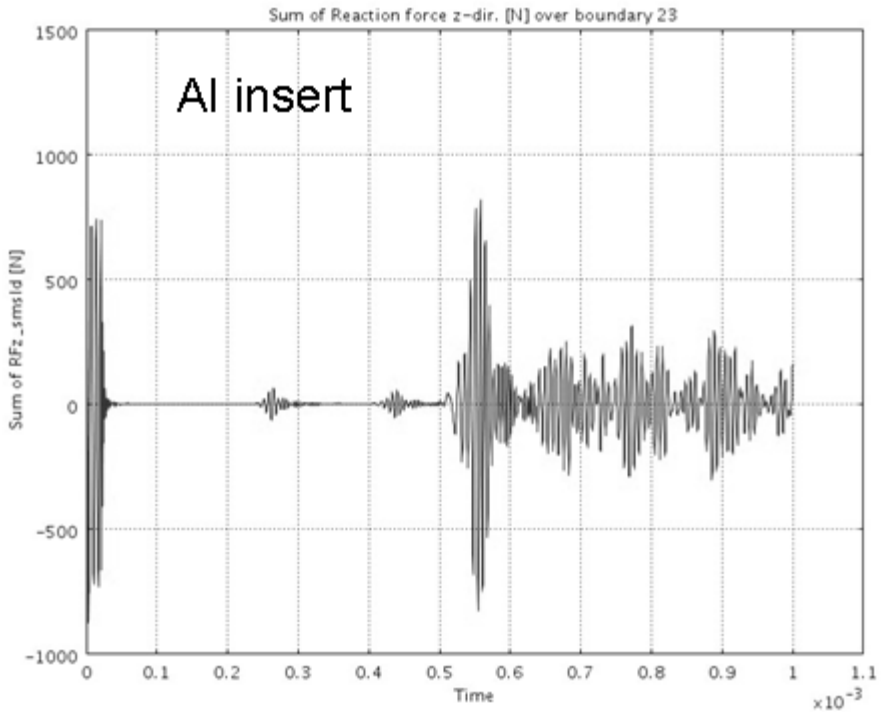

Figure 5.28: Simulated waveform for a hypothetical Aluminum insert.

5.10 Hardening

As previously mentioned, the in-situ monitoring technique is intended for the measurement of specimens in a test reactor environment. Over time, radiation exposure leads to damage in the microstructure of materials. In many cases, this causes the material to "harden." Radiation hardening is often characterized by an increased elastic modulus and reduced ductility [84].

In the finite element models, the radiation hardening can be simulated by simply adjusting the material properties. Figure 5.29 compares a simulated waveform for the normal material properties for Zircaloy and a simulated waveform where the elastic modulus was increased by 10%. The waveforms in Figure 5.29 show that the increased elastic modulus produces a small decrease in the simulated time-of-flight.

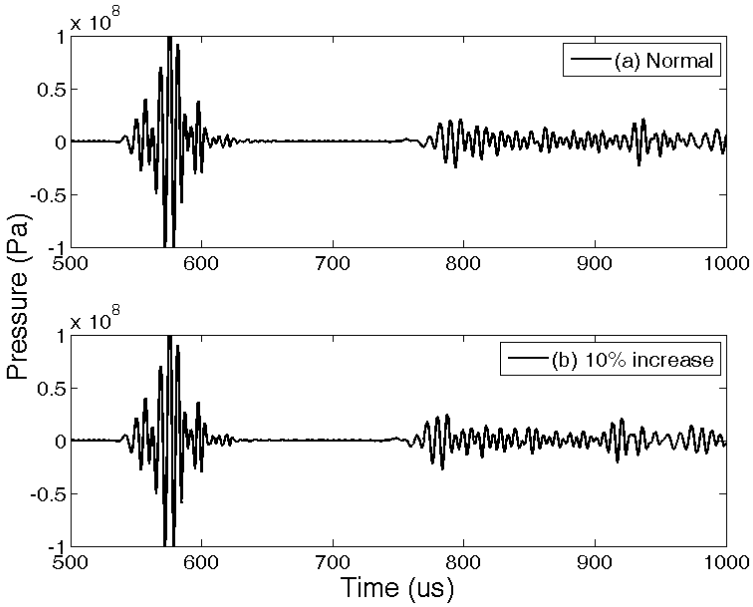

Figure 5.29: Simulated effect of radiation hardening assuming Zircaloy. (a) Normal material properties at 695K. (b) Elastic modulus increased by 10%. Group velocity increases due to hardening.

5.11 Swelling

As discussed in Appendix A, swelling due to radiation exposure is not common in Zircaloy. However, the hypothetical effects of swelling can still be modeled for illustrative purposes. In order to model isotropic swelling, an increase in volume must by coupled with a decrease in density. For a 10% increase in volume, there is approximately a 9% decrease in density. The 10% increase in volume also corresponds to approximately a 3.25% increase in each linear dimension of the specimen.[25]

Figure 5.30a once again shows the simulated waveform for a Zircaloy specimen with normal material properties. Figure 5.30b shows the simulated waveform with a 10% increased volume, a 9% decreased density, and no change in the elastic modulus. Figure 5.30c shows the simulated waveform with a 10% increased volume, a 9% decreased density, and a 10% increase in modulus to represent radiation hardening. As the results show, each set of parameters result in a slightly different simulated time-of-flight.

[25] See Section A.2 for addition details.

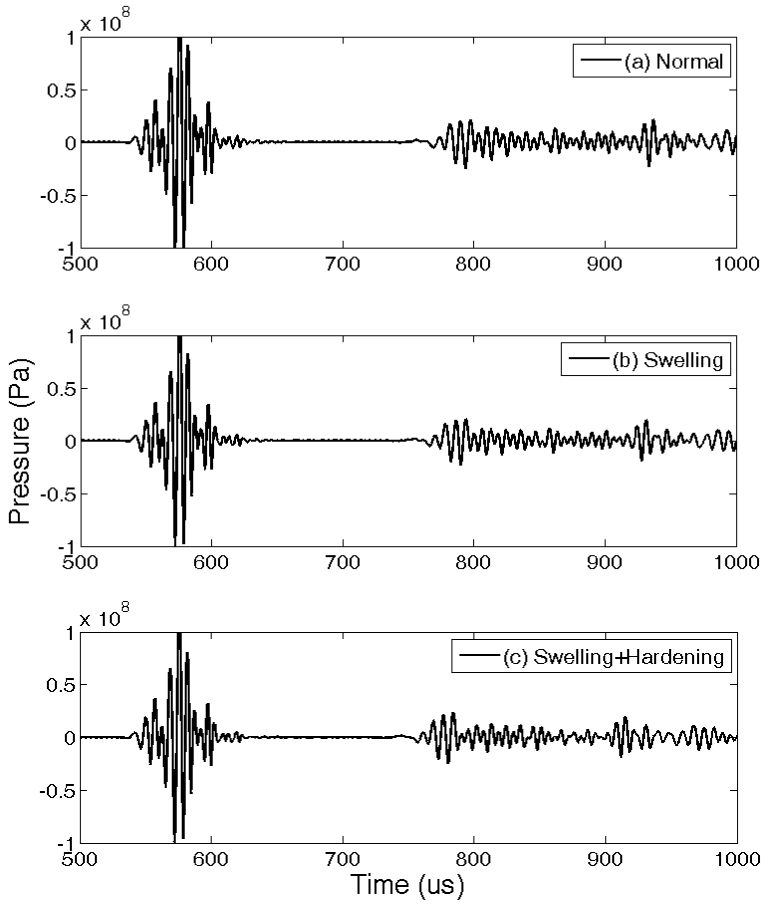

Figure 5.30: Simulated effect of isotropic swelling assuming Zircaloy. (a) Normal material properties at 695K. (b) 10% increase in volume, 9% decrease in density, and no change in modulus. (c) 10% increase in volume, 9% decrease in density, and a 10% increase in modulus to represent hardening.

5.12 Bending

The deformation of bar specimens is not always isotropic. Figure 5.31 shows a hypothetical case where the bar is bent in the middle. In this test case the curvature of the bent regions was defined by a 10° arc with a radius of curvature equal to 31 m. The finite element geometry shown in Figure 5.31 divided the bent region into 10 equal segments in order to provide improved resolution of the curvature. Figure 5.32a once again shows the simulated waveform for a Zircaloy specimen with normal material properties, and Figure 5.32b shows the simulated waveform for the bent section. In this particular test case, the guided wave did not appear to be sensitive to the bend in the specimen.

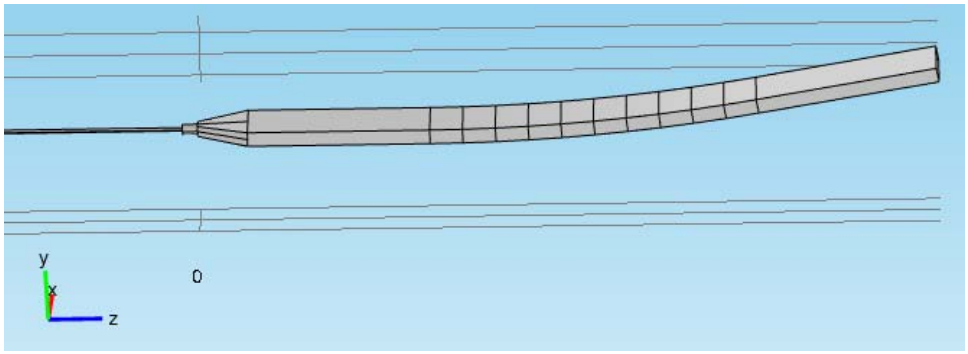

Figure 5.31: Finite element geometry of a bar specimen with a bent region in the center of the specimen.

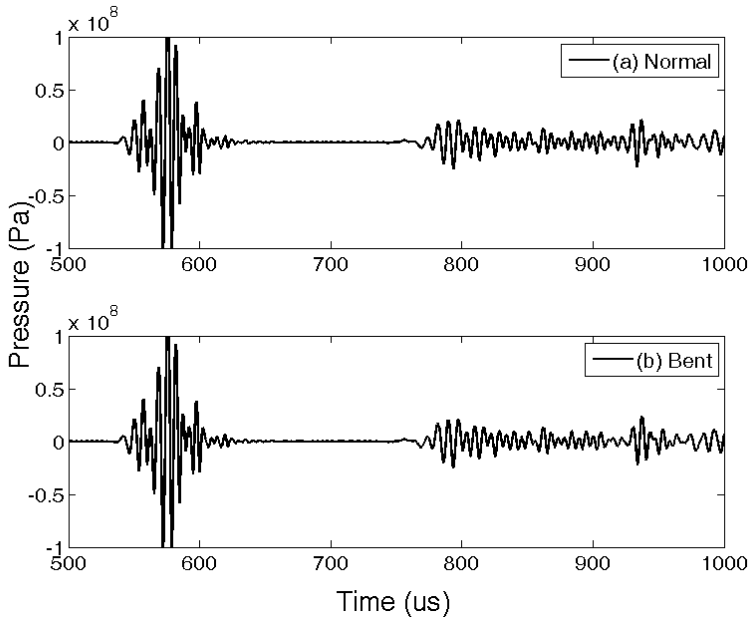

Figure 5.32: Simulated effect of a bent specimen assuming Zircaloy. (a) Simulated reference signal from a straight specimen. (b) Simulated signal for the bent geometry.

5.13 Summary

When studying the in-situ monitoring system, the characteristics of each specimen must as be considered as part of the guided wave analysis. In this chapter, a 'blister' specimen having a rectangular cross-section was considered. Theoretically driven semi-analytical finite element (SAFE) calculations, time-domain finite element calculations, and experimental measurements were performed to investigate the guided wave propagation in this specimen. The SAFE calculations, finite element predictions, and experimental results all demonstrated good agreement.

In general, the guided wave mode with the fastest group velocity appeared to be the most prominent in both the simulated and experimental measured waveforms. Very little change in the signal was observed when varying the operating frequency.[26]

The temperature dependence of the guided wave propagation was also studied. The experimental measurements at 150 kHz were reasonably close to the numerical predictions. Based on the experimental conditions, it is very likely that the temperature recorded by the thermocouple was different that the average temperature of the specimen.

Several types of defects were modeled to estimate the detection capabilities of the in-situ monitoring system. Due to the low frequency of the magnetostrictive transducers, the models predicted that it would be difficult to identify defects based on reflections in the signal. However, defects can sometimes produce temperature anomalies in the specimen. The models indicated that detection of a defect induced temperature gradient was possible. Future work should investigate the detection of temperature gradients.

Since the in-situ monitoring system was inspired by the need for novel techniques for use in materials and test reactor (MTR) environments, several types of radiation effects were also modeled. The models indicated that the in-situ monitoring system was most sensitive to radiation hardening of the specimen. The models also indicated that swelling and bending would be difficult to detect with frequencies associated with magnetostrictive materials.

[26] As shown in Chapter 4, the magnetostrictive transducers used in this work do not allow for much adjustment of the frequency content in the signal.

CHAPTER 6: CREEP SPECIMENS

There are several examples of using ultrasound for the detection of creep damage in the literature [85-87]. However, conventional ultrasonic techniques must be adapted for in-situ use in a reactor environment. Thus, a second potential application of the in-situ monitoring technique is to measure the change in length of creep specimens in real time.

Figures 6.1a and 6.1b show the Zircaloy and stainless steel specimens tested with the in-situ monitoring setup. The dimensions are based on the standard ASTM creep specimen (Figure 6.1c) [88]. However, the gauge lengths of the in-situ specimens were increased to improve the time-of-flight separation of the reflections in the received ultrasonic signals, because the magnetostrictive transducer operates at relatively low frequencies.

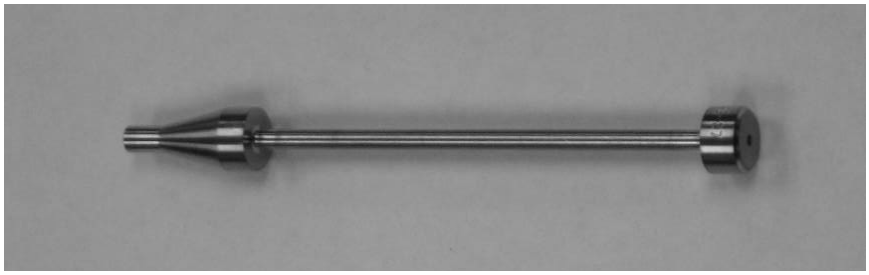

(a)

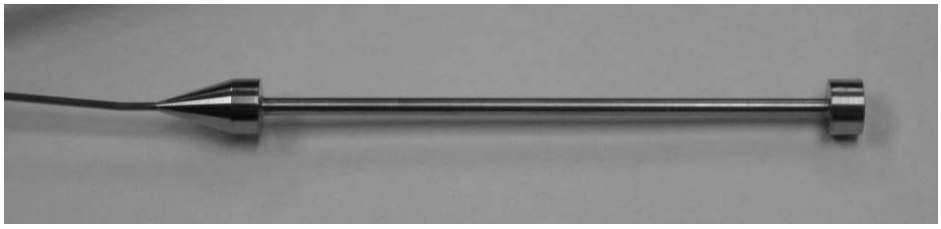

(b)

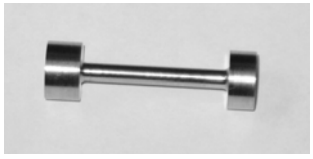

(c)

Figure 6.1: Photographs of creep specimens used in this investigation. (a) Older design with brazed joint between the waveguide and a 3 inch Zircaloy specimen. (b) Newer design with butt-weld between the waveguide and 4 inch stainless steel specimen. (c) Standard 1 inch ASTM stainless steel creep specimen.

6.1 Dispersion Curves

As discussed in Chapter 2, all wave propagation in solids is governed by the Navier-Cauchy equations. For the cylindrical gage length of the creep specimen, the boundary conditions are most easily defined in cylindrical coordinates. Assuming a homogeneous, isotropic medium, Equations 6.1 through 6.3 give the cylindrical form of the Navier-Cauchy equations, where λ_{Lame} is Lame's constant, E is elastic modulus, G is shear modulus, ρ is density, $\bar{u}$ is the displacement vector, and t is time. The symbol Φ stands for the dilatation in cylindrical coordinates [34-36].

$$(\lambda+2G)\frac{\partial\Phi}{\partial r}-\frac{2G}{r}\frac{\partial\omega_z}{\partial\theta}+2G\frac{\partial\omega_\theta}{\partial z}=\rho\frac{\partial^2 u_r}{\partial t^2} \tag{6.1}$$

$$(\lambda+2G)\frac{1}{r}\frac{\partial\Phi}{\partial\theta}-2G\frac{\partial\omega_r}{\partial z}+2G\frac{\partial\omega_z}{\partial r}=\rho\frac{\partial^2 u_\theta}{\partial t^2} \tag{6.2}$$

$$(\lambda+2G)\frac{\partial\Phi}{\partial z}-\frac{2G}{r}\frac{\partial(r\omega_\theta)}{\partial r}+\frac{2G}{r}\frac{\partial\omega_r}{\partial\theta}=\rho\frac{\partial^2 u_z}{\partial t^2} \tag{6.3}$$

$$\text{where: } \Phi=\frac{1}{r}\frac{\partial(ru_r)}{\partial r}+\frac{1}{r}\frac{\partial u_\theta}{\partial\theta}+\frac{\partial u_z}{\partial z}$$

For an infinitely long cylindrical waveguide, the boundary conditions are such that the cylindrical Navier-Cauchy equations can be reduced to the form given in Equations 6.4 and 6.5. Here, C_L is bulk longitudinal velocity, C_T is bulk shear velocity, C_p is phase velocity, k is wave number, a is radius, ω is angular frequency and J_n are Bessel equations. Equations 6.4 and 6.5 are often referred to as the Pochhammer equations [34-36].

$$\frac{2\alpha}{a}(\beta^2+k^2)J_1(\alpha a)J_1(\beta a)-(\beta^2-k^2)J_0(\alpha a)J_1(\beta a)-4k^2\alpha\beta J_1(\alpha a)J_0(\beta a)=0 \text{ axial} \tag{6.4}$$

$$(\beta a)J_0(\beta a)-2J_1(\beta a)=0 \quad \text{torsional} \tag{6.5}$$

$$\text{where: } \alpha^2=\left(\frac{\omega}{C_L}\right)^2-k^2=\left(\frac{\omega}{C_L}\right)^2-\left(\frac{\omega}{C_p}\right)^2$$

$$\text{and } \beta^2=\left(\frac{\omega}{C_T}\right)^2-k^2==\left(\frac{\omega}{C_T}\right)^2-\left(\frac{\omega}{C_p}\right)^2$$

As Equations 6.4 and 6.5 show, the solution of a cylindrical waveguide involves Bessel equations. A MATLAB computer program [43] was used to determine the phase velocity dispersion curve by numerically finding the roots to Equations 6.4 and 6.5.

Group velocity (C_g) dispersion curves were then determined from the phase velocity solution via Equation 6.6 where *fa* denotes frequency times radius [34,43]. The group velocity determines the time-of-flight observed in experimental measurements.

$$C_g = C_p^2\left[C_p - (fa)\frac{\partial C_p}{\partial (fa)}\right]^{-1} \tag{6.6}$$

Figures 6.2 and 6.3 show the dispersion curves calculated for Zircaloy and stainless steel specimens (respectively) having a 1/8 inch diameter gauge section. Only the axial guided wave modes are shown in Figure 6.2 and 6.3. The torsional and flexural modes were not of interest in this study. The dispersion curves show that a stainless steel creep specimen has higher group velocity compared to a Zircaloy creep specimen. Therefore, the stainless steel specimen required a longer gauge length (4 inch) compared to a Zircaloy specimen (3 inch) in order to have sufficient time-of-flight between reflections in the received ultrasonic signals.

6.2 Finite Element Analysis

The theoretical group velocity is only applicable to the gauge section of the creep specimen. As shown in Figures 6.1a and 6.1b, there is an abrupt transition between the gage section and the ends on the creep specimens. For the in-situ specimens, there is also a transition between the specimen and wire waveguide which must be taken into account.

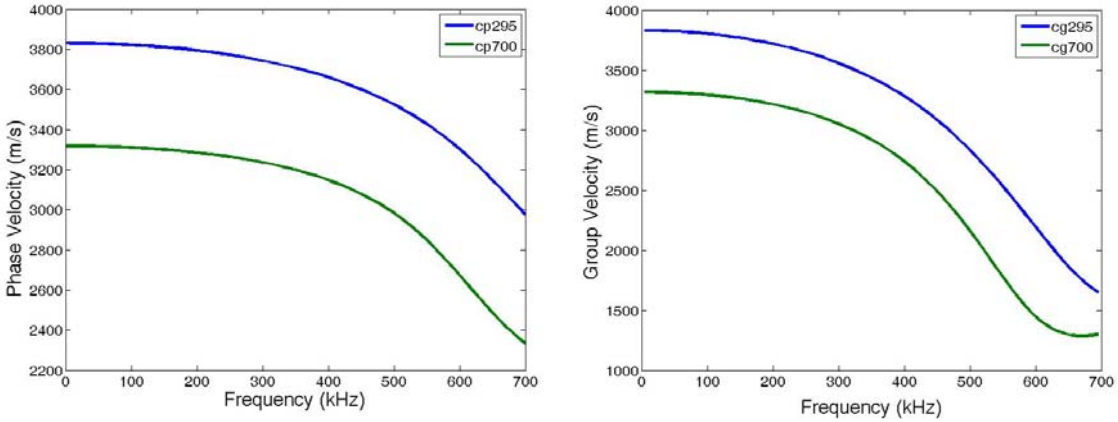

Figure 6.2: Dispersion curves for a 1/8 inch diameter Zircaloy rod. (a) Phase velocity. (b) Group velocity. Results shown for 295K and 700K.

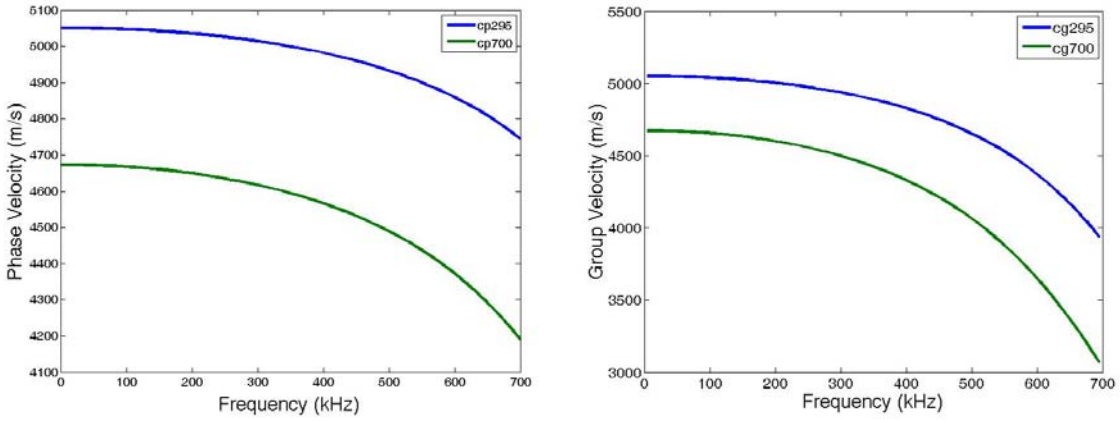

(a) (b)

Figure 6.3: Dispersion curves for a 1/8 inch diameter stainless steel rod. (a) Phase velocity. (b) Group velocity. Results shown for 295K and 700K.

Time-domain finite element models were used to estimate the effects of the geometric transitions inherent to the in-situ creep specimens. In addition, time-domain finite element models were also used to simulate several variations of the in-situ measurement configuration. For this series of models, a Zircaloy specimen attached to a stainless steel waveguide was modeled.

Through Transmission, No Acoustic Horn

Figure 6.4 shows an axi-symmetric finite element model of an in-situ test setup using a through transmission measurement. In this first case, an acoustic horn was not included in the geometry. A simulated ultrasonic wave was transmitted into the specimen via the wire[27] on the left side using a displacement boundary condition. The simulated displacements in the wire on the right side were then analyzed to estimate the through transmission signal. The simulated received signal is shown in Figure 6.5. Although the signal is relatively weak, the through-transmission measurement provides a well defined arrival time. However, the observed time-of-flight consists of travel in two wire waveguides in addition to the specimen. Thus, there is a significant challenge in trying to separate the changes in the time-of-flight in the specimen from the change in total-time-of-flight.

[27] 10 inch length

Figure 6.4: Axi-symmetric geometry for a through-transmission measurement without using transitional 'horns.' Time-domain finite element modeling was performed for a specimen in water (shown) and for a specimen in air (not shown).

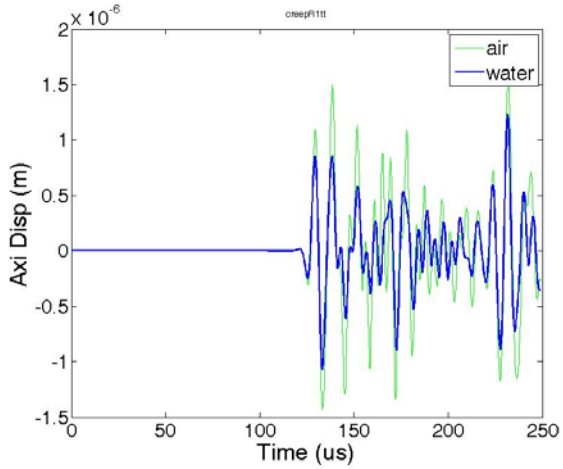

Figure 6.5: Results of the time-domain finite element modeling for the geometry shown in Figure 6.4. Simulated A-scan time-of-flight measurement has a well defined arrival time consistent with theory.

Through Transmission, With Acoustic Horn

Figure 6.6 shows an axi-symmetric finite element model of an in-situ test setup where acoustic horns were included on both sides of the through transmission measurement. Once again, a simulated ultrasonic wave was transmitted into the specimen via the wire on the left side using a displacement boundary condition. The simulated displacements in the wire on the right side were then analyzed to estimate the through transmission signal. The simulated received signal is shown in Figure 6.7. As expected, the through-transmission measurement provides a well defined arrival time. However, there is still the problem of separating the changes in the time-of-flight in the specimen from the change in total-time-of-flight.

Figure 6.8 shows a comparison of the two versions of the simulated through transmission. By including the acoustic horns, the amplitude of the simulated received signal was significantly increased. Thus, suggesting that the inclusion of the acoustic horns is beneficial to the in-situ measurement setup.

Figure 6.6: Axi-symmetric geometry for a through-transmission measurement with transitional 'horns.' Time-domain finite element modeling was performed for a specimen in water (shown) and for a specimen in air (not shown).

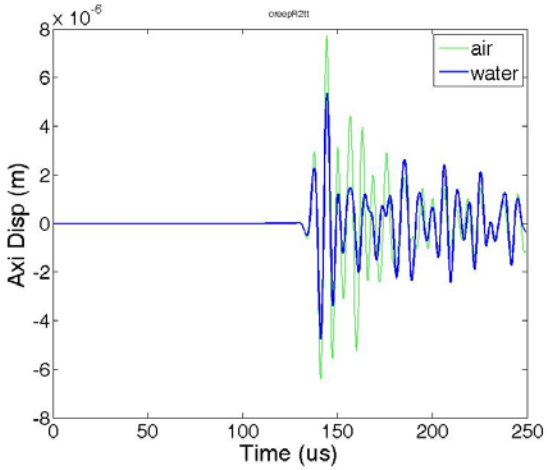

Figure 6.7: Results of the time-domain finite element modeling for the geometry shown in Figure 6.6. Simulated A-scan time-of-flight measurement has a well defined arrival time consistent with theory.

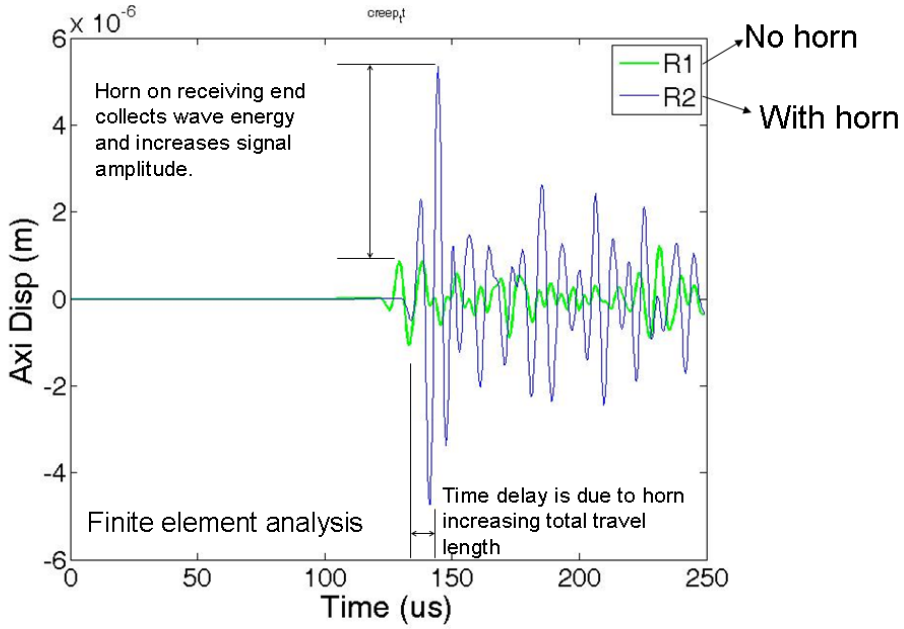

Figure 6.8: Comparison of the results shown in Figures 6.5 and 6.7. The received waveform amplitude is higher when using the transitional horns.

Pulse-Echo, No Acoustic Horn

Figure 6.9 shows an axi-symmetric finite element model of a pulse-echo in-situ test setup with no acoustic horn. A simulated ultrasonic wave was transmitted into the specimen via the wire on the left side using a displacement boundary condition. Note that the length of the wire[28] was chosen so that round-trip reflections in the wire waveguide would not interfere with observing reflections form the end of the specimen. The simulated displacements at the end of the wire on the left side were then analyzed to estimate the pulse-echo signal. The simulated received signal is shown in Figure 6.10. The simulated signal showed virtually not reflection amplitude at a time-of-flight consistent with ultrasonic wave traveling down and back through the gage length of the specimen.

Figure 6.9: Axi-symmetric geometry for a pulse-echo measurement without using transitional 'horns.' Time-domain finite element modeling was performed for a specimen in water (shown) and for a specimen in air (not shown).

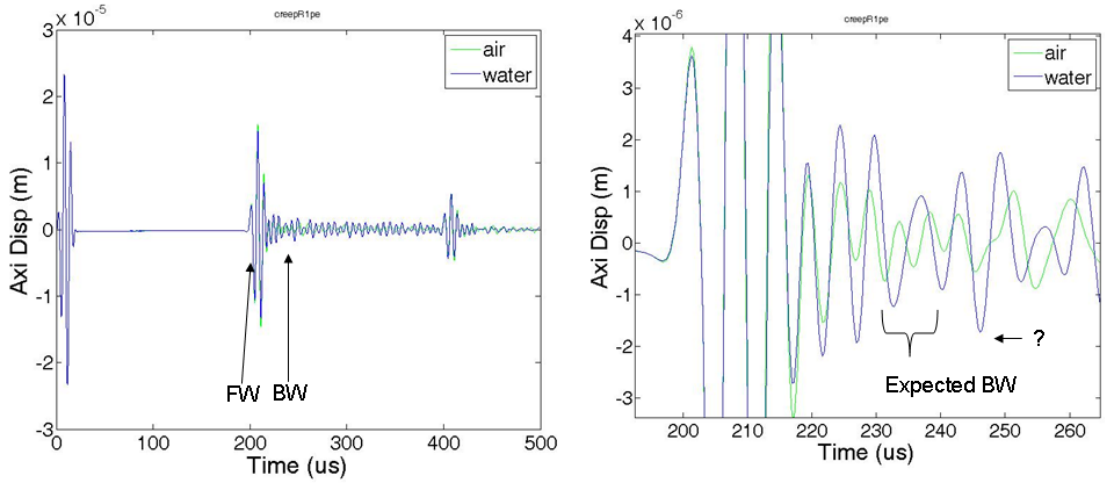

Figure 6.10: Results of the time-domain finite element modeling for the geometry shown in Figure 6.9. (a) Simulated waveform with the wire-specimen joint reflection (FW) and the expected location of the reflection from the end of the specimen (BW) labeled. (b) Zoomed in view of the region of interest. The reflection identified with the '?' may be the reflection form the end of the specimen.

[28] 20 inch length

Pulse-Echo, With Acoustic Horn

Figure 6.11 an axi-symmetric finite element model of a pulse-echo in-situ test setup with an acoustic horn between the wire waveguide and specimen. Once, again a simulated ultrasonic wave was transmitted into the specimen via the wire on the left side using a displacement boundary condition. The simulated displacements at the end of the wire on the left side were then analyzed to estimate the pulse-echo signal.

The simulated received signal is shown in Figure 6.12. In this case, the amplitude of the reflection from the end of the specimen is larger, so it is easier to distinguish it from the simulated waveform. The acoustic horn also produces a small time delay which increases the separation between the wire-specimen joint reflection and the reflection from the far end of the specimen. Based on the finite element studies, the pulse-echo measurement with an acoustic horn was expected to yield the best signals for an in-situ monitoring system.

Figure 6.11: Axi-symmetric geometry for a pulse-echo measurement with a transitional 'horn.' Time-domain finite element modeling was performed for a specimen in water (shown) and for a specimen in air (not shown).

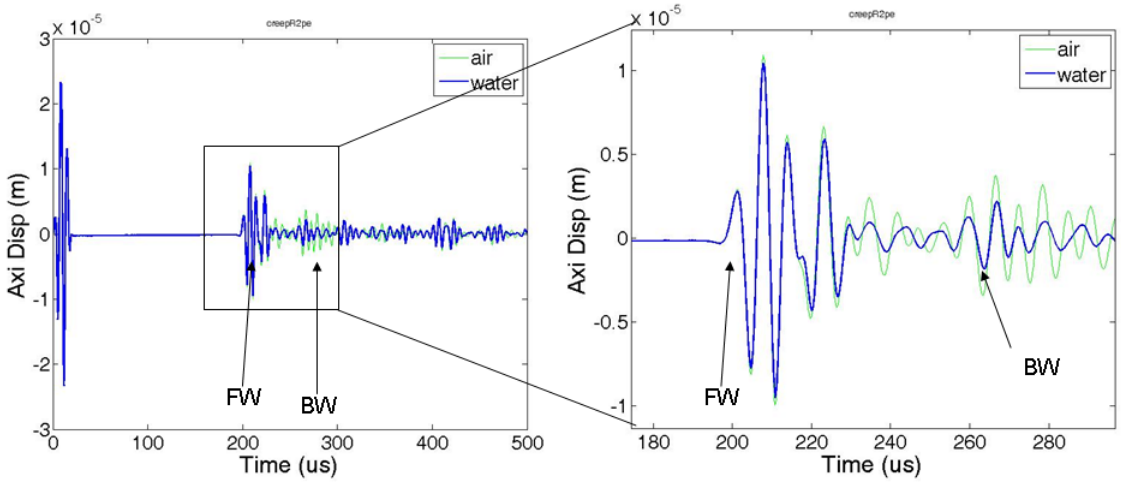

Figure 6.12: Results of the time-domain finite element modeling for the geometry shown in Figure 6.11. (a) Simulated waveform. (b) Zoomed in view of the region of interest. The wire-specimen joint is labeled as 'FW' and the reflection from the end of the specimen is labeled as 'BW.'

Variation of Gage Length

After establishing that the pulse-echo measurement with an acoustic horn was the most favorable for in-situ monitoring, a series of finite elements models were performed to predict how the ultrasonic waveform changed as the length of the creep specimen varied. Figure 6.13 shows selected results from this parametric model series. As the gage length was decreased from 3 inch, to 2 inch, and then to 1 inch; the echo from the far end of the specimen became increasingly difficult to resolve.

It is important to note that the finite element model is highly idealized. In practice there will be more noise in real signals compared to the finite element results.

6.3 Validation Experiments

In order to validate the finite element models, a series of experimental measurements were performed on a Zircaloy creep specimen with dimensions matching the model shown Figure 6.11. Figure 6.14 shows a comparison of the finite element results and early experiments performed with the old 'wire-wire' magnetostrictive transducer (Figure 4.1). The predicted time-of-flight is in good agreement with the experiments.

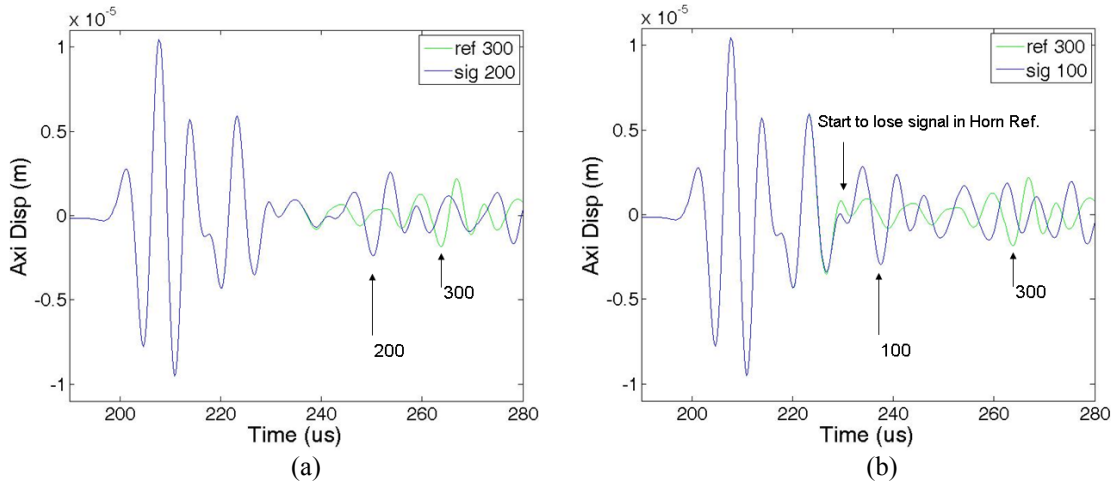

Figure 6.13: Selected results from the parametric study of creep specimen gage length. (a) Simulated waveform of a 50.8 mm (2 inch) gage length specimen (blue line) compared to the simulated waveform of a 76.2 mm (3 inch) gage length specimen (green line). (b) Simulated waveform of a 25.4 mm (1 inch) gage length specimen (blue line) compared to the simulated waveform of a 76.2 mm (3 inch) gage length specimen (green line).

Figure 6.15 shows results for a series of experiments performed with the new magnetostrictive sleeve transducer (Figure 4.4). The results show that submerging the specimen in water decreases the signal amplitude slightly. However, there is not a significant difference relative to finite element models which do not contain the water loading.

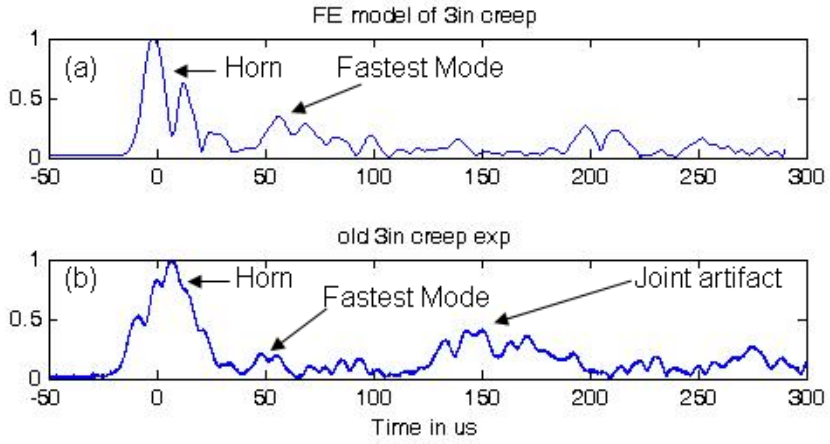

Figure 6.14: Comparison of finite element and experimental results. Normalized analytic envelopes of (a) the waveform predicted by time-domain finite element analysis, and (b) the experimental waveform obtained for a 3 inch Zircaloy creep specimen.

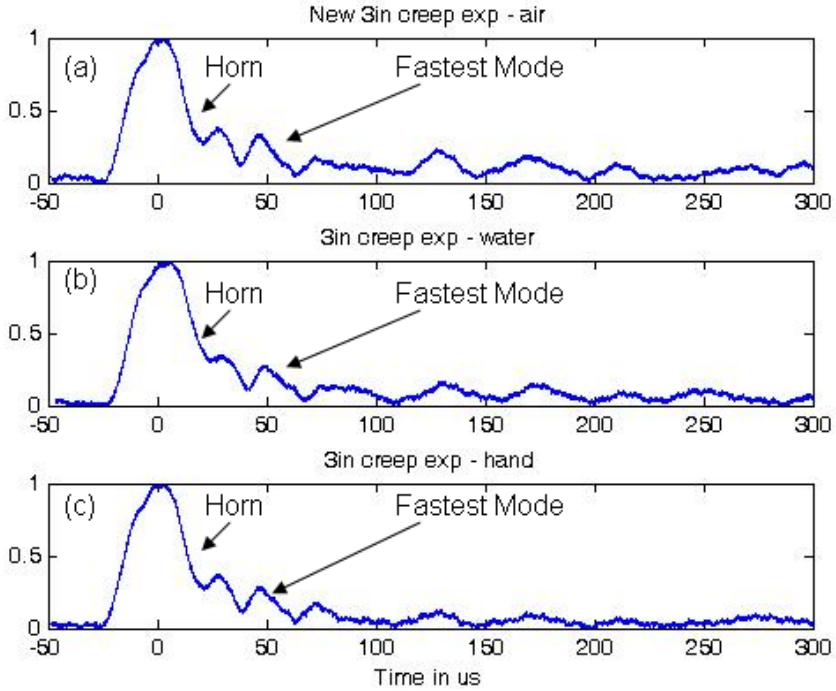

Figure 6.15: Comparison of experimental conditions. Normalized analytic envelopes of experimental waveforms recorded for a 3 inch Zircaloy creep specimen when the specimen is in (a) air, (b) water, and (c) held tightly in hand. Water and hand pressure dampen the signal. Experiments done at 150 kHz and 20μs pulse width.

6.4 Temperature Dependence

As shown in Figures 6.2 and 6.3, both the phase velocity and group velocity of the guided waves vary as a function of temperature. In order to model the effect of elevated temperature, temperature dependent material properties were defined for each material studied.[29] By varying the material properties as a function of temperature, dispersion curve calculations and finite element models can be performed for any temperature. Figure 6.16 shows the temperature dependence of group velocity for both materials at 125 kHz.[30] The results for stainless steel indicate approximately an 8% change in group velocity, while the results for Zircaloy indicate approximately a 14% change in group velocity over the temperature range of interest.

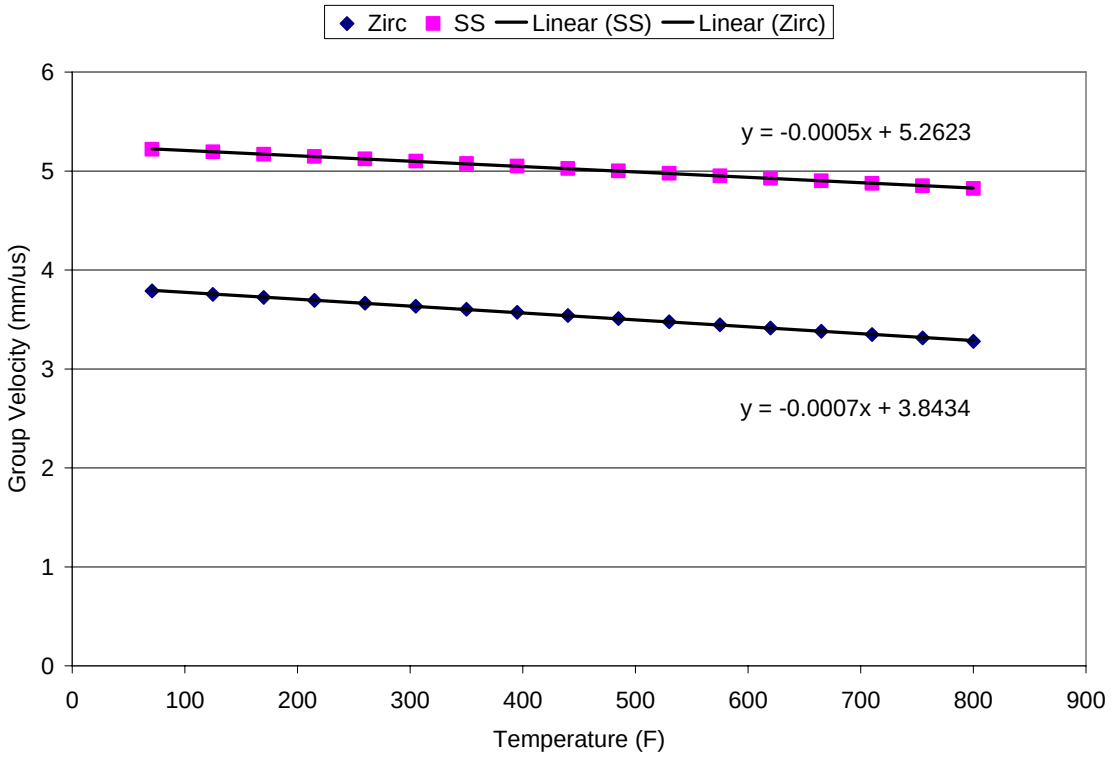

Figure 6.16: Group velocity at 125 kHz vs. temperature for Zircaloy (blue diamonds) and stainless steel (pink squares) creep specimens (1/8 inch gauge diameter). The black lines indicate the linear best fit trend lines.

[29] See Appendix A for more information on the temperature dependent material properties.
[30] The magnetostrictive sleeve operates at approximately 125 kHz.

As temperature increases, thermal expansion occurs. In principal, this changes the dimensions of the specimen. However, the effect of thermal expansion is relatively small.

Take stainless steel for example. Stainless steel has a coefficient of thermal expansion of approximately 18 μ/K.[31] For a 3.15 mm (1/8 inch) diameter stainless steel specimen, increasing the temperature from 295°K (22°C / 70°F) to 700°K (427°C / 800°F) will yield a change in diameter of approximately 0.023 mm. This is a relatively small change which should have a negligible effect on guided wave propagation in the gage length. Since it is valid to analyze a cylindrical waveguide in terms of *fa* (frequency times radius) product, an equivalent frequency shift can be calculated. Equation 6.7 shows that a 0.023 mm change in diameter corresponds to a 0.00345 mm-MHz shift in *fa* product. As shown in Equation 6.8, this corresponds to a 1.1 kHz shift in frequency for a cylindrical waveguide at room temperature. Such a small differential is negligible, especially since 125 kHz corresponds to a non-dispersive region of the dispersion curves (Figure 6.2 and 6.3).

$$F \cdot \Delta D = (0.15MHz)(0.023mm) = 0.00345mm \cdot MHz \tag{6.7}$$

$$0.00345mm \cdot MHz = \Delta F \cdot D = (\Delta F)(3.15mm) \rightarrow \Delta F = 0.0011MHz = 1.1kHz \tag{6.8}$$

6.5 Temperature Experiments

A Lindberg furnace was used to perform preliminary time-of-flight (TOF) measurements on two stainless steel creep specimens at 525°F. Figure 6.17 shows a comparison of the recorded waveforms from a 4 inch and a 6 inch long stainless steel specimen. The data indicates a 58.46 μs time-of-flight for the 4 inch gauge length specimen and a 78.72 μs time-of-flight for the 6 inch gauge length specimen. Thus, the ultrasonic velocity in the gauge length of the specimen is approximately 5 mm/μs. This value is consistent with guided wave theory predictions for the cylindrical gauge section at 525°F (See Figure 6.16).[32]

[31] See Appendix A for reference.

[32] In addition, the data demonstrates that the butt-welding on the specimen to the waveguide allows sufficient transmission of the ultrasonic signal.

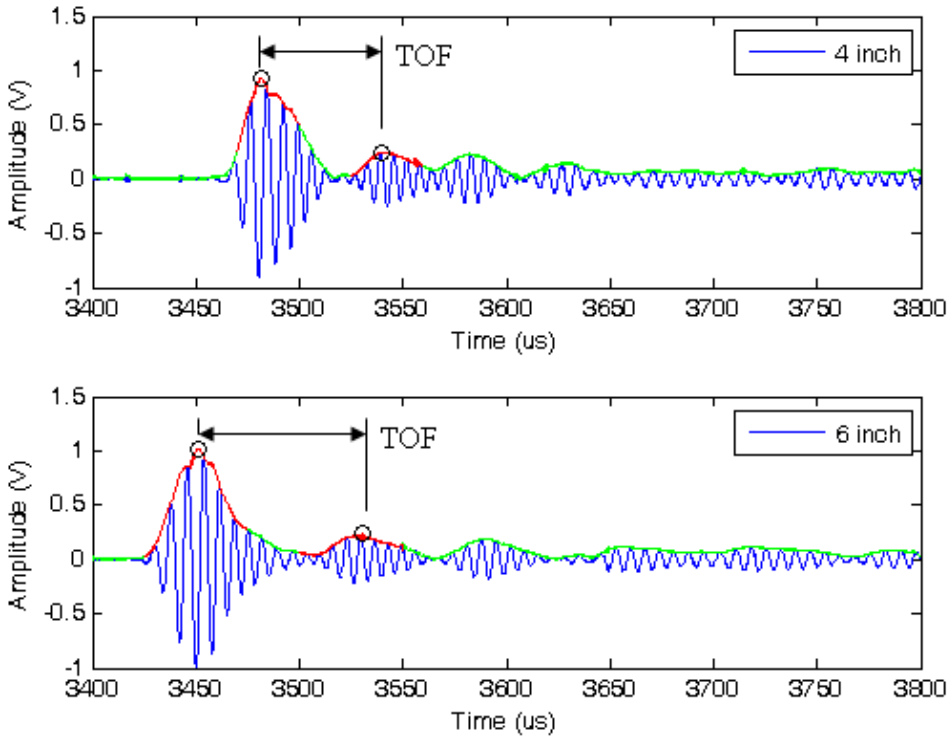

Figure 6.17: Experimental waveforms recorded for two stainless steel specimens of different length. The longer specimen has greater time-of-flight spacing between the reflection from the horn and the reflection from the flat end of the specimen.

In another series of experiments, the Lindberg furnace was heated to approximately 550°F, and was then allowed to slowly cool down. Time-of-flight data was recorded as a function of temperature. The results shown in Figure 6.18 compare four different methods of calculating the time-of-flight in a 4 inch stainless steel specimen. The two methods utilizing the analytic envelope are not consistent for all sampled temperature values. The methods based on either the maximum or minimum peaks in the reflections were approximately linear excluding the data taken at room temperature. The approximately linear behavior at the higher temperatures is consistent with the theoretical predictions given in Figure 6.16. The discrepancy with the room temperature data is a manifestation of a phase shift between the two reflections. (The phase shift effect is easier to see in the data collected from the 6 inch specimen.)

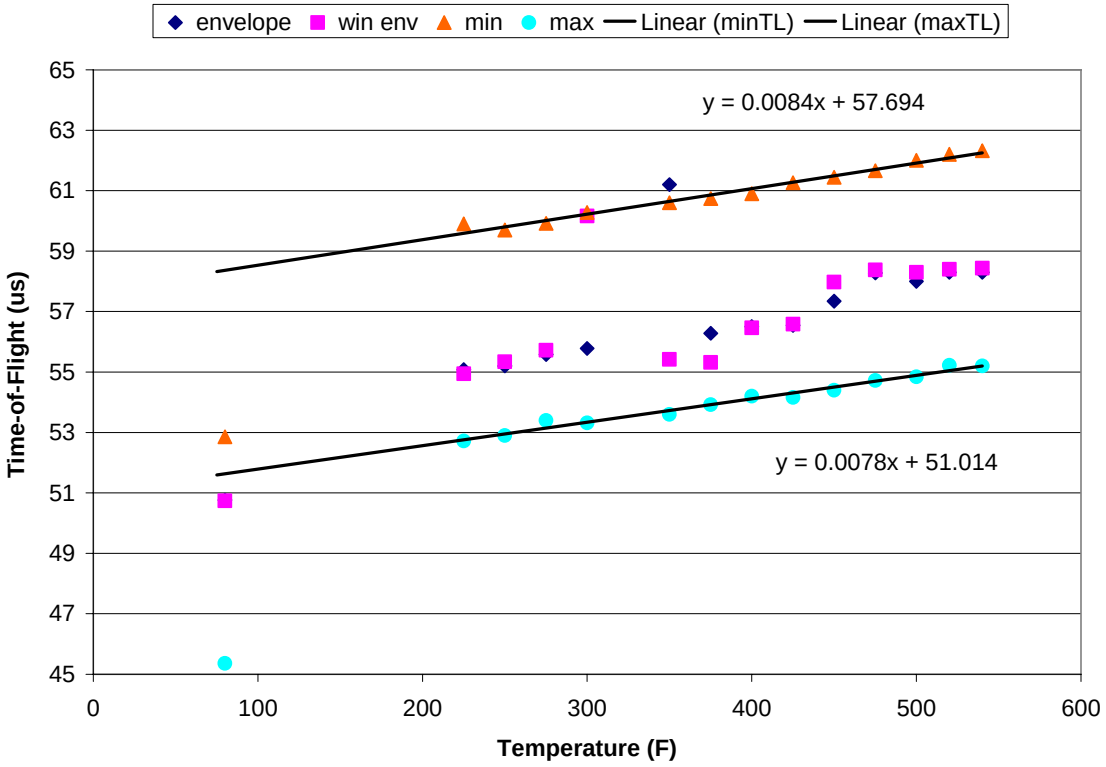

Figure 6.18: Experimental time-of-flight in a 4 inch stainless steel specimen vs. temperature. Results are shown for four methods on calculating the time-of-flight. Blue diamonds represent the results for an analytic envelope. Pink squares represent the results for a windowed analytic envelope approach. Orange triangles represent the results based on the minimum peak in the two reflections. Light blue circles represent the results based on the maximum peak in the two reflections. Excluding the data point taken at room temperature, the relatively linear response (maximum and minimum techniques) is consistent with the theoretical predictions in Section 2.

The results shown in Figure 6.19 compare four different methods of calculating the time-of-flight in a 6 inch stainless steel specimen. Figure 6.19a shows the discrete data points for time-of-flight versus temperature. There is no obvious trend seen in this representation of the data. In Figure 6.19b, the data points for each method were artificially connected with smooth lines. In this representation, discrete 'jumps' in the data are seen near 275°F and 450°F.

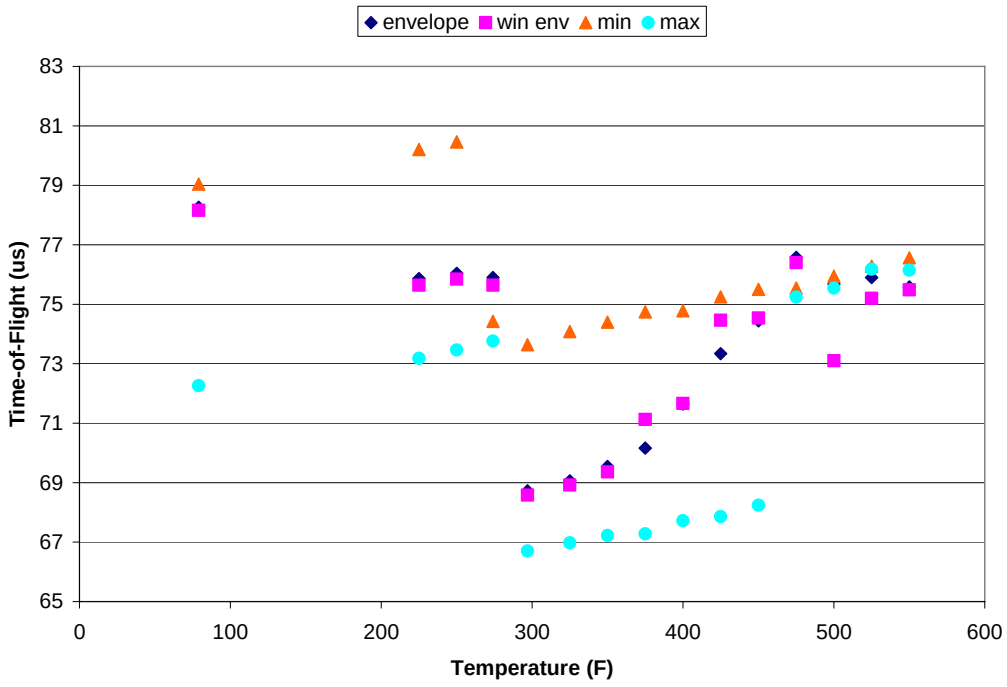

(a)

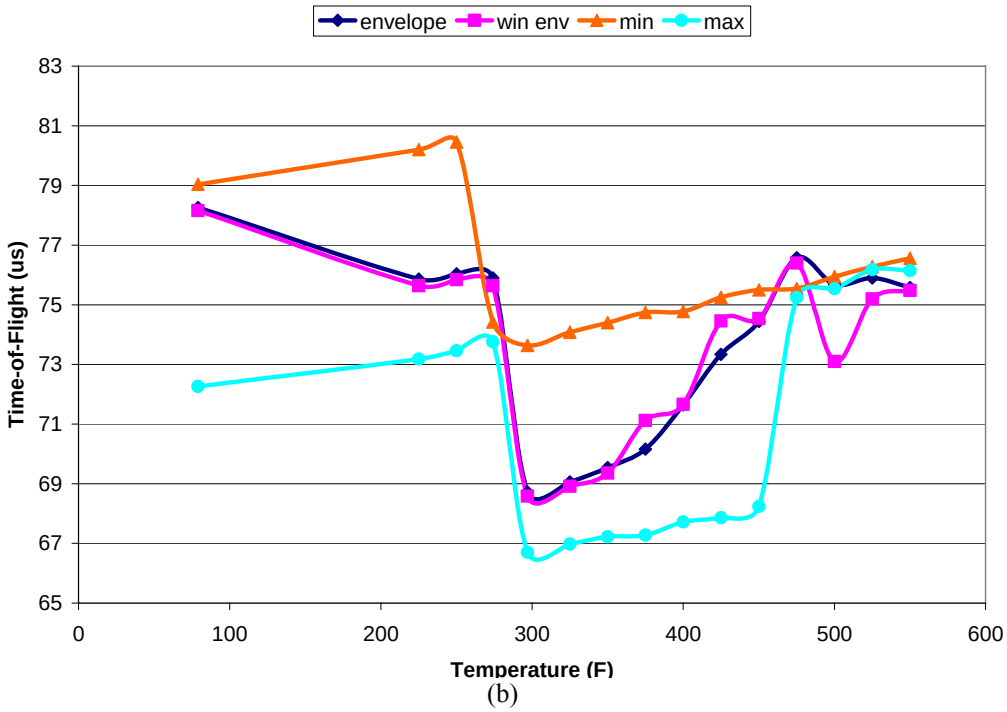

(b)

Figure 6.19: Experimental time-of-flight in a 6 inch stainless steel specimen vs. temperature. (a) Shows the actual results of the analysis. (b) Shows the results artificially connected with smooth lines to help shown where there are abrupt changes in the results of each method. Results are shown for four methods on calculating the time-of-flight. Blue diamonds represent the results for an analytic envelope. Pink squares represent the results for a windowed analytic envelope approach. Orange triangles represent the results based on the minimum peak in the two reflections. Light blue circles represent the results based on the maximum peak in the two reflections.

In order to further study these apparent 'jumps' in the data, the results based on the local minimum in each reflection were re-plotted in Figure 6.20a. Trend lines were plotted for the data above and below 275°F. The equations shown in Figure 6.20a indicate that there is approximately a 7 μs shift in time-of-flight between the two trend lines. A 7 μs time-of-flight corresponds to one period at 143 kHz. Therefore, the 'jumps' observed in the data are simply by-products of the signal process method. In Figure 6.20b, the 7 μs shift in time-of-flight has been manually subtracted from the data below 275°F. By accounting for this phase shift error, the results shown in Figure 6.20b demonstrate that the true trend versus temperature is in fact linear as expected.

Figure 6.21a re-plots the results based on the local maximum in each reflection. Trend lines were plotted for the three temperature ranges: 0-275°F, 275-450°F, and 450-550°F. The shift in time-of-flight between the three trend lines is once again approximately 7 μs or one period at 143 kHz. In Figure 6.21b, a 7 μs shift in time-of-flight has been manually added to the data in the 275-450°F temperature range. After accounting for the phase shift error, the true trend versus temperature is once again shown to be linear as expected. Also, the time-of-flight values shown in Figure 6.21b are in good agreement with the time-of-flight values shown in 6.20b.

The data processing methods based on the analytic envelopes of the signal were expected to correct for the observed phase shift errors. However, the experimental results (Figures 6.18 and 6.19) demonstrate that the analytic envelopes did not perform as expected. It is not clear as to why the analytic envelope method did not work in this case. Since the Hilbert transform used to calculate the analytic function is based on a Fourier transform and an inverse Fourier transform, it is possible that the envelope results are affected by the window applied to the data.

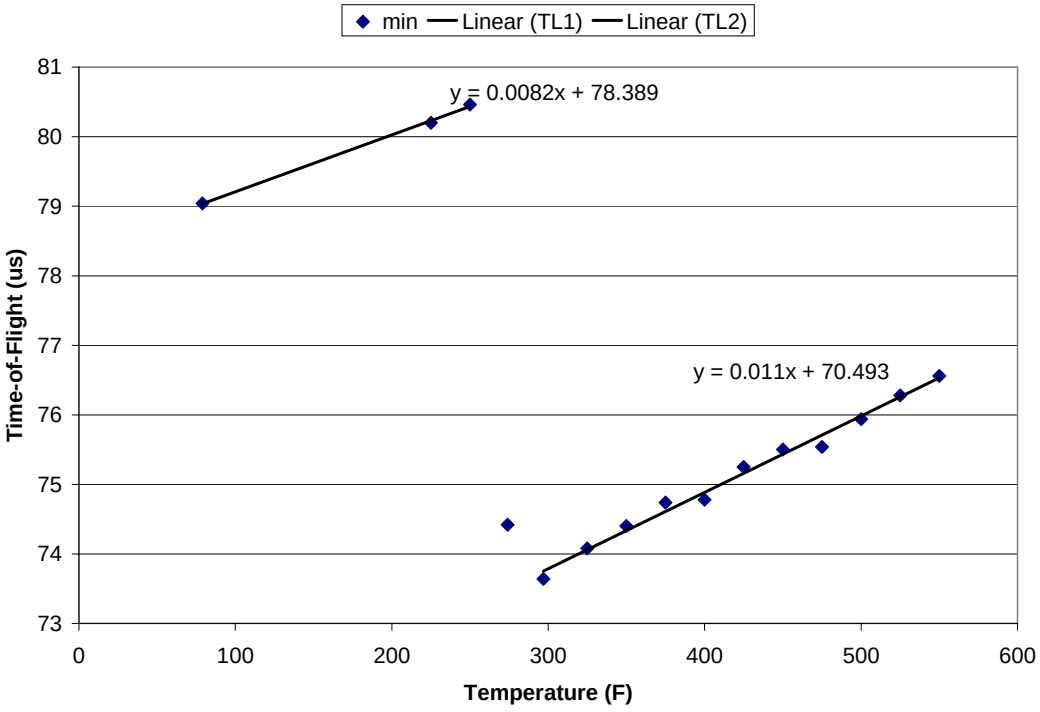

(a)

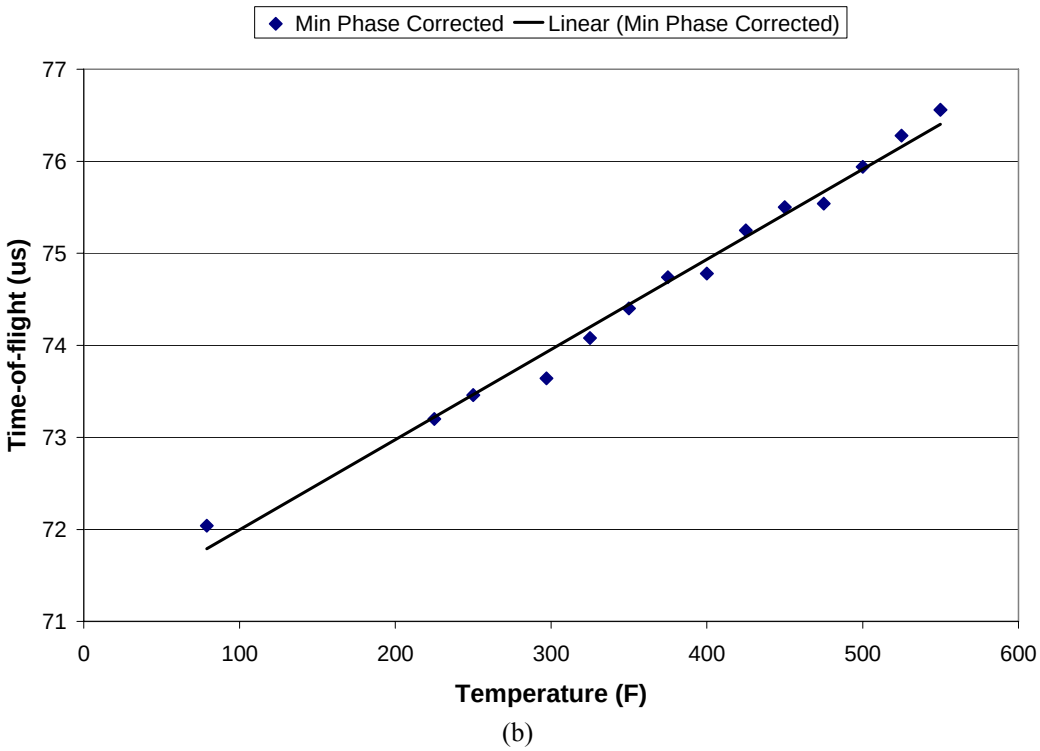

(b)

Figure 6.20: Time-of-flight in a 6 inch stainless steel specimen vs. temperature based on the minimums in the two specimen reflections. (a) Raw experimental data showing linear trend lines for two distinct regions of the data. (This is the same data as the orange triangles shown in Figure 6.19). (b) Experimental data after manually subtracting 7 μs from the data below 275°F to account for phase shift error. The 7 μs difference between the two trend lines equals one period at approximately 143 kHz.

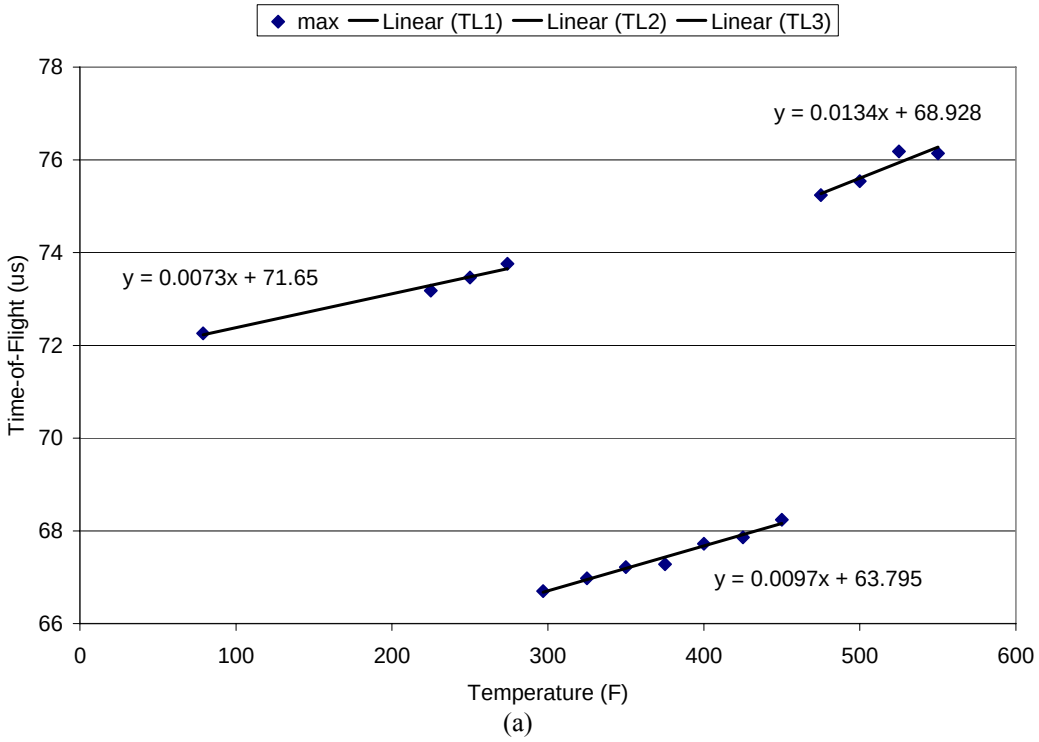

(a)

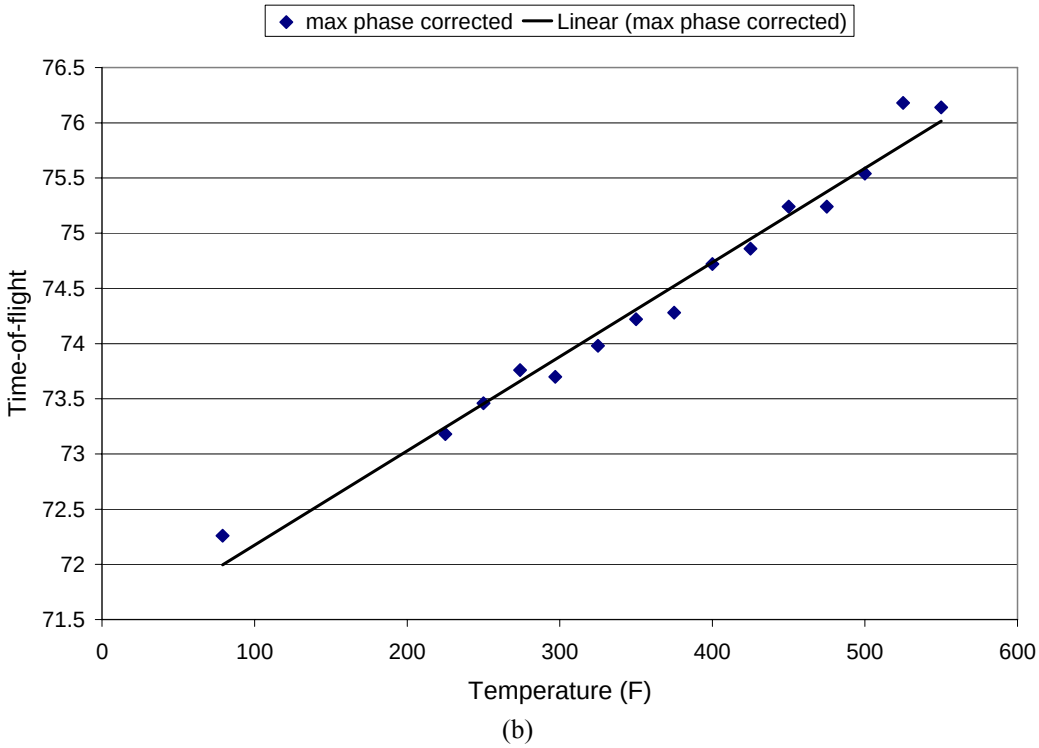

(b)

Figure 6.21: Time-of-flight in a 6 inch stainless steel specimen vs. temperature based on the maximums in the two specimen reflections. (a) Raw experimental data showing linear trend lines for three distinct regions of the data. (This is the same data as the light blue circles shown in Figure 6.19). (b) Experimental data after manually adding 7 μs to the data in the 275-450°F range to account for phase shift error. The approximately 7 μs difference between the three trend lines equals one period at approximately 143 kHz.

6.6 Creep Experiment

A creep test was performed using the static load creep frame shown in Figure 6.22. A 3 inch Zircaloy creep specimen was loaded into the frame using custom fabricated grips (Figure 6.23a) and the heater was turned on. The initial goal was to perform the creep test at 550°F. However, the maximum temperature achieved by the heater was recorded to be only 400°F. Once the temperature was stable at 400°F, 150 lbs of weight and a calibration weight was added to the creep frame lever. With a 3:1 lever arm, this corresponds to 450 lbs[33] of load applied to the Zircaloy specimen. Time-of-flight data was then recorded periodically until the specimen failed. Failure of the specimen (Figure 6.23b and 6.23c) occurred in less than 60 hrs.

Figure 6.24 shows a comparison of the recorded waveforms after 0 hrs and 47 hrs in the static creep frame with 150 lbs of load (450 lbs of force due to lever arm). The recorded waveforms are almost identical except for a small time-of-flight shift in the reflections following the wire-specimen reflection at 200 μs.

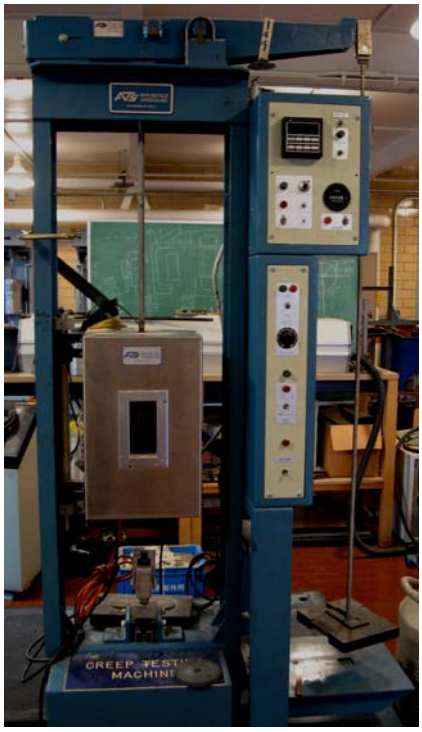

Figure 6.22: Creep frame used for the creep test at PSU.

[33] The load was increased from 300 lbs to speed up the test and to compensate for the lower temperature.

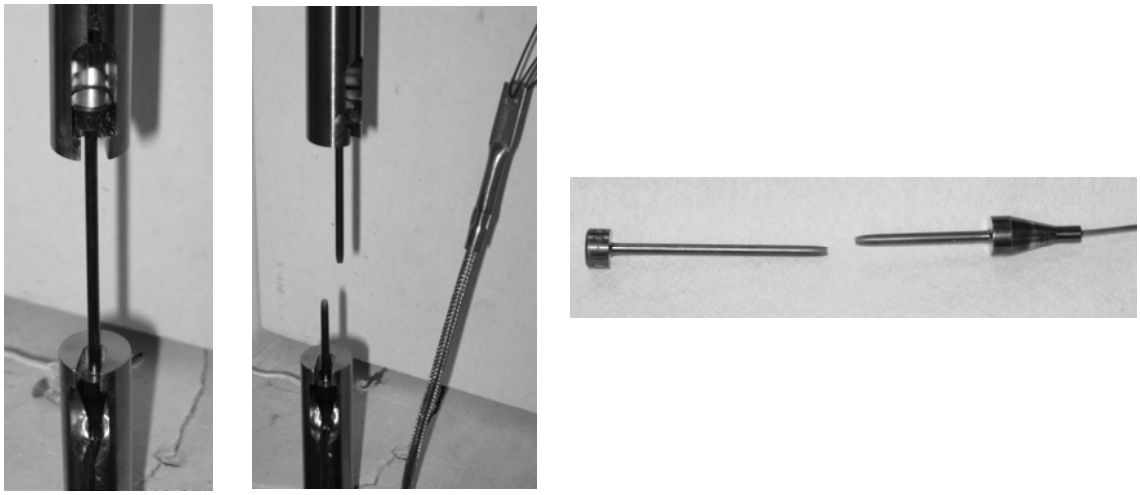

(a) (b) (c)

Figure 6.23: Zircaloy creep specimen used in the creep test at PSU. (a) Original specimen in frame prior to starting the creep test. (b) and (c) show the specimen after failure.

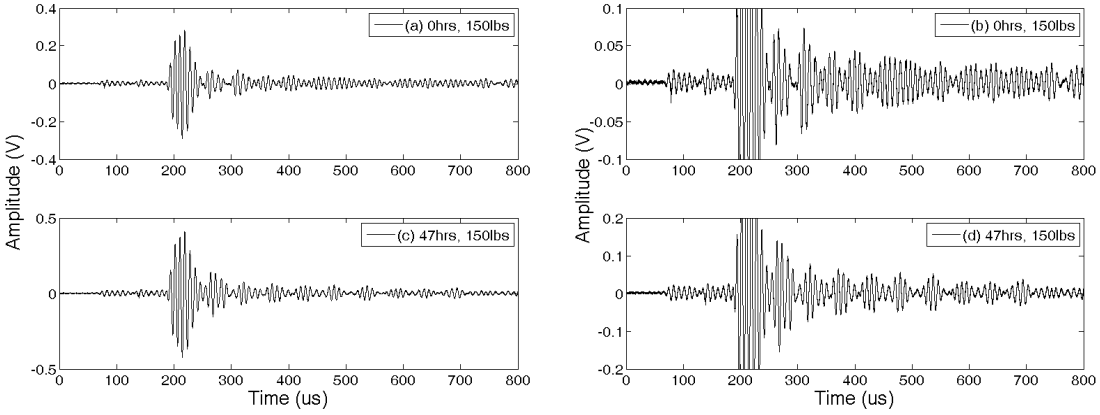

Figure 6.24: Selected waveforms from the PSU creep experiment obtained using the wire waveguide technique. (a) After 0 hrs in creep frame. (b) After 0 hrs in creep frame, with magnified voltage scale to help show first reflection. (c) After 47 hrs in creep frame. (d) After 47 hrs in creep frame, with magnified voltage scale to help show first reflection.

Figure 6.25a shows the recorded time-of-flight results versus time in the creep frame. Figure 6.25b shows the time-of-flight values converted to an estimated length of the creep specimen. The estimated length after 57 hrs is in good agreement with the final length of the specimen after failure (3.53 inch). In principal, the trend in elongation versus time is also reasonable. There is a period of rapid elongation (primary creep) followed by an approximately linear rate of elongation (secondary creep) [89-91]. The time-to-failure was less than expected. This could be explained by excessive load (too much calibration weight) or the temperature being higher than recorded.

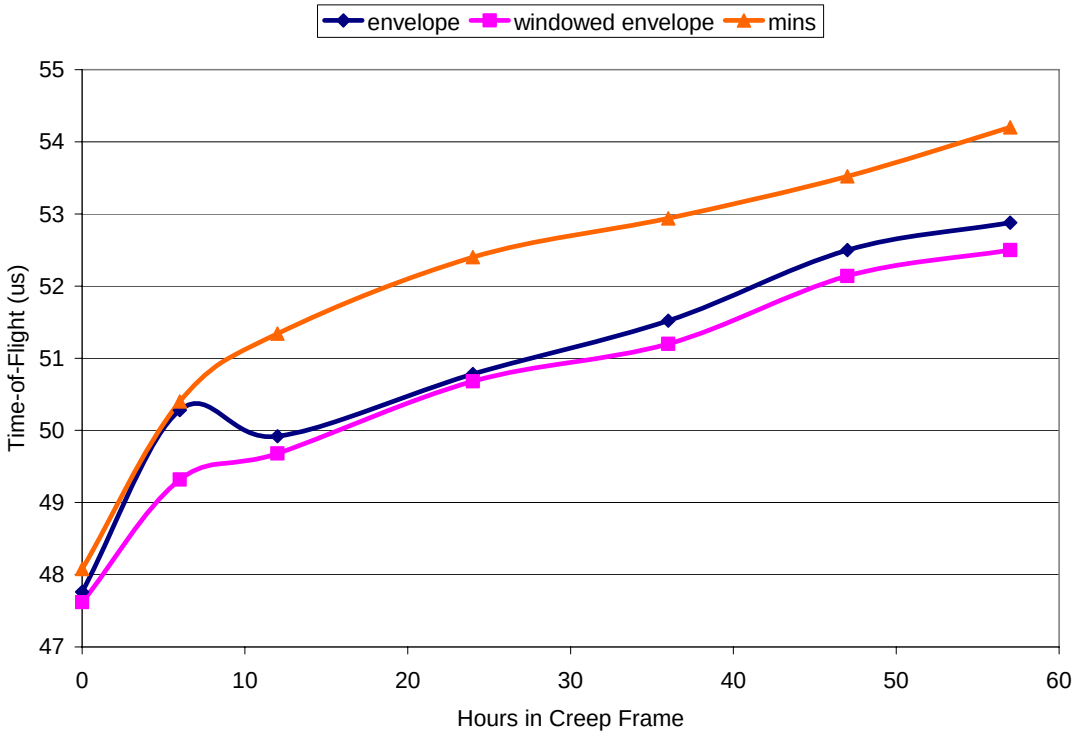

(a)

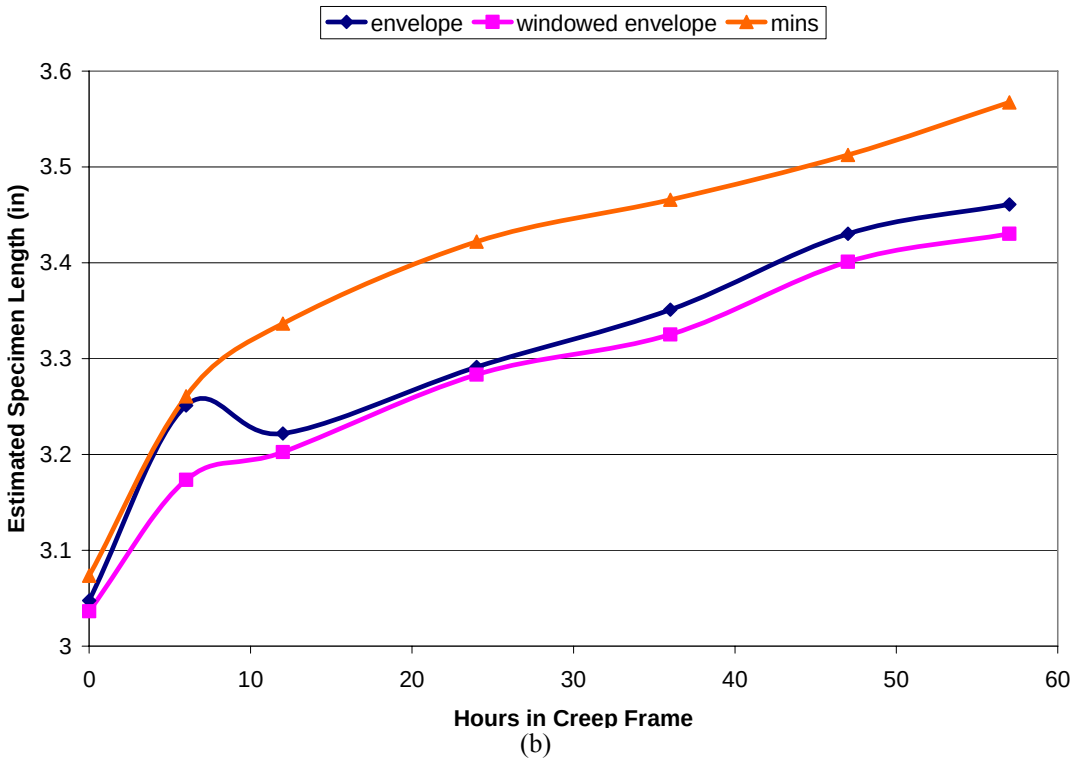

(b)

Figure 6.25: PSU creep experiment results. (a) Recorded time-of fight vs. time in the creep frame. (b) Time-of-flight values converted to an estimated specimen length. The total gauge length of the specimen after failure was about 3.53 inch.

6.7 Plastic Deformation Experiments

As a comparison, measurements were performed on a standard 1 inch gage length stainless steel specimen using commercial contact transducers. Figure 6.26 shows that very poor results were obtained using a 2.25 MHz piezoelectric transducer. Figure 6.27 shows that easily identifiable arrival times were observed when using a 20 MHz piezoelectric transducers.

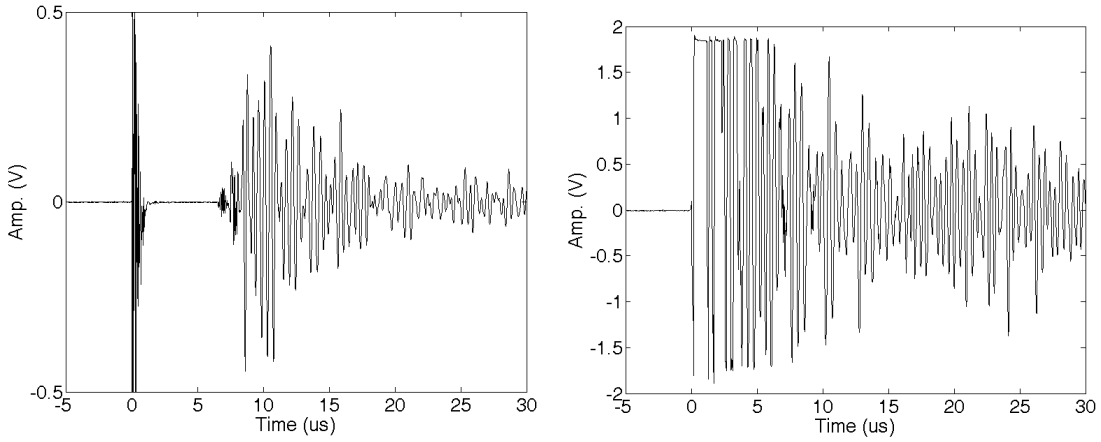

Figure 6.26: Waveforms from experimental measurements on a 1 inch long gage length stainless steel specimen obtained with 2.25 MHz 0.25 inch diameter commercial piezo-composite transducers. (a) Through-transmission and (b) pulse-echo measurements. There is significant ringing in the dumbbell ends. A backwall echo was not observed in the pulse-echo measurement.

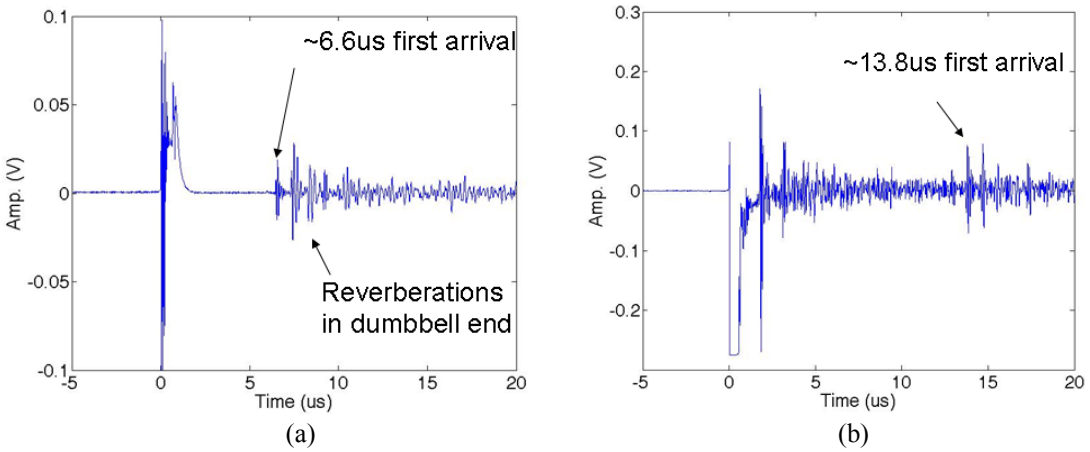

Figure 6.27: Waveforms from experimental measurements on a 1 inch long gage length stainless steel specimen obtained with 20 MHz 0.125 inch diameter commercial piezo-composite transducers. (a) Through-transmission and (b) pulse-echo measurements. Backwall reflection appears to be visible in the pulse-echo measurement.

Since 20 MHz ultrasonic signals could be easily transmitted in a standard 1 inch creep specimen, it was worth trying to see what kind of elongation resolution as possible with piezoelectric transducers. To test this, a series of 1 inch stainless steel creep specimens were pulled in a load frame at a constant rate.[34] After a fixed amount of pull length, each specimen was removed from the load frame. Calipers were used to measure the gage length, and ultrasonic measurements were performed to measure any change in time of flight.

Figures 6.28 and 6.29 show the results for the pulse-echo measurements. The trend in pulse-echo time-of-flight versus gage length is linear. A small amount of scatter in the data is due to the resolution of the oscilloscope and the calipers. The results shown in Figure 6.29b suggest that a change in length on the order of 0.025 in (0.6 mm) could be resolved in the bench-top test. Better resolution should be possible with fixed transducers and a higher sampling rate.

Figures 6.30 and 6.31 show the results for the through-transmission measurements. The trend is again linear. However, the resolution is lower because the ultrasound only propagates once through the gage length. In the pulse-echo measurements there is twice as much change in time-of-flight per unit elongation.

[34] Displacement control mode.

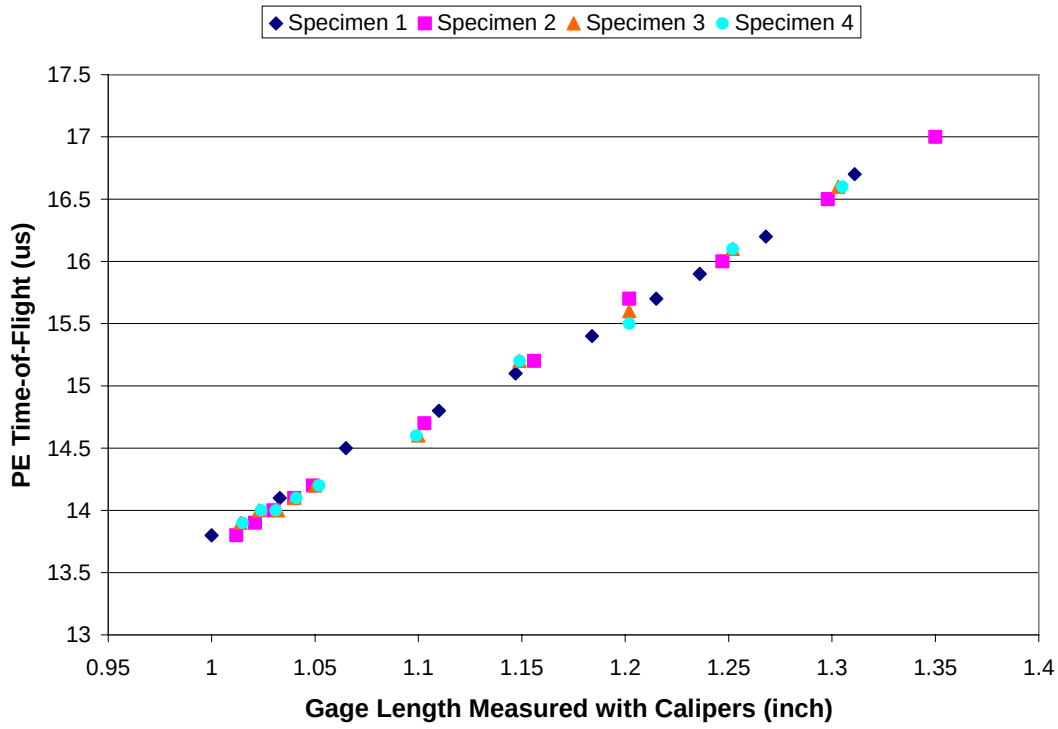

(a)

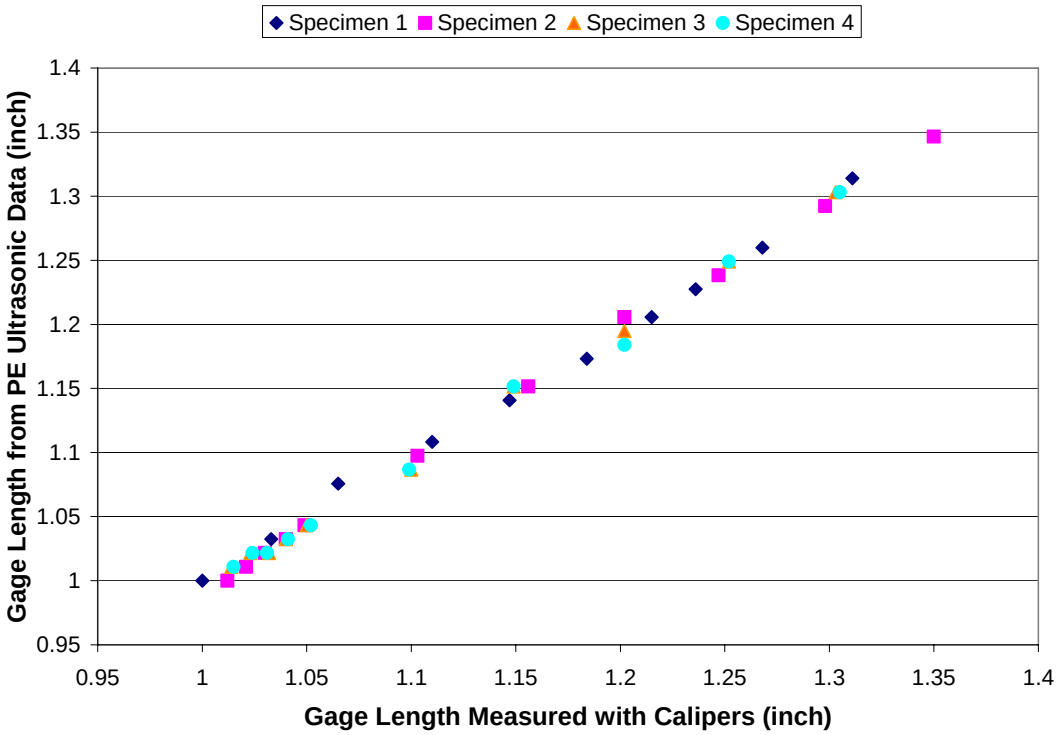

(b)

Figure 6.28: Results for the pulse-echo measurements with 20MHz commercial piezoelectric transducers showing the full elongation range (up to 35% elongation). (a) Time-of-flight versus measured gage length. (b) Gage length calculated from the ultrasonic data versus measured gage length.

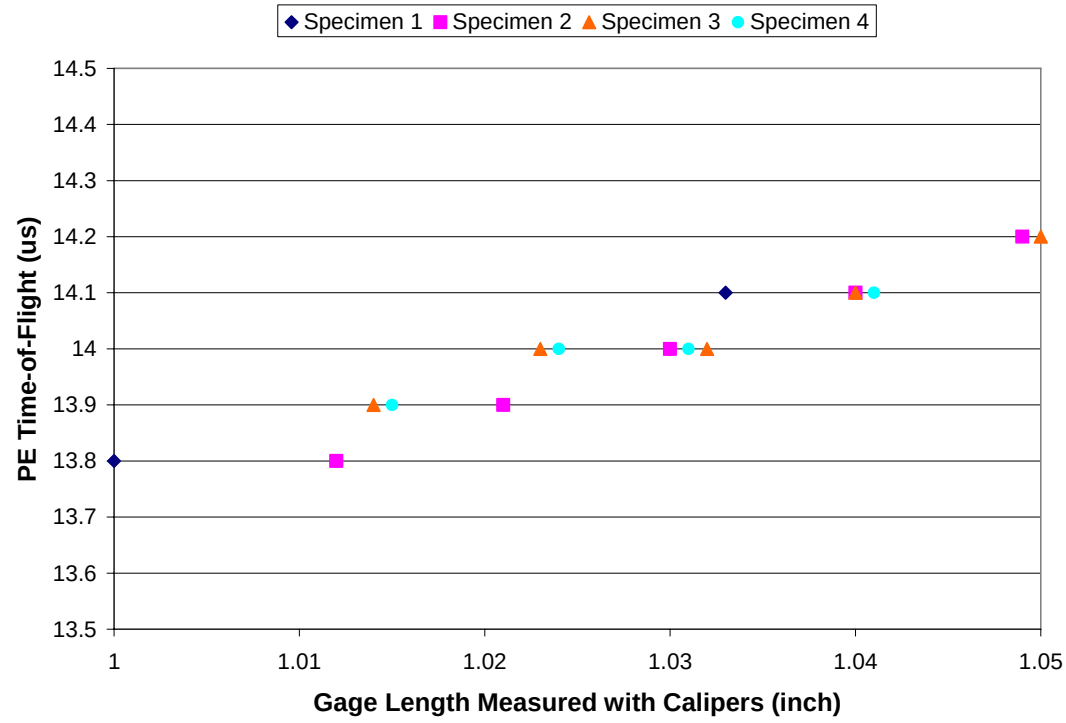

(a)

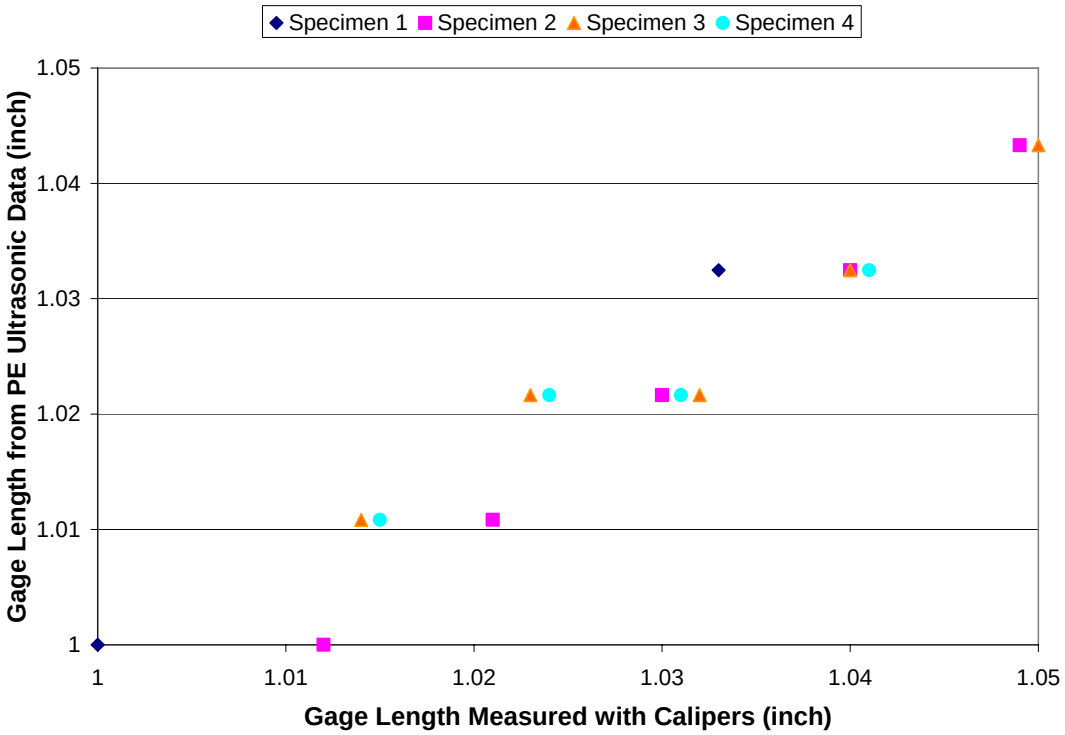

(b)

Figure 6.29: Results for the pulse-echo measurements with 20MHz commercial piezoelectric transducers showing the resolution of small length changes. (a) Time-of-flight versus measured gage length. (b) Gage length calculated from the ultrasonic data versus measured gage length.

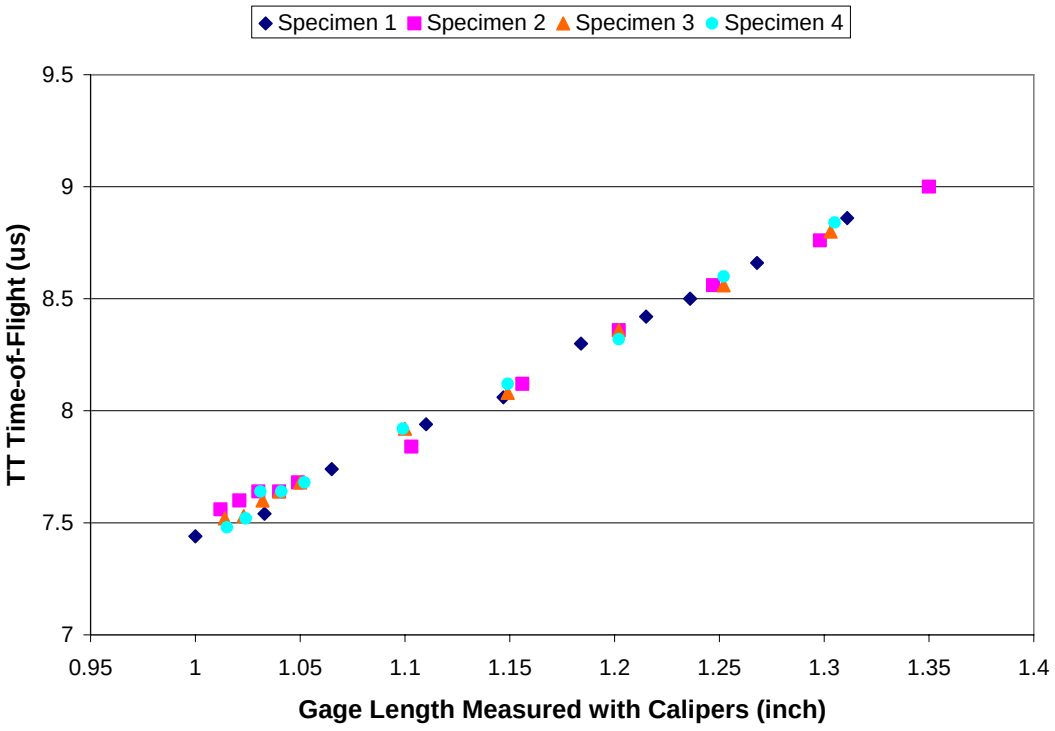

(a)

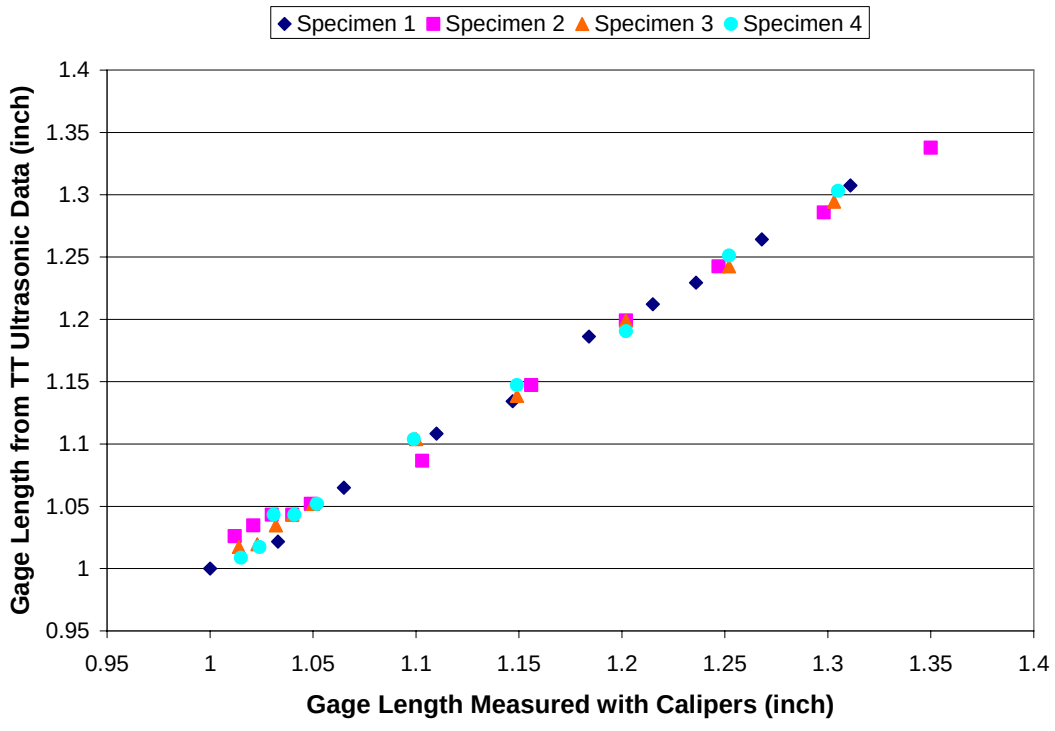

(b)

Figure 6.30: Results for the through-transmission measurements with 20MHz commercial piezoelectric transducers showing the full elongation range (up to 35% elongation). (a) Time-of-flight versus measured gage length. (b) Gage length calculated from the ultrasonic data versus measured gage length.

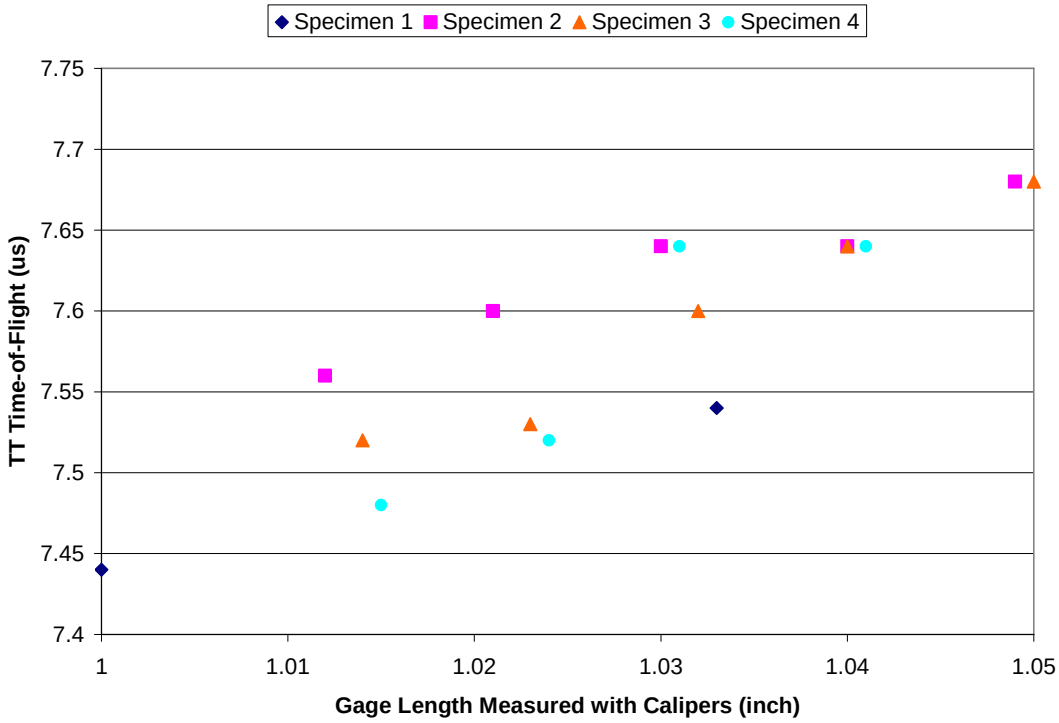

(a)

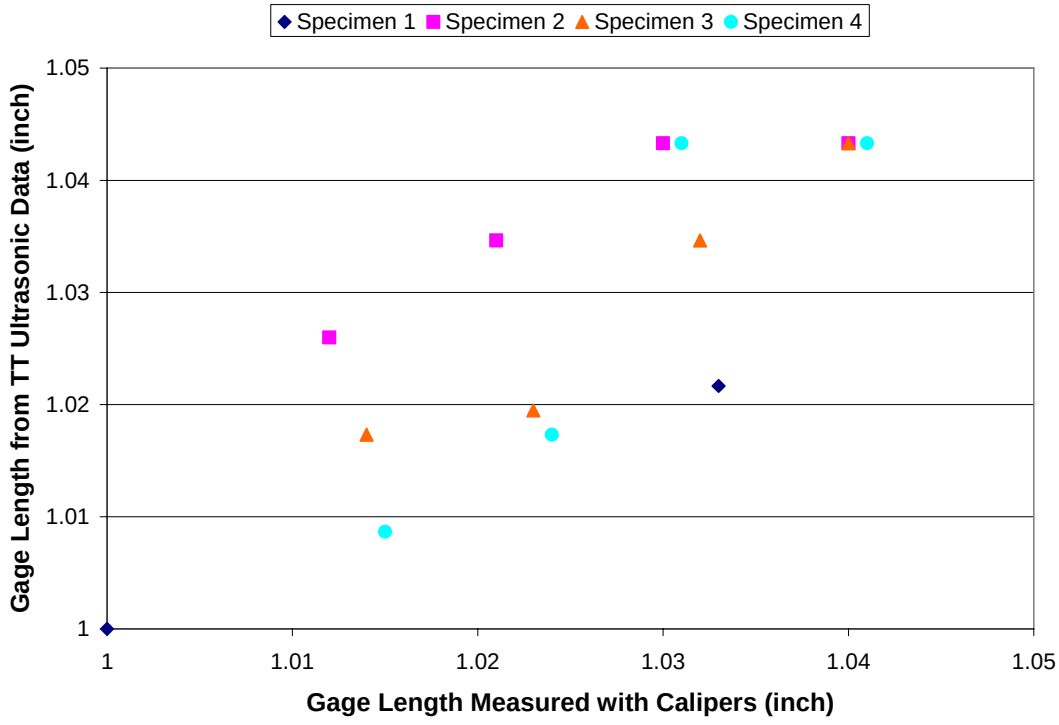

(b)

Figure 6.31: Results for the through-transmission measurements with 20MHz commercial piezoelectric transducers showing the resolution of small length changes. (a) Time-of-flight versus measured gage length. (b) Gage length calculated from the ultrasonic data versus measured gage length.

6.8 Resonant Frequency Concept

A theoretical study was also performed to investigate any resonance frequency characteristics of the 1 inch gage length ASTM creep specimen geometry. As a starting point, a simple cylinder geometry was considered first.

A finite element model was used to calculate the Eigen frequencies associated with a simple cylinder of 3.15 mm diameter. Figure 6.32 shows selected modes from the finite element calculations for a 26 mm long cylinder. The axial mode shown in Figure 6.32a may be potentially useful since it corresponds to the length of the cylinder. The finite element models also showed that several flexural modes (i.e. Figure 6.32b) were possible in the numerical results. However, the analysis presented here only focused on the mode with axial vibration.

The finite element calculations predicted an axial mode with an Eigen frequency of 95.57 kHz for a 26 mm ling cylinder. When the length of the cylinder is decreased to 25 mm, the finite element calculations predict an Eigen frequency of 99.26 kHz. A very simple comparison to theoretical expectation can be made using Equation 6.9 where C is bulk wave velocity, f is frequency, λ is wavelength, and L is cylinder length. As Table 6.1 shows, the finite element results are in agreement with Equation 6.9.

$$C = f\lambda = f(2L) \tag{6.9}$$

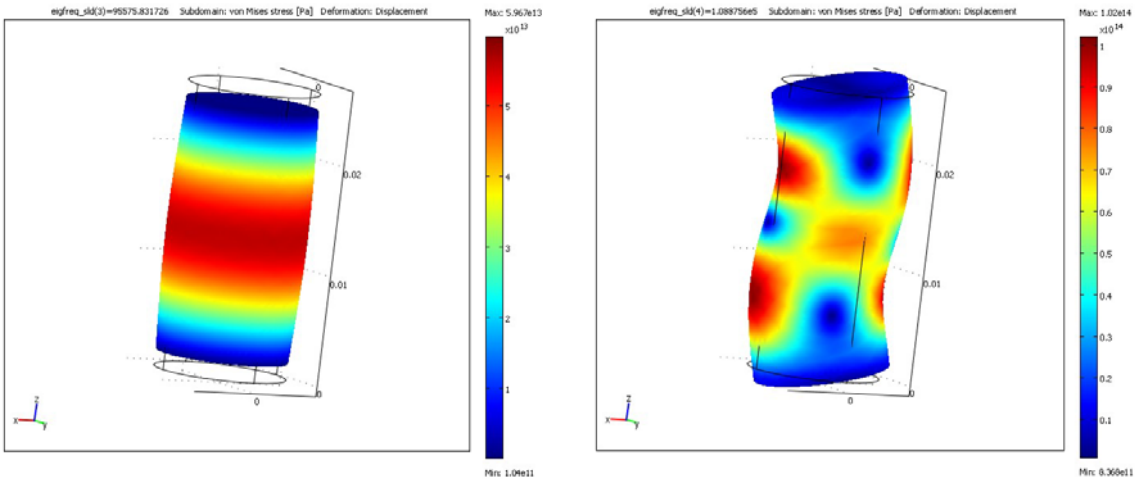

(a) (b)

Figure 6.32: Eigen frequency results for 26 mm long steel cylinder. (a) 95.57 kHz mode has vibration along the central axis of the cylindrical rod. This is consistent with sending and receiving ultrasonic waves along the central axis. (b) 108.88 kHz mode does not have vibration along the central axis of the cylindrical rod. This is not consistent with sending and receiving ultrasonic waves along the central axis.

Table 6.1: Eigen frequencies of a simple cylinder. (Effect of a change in length of the 3D solid cylinder.)

Gage length	Theoretical Estimate	Finite Element, Axial Mode
25 mm	100 kHz	99.26 kHz
26 mm	96.15 kHz	95.57 kHz

Finite element models were then performed on a 1 inch gage length creep specimen geometry. The models used an axi-symmetric geometry where the nodes along the axis-of-symmetry were defined to have zero radial displacement. This eliminates any Eigen frequency solution containing flexural type vibrations. Figure 6.33 shows the first five Eigen frequency modes predicted by the numerical calculations. The mass associated with the dumbbell ends of the creep specimen changes the solution slightly from the results for a simple cylinder.

By varying the gage length of the modeled specimen, it was then possible to predict how the Eigen frequency of the creep specimen would vary as a gage length increased. In one series of calculations, it was assumed that the radius of the gage section would remain constant as the specimen elongated. However, this is not physically accurate. A second series of calculations was then performed assuming constant volume. As the gage length increased, the radius decreased to maintain constant volume in the gage section. Both a uniform reduction in radius and necking (maximum reduction in radius at center of gage, zero reduction at ends) were considered.

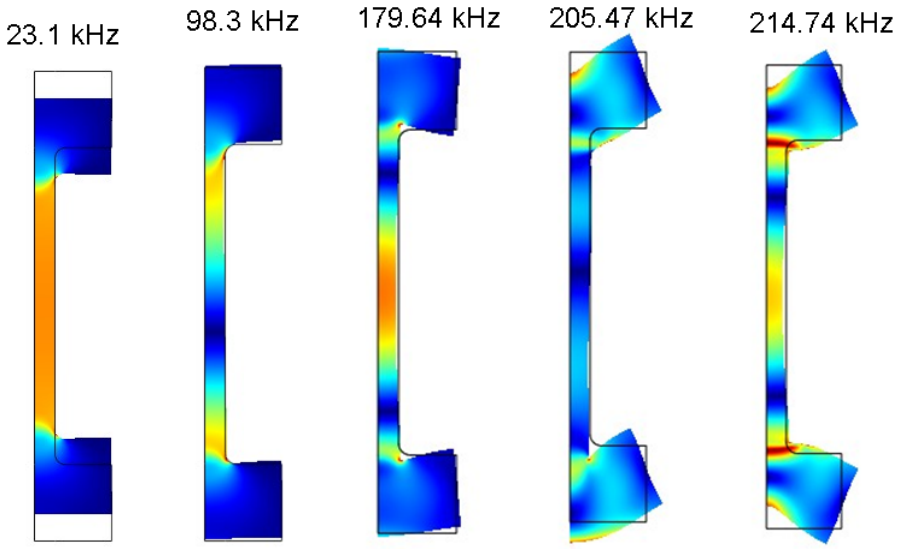

Figure 6.33: Eigen frequency results (first 5 modes) for 25 mm gage length ASTM creep specimen. The mass of the dumbbell ends affects the solutions. The 98.3 kHz mode appears promising because it appears to be associated with vibrations concentrated in the gage length of the specimen, and it is within the frequency range of the remote magnetostrictive transducer.

Table 6.2 and Figure 6.34 summarize the results for the finite element modes as the gage length was varied. Both the constant radius results and the constant volume results with a uniform reduction in radius are in good agreement with the theoretical expectation based on Equation 6.9. The finite element results also showed that the models with the 'necked' gage section had a slightly different frequency response.

Table 6.2: Eigen frequencies of a 1 inch gage length stainless steel creep specimen. Units are in kHz.

Gage Length	Theory	Simple Cylinder	Axi-symm. Const. Rad.	Axi-symm. Const. Volume Uniform radius	Axi-symm. Const Volume 'Necked'
25mm	100.00	100.84	98.27	98.14	98.14
26mm	96.15	96.97	95.03	94.82	95.89
27mm	92.59	93.39	92.00	91.71	93.78
28mm	89.29	90.06	89.16	88.78	91.74
29mm	86.21	86.96	86.50	86.03	89.84
30mm	83.33	84.06	84.00	83.44	88.03

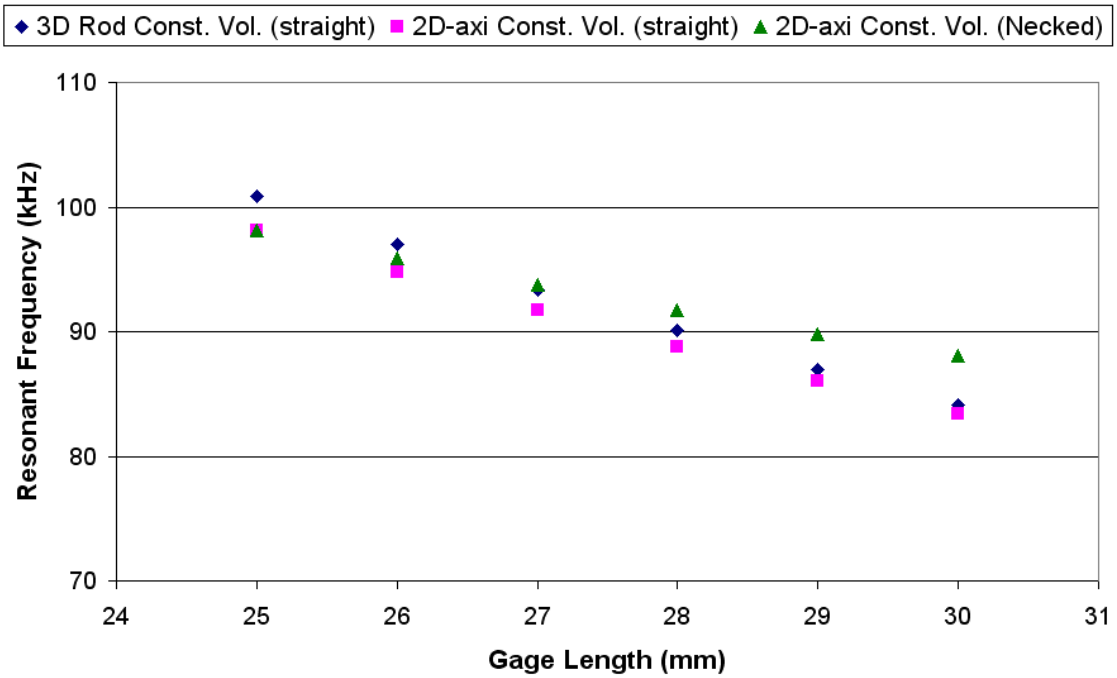

Figure 6.34: Finite element results for the Eigen frequency as a function of specimen gage length. The numerical calculations showed that the models which included necking of the gage volume had a slightly different response.

6.9 Summary

In this chapter, the in-situ monitoring system was studied for use in measuring the change in length of creep specimens. Four measurement configurations were considered: through-transmission without a horn, through-transmission with a horn, pulse-echo without a horn, and pulse-echo with a horn. It was shown that the characterizes of each configuration influenced system performance. Ultimately, the pulse-echo measurement with an acoustic horn was found to provide the best signals.

The temperature dependence of the in-situ creep measurement was also studied. Both theoretical calculations and experiments showed that the temperature dependence was approximately linear for the creep specimen geometry. The experimental tests demonstrated that careful consideration must also be given to the digital signal processing of the data. In this particular case, the use of an analytic envelope was counterproductive. Reliable results were only obtained by using the peak of each reflection in conjunction with a phase shift correct.

Successful measurements of the creep elongation of a 3 inch gage length Zircaloy specimen were also demonstrated using the pulse-echo configuration of the in-situ monitoring system. Although the in-situ system was successful, it did require longer gage lengths (3 inch for Zircaloy, 4 inch for stainless steel) compared to a standard 1 inch ASTM creep specimens. Therefore, the specimens required for use with the in-situ monitoring system require a larger volume of space in a materials and test reactor (MTR).

The low frequencies associated with magnetostrictive transducers limits the resolution of the in-situ monitoring system. As a comparison, bench top test were performed on standard 1 inch ASTM creep specimens using commercial high frequency piezoelectric transducers. Much higher resolution of elongation was demonstrated in the bench-top tests using conventional piezoelectric transducers because of the higher frequencies. As discussed in Chapter 4, a piezoelectric sleeve is one potential method to increase the operating frequency of the in-situ system.

CHAPTER 7: CONCLUSIONS

There are a wide variety of engineering applications where it can be advantageous to perform real time ultrasonic measurements. In structural health monitoring (SHM) applications (aircraft, bridges, etc.), real time data can be used to improve safety and reduce maintenance costs. In other applications (such as carbon-carbon production and ceramic sintering) in-situ ultrasonic measurements can be used to study how a material is affected by different manufacturing conditions. Ultrasonic measurements can also be used in place of convention temperature, pressure, fluid flow, or level sensors.

The work presented in this dissertation focused on studying an ultrasonic guided waves based system for performing in-situ measurements on specimens which are commonly used in the accelerated life tests conducted in materials and test reactors (MTRs). Using this system, ultrasonic waves could be sent down a thirty foot long waveguide to a specimen while locating the transducer outside of the hostile environment. Both the theoretical and experimental results demonstrated how individual components of the system influenced the monitoring capabilities.

As one example, the in-situ monitoring system was studied for use in measuring the change in length of creep specimens. Four measurement configurations were considered: through-transmission without a horn, through-transmission with a horn, pulse-echo without a horn, and pulse-echo with a horn. It was shown that the characteristics of each configuration influenced system performance. Ultimately, the pulse-echo measurement with an acoustic horn was found to provide the best signals. In addition, the temperature dependence of the in-situ creep measurement was also studied. Both theoretical calculations and experiments showed that the temperature dependence was approximately linear for the creep specimen geometry.

Successful measurements of the creep elongation of a 3 inch gage length Zircaloy specimen were also demonstrated using the pulse-echo configuration of the in-situ monitoring system. Although the in-situ system was successful, it did require longer gage lengths (3 inch for Zircaloy, 4 inch for stainless steel) compared to standard 1 inch long ASTM creep specimens. Therefore, the specimens required for use with the in-situ monitoring system require a larger volume of space in a MTR.

The results were very encouraging because creep elongation could be measured under conditions where the specimen is not easily accessible. In principal, the in-situ monitoring system could be used for any creep test where it is advantageous to have no equipment (such as an extensometer) in contact with the gage section. The in-situ monitoring system could also potentially be used to measure dimensional changes in other high temperature or corrosive environments. For example, the system could be adapted to measure shrinkage of ceramics during sintering.

'Blister' specimens having a rectangular cross-section were also considered in this work. Theoretically driven semi-analytical finite element (SAFE) calculations, time-domain finite element calculations, and experimental measurements were performed to investigate the guided wave propagation in this specimen. The SAFE calculations, finite element predictions, and experimental results all demonstrated good agreement. In general, the guided wave mode with the fastest group velocity appeared to be the most prominent in both the simulated and experimentally measured waveforms. Very little change in the signal was observed when varying the operating frequency.

Several types of defects were considered. In principal, defects can sometimes produce temperature anomalies in the specimen. The models indicated that detection of a defect induced temperature gradient in the rectangular 'blister' specimen was possible. This result is particularly interesting because temperature gradients can also exist in many SHM applications. Temperature compensation strategies for guided wave SHM typically assume uniform temperatures [37-39]. The results presented here suggest that SHM applications may need to account for temperature gradients or that temperature gradient effects can be exploited for indirect defect detection.

The temperature gradient can in essence be thought of as an induced anisotropy. Thus, further study of the temperature gradient effect could benefit from the works published on anisotropic composite inspection. Furthermore, temperature is not the only possible source of induced anisotropy. Radiation damage and hydrogen absorption processes do not necessarily affect the specimen volume uniformly. Gradients in the material properties caused by these effects could be detected in the same manner as the temperature gradient example.

In the design and operation of an in-situ monitoring system based on guided ultrasonic waves, the transducer design also plays an important roll in the performance of the system. In this work, a magnetostrictive sleeve design was tested as an alternative to the previous wire-wire joint configuration. Results showed that the sleeve design was effective for generating ultrasonic guided waves in the wire waveguide. In addition, the sleeve design simplifies specimen fabrication, minimizes the amount of magnetostrictive material required, and eliminates the artifacts associated with the wire-wire joint. By eliminating the wire-wire joint artifacts, some sources of error are removed and the data obtained with the in-situ monitoring system are easier to interpret. The experimental results showed that the sleeve design generated a narrower bandwidth (less low frequency content). In guided wave applications, this can be advantageous because a more narrow-banded transducer excites a smaller region on the dispersion curves.

7.1 Future Work

The main limitation of the in-situ monitoring system is that it has limited resolution because the magnetostrictive transducers operate in the 125 to 150 kHz range. Ideally, higher frequencies should be used to improve resolution. Future efforts should attempt to optimize the piezoelectric sleeve discussed in Chapter 4 to increase the operating frequency of the in-situ monitoring system. However, it is a non-trivial task to transmit higher frequencies down the wire waveguide.

A more promising concept is to attach piezoelectric elements directly to the specimen and simply run an electric connection to the specimen. However, conventional piezoelectric materials may not be suitable for use in hostile environments. Works by Parks and Tittmann [92,93] have shown that Aluminum Nitride has significant potential for surviving both high temperatures and radiation. Future efforts made towards improving the in-situ measurement technique should investigate attaching Aluminum Nitride transducers directly to a specimen. Work by Stephanou and Pisano [94] has shown that micro-electro-mechanical devices (MEMS) can be fabricated in Aluminum Nitride. It is conceivable that electronics could be integrated with the piezoelectric element if desired.

The detection of the micro-voids associated with specimen swelling presents an interesting challenge. Future work should consider the possibility of detecting micro-voids using nonlinear techniques [95-98]. The nonlinear techniques could also potentially be used to measure the plastic deformation associated with creep to improve the creep length measurement.

The calculations presented in Section 6.8 suggested that measurements based on resonant frequencies could provide a very accurate measurement of a creep specimen's gage length. The challenge would be to develop an accurate experimental measurement. A technique based on Resonant Ultrasound Spectroscopy (RUS) [99] is one possibility. However, there are several challenges to address. A RUS based measurement may require through-transmission of the ultrasonic signals. If using the wire waveguide approach, the guided wave behavior will most likely influence the frequency measurement. If a directly mounted piezoelectric transducer is used, there may be design difficulties in matching the transducer frequency to the resonant frequency of the gage length.

Additional efforts should also be made to further understand the roll of signal processing in the performance of the in-situ monitoring system. The analytic envelope technique is commonly used in both bulk wave [25] and guided wave applications [100,101]. Authors typically claim that an envelope method is advantageous for use in guided wave applications because it eliminates errors associated with the inherent difference between group and phase velocity. However, the results presented in Chapter 6 showed that an envelope method can be less accurate that other data processing methods. One potential way to improve the processing of experimental data is to use dispersion compensation as discussed by Xu et al. [101,102].

7.2 Analysis Framework

As this work demonstrated, each component of an in-situ monitoring system has unique wave propagation characteristics. In addition, each component has a unique interaction with adjacent components. Thus, it can be quite challenging to study and understand overall system capabilities. It is therefore helpful to have a framework to guide future endeavors of similar nature.

When tackling this class of problems, the first (and arguably the most important) step is to evaluate the guide wave propagation in each component. Generally, the 'hybrid analytical-FEM' method discussed by Lee and Rose [103] is the preferred approach. First, accurate dispersion curves must be determined based on the actual boundary conditions of the problem. Approximations should not be made using 'simplified' boundary conditions. The semi-analytical finite element (SAFE) method used in this work is capable of evaluating ultrasonic propagation in specimens with an arbitrary cross-section. Once the dispersion curves are solved for using the true boundary conditions, mode structures can also be calculated. The dispersion curve and mode structure data can then be used to optimize wave propagation and sensitivity in a given specimen.

The second step in evaluating such a system is to examine how the components interact. One promising way to approach this is to develop a 'transfer function' for the system as described by Puthillath [104]. A wave-structure matching coefficient can be defined to quantify the guided wave transmission from one system component to the next. Since the transmission between components may be directionally dependent, a separate set of calculations is required for quantifying reflected signals. After determining all the necessary wave-structure matching coefficients, the transfer function for the entire system can be determined. In principal, the transfer function concept can be adapted to also include the characteristics of the transducer(s).

The final step is to evaluate the impact of any required engineering trade-offs. For example, the optimal frequency for guided wave transmission in 'component A' may correspond to an unusable mode in 'component B.' An iterative approach guided by the theoretical understanding of guided wave propagation can then be used to design the best overall system.

7.3 Contributions

The work presented in this dissertation examined a system for the in-situ monitoring of remote specimens. Both the theoretical and experimental results demonstrated how individual components of the system influenced the overall monitoring capabilities. Through this work, valuable knowledge about the different system components has been gained. Specific contributions include:

- A magnetostrictive sleeve design for the transmission and reception of ultrasonic guided waves in a wire waveguide was demonstrated in this work.
    - The sleeve design required less material, was easier to fabricate, and eliminated the joint artifact compared to the previous magnetostrictive method. By eliminating the wire-wire joint artifacts, some sources of error are removed and the data obtained with the in-situ monitoring system is easier to interpret.
    - The center frequency of the sleeve design was found to be approximately 123 kHz. In addition, the frequency spectrum of the sleeve design contained less content below 100 kHz. In guided wave applications, the narrower bandwidth of the sleeve transducer can be advantageous because a smaller region on the dispersion curve will be excited.
    - The center frequency of the sleeve and the hysteresis of the magnetostrictive material limit the maximum operating frequency of the system. This in turn limits the resolution of system. A piezoelectric sleeve was shown to work as one way to increase frequency and system resolution. Additional work would be required to optimize a system with a piezoelectric sleeve.
    - Both tone-burst and 'square' pulse excitation were tested for optimizing the performance of the transducer. The 'square' pulse did not result in a sharper (wider bandwidth) signal due to the sleeve's frequency response characteristics. Thus, tone-burst excitation is arguably superior because it provides higher signal amplitudes.
- Accurate dispersion curves were calculated for a bar specimen with rectangular cross-section using the SAFE method. With accurate dispersion curves, predicted guided wave modes can be distinguished from artifacts or other anomalies in the recorded data. Also, the dispersion curve information can be used to optimize system performance (i.e. dispersive versus non-dispersive waves). The predicted group velocities were in agreement with experiments.

- 3D wave structures were determined for the rectangular bar using SAFE. The wave structure information explains why the system's sensitivity to defects varies based on the location of the defect. In principal, the wave structure information can be used to optimize the system for detecting a specific defect.

- The work presented in this dissertation studied the ability of the in-situ monitoring systems to detect changes in a rectangular bar specimen.
  - The results indicated that reflections from small defects would be difficult to detect using the low frequency magnetostrictive transducer excitation.
  - The results also indicated that system was sensitive to temperature. By tuning frequency, the change in group velocity versus temperature could be maximized or minimized. Temperature gradients were also shown to affect the dispersion of the guided waves. In principal, detection of temperature gradients could be used as an indirect indication of changes in the specimen.
  - For a proposed materials and test reactor (MTR) application, calculations indicated that the in-situ monitoring system would also be sensitive to radiation hardening (change in elastic modulus).
- The work presented in this dissertation studied the ability of the in-situ monitoring systems to detect changes in the gage length of a creep specimen.
  - Four measurement configurations were studied, and a pulse-echo measurement with an acoustic horn was found to provide the best signals.
  - Results showed that careful consideration had to be given to the signal processing. In this case, reliable results were only obtained by using the peak of each reflection in conjunction with a phase shift correction.
  - Successful measurement of creep elongation was demonstrated with the in-situ measurement system. Additional work would be required to quantify resolution of a system using magnetostrictive transducers.

APPENDIX A: MATERIAL PROPERTIES

A.1 Zircaloy

Zirconium and Zirconium based alloys are commonly used in the nuclear industry because their material properties are well suited for use in a nuclear reactor environment. In particular, the zirconium based materials possess excellent corrosion resistance, good mechanical strength, and have a low thermal neutron cross-section. Reactor grade allows, such as Zircaloy-2 and Zircaloy-4, are commonly used in Boiling Water Reactors (BWR) and Pressurized Water Reactors (PWR), respectively [1,105].

Several references have described the elastic modulus, E(T), of Zircaloy as a function of temperature [106-109]. The reported equations for E(T) are summarized in Table A.1. Figure A.1 shows a graphical comparison of the equations for E(T). The average of all the equations found in the literature is in good agreement with the work by Northwood et al. [109]. The default values in the COMSOL Material Library [110] also appear to in good agreement with the values reported by Northwood et al. [109].

Only the Northwood et al. [109] reference provided information on the shear modulus, G(T), of Zircaloy as a function of temperature. The COMSOL Material Library [110] specifies Poisson's ratio, υ, instead. In order to compare these material properties, the corresponding shear modulus for the COMSOL values was calculated according to Equation A.1. A plot of the results is shown in Figure A.2. Once again the COMSOL Material Library values are in good agreement with the literature.

$$G = \frac{E}{2(1+\upsilon)} \tag{A.1}$$

Table A.1: Material properties of Zircaloy as a function of temperature. (T in Kelvin)

	E(T) GPa	Other Properties
Nam et al. [106]	114.8-0.060T	NA
Dubey et al. [107]	107.3-0.048T	NA
Rosinger and Northwood [108]	112.9-0.058T 119.6-0.076T	NA
Northwood et al. [109]	112.9-0.0579T 116.6-0.0634T	G(T) = 40.9-0.0198T (GPa)
Average of values in the literature	114.0-0.0606T	NA
COMSOL 4.1 Material Library [110]	112.9-0.0579T	υ(T) ≈ 0.377-0.0000219T

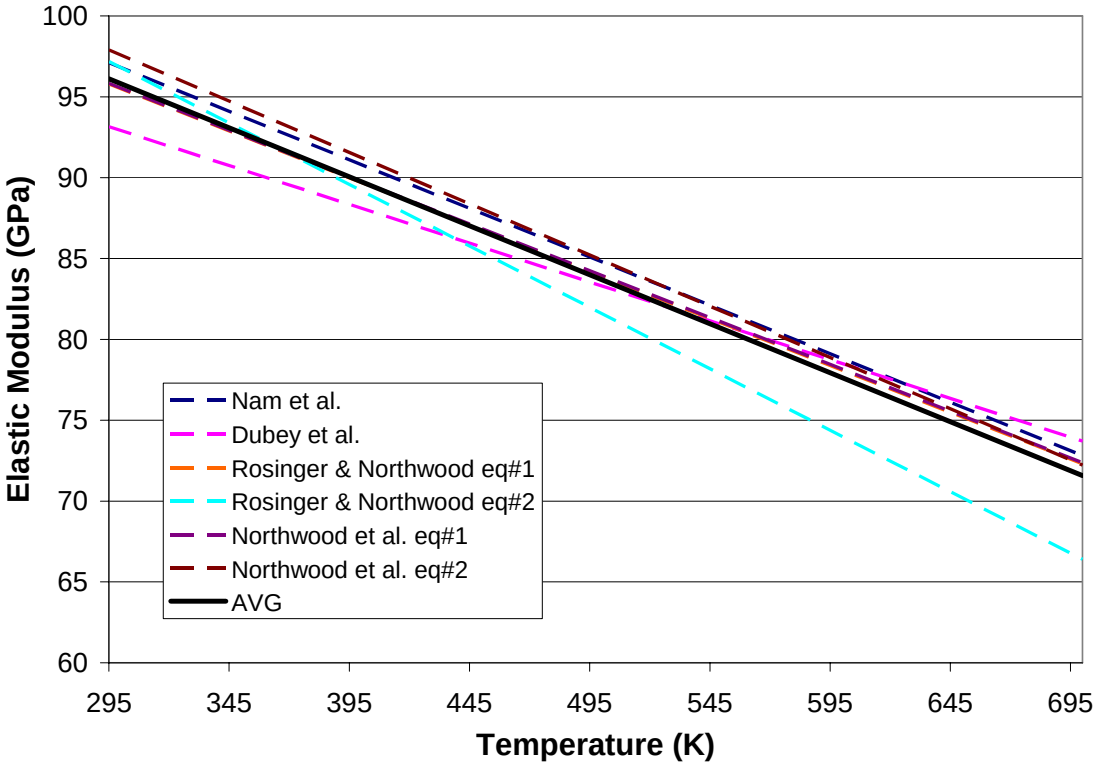

Figure A.1: Elastic modulus of Zircaloy as a function of temperature.

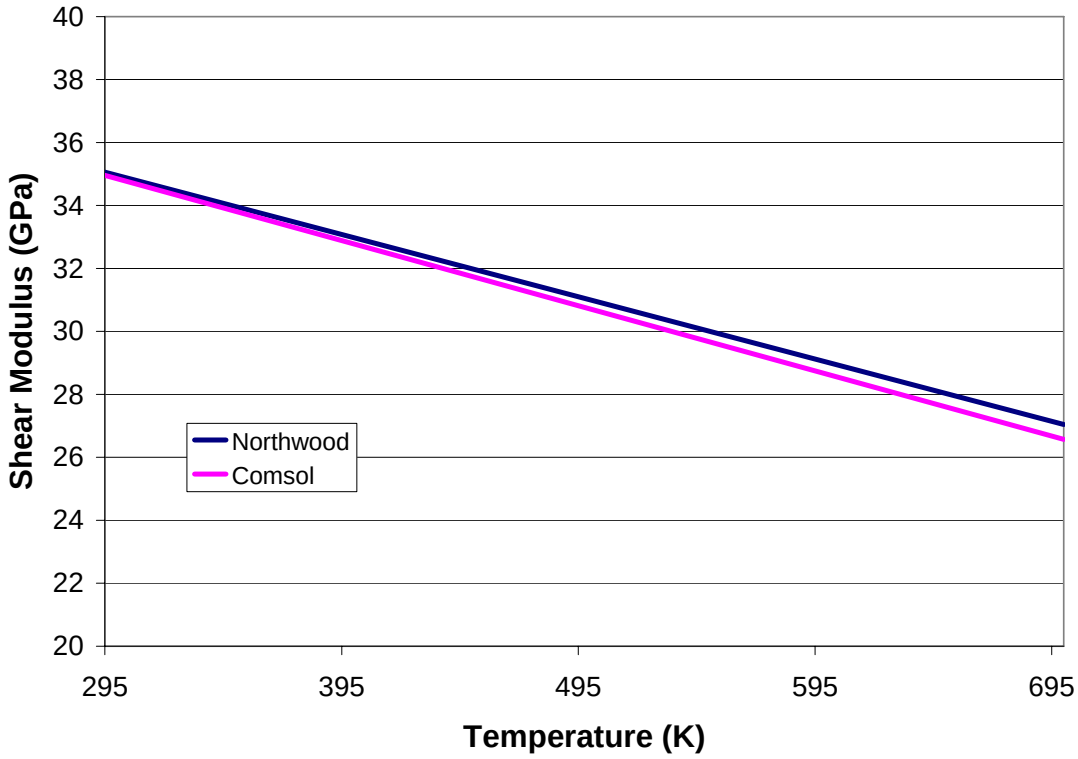

Figure A.2: Shear modulus of Zircaloy as a function of temperature.

The COMSOL Material Library [110] describes the density of Zircaloy as a function of temperature as shown in Equation A.2. Corresponding data on the temperature dependence of Zircaloy's density was not found in the literature. However, the coefficient of thermal expansion for Zircaloy was found in the literature. For Zircaloy crystals, the coefficient of thermal expansion was reported to range from 3 to 5 μ/K depending on the orientation of the crystal [111]. For bulk Zircaloy, the coefficient of thermal expansion (α) was reported to be 6 μ/K [105]. If constant mass is assumed, the density of Zircaloy can then be approximated using Equation A.3. A plot of Equations A.2 and A.3 is shown in Figure A.3 for comparison. There is a small amount of offset between the two equations. However, there is a similar change in density as a function of temperature. Therefore, the relative influence of temperature is consistent.

$$\rho_{Zircaloy} = 6.636 - 0.000147T \,(\mathrm{g/cm^3}) \tag{A.2}$$

$$\rho_{Zircaloy} = \frac{mass}{volume} = \frac{6.55}{(0.99823 + 6\times10^{-6}T)^3} \,(\mathrm{g/cm^3}) \tag{A.3}$$

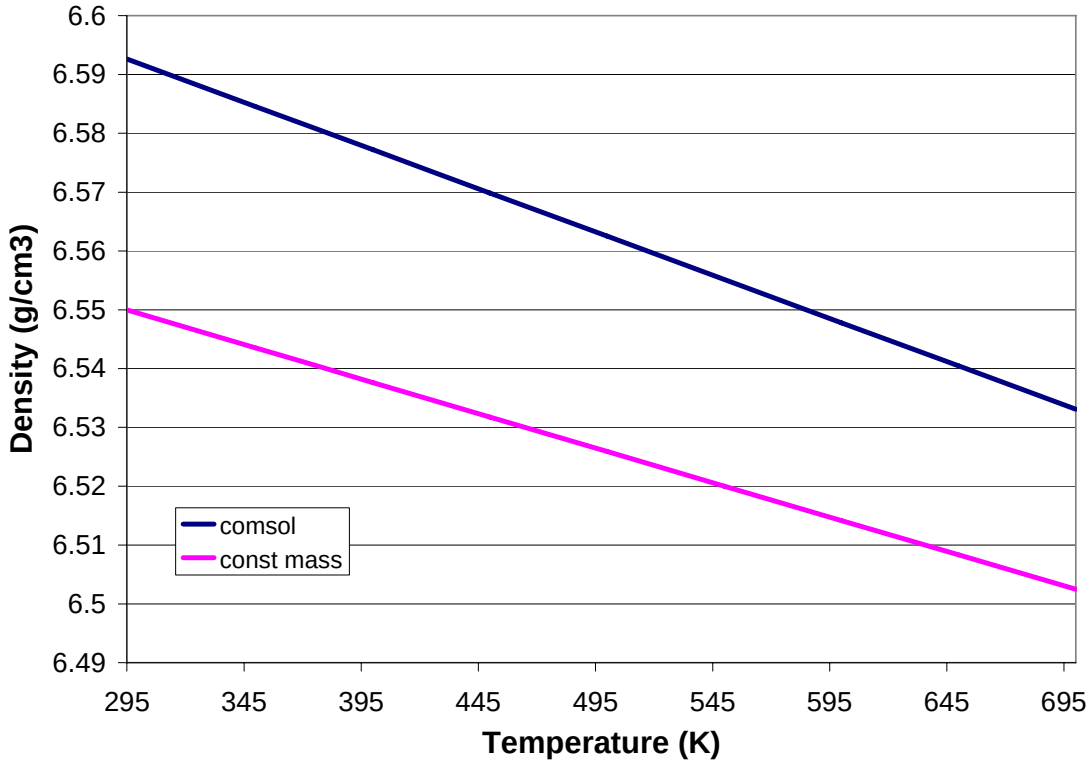

Figure A.3: Density of Zircaloy as a function of temperature.

Although a thorough description of Zircaloy's response to radiation exposure is beyond the scope of this work, it is useful to be aware of relevant effects of "radiation damage." As with any material, a neutron flux will modify the microstructure of Zircaloy. In general, embrittlement and a small increase in the elastic modulus occur over time. However, changes in the material properties are a result of a complex process which depends on several variables. Unlike other metals, both void and precipitation swelling are negligible in Zircaloy. Therefore, an increased volume coupled with a decreased density is not typical in Zircaloy. Most observed dimensional changes observed for Zircaloy in a radiation environment are associated with applied stress [112].

A.2 Stainless Steel

Stainless steels are iron based alloys which possess material properties suitable for use in a nuclear reactor environment. In particular, stainless steels are low cost and easily obtained materials which possess excellent corrosion resistance, and good mechanical strength. Although stainless steels have a higher neutron cross-section compared to Zircaloy, a stainless steel may be preferable for use at higher operating temperatures [1].

Tables A.2 and A.3 summarize the linear trend lines fit to the temperature dependent data reported by Cooke [113] and Rothman [114]. The corresponding equations from the COMSOL material library [110] are also shown in Tables A.2 and A.3 for comparison. Rothman [114] reported both shear modulus and Poisson's ratio data. However, the values given for Poisson's ratio are not consistent with the Poisson's ratio derived from the reported values of elastic modulus and shear modulus. It is unclear why this discrepancy exists in the data reported by Rothman [114].

Table A.2: Elastic and shear modulus of stainless steel as a function of temperature. (T in Kelvin)

	Material	E(T) GPa	*G*(T) GPa
Cooke [113]	"Steel"	240.64-0.0865T	93.1-0.0343T
Rothman [114]	AISI 304	219.51-0.0757T	Quadratic
Rothman [114]	AISI 316	223.62-0.0802T	89.3-0.0379T
COMSOL [110]	316L	218.44-0.0839T	NA

Table A.3: Additional material properties of stainless steel as a function of temperature. (* The Poisson's ratio data reported in [114] are inconsistent with the values of Poisson's ratio derived from the elastic and shear moduli.) (T in Kelvin)

	Material	ρ(T) g/cm^3	υ(T)
Cooke [113]	"Steel"	NA	0.2785+0.0000313T
Rothman [114]	AISI 304	NA	*
Rothman [114]	AISI 316	8.076-0.000406T	*
COMSOL [110]	316L	8.077-0.000379T	0.2703+0.0000805T

Figure A.4 shows a graphical comparison of the equations for the elastic modulus, E(T). The defaults values in the COMSOL Material Library [110] appear to be in good agreement with the data reported by Rothman [114]. Cooke [113] does not identify which steel alloy was used in his work. The difference in the reported elastic modulus is easily explained by a difference in alloy composition.

Figure A.5 shows a graphical comparison of the equations for the shear modulus, G(T). Since the COMSOL Material Library [110] specifies Poisson's ratio (υ), the shear modulus shown was calculated according to Equation A.1. Figure A.5 shows that the COMSOL values are consistent with the shear modulus values found in the literature.

The coefficient of thermal expansion (α) for stainless steel was reported to be approximately 18 μ/K [114,115]. If constant mass is assumed, the density of stainless steel can then be approximated using Equation A.4. Figure A.6 shows a comparison of the constant mass approximation and the reference values. There is a small amount of offset between the constant mass approximation and the reference values. However, there is a similar change in density with respect to temperature. Figure A.6 also shows that the COMSOL Material Library values [110] for density are in good agreement with Rothman's data [114].

$$\rho_{SS} = \frac{mass}{volume} = \frac{7.86}{(0.99569 + 18\times10^{-6}T)^3}\ \text{g/cm}^3 \qquad \text{(A.4)}$$

The response of stainless steel to radiation exposure is very complex and highly temperature dependent. Although a thorough description this behavior is beyond the scope of this work, a few general trends should be noted. Embrittlement and a small increase in the elastic modulus occur over time. Unlike Zircaloy, volumetric swelling occurs in stainless steel. Depending on the intended application, the swelling of stainless steel can be a significant issue [1,112].

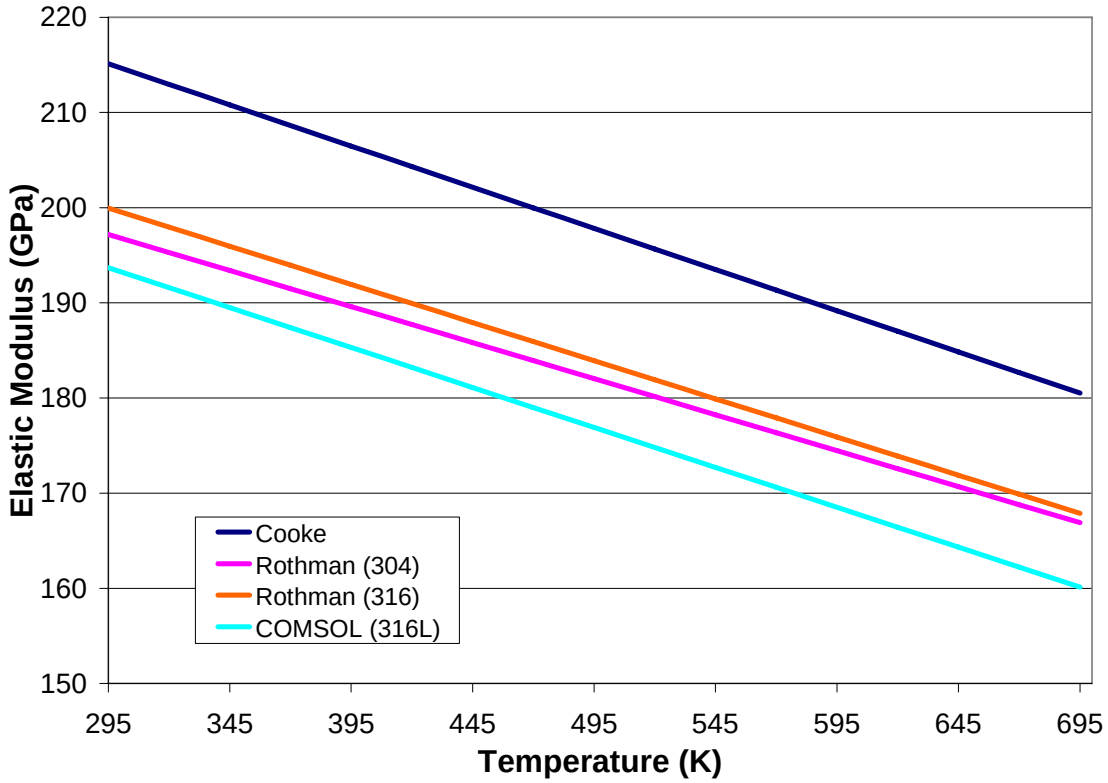

Figure A.4: Elastic modulus of stainless steels as a function of temperature.

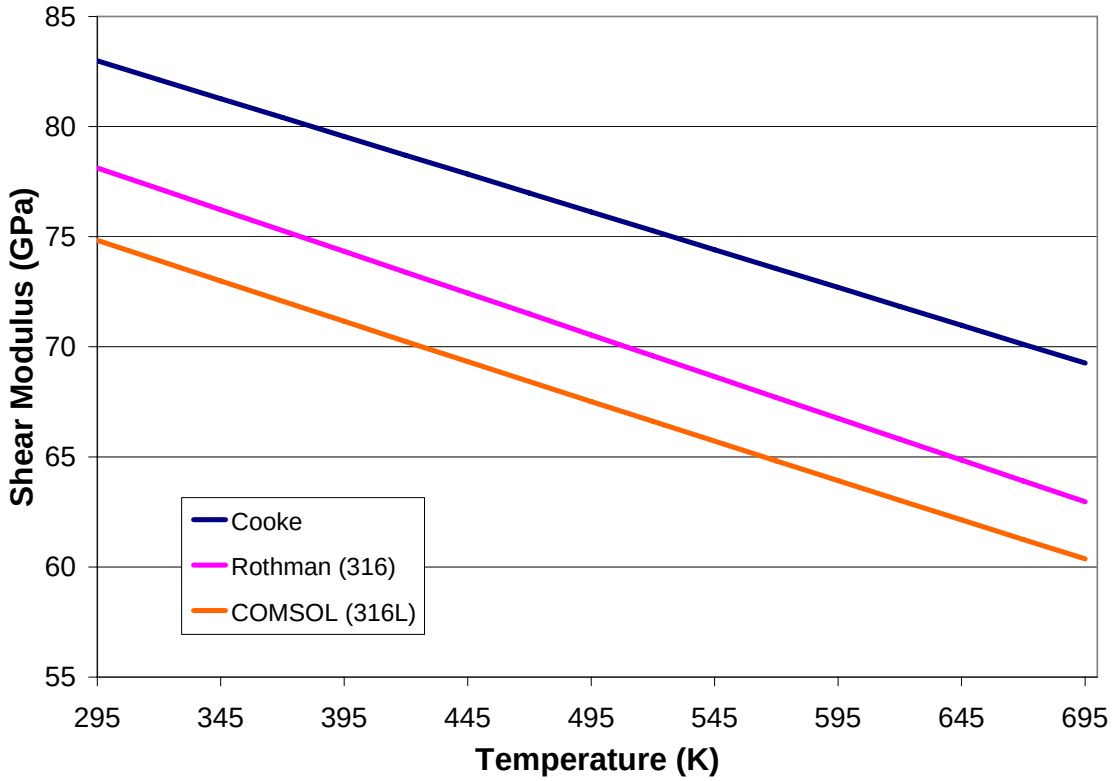

Figure A.5: Shear modulus of stainless steel as a function of temperature.

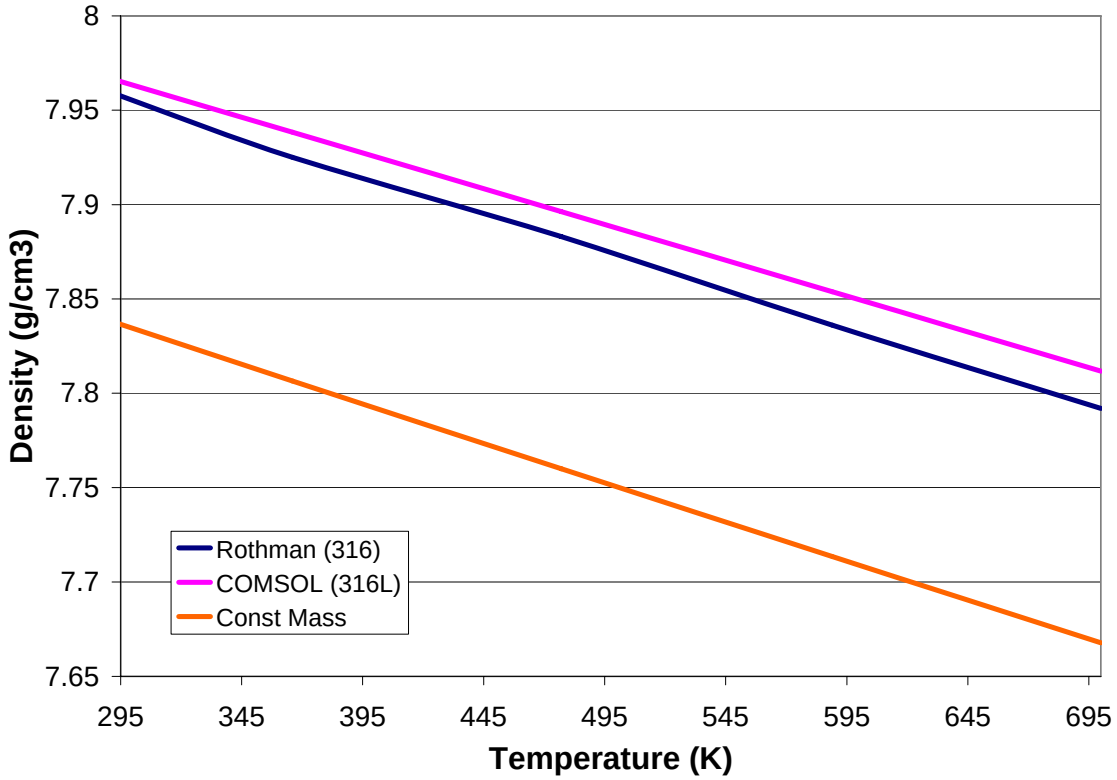

Figure A.6: Density of stainless steel as a function of temperature.

When stainless steel swells, an increased volume is coupled with a decreased density. Form a finite element modeling standpoint, swelling can be approximated by adjusting the dimensions and density of the model appropriately. For a 10% increase in volume, there is approximately a 9% decrease in density (as shown in Equations A.5 and A.6). A 10% increase in volume also corresponds to approximately a 3.25% increase in the linear dimensions of the specimen (as shown in Equations A.7 and A.8).

$$\frac{mass}{volume} = \rho_{SS} \tag{A.5}$$

$$\frac{mass}{1.1 \times volume} = \frac{0.909 \times mass}{volume} = 0.909 \times \rho_{SS} \tag{A.6}$$

$$L \times W \times H = V \tag{A.7}$$

$$1.0325L \times 1.0325W \times 1.0325H \approx 1.1 \times V \tag{A.8}$$

A.3 Inconel

Nickel based alloys (such as Inconel) also possess material properties suitable for use in a nuclear reactor environment. Typically, Nickel alloys are attractive for use in higher temperature applications which require superior fatigue or creep properties compared to stainless steel [1].

The International Nickel Co. Inc. has published several references [116-119] which give detailed tables on the properties of several Nickel based alloys. Table A.4 summarizes the linear trend lines calculated for the tabularize data. The polynomial equations found in the COMSOL Material Library [110] are also shown in Table A.4.

Figure A.7 shows a graphical comparison of the equations for the elastic modulus, E(T). Overall, there is very good agreement between the COMSOL Material Library [110] values and the linear trend lines calculated for each of the alloys.

Figure A.8 shows a graphical comparison of the equations for the shear modulus, G(T). Since the COMSOL Material Library [110] specifies Poisson's ratio (υ), the shear modulus shown was calculated according to Equation A.1. Figure A.8 shows that the COMSOL values are in very good agreement with the reference data.

The reference works published by the International Nickel Co. Inc. [116-119] did not report data on density versus temperature. However, the reference works did provide data on the thermal expansion coefficients (α). Using the thermal expansion coefficients, a constant mass approximation can be used to estimate the density versus temperature. Table A.5 summarizes the corresponding thermal expansion coefficients and density equations. Figure A.9 shows a graphical comparison of density versus temperature. The density values shown are in good agreement except for a small amount of offset.

Table A.4: Material properties of Inconel as a function of temperature. The linear best fit lines calculated for published data is indicated by the initials "L.F." (T in Kelvin)

	E(T) GPa	Other Properties
Inconel 600 (L.F.) [116]	231.24-0.0568T	G(T) = 86.53-0.0185T (GPa)
Inconel 600 (COMSOL) [110]	$221.22-0.0140T-0.000037T^2$	$\upsilon(T) \approx 0.356-1.41E-4T+1.41E-4T^2-8.56E-11T^3+3.92E-14T^4$
Inconel 625 (L.F.) [117]	221.27-0.0539T	G(T) = 85.131-0.022T (GPa)
Inconel 625 (COMSOL) [110]	$215.80-0.0270T-0.000028T^2$	$\upsilon(T) \approx 0.280+3.35E-5T-2.92E-9T^2$
Inconel 718 (L.F.) [118]	215.65-0.054T	G(T) = 82.791-0.0183T (GPa)
Inconel 718 (COMSOL) [110]	$221.62-0.107T+0.000119T^2-77E-9T^3$	$\upsilon(T) \approx 0.305-9.70E-5T+7.92E-8T^2$
Incoloy 800 (L.F.) [119]	215.99-0.0658T	G(T) = 81.524-0.0275T (GPa)

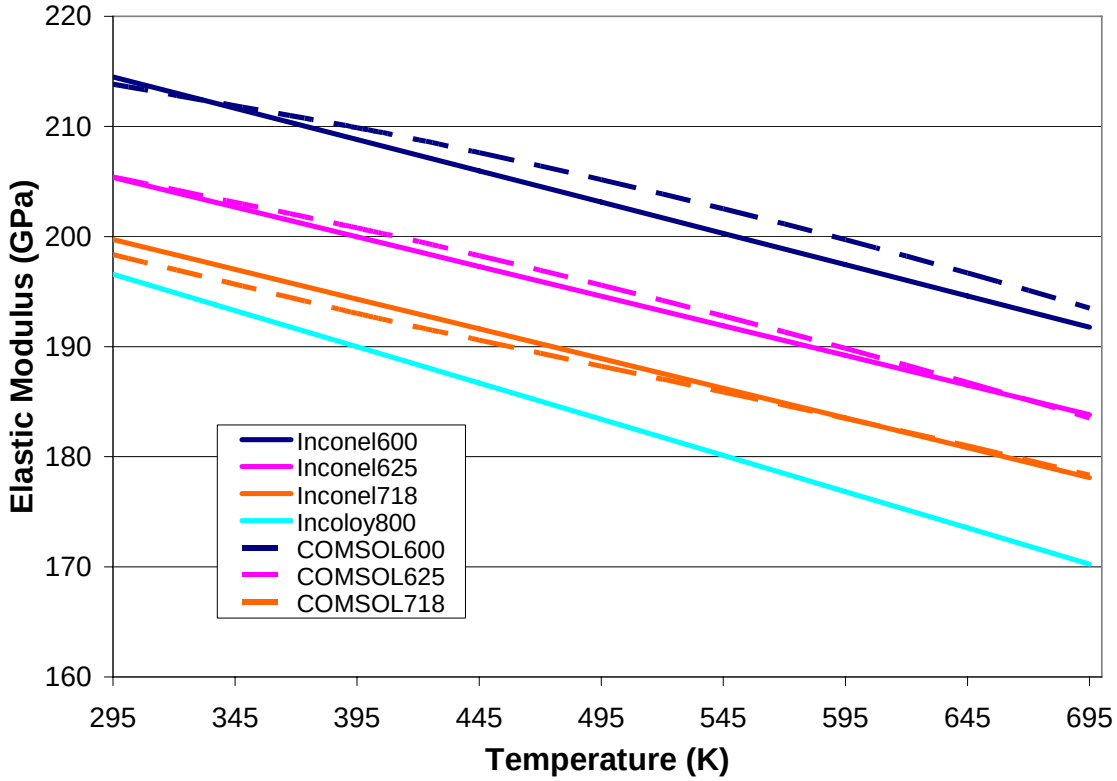

Figure A.7: Elastic modulus of Inconel as a function of temperature.

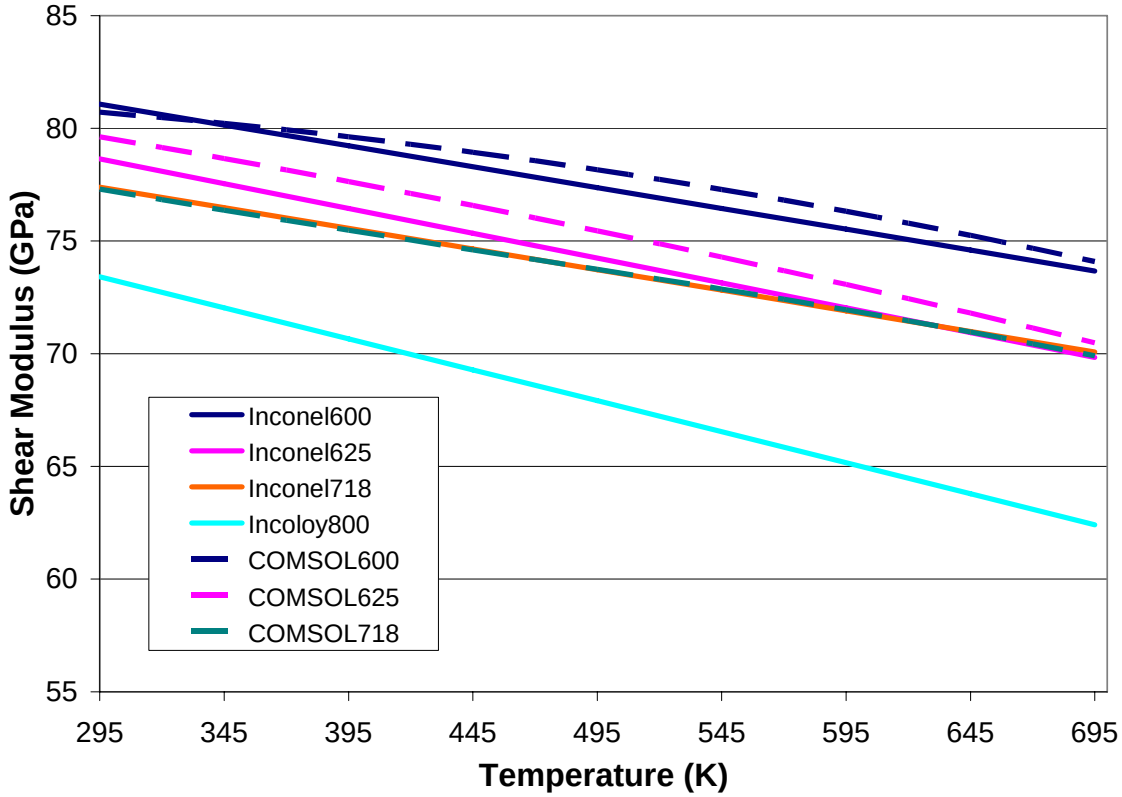

Figure A.8: Shear modulus of Inconel as a function of temperature.

Table A.5: Additional material properties of Inconel as a function of temperature. The constant mass approximation is indicated by the initials "C.M." (T in Kelvin)

	α μm/mK	ρ(T) g/cm^3
Inconel 600 (C.M.) [116]	14.04	$8.47/(0.995858+14.04E\text{-}6T)^3$
Inconel 600 (COMSOL) [110]		$8.43\text{-}2.67E\text{-}4T\text{-}8.23T^2\text{-}7.34E\text{-}9T^3$
Inconel 625 (C.M.) [117]	13.68	$8.44/(0.995964+13.68E\text{-}6T)^3$
Inconel 625 (COMSOL) [110]		$8.32\text{-}0.22T\text{-}1.10T^2$
Inconel 718 (C.M.) [118]	14.58	$8.19/(0.995699+14.58E\text{-}6T)^3$
Inconel 718 (COMSOL) [110]		$8.29\text{-}5.55E\text{-}2T\text{-}7.19T^2+7.97E\text{-}7T^3\text{-}3.48T^4$
Incoloy 800 (C.M.) [119]	16	$8.02/(0.995115+16E\text{-}6T)^3$

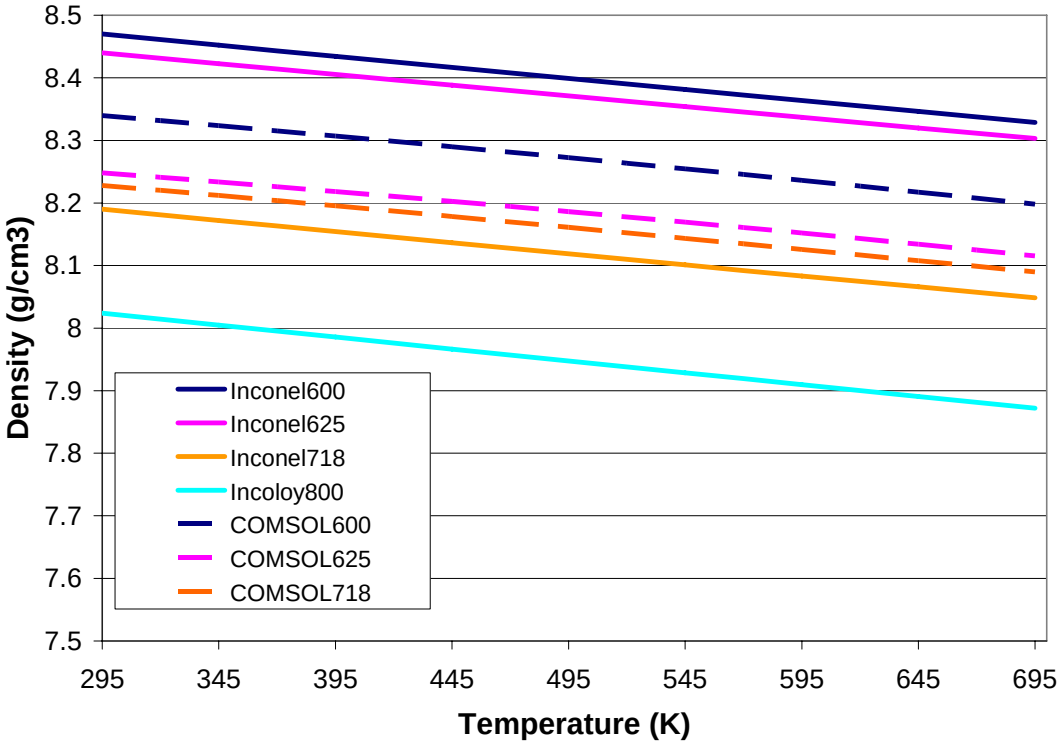

Figure A.9: Density of Inconel as a function of temperature.

A thorough description of how Nickel alloys respond in a radiation environment is beyond the scope of this work. However, it is valuable to note that the response of Nickel alloys is very similar to stainless steel. Volumetric swelling of Nickel alloys can be significant depending on the application, and the observed changes in Nickel alloys are highly temperature dependent [1]. When Nickel alloys swell, an increased volume is coupled with a decreased density. Form a finite element modeling standpoint, swelling can be approximated by adjusting the dimensions and density of the model as discussed in Section A.2.[35]

[35] See Equations A.5 through A.8.

A.4 Aluminum

Aluminum and Aluminum alloys can be used as a Zircaloy substitute in certain low temperature applications such as test reactors. The main advantages of Aluminum based materials are low cost, low neutron cross-section, and high ductility. The main limitation is the low melting temperature of Aluminum based materials [1].

The COMSOL Material Library [110] utilizes the same temperature dependent equations for both pure Aluminum and Aluminum 6061. Figure A.10 shows a plot of both the elastic modulus and shear modulus based on the COMSOL equations for Aluminum. Qualitatively, the data shown in Figure A.10 is reasonably close to the plots of temperature dependent data shown in the work by McLellan and Ishikawa [120]. (See Arnoult and McLellan [121] for a complete description of the experimental procedure used.) McLellan and Ishikawa [120] also claim that their results were in good agreement with the work by Sutton [122].

Augereau et al. [123] utilized a high frequency (7 MHz and 50 MHz) method to measure the elastic modulus of Aluminum 6061. The data obtained by Augereau et al. [123] had an "8%" higher elastic modulus compared to the more widely accepted values [110,120,124]. Augereau et al. theorized that the higher values were observed because the high frequency technique is in fact measuring the dynamic modulus of Aluminum. The work by Prassianakis [125] (see Table A.6) confirms that that the measured dynamic modulus is higher than static measurements and also shows that the measured dynamic modulus is slightly frequency dependent. Although, Augereau et al. [123] used equations based on ideally isotropic materials to estimate the anisotropy in their "rolled" specimens, this does not constitute a significant source of error in their results.

Equation A.9 estimates the density of Aluminum as a function of temperature based on the constant mass assumption. (Note that the work by Augereau et al. [123] also employs the same constant mass approximation.) Figure A.11 shows a comparison of the COMSOL Material Library [110] function for density and the constant mass approximation. In this case the constant mass approximation is not very accurate because the coefficient of thermal expansion varies significantly with temperature.

$$\rho_{Al} = \frac{mass}{volume} = \frac{2.70}{(0.99317 + 23.3\times10^{-6}T)^3}\ \mathrm{g/cm^3} \tag{A.9}$$

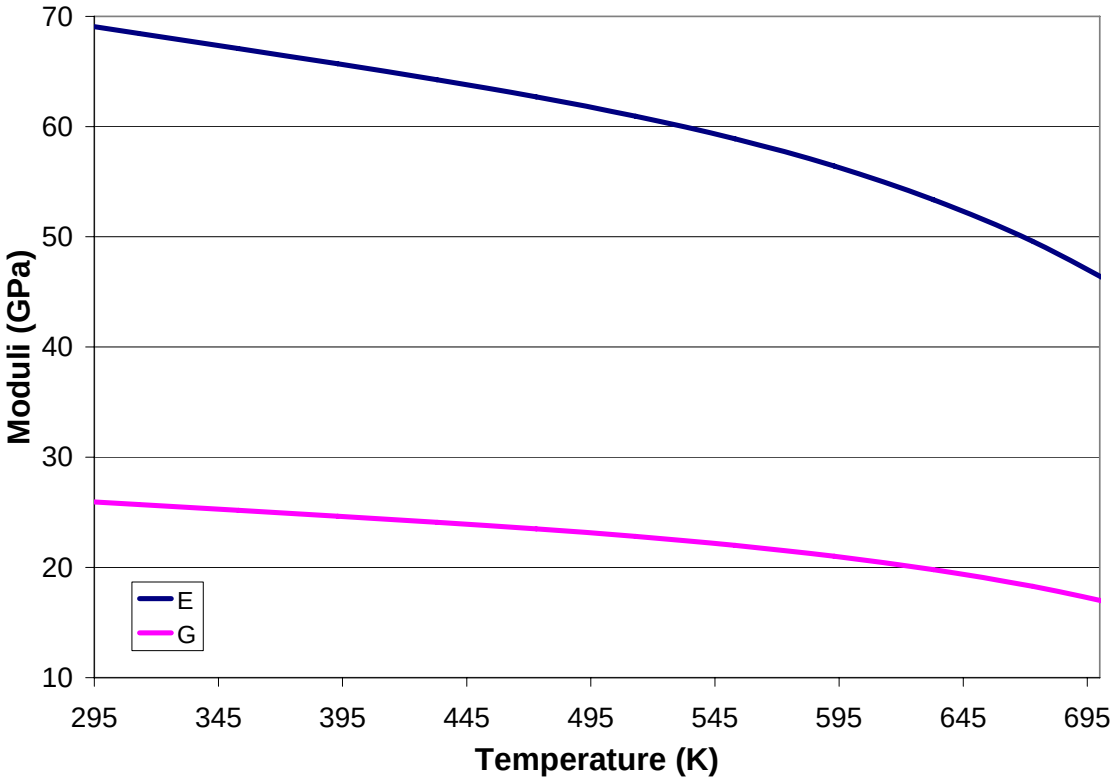

Figure A.10: Elastic and shear moduli of Aluminum as a function of temperature.

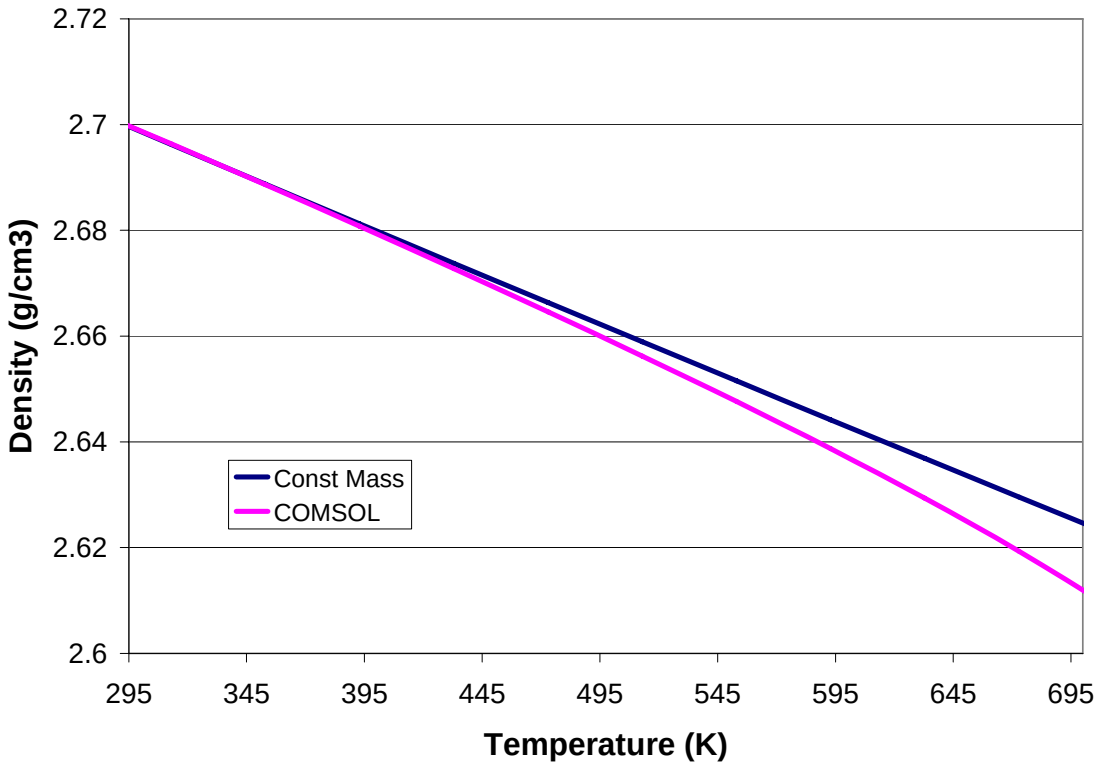

Figure A.11: Density of Aluminum as a function of temperature.

Table A.6: Dynamic modulus versus frequency in GPa. Based on work by Prassianakis [125].

	Static	1 MHz	2 MHz	4 MHz
Steel	209.33	219.78	224.66	227.79
Aluminum	67.38	70.51	72.71	74.93

A thorough description of how Aluminum and Aluminum alloys behave in a radiation environment is beyond the scope of this work. However, it is valuable to note that the swelling of Aluminum and Aluminum alloys is relatively small. Generally, any swelling is not a significant issue because Aluminum and Aluminum alloys retain ductility [1].

A.5 Water

In the proposed in-reactor application, both the bar and creep specimens would be submerged in water at elevated pressure and temperature. If necessary, the underwater environment can be included in the finite element analysis. However, the results shown in Chapters 5 and 6 indicated that submersion in water produced only a small reduction in signal amplitude for the frequency range tested. Including the underwater environment in the finite element analysis significantly increases the model size and solution time for a relatively small improvement in model accuracy.

In COMSOL 4.1, fluid media (such as liquid water) is modeled via a pressure acoustic formulation. Thus, the physical properties of the fluid can be defined by using the speed of sound and density of the fluid.

Figure A.12 shows the speed of sound in water as functions of temperature, and Figure A.13 shows the density of water as a function of temperature. By default, the COMSOL Material Library [110] contains data for water between 273K (0°C) and 373K (100°C) at atmospheric pressure. In order to model water at higher pressures and temperatures, data from steam tables [126] must be used.

As shown in Figures A.12 and A.13, the COMSOL data are in good agreement with the steam tables at atmospheric pressure. At sufficiently high pressure (i.e. 5000 psia) there is no distinct change from liquid to gas.

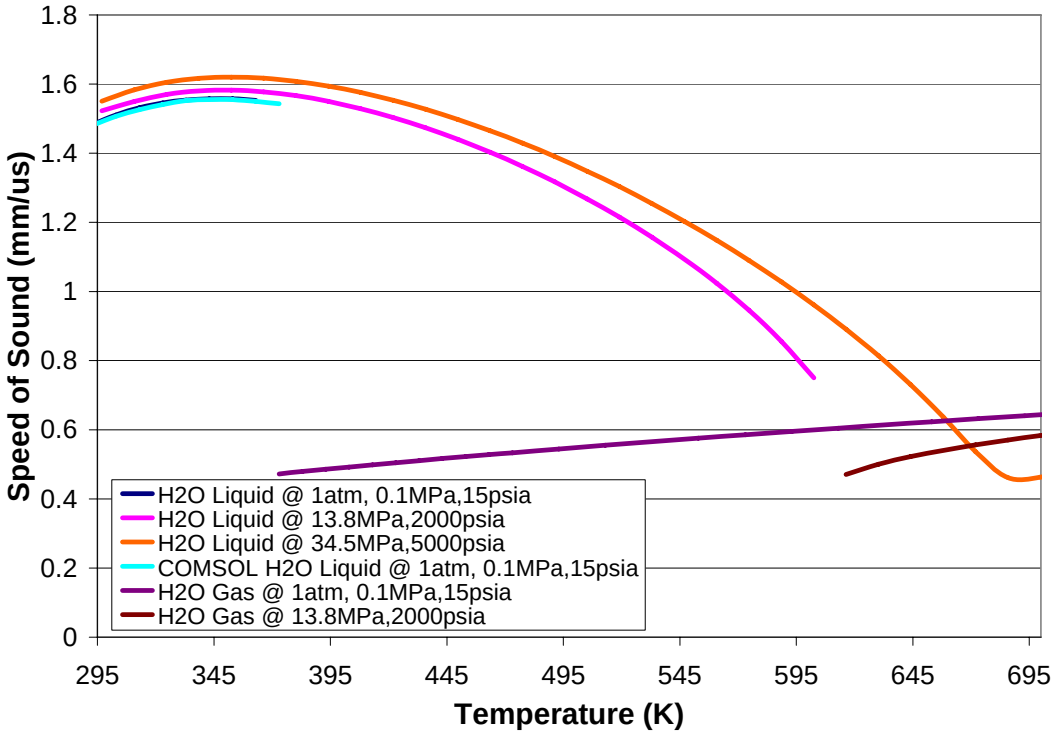

(a)

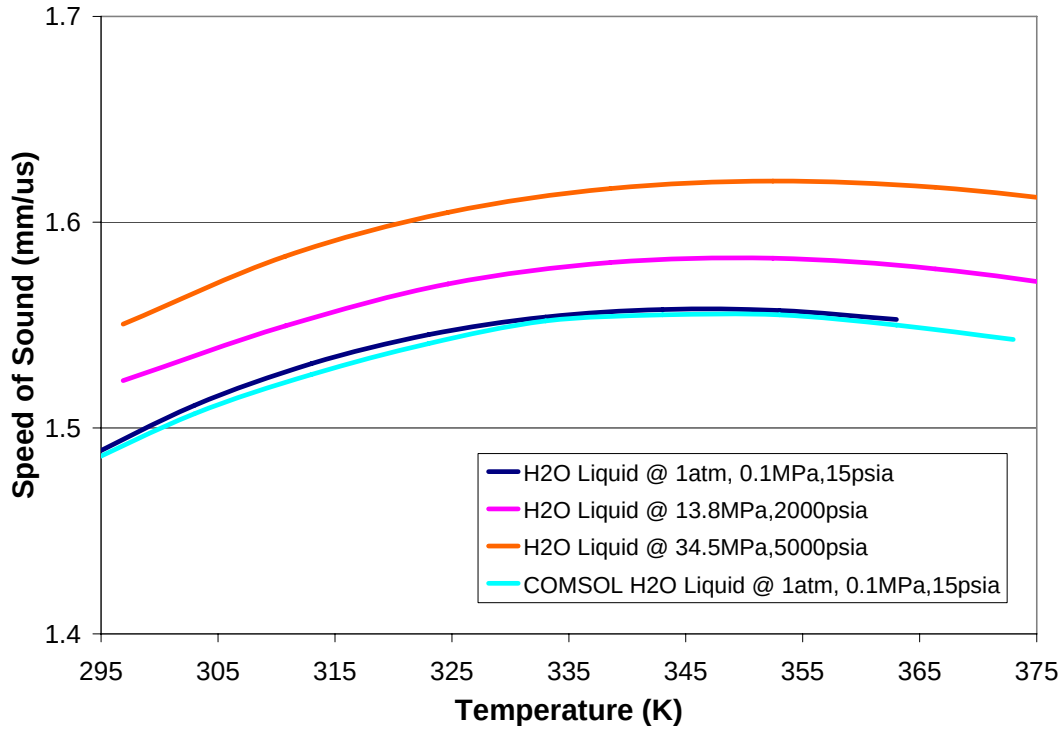

(b)

Figure A.12: Speed of sound in water as a function of temperature. (a) Full temperature range of interest. At sufficient high pressure (i.e. 5000 psia) there is no distinct change from liquid to gas. (b) Detailed view of the data below 373K (100°C).

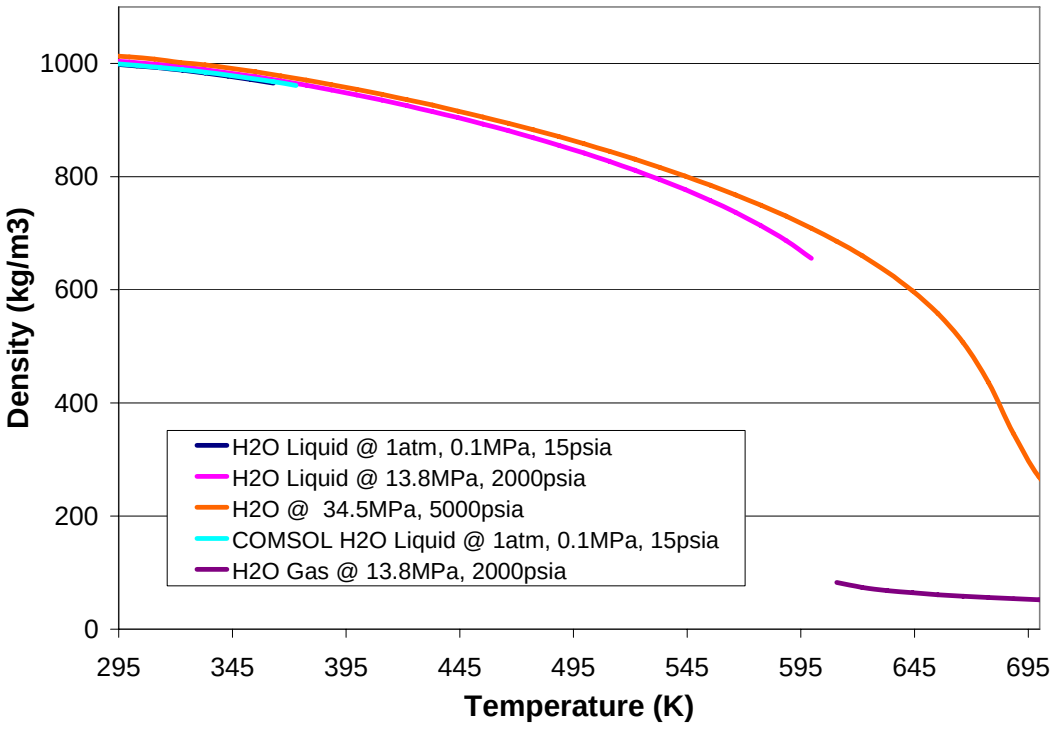

(a)

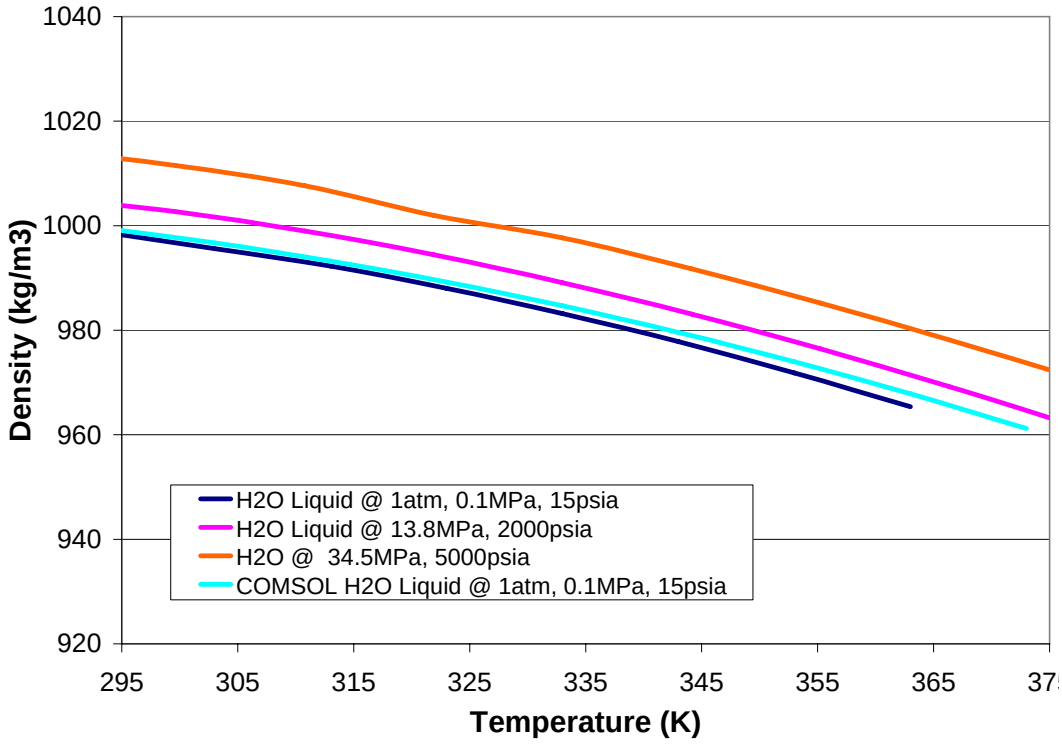

(b)

Figure A.13: Density of water as a function of temperature. (a) Full temperature range of interest. At sufficient high pressure (i.e. 5000 psia) there is no distinct change from liquid to gas. The density of steam at 1 atm (15 psia) is essentially zero and is not shown. (b) Detailed view of the data below 373K (100°C).

A.6 Piezoelectrics

Commercial ultrasonic transducers typically use Lead Zirconate Titanate[36] (PZT) as the piezoelectric material. Generally speaking, PZT based piezoelectric are not suitable for in-reactor applications. PZT is a perovskite material which requires poling in order to have piezoelectric properties. The Curie temperature of PZT is only about 300 to 350°C [127,128]. For long term operation, manufactures generally recommend that operating temperatures not exceed approximately half of the Curie temperature (approximately 160°C). Therefore, PZT will function poorly or not at all at typical reactor operating temperatures. Kazys et al. [127] suggests a higher maximum operating temperature is acceptable for PZT. However, it is unclear if this would impact the life expectancy of a PZT transducer.

PZT based materials are also know to respond poorly to neutron radiation. Broomfield [128] reported that a fluence of $3.5x10^{19}$ n/cm^2 thermal neutrons and $1.4x10^{19}$ n/cm^2 fast neutrons resulted in ultrasonic signals with only 1/8 to 1/15 of the original amplitude before irradiation. Baranov et al. [129] reported a 90% loss of ultrasonic signal for a fluence of $1.4x10^{19}$ n/cm^2 thermal neutrons.

Lithium Niobate ($LiNbO_3$) is a popular high temperature piezoelectric material with a reported Curie temperature of approximately 1200°C [127]. However, Lithium Niobate is problematic in a neutron environment. Primak and Anderson [130] reported a complete loss of piezoelectric response for a fluence of $8x10^{19}$ n/cm^2 thermal neutrons at room temperature. Other reports indicated that Lithium Niobate completely disintegrated for a fluence of $2x10^{21}$ n/cm^2 thermal neutrons below 450°C [131].

There are two naturally occurring isotopes of Lithium: ^{6}Li and ^{7}Li. ^{6}Li has a large thermal neutron cross-section and readily transmutates to an Alpha particle (^{4}He) and Tritium (^{3}H). The use of $^7LiNbO_3$ was reported to have overcome the problem with thermal neutrons [131]. However, fast neutrons can react with ^{7}Li to produce an Alpha particle (^{4}He) and Tritium (^{3}H).

Because established piezoelectric materials are not well suited for in-reactor applications, less common piezoelectric materials must be considered. Aluminum Nitride (AlN), Zinc Oxide (ZnO), and Bismuth Titanate ($Bi_4Ti_3O_{12}$) are known for their high

[36] $PbZr_xTi_{1-x}O_3$ with $0<x<1$

temperature capabilities. However, AlN has the best potential for use in a reactor environment.

Compared to PZT, the high temperature piezoelectric materials (AlN, $Bi_4Ti_3O_{12}$) are considered 'hard' piezoelectric materials. They have a high mechanical quality factor, low dielectric losses, low permittivity, and a low electromechanical coupling factor. This means that that these materials are less efficient when converting electrical pulses into ultrasonic waves, but they are more sensitive for detecting ultrasonic waves.

A.6.1 Aluminum Nitride

Aluminum Nitride (AlN) is an attractive candidate for high temperature piezoelectric transducers. AlN normally has a wurtzite crystal structure. Thus, its piezoelectric properties are a result of the tetrahedral orientation of the Al and N atoms. Since it is not a poled piezoelectric, AlN can theoretically maintain its piezoelectric properties up to its melting temperature (1900°C, 2200K).[37] It is worth noting that AlN can experience detrimental oxidation at lower temperatures (700°C, 1000K) [132]. Therefore, Kazys et al. [127] recommended a maximum operating temperature which does not exceed the oxidation temperature. However, oxidation should not be an issue for transducer applications if an appropriate housing is used.

Parks and Tittmann [92,93] have demonstrated pulse-echo ultrasonic measurements up to 1100°C with excellent signal-to-noise characteristics using an encapsulated AlN crystal. Kazys et al. [127] separately claimed AlN was unaffected by a fluence of $8x10^{18}$ n/cm^2 thermal neutrons. However, this is well below prototypical conditions. Yano et al. [133-135] have studied several characteristic of radiation damage in AlN, but did not test piezoelectric performance.

Atobe et al. [136] examined defect formation in AlN. Atobe et al.'s data indicated that defects are rapidly annealed. This led Atobe et al. to conclude "that the nuclear reaction simultaneously leads to the irradiation annealing of induced point defects regardless of irradiation temperature."

[37] In vacuum.

For use in a reactor environment, the transmutation of the component elements must be considered. Figures A.14 and A.15 show several nuclides near the primary isotopes of Aluminum and Nitrogen, respectively. For thermal neutron absorption, no problems are anticipated [137].

Shikama et al. studied the fission gas production of two variants of AlN ($Al^{14}N$ and $Al^{15}N$). For conditions typical of commercial nuclear power plants (< 2MeV), fission gas production was not significant. However, the ^{14}N isotope produces significant amounts of fission gas when exposed to very high energy neutrons (10 MeV). Conversely, ^{15}N did not produce significant amounts of fission gas when exposed to high energy neutrons. Thus, $Al^{15}N$ may be preferable in applications where high energy neutrons are present [133,138].

Si27 4 seconds Positron	Si28 92% NA	Si28 5% NA
Al26 6 seconds Positron 7x10^5 years Positron	Al27 100% NA	Al28 2.25 minutes Beta decay
Mg25 10% NA	Mg26 11% NA	Mg27 9.45 minutes Beta decay

Figure A.14: Nuclides near Aluminum (^{27}Al). (See [139] for complete nuclide chart and higher precision values.) Neutron absorption by ^{27}Al produces ^{28}Al. ^{28}Al primarily undergoes Beta decay to ^{28}Si [137]. NA stands for "natural abundance."

O14 70 seconds Positron	O15 2.25 minutes Positron	O16 99.7% NA	O17 0.04% NA
N13 10 minutes Positron	N14 99.6% NA	N15 0.4% NA	N16 7 seconds Beta decay
C12 99% NA	C13 1% NA	C14 5715 years Beta decay	C15 2.5 seconds Beta decay

Figure A.15: Nuclides near Nitrogen (^{14}N and ^{15}N). (See [139] for complete nuclide chart and higher precision values.) Neutron absorption by ^{14}N produces ^{15}N. Neutron absorption by ^{15}N produces ^{16}N. ^{16}N primarily undergoes Beta decay to ^{16}O [137]. NA stands for "natural abundance."

A.6.2 Zinc Oxide

Zinc Oxide (ZnO) is another high temperature piezoelectric material which is potentially of interest for in-situ ultrasonic transducers. Like AlN, ZnO possesses the wurtzite crystal structure. Therefore, ZnO can also maintain piezoelectric behavior up to its melting point (approximately 1900 to 1975°C). Thus, ZnO's maximum operating temperature would be similar to that of AlN. In addition, the piezoelectric coefficients of ZnO are comparable to or better than AlN [140,141].

For use in a reactor environment, the transmutation of Zinc must be taken into consideration. Figure A.16 shows several nuclides near the primary isotopes of Zinc. Neutron absorption by ^{64}Zn produces ^{65}Zn. ^{65}Zn is a Gamma emitting isotope with a long half-life (~245 days). In the work by H. Kim et al. [140] 153 days were allowed to elapse to allow some of the ^{65}Zn to decay. Therefore, a depleted ZnO would be preferred for in-reactor applications. It is possible to obtain depleted ZnO. However, further study would be required to confirm the piezoelectric nature of depleted ZnO [140]. Figure A.17 shows several nuclides near the primary isotopes of Oxygen. There are no obvious problems associated with neutron absorption by Oxygen.

Ga64 2.6 minutes Positron	Ga65 15 minutes Positron	Ga66 9.5 hours Positron	Ga67 3.3 days Gamma	Ga68 1.1 hours Positron	Ga69 60% NA	Ga70 21 minutes Beta decay
Zn63 39 minutes Positron	Zn64 49% NA	Zn65 245 days Gamma	Zn66 28% NA	Zn67 4% NA	Zn68 19% NA	Zn69 14 hours Isomeric Transition 56 minutes Beta decay
Cu62 9.7 minutes Positron	Cu63 69% NA	Cu64 12.7 hours Beta decay	Cu65 31% NA	Cu66 5 minutes Beta decay	Cu67 2.6 days Beta decay	Cu68 4 minutes Isomeric Transition 31 seconds Beta decay

Figure A.16: Nuclides near Zinc (^{64}Zn, ^{66}Zn, ^{67}Zn, and ^{68}Zn). (See [139] for complete nuclide chart and higher precision values.) Neutron absorption by ^{64}Zn produces ^{65}Zn. The ^{65}Zn isotope is problematic because it is a Gamma emitter with a long half-life. Neutron absorption by ^{66}Zn produces ^{67}Zn. Neutron absorption by ^{67}Zn produces ^{68}Zn. Neutron absorption by ^{68}Zn produces ^{69}Zn. ^{69}Zn primarily undergoes Beta decay to ^{69}Ga [137]. NA stands for "natural abundance."

F16	F17	F18	F19	F20
~ 0 seconds Proton	1 minute Positron	1.8 hours Positron	100% NA	11 seconds Beta decay
O15	O16	O17	O18	O19
2.25 minutes Positron	99.7% NA	0.04% NA	0.2% NA	27 seconds Beta decay
N14	N15	N16	N17	N18
99.6% NA	0.4% NA	7 seconds Beta decay	4 seconds Beta decay	0.6 seconds Beta decay

Figure A.17: Nuclides near Oxygen (^{16}O, ^{17}O and ^{18}O). (See [139] for complete nuclide chart and higher precision values.) Neutron absorption by ^{16}O produces ^{17}O. Neutron absorption by ^{17}O produces ^{18}O. Neutron absorption by ^{18}O produces ^{19}O. ^{19}O primarily undergoes Beta decay to ^{19}F [137]. NA stands for "natural abundance."

A.6.3 Bismuth Titanate

Bismuth Titanate ($Bi_4Ti_3O_{12}$) is an attractive candidate for use as a piezoelectric material in high temperature environments because its Curie temperature (approximately 650°C) is approximately twice that of conventional piezoelectric materials. As with PZT, Kazys et al. [127] suggested that maximum operating temperature could be higher than half of the Curie temperature. However, it is unclear if this would impact the life expectancy of a Bismuth Titanate transducer.

Searfass et al. [142] showed that a high temperature capable Bismuth Titanate transducer can be fabricated via a sol-gel deposition process. This is particularly appealing for applications when the transducer must conform to complex shapes.

For use in a reactor environment, the transmutation of Bismuth and Titanium must be taken into consideration.[38] Figure A.18 shows several nuclides near the primary isotopes of Bismuth. Although ^{209}Bi is relatively stable, neutron absorption by ^{209}Bi produces ^{210}Bi. ^{210}Bi then Beta decays to ^{210}Po (Polonium). Figure A.19 shows several nuclides near the primary isotopes of Titanium. Although thermal neutrons are not a serious concern with respect to Titanium isotopes, Akers [137] has indicated that there are additional factors to consider.

[38] Oxygen was discussed in section A.6.2. See Figure A.17.

Po208	Po209	Po210	Po211
2.9 years Alpha emit	102 years Alpha emit	138 days Alpha emit	25 seconds Alpha emit 0.5 seconds Alpha emit
Bi207	Bi208	Bi209	Bi210
32 years Positron	3.7E5 years Gamma	100% NA	3E6 years Alpha emit 5 days Beta decay
Pb206	Pb207	Pb208	Pb209
24% NA	0.8 seconds Isometric Transition Stable	52% NA	3.25 hours Beta decay
Tl205	Tl206	Tl207	Tl208
70% NA	3.7 minutes Isometric Transition 4.2 minutes Beta decay	1.3 seconds Isometric Transition 4.8 minutes Beta decay	3 minutes Beta decay

Figure A.18: Nuclides near Bismuth (^{209}Bi). (See [139] for complete nuclide chart and higher precision values.) Neutron absorption by Bi209 produces Bi210. Depending on the isometric state, Bi210 can Beta decay to Po210 [137]. The Alpha emission and self-heating associated with Po210 is problematic. NA stands for "natural abundance."

V46	V47	V48	V49	V50	V51	V52
422 milliseconds Positron	32.6 minutes Positron	16 days Positron	331 days	See [139]	99.75% NA	3.76 minutes Beta decay
Ti45	Ti46	Ti47	Ti48	Ti49	Ti50	Ti51
3 hours Positron	8% NA	7% NA	74% NA	5% NA	5% NA	5.76 minutes Beta decay
Sc44	Sc45	Sc46	Sc47	Sc48	Sc49	Sc50
2.4 days Isometric Transition 4 hours Positron	100% NA	19 seconds Isometric Transition 84 days Beta decay	3.35 days Beta decay	43.7 hours Beta decay	57.3 minutes Beta decay	1.7 minutes Beta decay

Figure A.19: Nuclides near Titanium (^{46}Ti, ^{47}Ti, ^{48}Ti, ^{49}Ti, and ^{50}Ti). (See [139] for complete nuclide chart and higher precision values.) Neutron absorption by Ti46 produces Ti47. Neutron absorption by Ti47 produces Ti48. Neutron absorption by Ti48 produces Ti49. Neutron absorption by Ti49 produces Ti50. Neutron absorption by Ti50 produces Ti51. Ti51 primarily undergoes Beta decay to stable V51. Although technically acceptable, addition considerations beyond neutron absorption are necessary for Titanium [137]. NA stands for "natural abundance."

APPENDIX B: FINITE ELEMENT MODELING

B.1 Software Selection

At the beginning of this work, finite element studies were performed using a combination of ANSYS [143] and a coupled field program called CAPA [144]. Pre-processing of the models was done using the ANSYS interface. However, custom CAPA elements were used instead of standard ANSYS elements. The models were then solved using the CAPA solver. Post-process was then performed using ANSYS or one of the utilities included with CAPA.

Several arguments can be made in favor of utilizing CAPA. First, the coupled field elements[39] in CAPA are designed to allow for a direct or explicit numerical solution. This generally yields faster solutions. Second, coupling between domains is automatically assumed. For example, this means that a user of CAPA does not have to define the coupling between waves in a solid structure and pressure waves in a fluid environment. Third, the input parameters to the CAPA solver are tailored for the specific applications CAPA was designed for. Fourth, CAPA allows the user to only store output data of interest. For example, it is possible to record the output voltage of a simulated transducer to an output file while not storing unwanted displacement data.

However, the features inherent to CAPA can also be a hindrance when modeling applications beyond the designed scope of CAPA. First, the custom CAPA elements rely on a CAPA formatted materials table. Compared to other programs, the reliance on the CAPA material table makes it very difficult to model advanced material characteristic such and nonlinearity and temperature dependence. Second, the coupling cannot be controlled by the user. Third, by learning how to input a model into the CAPA solver, the user does not necessarily learn how to execute other types of finite element studies in ANSYS. Since the scope of CAPA is limited, learning how to solve the same model without CAPA provides the user with a more diverse skill set.

Because CAPA relies on ANSYS for pre-processing, the initial modeling performed for this work was also limited by the ANSYS license restrictions. As shown

[39] Piezoelectric elements are one example of the coupled field elements.

in Table B.1, both ANSYS and CAPA models were limited to 256,000 nodes or elements when using the ANSYS academic license [143,145]. The models of time-dependent ultrasonic wave propagation required for this work routinely exceeded this limit. An ANSYS license with unlimited elements is available for purchase, but it is very expensive (>$10,000) [145].

In addition to ANSYS, the High Performance Computing (HPC) Group at the Pennsylvania State University (PSU) supports several other finite element programs. Of those, ABAQUS is a very popular program for modeling ultrasonic wave propagation because of its efficient explicit solver and its support of very large models. However, it was not the best choice for the present work. Instead, COMSOL was selected for this work because it provided better support for explicit solutions of piezoelectric materials, and better support of temperature dependent material properties, while still allowing for very large model sizes.

B.2 Background on COMSOL

As with all finite element software, COMSOL uses the finite element method to find a numerical solution to the partial differential equations governing physical phenomena. However, unlike other finite element programs, COMSOL provides enhanced flexibility in defining the physical phenomena under consideration. Any partial differential equation can be entered into COMSOL through the software's PDE mode. In addition, there are no limitations on what physical domains can be coupled. For example, a 2D and 3D analysis can be coupled and solved simultaneously. COMSOL also supports using nonlinear partial differential equations [146,147].

Table B.1: Comparison of available finite element programs. (Based on the PSU HPC academic licenses.)

	ANSYS 12	ANSYS + CAPA[40]	ABAQUS	COMSOL 4.1
Size limit	256,000 elements or nodes	256,000 elements or nodes	Token system[41]	None
Core limit	4 total (2 per seat)	unknown	Token system[3]	None
Scripting	FORTRAN based	FORTRAN based	Python based	MATLAB based

[40] CAPA is a user supplied add-on package to ANSYS and is not supported by the HPC.

[41] A token check out system controls the size of ABAQUS models based on both the number of elements and the number of processing cores. At PSU there are typically enough unused seats at any given time that there are usually enough available tokens.

COMSOL's licensing structure is based on selecting the components or 'Modules' a user pays for. When purchasing COMSOL, the base COMSOL Multiphysics component must be purchased. All other modules are optional. However, the base module does not provide built-in support for modeling piezoelectric materials or transient pressure waves in fluids. A user would have to manually code all of the equations and couplings to model piezoelectric materials or transient pressure waves in fluids using only the base module of COMSOL.

Both the Structural Mechanics Module [148] and the Acoustics Module [149] have built-in support for modeling piezoelectric materials. Therefore, either the Structural Mechanics Module or the Acoustics Module would be sufficient for studying many nondestructive evaluation (NDE) and structural heath monitoring (SHM) applications. However, the user should be aware of several features of COMSOL and the Modules:

- Only the Structural Mechanics Module provides several advanced material models in addition to the basic linear isotropic material model. Therefore, the Structural Mechanics Module is required for modeling nonlinear materials (i.e. Murnaghan materials).
- Only the Acoustics Module supports transient (time-domain) waves in fluids. In addition, the Acoustics Module has additional support for absorbing/infinite boundary conditions depending on modeling domain.
- Therefore, both the Structural Mechanics Module and the Acoustic Module would be required for a model involving both fluid media and nonlinear solids.
- A model which utilizes the Structural Mechanics Module can only be opened on a computer system having a working Structural Mechanics Module. Likewise, a model which utilizes the Acoustics Module can only be opened on a computer system having a working Acoustic Module. (For example, a model of waves in a solid built with the Structural Mechanics Module cannot be open by a system having only the Acoustics Module installed even though such an analysis can also be performed using the Acoustics Module.)
- COMSOL models are not back compatible.

In addition to the physics modules, there is an optional database of material properties available for integration with COMSOL. The materials library contains over 2500 materials including piezoelectric material such as Lead Zirconate Titanate (PZT), Zinc Oxide, and Aluminum Nitride. This reduces or eliminates the need to generate material property matrices needed for a finite element analysis. Furthermore, COMSOL has the capability to define arbitrary user coordinates for each sub-domain. This allows a user to always work with industry standard material property definitions regardless of orientation in the global coordinates of the model (i.e. poling direction of a piezoelectric) [146,147].

COMSOL also provides a diverse set of post-processing capabilities. Slice planes, transparency, and boundary integrations are examples of post-processing that are natively supported in COMSOL. Slice planes are particularly useful for visualizing wave propagation within the volume of a geometry. Since, COMSOL is built on the MATLAB programming language, COMSOL results are inherently compatible with MATLAB for customized analysis [147].

Practical Considerations

The user should be aware that a significant amount of memory may be required to run COMSOL models depending on various modeling parameters. In many of the cases tested in this work, "out of memory" errors occurred when using a 32-bit computer system. Typically, successful solutions required using a 64-bit system or a cluster computer with distributed memory.

Several of the COMSOL solvers provide "out-of-core" options which are intended to allow large models to be solved on systems without enough RAM installed. However, the user should be aware that this only provides a small amount of help on 32-bit systems. A 32-bit system cannot address more than 4 GB of total memory regardless of the solver options selected in COMSOL. Thus, the out-of-core solver option cannot compensate for a model requiring more than 4 GB of memory on a 32-bit system.[42] When using a 64-bit system, the addressable memory is only limited by the hardware

[42] On a 32-bit system, the COMSOL model requirements cannot exceed 4 GB of total memory. However, the out-of-core solver option can compensate for memory used by the operating system and other processes running on the 32-bit system.

resources of the computer system or the operating system.[43] The out-of-core solver option can then utilize hard drive space to act as extra memory when solving very large models.[44]

The user should also be aware that COMSOL versions 4.0 and 4.0a have a known file size limit of 4 GB regardless of the computer system used [150]. This issue and several other software bugs were corrected in the COMSOL 4.1 release. Therefore, this appendix assumes use of **COMSOL 4.1**.[45]

B.3 Running COMSOL on the PSU Clusters

When running COMSOL models on the PSU cluster systems, the output files were frequently missing some of the time steps in the transient solution. This issue was observed both when running a single model with a large output file and when running multiple small models in parallel. After lengthy discussion with COMSOL support [151], it was determined that this issue was caused by the COMSOL "recovery files" exceeding the "home" directory size limit imposed on the PSU clusters.

The "recovery files" are a new feature introduced in COMSOL 4.1 which is intended to allow a user to resume solving a COMSOL model which was interrupted part way through the study. By default, the "recovery files" are stored in the user's "home" directory.[46] Since the PSU cluster system limits the size of each user's "home" directory, the recovery files (and by extension the solution files) would stop storing output when the "home" directory limit was reached.[47]

The "recovery files" issue is easily solved when running the COMSOL GUI. The "recovery files" can be disabled from the options menu. Alternatively, the directory where the recovery files are stored can be changed by editing the comsol.prefs file.

The "recovery files" issue is a bit more challenging when running COMSOL in batch mode because the comsol.prefs file is apparently not utilized in batch mode. If the

[43] The operating system may restrict the maximum amount of addressable memory to a value lower than the physical limits of the computer hardware.
[44] Utilizing hard drive space as virtual memory results in slower calculations and therefore longer solution times. At some point the model becomes impractical.
[45] COMSOL 4.1 also appears to use less memory compared to versions 4.0 and 4.0a.
[46] Typically, /home/.comsol on Linux and \Documents and Settings\user\.comsol on Windows.
[47] The user should delete any unwanted "recovery files" which are not automatically deleted by COMSOL so that the unwanted recovery files do not consume hard drive space.

user wishes to generate the "recovery files," the '–prefsdir' command can be used to change the directory where the "recovery files" are stored. If the users does not want to generate "recovery files," the '–autosave off' command can be used to prevent batch mode from generating the "recovery files."

The user should also be aware that there is a way to force COMSOL to perform post-processing steps when running in batch mode. To do this, the user must first add a "batch" node in the model builder as part of the "Study." Under the batch node, the user must add a "solution" entry and then add any desired post processing items (plot, export data, etc.). The user should then select the option to "show tag names." The batch node should be "b1" by default. The batch node will not execute automatically when submitting the batch job from the command line (as on PSU clusters). To force the batch node to execute, the "–job" command must be used.

For a (Linux) batch job on the PSU cluster with automatic post-processing, the command line should have the following format:[48]

comsol batch –autosave off –inputfile in.mph –job b1 –outputfile out.mph

B.4 Summary of Modeling Procedure for COMSOL

The example procedure given here is intended to provide a step-by-step overview of setting up a time-domain model of ultrasonic wave propagation using COMSOL 4.1. An attempt has been made to provide as complete of a description as possible. However, certain proprietary information (i.e. exact dimensions) has been omitted in compliance with the sponsor's requirements.

Initial Setup with the "Model Wizard"

Begin by launching COMSOL 4.1. By default the "Model Wizard" is shown to help initialize the COMSOL model. Select a "3D" model. Then, add "Heat Transfer in Solids (ht)" and "Solid Mechanics (solid)" physics to the model. The steady state heat transfer solution is needed as an input to the solid mechanics calculation because

[48] Please refer to the COMSOL 'installation and operations' guide for a complete description of the command line syntax and any difference in formatting for Windows.

temperature dependent material properties are of interest. In order to accomplish this, select a "Stationary" study as the first study type in the "Model Wizard." (Note that the transient solution step will be added to the model in a later step.) Click on the finish flag to complete the "Model Wizard."

After completing the "Model Wizard," then next menu allows the user to select which dimensional units to work in. For this example, the units may be left as meters. At this point in the modeling process, the user should take time to consider if any parameters or variables are advantageous to the problem being studied. Although parameters and variables are not used in this example, a user of COMSOL can save significant effort by defining desirable parameters or variables at the beginning of the modeling procedure.

Defining the Geometry

The next step is to define the geometry. Because of the complex dimensions involved, the trapezoidal horn and the cylindrical slot for the brazed joint are defined first, about the origin. This simplifies how the necessary dimensions for this shape are specified.

In order to define the trapezoidal horn, two "Working Planes" are required: the yz-plane (wp1) and the zx-plane (wp2). To create each "Working Plane," right click on "Geometry" in the "Model Builder" and then select add "Working Plane." On each "Working Plane," the appropriate trapezoidal cross-section can be defined using linear segments. The cross-section defined on each "Working Plane" must then be extruded to create a 3D volume. To generate an "Extrude" feature, right click on "Geometry" in the "Model Builder" and then select add "Extrude."[49] Set each extrude to the appropriate "distance."[50] Next, right click on "Geometry" in the "Model Builder" and select "Boolean Operations." Select an "Intersection," and then select the two extruded volumes. If done correctly, the desired trapezoidal horn will be created.

[49] In COMSOL 4.0, the extrude features are sometimes listed out of order in the Model Builder. Although this problem has not been observed in COMSOL 4.1, the user should be aware that this could affect the model.

[50] In the Extrude setting, the user may need to adjust the choices of when to keep or not keep the input objects and cross-section faces to get the correct sub-domain definitions.

In order to define the cylindrical slot, two cylinders are required. To create each cylinder, right click on "Geometry" in the "Model Builder" and then select add "Cylinder." To create the slot, right click on "Geometry" in the "Model Builder" and select "Boolean Operations." Select a "Difference," and then subtract the smaller diameter cylinder from the larger diameter cylinder. This forms the slot where the wire waveguide is brazed into the trapezoidal horn. Creating the slot is necessary to correctly assign material properties for each part of the joint.

The next volume to define is the rectangular bar. This can be easily accomplished by right clicking on "Geometry" in the "Model Builder" and then choosing to add a "Block." In the setting for the "Block," either the center of the volume or a corner of the "Block" can be used for the reference position. In this work, selecting the corner is advantageous because it makes it easier to vary the length of the bar.

The last volume to define is the wire wave guide. To model the waveguide, right click on "Geometry" in the "Model Builder" and then select add "Cylinder." The "Cylinder" must be defined to have a length of at least 1270 mm (50 inch). A sufficiently long waveguide must be used in the model to prevent errors associated with the simulated ultrasonic waves reflecting off of the free end of the wire waveguide. Also, note that the starting position of the waveguide mush be set to correctly fit into the slot created earlier.

Setting Material Properties

The next step is to set the material properties for the geometry. If the Material Library is included with the COMSOL license, simply use the material browser to add Zircaloy-2 and 316L stainless steel to the materials list. These two materials have temperature dependent material properties. The user should take note of the valid temperature range for the Zircaloy-2 equations. (See Appendix A for more information on specific material properties.) The user should also be aware that any warnings shown for the tangent moduli are not a problem in this example because an elastoplastic material model will not be used.

If the Material Library is not included with the COMSOL license, the material properties must be defined manually. Begin by right clicking on "Materials" in the "Model Builder" and select add "Material." Rename it "Zircaloy-2." In addition to

"Basic" properties, the "Young's modulus and Poisson's ratio" properties must also be selected from the list on the settings tab. For the "Basic" properties, the appropriate expression must be supplied for density (rho), thermal expansion coefficient (alpha), heat capacity (Cp), and thermal conductivity (k). For "Young's modulus and Poisson's ratio," the appropriate expressions must be supplied for E and nu (ν), respectively. Temperature must be set as an input variable for both categories of material properties. Finally, repeat this process to manually enter the material properties of 316L stainless steel.

After selecting or creating the materials, assign Zircaloy-2 to be the material for the volumes associated with the bar specimen. Then set the wire waveguide volume to 316L stainless steel.

Setting Boundary Conditions

The next step in the modeling process is to define boundary conditions for each physics domain. Begin with the "Heat Transfer (ht)" settings. Set the "strain reference temperature" to 293 K. Right click on "Heat Transfer" in the "Model Builder," and a "Temperature" boundary condition. To create a uniform temperature distribution in the bar specimen, select all of the exterior boundaries of the bar specimen and set the temperature to 300 K.

For the "Solid Mechanics (solid)" physics, click on the "linear elastic material model" and set the "strain reference temperature" to 293 K. Also, be sure to change the "Model Inputs" from "user defined" to "Temperature (ht/solid1)." This step makes the mechanical properties (Young's modulus, Poisson's ratio) a function of the steady state temperature solution. Next, right click on "Solid Mechanics" in the "Model Builder," and a "Prescribed Displacement" boundary condition on the end of the wire waveguide. For a 2 cycle, 125 kHz pulse, set the Z-direction displacement to: $w = 10e-6*\sin(2*pi*t*125e3)*(t<16e-6)$.

Mesh

Based on theoretical calculations, a phase velocity of approximately 4 mm/μs is expected in the bar. At 125 kHz, this corresponds to a wavelength of 32 mm. A minimum of 10 elements per wavelength is required for accuracy when using linear

elements (~ 3 mm between nodes). However, COMSOL uses a quadratic element by default. A 4 mm quadratic element was selected in order to have 2 mm spacing between nodes. In order to define the mesh in COMSOL, select a "user-controlled mesh" with a "custom" element size. Set maximum = 4e-3. A minimum element size is not necessary.

Defining a Study

Under "Study," the "Stationary" step (for solving temperature) is already there because this entry was created as part of the "Model Wizard." Right click on "Study" and add a "Time Dependent" solution step so that the transient wave propagation can be modeled. Set the range to: range(0,0.25e-6,1000e-6). Linear elements require at least 15 time steps per period for accuracy (~0.5e-6 @ 125 kHz). Since a quadratic element is used by default in COMSOL, at least 30 time steps per period are required for accuracy because of the shorter distance between nodes (~0.25e-6 @ 125 kHz).

Before trying to solve the model, the user should also be aware that stationary solver in COMSOL 4.1 will generate an error because of the time dependent boundary condition used to simulate the ultrasonic excitation.[51] In order for the model to run, the solid mechanics physics must be disabled in the stationary solver step. To do this, simply un-check the "used in this study" box on the stationary solver menu as shown in Figure B.1.

The heat transfer physics can be disabled during the time dependent solution. Preliminary testing indicated that the simulated waveform results were practically the same regardless of whether heat transfer physics was enabled or disabled for the transient analysis. Disabling the heat transfer physics in the time dependent solver appears to significantly decrease the solution time.

When defining the study, the user should be aware that the "solver" and "job" entries in the model builder are hidden in COMSOL 4.1. In order to view the "solver" and "job" menus, the "show more options" must be selected from the "view menu" (downward pointing triangle) as shown in Figure B.2.

When using COMSOL 4.1 then next step is to select "show default solver." For the solver sequence described in this example, a direct solver should be the default solver

[51] Such an error was not observed with COMSOL 4.0.

selected for the time dependent analysis when using COMSOL 4.1 with the Windows operating system.[52] In the event that a direct solver is not the default selection, changing to a direct solver in COMSOL is accomplished by simple "enabling" the direct solver in the "Molder Builder."

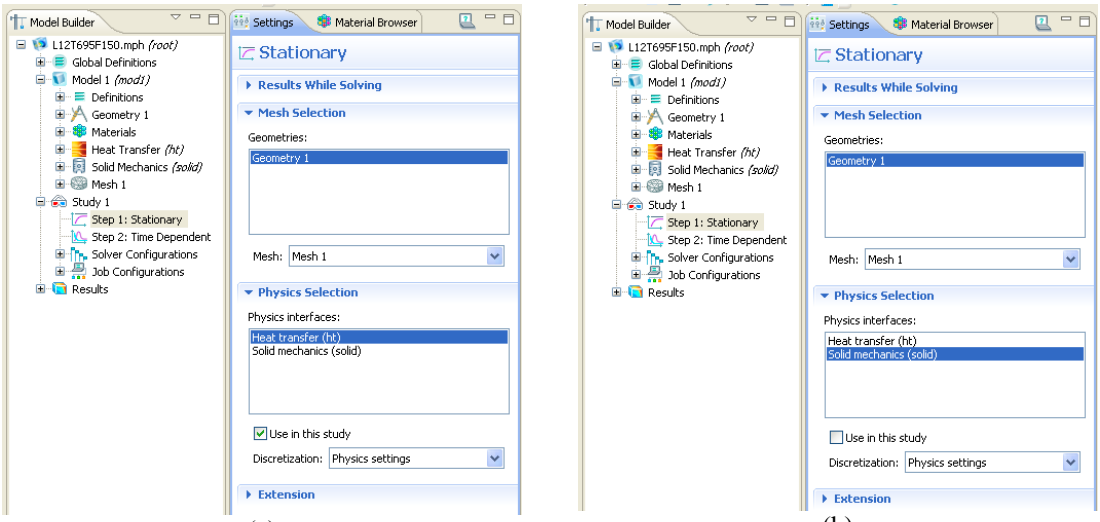

(a) (b)

Figure B.1: "Stationary" solver settings in COMSOL. (a) "Heat Transfer" physics (highlighted in blue) are enabled in the "Stationary" solver because the "use in this study box" is checked. (b) "Solid mechanics" physics (highlighted in blue) are disabled in the "Stationary" solver because the "use in this study box" is checked.

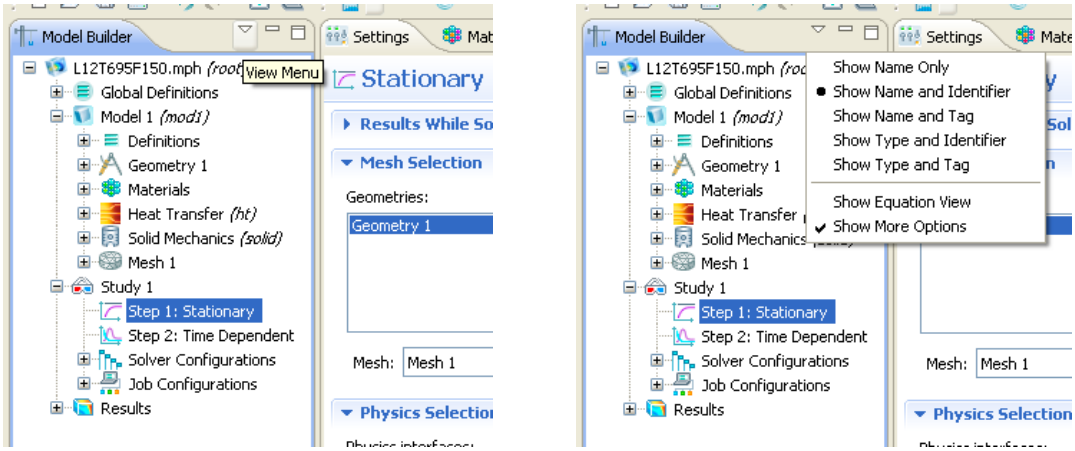

(a) (b)

Figure B.2: Accessing the "solver" and "job" menus in COMSOL. (a) The "view menu" is accessed by clicking on the downward pointing triangle located near the "Model Builder" tab. (b) Select "show more options" (check marked) for the "solver" and "job" menus to be displayed.

[52] For modeling ultrasonic wave propagation, a direct (a.k.a. explicit) solver should be used for accuracy and efficiency. Iterative solvers are inefficient and potentially inaccurate because there is not explicit control of the time step size.

On the "Time Dependent Solver" menu (Figure B.3), switch to the "generalized alpha" time stepping with "manual" steps of 0.25 μs (0.25e-6). Without forcing COMSOL to take sufficiently small time step, the results will not be accurate. Also, the "amplification for high frequency" value should be set to 0.5. The default value for the "amplification for high frequency" value varies depending on the version of COMSOL. Testing showed that a value of 0.5 reduces the noise in the simulated waveforms.

The user should also be aware of the output options on the "Time Dependent Solver" menu (Figure B.3). The reaction forces must be stored for post-processing, and the solution should be stored out-of-core to reduce the memory required. Storing the time derivatives is optional. COMSOL 4.1 does not suffer form an inherent file size limit. Thus, storing the time-derivatives is not a problem and provides a slightly more accurate result in post-processing. However, not storing the time derivatives only changes the results by ~0.1%. The user may wish not to store the time derivatives to reduce the file storage required and ease post-processing.[53]

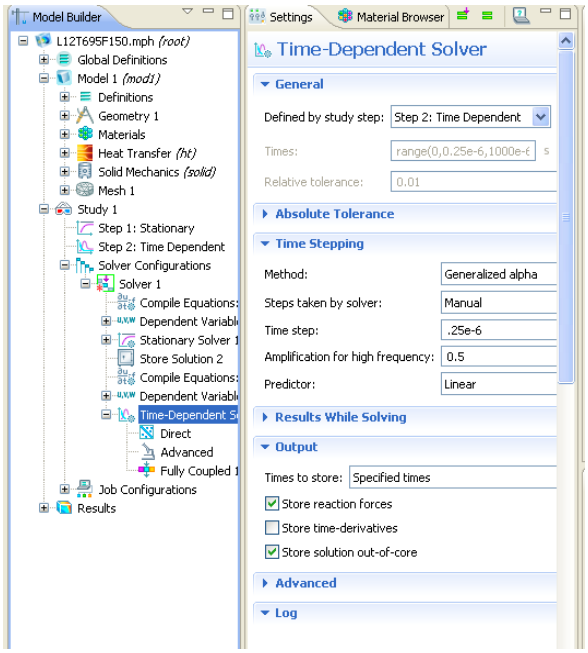

Figure B.3: Time-Dependent Solver settings in COMSOL. The "generalized alpha" time stepping method with manual time steps of 0.25μs is required for accuracy. The "amplification for high frequency" parameter should be set at 0.5 to reduce noise in the simulated waveforms. Turning off the option to "store time-derivatives" significantly reduces the output file size.

[53] A smaller output file is faster to load and post-process.

Solution

The next step in the modeling process is to calculate the solution. When using the graphical user interface of COMSOL, the model can be run by selecting the "compute all" icon (the green "equals" sign shown in Figure B.3). The solution can also be calculated by submitting a "batch" job.[54] Section B.3 discusses how to run a batch job on the PSU HPC cluster systems.

Post-Processing

The final step is to post-process the results of the finite element model. COMSOL provides an extensive list of properties which can be plotted in the "Results" menu of the "Model Builder." In order to determine the simulated waveform, a "1D Plot Group" must be added by right clicking on the "Results" menu in the "Model Builder." Then right click on the "1D Plot Group" and add a "Point Graph."[55] Because a "Prescribed Displacement" boundary condition was used to simulate the incident ultrasonic wave, the simulated waveform cannot be obtained by plotting displacement versus time. Fortunately, COMSOL can plot "Pressure" (solid.p) for a selected point at the end of the wire waveguide. Plotting "Pressure" yields an accurate waveform despite the prescribed displacement boundary condition.

B.5 Convergence Study

When modeling wave propagation (either in fluids [149], or in solids [152-154]), it is generally accepted that a minimum of 10 elements per wavelength and 15 time steps per period are required for accuracy in a finite element model when using linear elements. Since a quadratic element is used by default in COMSOL, this discretization rate must be adjusted slightly. For a linear element, a discretization rate of 10 elements per wavelength yields 10 nodes per wavelength. However, a discretization rate of 10 elements per wavelength yields 20 nodes per wavelength when using a quadratic element.[56] Since there are twice as many nodes per wavelength, there must also be twice

[54] Correct procedures for batch jobs depend on the configuration of the computer system in use.
[55] Use a "point graph" to plot data versus time.
[56] Equivalent to a discretization rate of 20 elements per node with linear elements.

as many time steps per period. Thus, 30 time steps per period are required when using a quadratic element with a discretization rate of 10 elements per wavelength.

In Section B.4, a 4 mm quadratic element and time steps of 0.25 μs were selected based on the theoretical discretization rate for a quadratic element. In order to confirm this, a convergence study was performed. Results for several element sizes and time steps are shown in Figures B.4 through B.7.

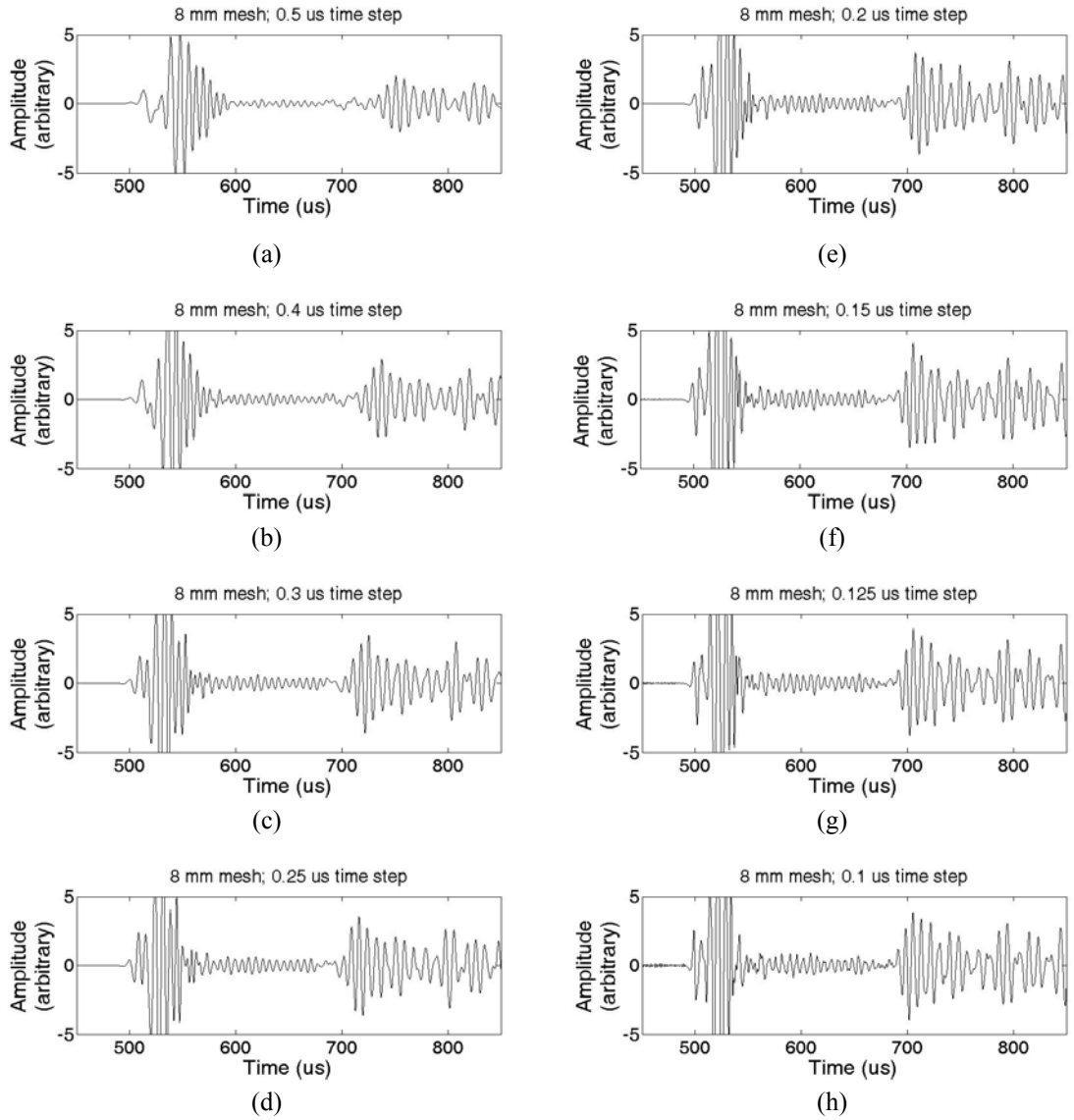

Figure B.4: Convergence study results obtained using an 8 mm quadratic element (4 mm spacing between nodes). (a) 0.5 μs time steps. (b) 0.4 μs time steps. (c) 0.3 μs time steps. (d) 0.25 μs time steps. (e) 0.2 μs time steps. (f) 0.15 μs time steps. (g) 0.125 μs time steps. (h) 0.1 μs time steps.

In all of the results shown (Figures B.4 through B.7), the simulated waveforms show the reflection from the brazed joint arriving at approximately 525 to 550 μs time-of-flight. The characteristics of the joint reflection change only slightly as the mesh size and time step size are varied because the wire waveguide has a relatively high phase velocity. In contract, the characteristics of the simulated waveforms after 525 to 550 μs time-of-flight are more sensitive to the mesh size and time step size because the bar specimen has a relatively low phase velocity.

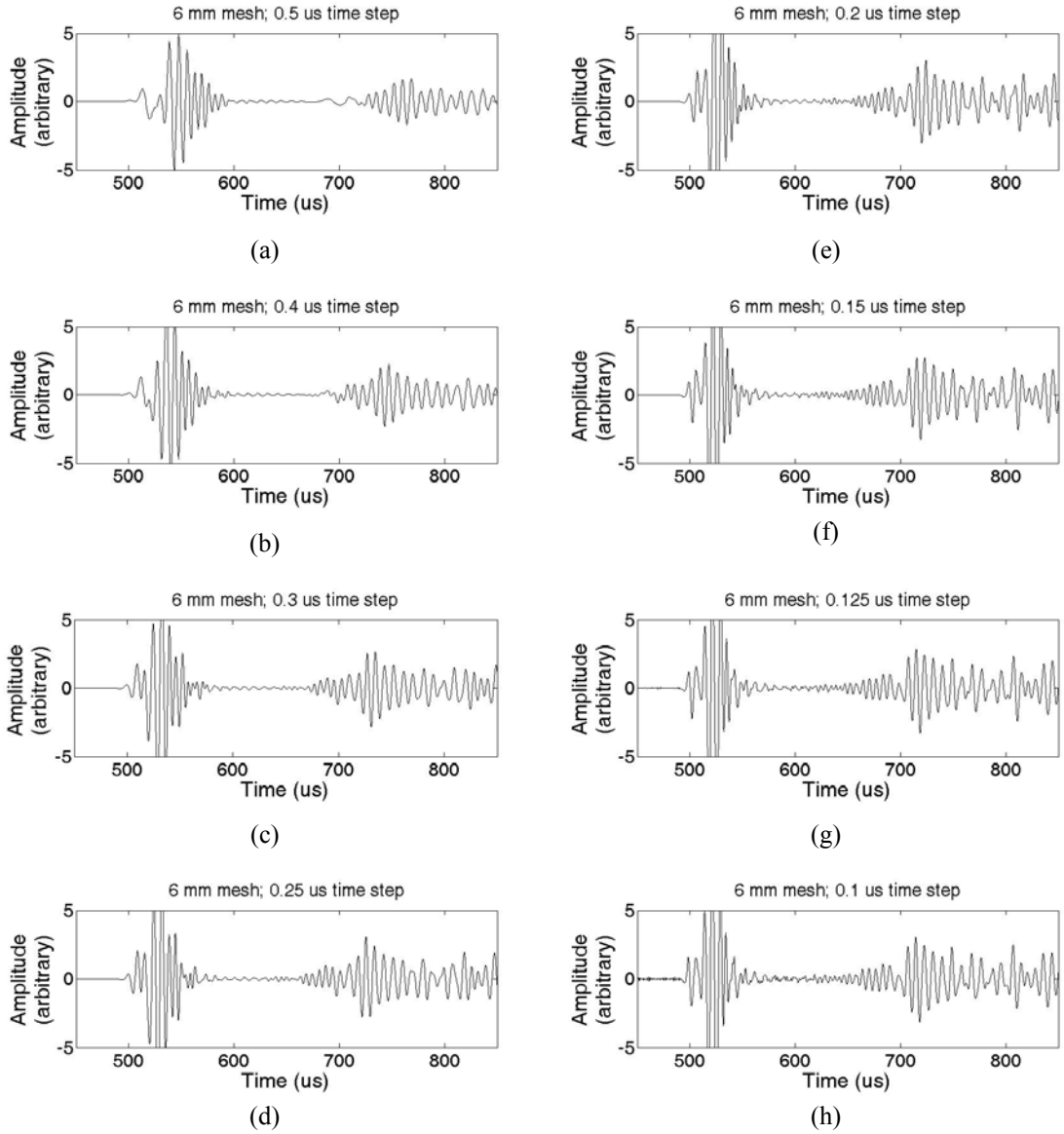

Figure B.5: Convergence study results obtained using a 6 mm quadratic element (3 mm spacing between nodes). (a) 0.5 μs time steps. (b) 0.4 μs time steps. (c) 0.3 μs time steps. (d) 0.25 μs time steps. (e) 0.2 μs time steps. (f) 0.15 μs time steps. (g) 0.125 μs time steps. (h) 0.1 μs time steps.

For the models with an 8 mm element size (Figure B.4), the quadratic elements have a node spacing of 4 mm. This is greater than maximum node spacing of 3 mm (1/10 of a 32 mm wavelength) determined in Section B.4. As shown in Figure B.4, there is significant noise in the simulated signals after 525 to 550 μs time-of-flight. In contrast, there is significantly less noise in the simulated signals for the results with a 6 mm element size (Figure B.5). The noise in the simulated signals is further reduced in the results with a 4 mm element size (Figure B.6).

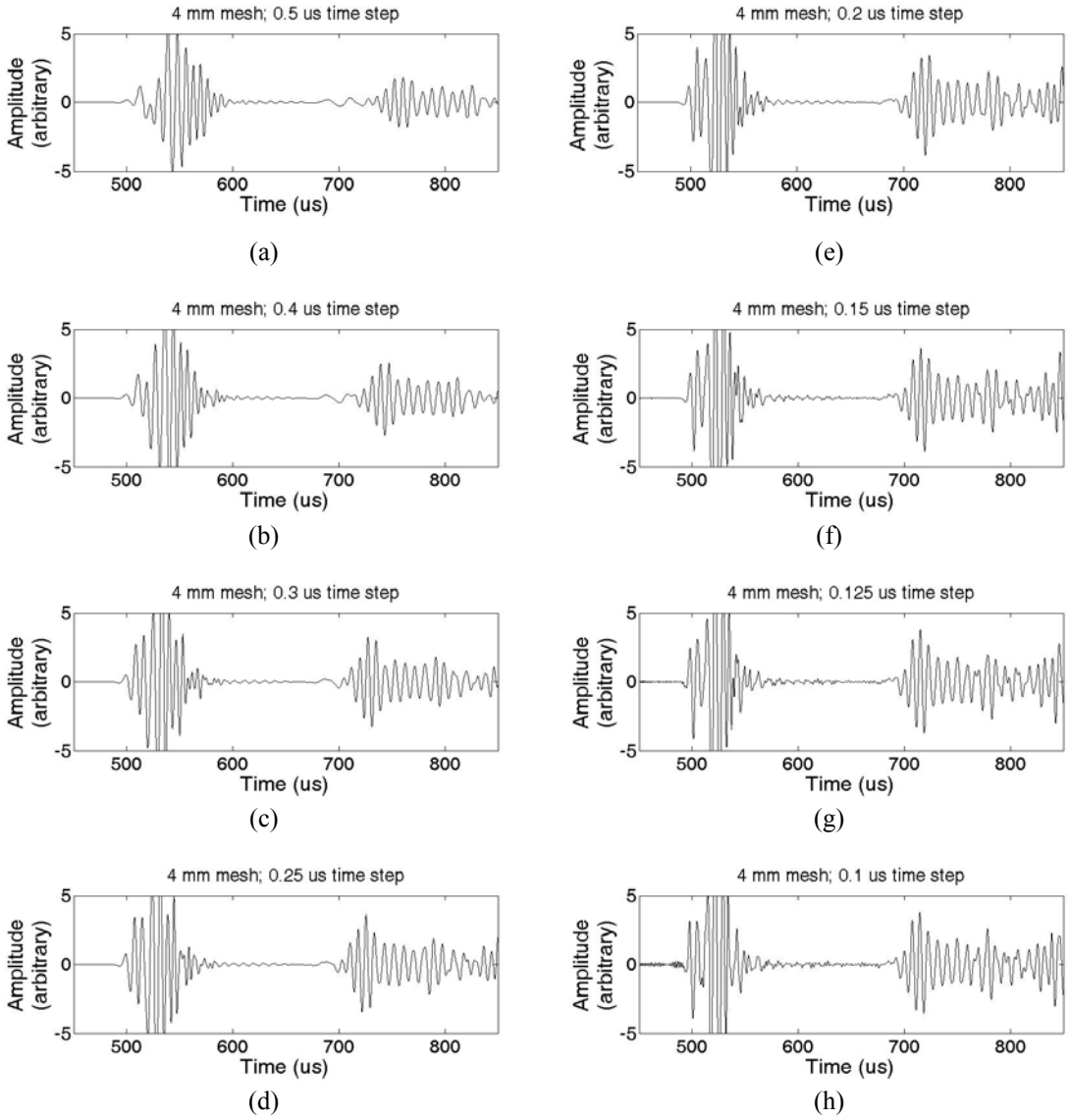

Figure B.6: Convergence study results obtained using a 4 mm quadratic element (2 mm spacing between nodes). (a) 0.5 μs time steps. (b) 0.4 μs time steps. (c) 0.3 μs time steps. (d) 0.25 μs time steps. (e) 0.2 μs time steps. (f) 0.15 μs time steps. (g) 0.125 μs time steps. (h) 0.1 μs time steps.

The simulated waveforms for the 4 mm element size (Figure B.6), also have more distinct reflections from the end of the bar (approximately 725 to 750 μs time-of-flight) compared to the simulated waveforms for the 6 mm element size (Figure B.5). This occurs because the guided wave propagation in the bar specimen includes multiple guided wave modes. The simulated waveforms for the 2 mm element size (Figure B.7) are only slightly better than the simulated waveforms for the 4 mm element size (Figure B.6).

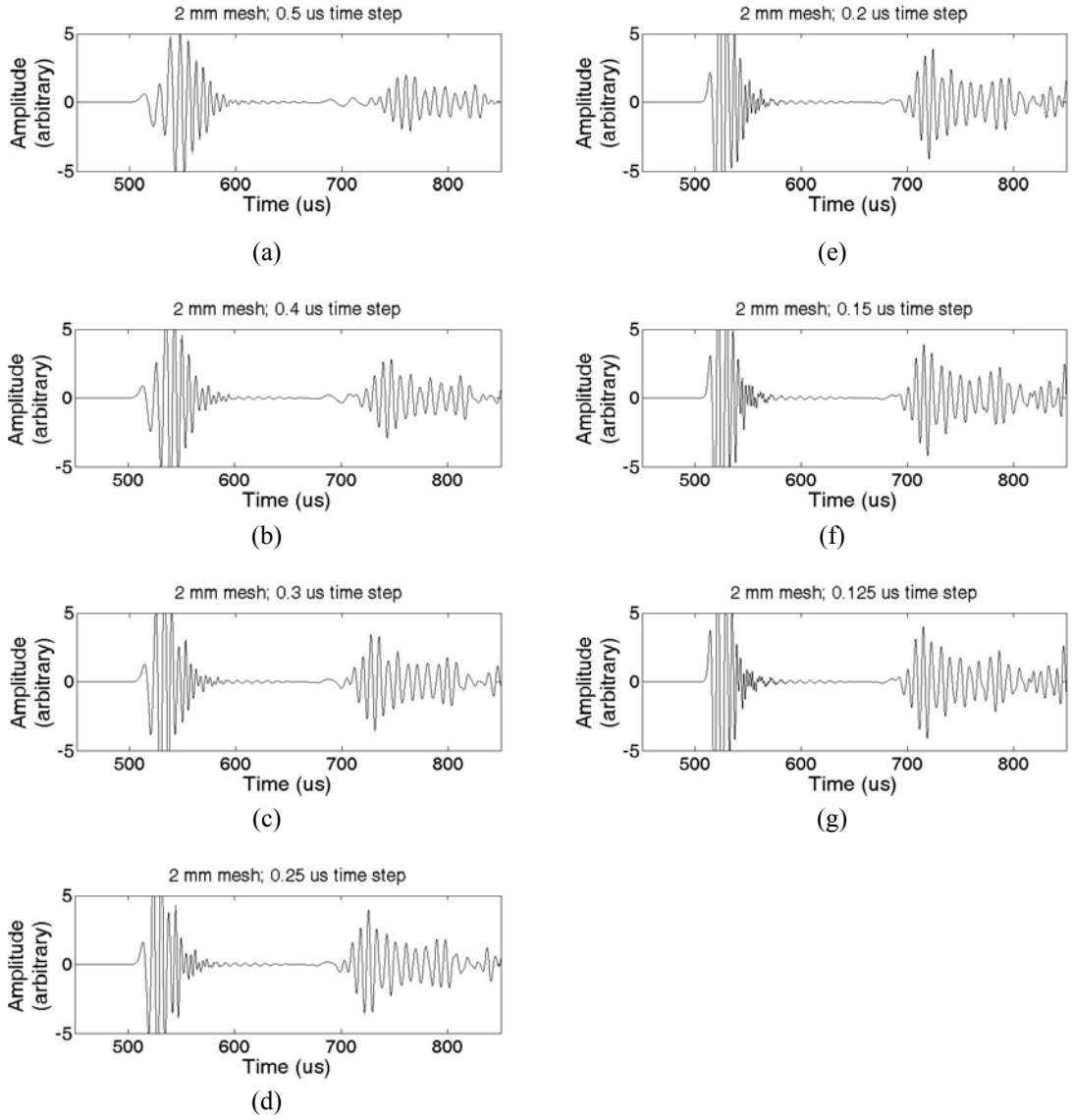

Figure B.7: Convergence study results obtained using a 2 mm quadratic element (1 mm spacing between nodes). (a) 0.5 μs time steps. (b) 0.4 μs time steps. (c) 0.3 μs time steps. (d) 0.25 μs time steps. (e) 0.2 μs time steps. (f) 0.15 μs time steps. (g) 0.125 μs time steps. (The model with 0.1 μs time steps did not finish within the maximum run time allowed on the university clusters.)

In each set of results (Figures B.4 through B.7), a progressively smaller time step size produces a simulated waveform with more defined reflections. In all four cases, the arrival time and amplitude of the reflection from the end of the bar changes significantly as the time step size is reduced from 0.5 μs to 0.25 μs. Using a time step of 0.2 μs is only slightly better compared to using a time step of 0.25 μs. Reducing the time step size further below 0.25 μs or 0.2 μs has very little effect on the simulated waveforms (especially when a sufficiently small element size is used).

When selecting the final combination of element size and time step size, there has to be some trade off between accuracy and solution time. The 4 mm element size was chosen over the 2 mm element size because the relatively small improvement in accuracy did not justify doubling both the model size and solution time. When using a 4 mm element size, time step sizes of 0.25 μs and 0.2 μs (Figure B.6) produced very similar results. A time step size of 0.25 μs was ultimately chose for a 20% faster solution. In the end, the convergence study confirmed the choice of element size and time step size discussed in Section B.4.

APPENDIX C: DIGITAL SIGNAL PROCESSING

C.1 Convolution

In signal processing, the convolution of two signals expresses the amount of overlap which occurs as one signal is shifted over a second signal. Equations C.1 and C.2 give the mathematical definition for the convolution of discrete signal *f*[n] with discrete signal *g*[n], where n is the index of each point in the discrete signal. It is important to note two characteristics of the convolution. First, one of the discrete signals must be 'reflected' or 'folded' prior to performing the summation.[57] Second, the convolution is commutative. Thus, it does not matter which discrete signal is 'reflected' [155-157]. An example of the convolution of two discrete signals is shown in Figure C.1.

$$(f * g)[n] = \sum_k f[k] \cdot g[n-k] \tag{C.1}$$

$$(f * g)[n] = \sum_k f[n-k] \cdot g[k] \tag{C.2}$$

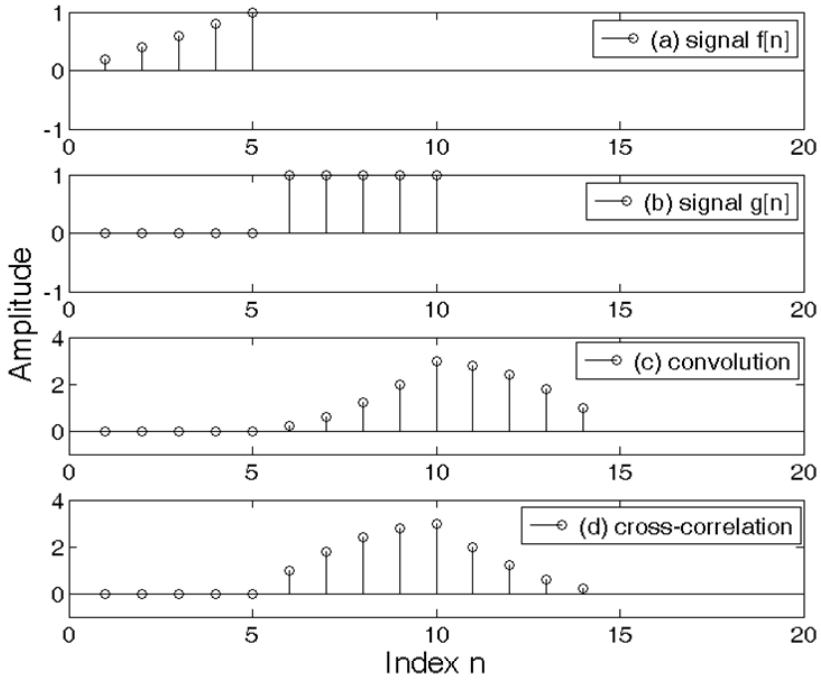

Figure C.1: Comparison of convolution and cross-correlation. (a) Discrete signal *f*[n]. (b) Discrete signal *g*[n]. (c) Convolution of *f*[n] with *g*[n]. (d) Cross-correlation of *f*[n] and *g*[n].

[57] The 'reflection' or 'folding' is indicated by the –k term.

C.2 Cross-correlation

The cross-correlation is a measure of the similarity of two signals. The cross-correlation is very similar to the convolution. However, neither signal is 'reflected' in the cross-correlation calculation. Equation C.3 gives the mathematical definition for the cross-correlation of discrete signals *f*[n] and *g*[n]. The $\bar{f}$ indicants calculating the complex conjugate of *f*. For signals with all real values, there are no imaginary terms, and Equation C.3, reduces to Equation C.4 [155,158]. An example of the cross-correlation of two discrete signals is included in Figure C.1.

$$(f \star g)[n] = \sum_k \bar{f}[n+k] \cdot g[k] \tag{C.3}$$

$$(f \star g)[n] = \sum_k f[n+k] \cdot g[k], \text{ if all real values} \tag{C.4}$$

From Equations C.1 and C.3, it can be shown than the cross-correlation of discrete signals *f*[n] and *g*[n] is equivalent to convolution of the reflected complex conjugate of *f*[n] with *g*[n].[58] For signals with all real values, there are no imaginary terms, and Equation C.5, reduces to Equation C.6 [158].

$$(f \star g)[n] = \sum_k \bar{f}[n+k] \cdot g[k] = \bar{f}[-n] * g[n] \tag{C.5}$$

$$(f \star g)[n] = f[-n] * g[n], \text{ if all real values} \tag{C.6}$$

Implementation

When using a program such as MATLAB [159] to calculate the cross-correlation, it is important to understand the assumptions inherent to the MATLAB commands. In MATLAB, there is a 'cross-correlation' function called 'xcorr.' However, it is critically important to realize that the 'xcorr' command is not identical to Equation C.3 or C.4. The 'xcorr' command only operates on sequences of equal length. Therefore, the shorter sequence is always zero padded. Thus, the output sequence always has a length of 2*m*-1, when *m* is the length of the longer sequence [160]. In the example shown in Figure C.2, the 5 element sequence *f*[n] is zero padded to match the length of the 10 element sequence *g*[n]. The output of the 'xcorr' command then has 19 elements.

[58] f[n] is intentionally reflected before it is run through the convolution algorithm which also performs a reflection. Thus, f[n] is ultimately reflected twice.

It is also important to pay attention to the syntax of the 'xcorr' command. Figure C.2c shows the results for xcorr(*f*,*g*). In this case, *g*[n] is stepped from left to right across *f*[n]. As shown in Figure C.2d, the syntax xcorr(*g*,*f*) steps *f*[n] from left to right across *g*[n]. It is important to note that this is different form the syntax of the convolution command ('conv') used to generate Figure C.1. For conv(*f*,*g*), *f*[-n] is stepped from left to right across *g*[n].

Because of the inherent behavior of the 'xcorr' command, an alternative algorithm must be used to obtain a cross-correlation without zero padding. As shown in Equation C.6, a convolution algorithm can be used to calculate the cross-correlation of real signals, if one of the signals is reflected before running the convolution algorithm. [59] Figure C.3, shows the results for the MATLAB command given in Equation C.7, where 'conv' performs the standard convolution algorithm and 'fliplr' reflects the input sequence prior to execution of the 'conv' command [160].

$$crosscorrelation = conv(fliplr(f), g) \tag{C.7}$$

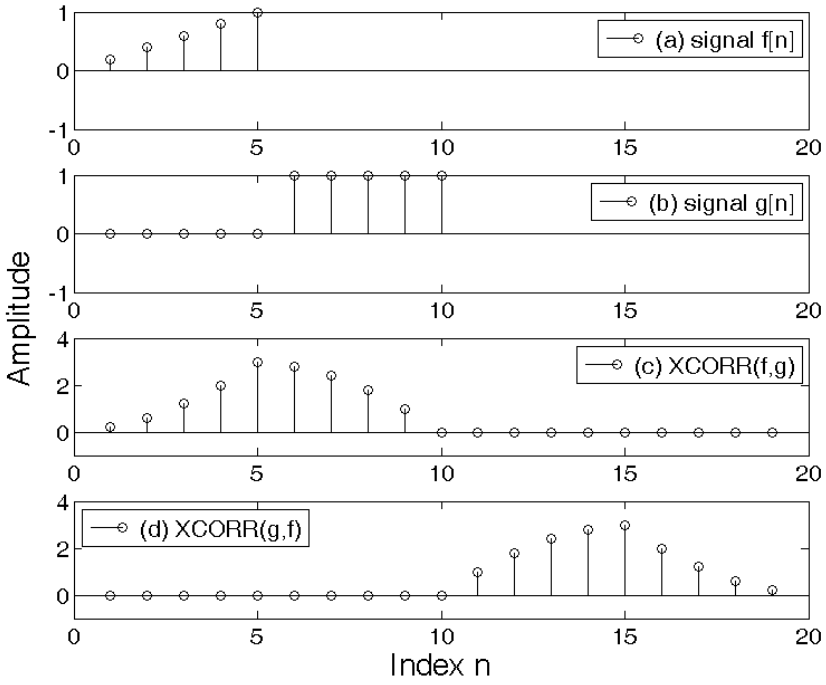

Figure C.2: Behavior of the 'xcorr' command in MATLAB. (a) Discrete signal *f*[n]. (b) Discrete signal *g*[n]. (c) Using the command xcorr(*f*,*g*), sequence *g*[n] is stepped from left to right across *f*[n]. (d) Using the command xcorr(*g*,*f*), sequence *f*[n] is stepped from left to right across *g*[n]. Note that the shorter sequence is always zero padded (to the left) when using the 'xcorr' command.

[59] Again, f[n] is intentionally reflected before it is run through the convolution algorithm where a second reflection takes place. Thus, f[n] is reflected twice.

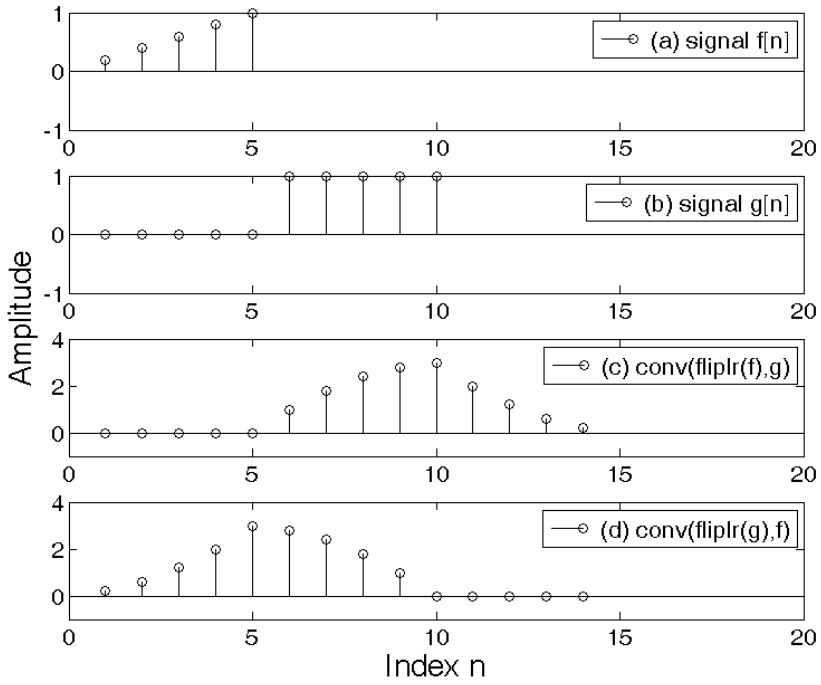

Figure C.3: Cross-correlation using the 'conv' and 'fliplr' commands in MATLAB. (a) Discrete signal *f*[n]. (b) Discrete signal *g*[n]. (c) Using the command conv(fliplr(*f*),*g*), sequence *f*[n] is stepped from left to right across *g*[n]. (d) Using the command conv(fliplr(*g*),*f*), sequence *g*[n] is stepped from left to right across *f*[n]. By introducing the second reflection of the first sequence, the commutative property of the convolution is lost.

The results shown in Figure C.3c match the results shown in Figure C.2d except that the Figure C.3c results do not include the zero padding. Since there is no zero padding, the output of the conv(fliplr(*f*),*g*) syntax has a length of *l*+*m*-1, where *l* and *m* are the length of each sequence. In the example shown in Figure C.3, the sequence *f*[n] has 5 elements and the sequence *g*[n] has 10 elements. The output of the conv(fliplr(*f*,*g*)) syntax then has 14 elements.

Figure C.3d shows the output of the conv(fliplr(*g*),*f*) syntax. Because the first sequence is reflected twice, the calculation for determining the cross-correlation is not commutative.

Application

Marioli et al. [161] and El Guerjouma et al. [162] have suggested using the cross-correlation technique for measuring time-of-flight between the reflections in ultrasonic signals. However, the results obtained by performing a cross-correlation calculation

depend on the characteristics of the signal studied. The work by Srinivasan et al. [163] shows several cases where a very sharp spike results from the cross-correlation calculation. As an example, Figure C.4 shows a contrived signal where the cross-correlation results are calculated for a chirp signal with a sinusoidal envelope. Both chirps are identical. Thus, there is high correlation for a certain point in the cross-correlation calculation.

In contrast, Queiros et al. [164] showed that dispersive waves do not yield cross-correlation results containing a sharp spike. Figure C.5 shows an example of a contrived signal simulating the results for a dispersive type wave. Notice that the signals contained in *f*(t) and *g*(t) have significantly different shapes. Since the cross-correlation is a measure of the similarity of two signals, a high correlation should not be expected for dissimilar signals.

Toiyama and Hayashi [165] have also reported on the difficulties associated with the measurement on dispersive waves. In their work, Toiyama and Hayashi proposed modifying the cross-correlation by including a dispersion compensation algorithm based on the change in wave number versus angular frequency. The main limitation in this work was that the dispersion curve information had to be calculated a priori. Thus, this compensation strategy would be of limited use for studying unknown defects types.

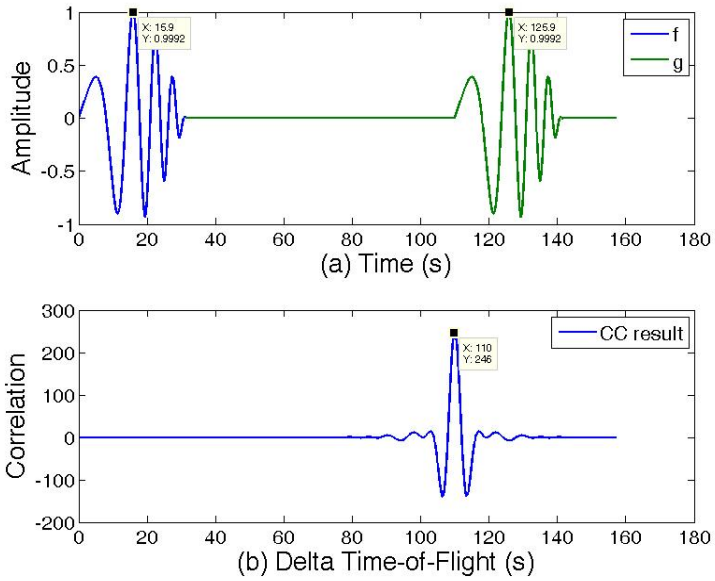

Figure C.4: Example of cross-correlation for a chirp signal with a sinusoidal envelope. (a) Discrete signals *f*[n] and *g*[n]. (b) Cross-correlation results using the command conv(fliplr(*f*),*g*). The peak in (b) represents the time-of-flight difference between the two chirps.

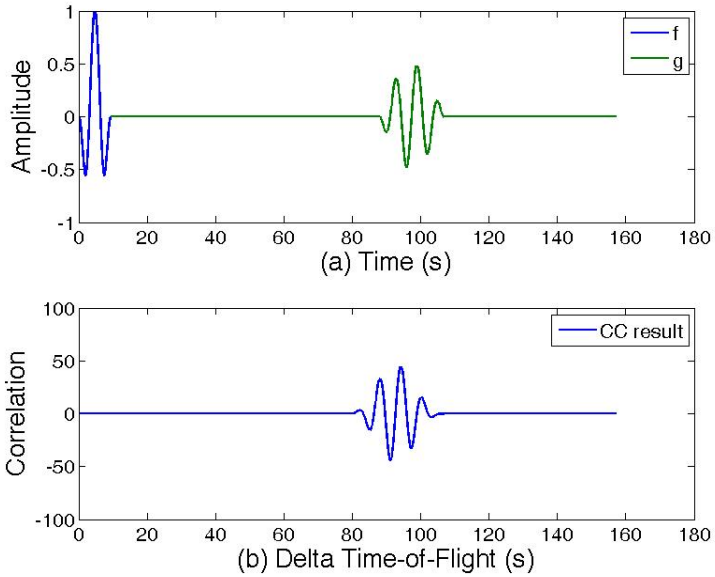

Figure C.5: Example of cross-correlation for a simulated dispersive wave. (a) Discrete signals *f*[n] and *g*[n]. (b) Cross-correlation results using the command conv(fliplr(*f*),*g*). Since the waveforms are dissimilar by definition, the cross-correlation results are poor.

C.3 Analytic Signal

A threshold crossing can be used to determine the arrival time of a signal. However, the recorded arrival time can jump by one period as the signal amplitude varies [166]. To solve this problem, the envelope of the signal is often used instead of the actual signal.

Duncan [167,168] and others have determined the envelope of a signal by calculating the analytic signal of the data. Equation C.8 shows that the analytic signal $S_a(t)$ is composed of the original signal $S(t)$ and the Hilbert Transform, $\hat{S}(t)$, of the original signal. The envelope of the signal $A(t)$ is then found by calculating the amplitude of $S_a(t)$ as shown in Equation C.9.

$$S_a(t) = S(t) + i\hat{S}(t) \tag{C.8}$$

$$A(t) = \left|S_a(t)\right| = \sqrt{S^2(t) + \hat{S}^2(t)} \tag{C.9}$$

When working with the analytic signal, it is valuable to note that determining the Hilbert Transform requires both a direct and inverse Fourier Transform [155,169]. Thus, the envelope is based on sinusoidal components [170]. Also, the definition of the analytic signal assumes that the signal is analytic. To be analytic, a signal must have no

negative frequency content. However, "practical signals are purely real" and have a "negative frequency component for every positive frequency component" [171].

Implementation

MATLAB includes the 'hilbert' command [160] which returns a vector of complex numbers for a real input signal $S(t)$. The data contained in the vector of complex numbers is formatted such that the real values are equal to $S(t)$ and the imaginary values are equal to $\hat{S}(t)$. The algorithm uses a one sided Fourier Transform so that all negative frequency components are made zero. Thus, the 'hilbert' command returns $S_a(t)$ as defined in Equation C.8. The envelope of the signal is then determined by calculating the absolute value $S_a(t)$. Equation C.10 shows the MATLAB syntax for calculating the envelope of a signal S based on the analytic signal.

$$A = abs(hilbert(S)) \tag{C.10}$$

Discussion

Figure C.6 shows the envelopes calculated for hypothetical sinusoidal signals which have the function sin(x+φ)*sin(x/3). The φ term allows a phase shift of the signal under the sin(x/3) envelope. In this case, the envelopes derived from the analytic signal match the sin(x/3) envelope defined in the hypothetical signals.

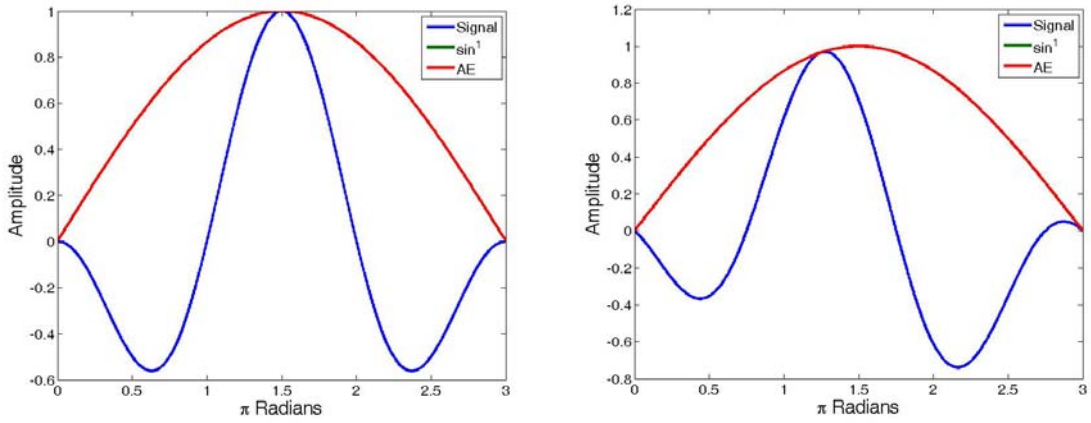

Figure C.6: Analytic envelopes (AE) for a hypothetical signal containing a sin(x/3) envelope function. (a) 1.5 cycle signal with 0° phase shift. (b) 1.5 cycle signal with 22.5° phase shift. The analytic envelopes derived from the analytic signal are directly on top of the actual sin(x/3) envelope.

Figure C.7 shows the envelopes calculated for hypothetical sinusoidal signals which have the function $\sin(N*x+\varphi)*\sin^2(x/3)$. As before, the φ term allows a phase shift under the $\sin^2(x/3)$ envelope. For Figures C.7a and C.7b, N=1 was used to obtain 1.5 cycles under the $\sin^2(x/3)$ envelope. For Figure C.7c and C.7d, N=3 was used to obtain 4.5 cycles under the $\sin^2(x/3)$ envelope.

In the results shown in Figure C.7a, the analytic envelope derived from the analytic signal has a slightly different shape compared to the prescribed $\sin^2(x/3)$ envelope. However, the maximum amplitude of analytic envelope occurs as the same index of the maximum amplitude of the prescribed $\sin^2(x/3)$ envelope. In the results shown in Figure C.7b, a phase shift of 22.5° under the envelope produces an analytic envelope which does not match the prescribed $\sin^2(x/3)$ envelope. In this case, the 22.5° phase shift causes the maximum amplitude of analytic envelope to be shifted by 20 bins ($\approx 0.060*\pi$ radians) relative to the maximum on the $\sin^2(x/3)$ envelope.

In figures C.7c and C.7d, the number of cycles under the envelope was increased to 4.5. In both cases, the analytic envelope derived from the analytic signal is in very good agreement with the prescribed $\sin^2(x/3)$ envelope. In Figure C.7d, the 22.5° phase shift results in the maximum amplitude of analytic envelope to be shift by only 1 bin ($\approx 0.003*\pi$ radians) relative to the maximum on the $\sin^2(x/3)$ envelope.

Figure C.8 shows the envelopes calculated for hypothetical sinusoidal signals which have the function $\sin(N*x+\varphi)*\sin^{1/2}(x/3)$. As before, the φ term allows a phase shift under the $\sin^{1/2}(x/3)$ envelope. For Figures C.8a and C.8b, N=1 was used to obtain 1.5 cycles under the $\sin^{1/2}(x/3)$ envelope. For Figure C.8c and C.8d, N=3 was used to obtain 4.5 cycles under the $\sin^{1/2}(x/3)$ envelope.

The results shown in Figure C.8 indicate that the envelopes derived from the analytic signal are less accurate in this case. The test cases with 0° phase shift continued to produce a maximum amplitude at the same index of the prescribed $\sin^{1/2}(x/3)$ envelope (Figures C.8a and C.8c). However, the test cases with 22.5° phase shift showed increased deviation. The maximum amplitude from the 1.5 cycle signal (Figure C.8b) was shifted 47 bins ($\approx 0.141*\pi$ radians) relative to the maximum on the $\sin^{1/2}(x/3)$ envelope. The maximum amplitude from the 1.5 cycle signal (Figure C.8b) was shifted 10 bins ($\approx 0.030*\pi$ radians) relative to the maximum on the $\sin^{1/2}(x/3)$ envelope.

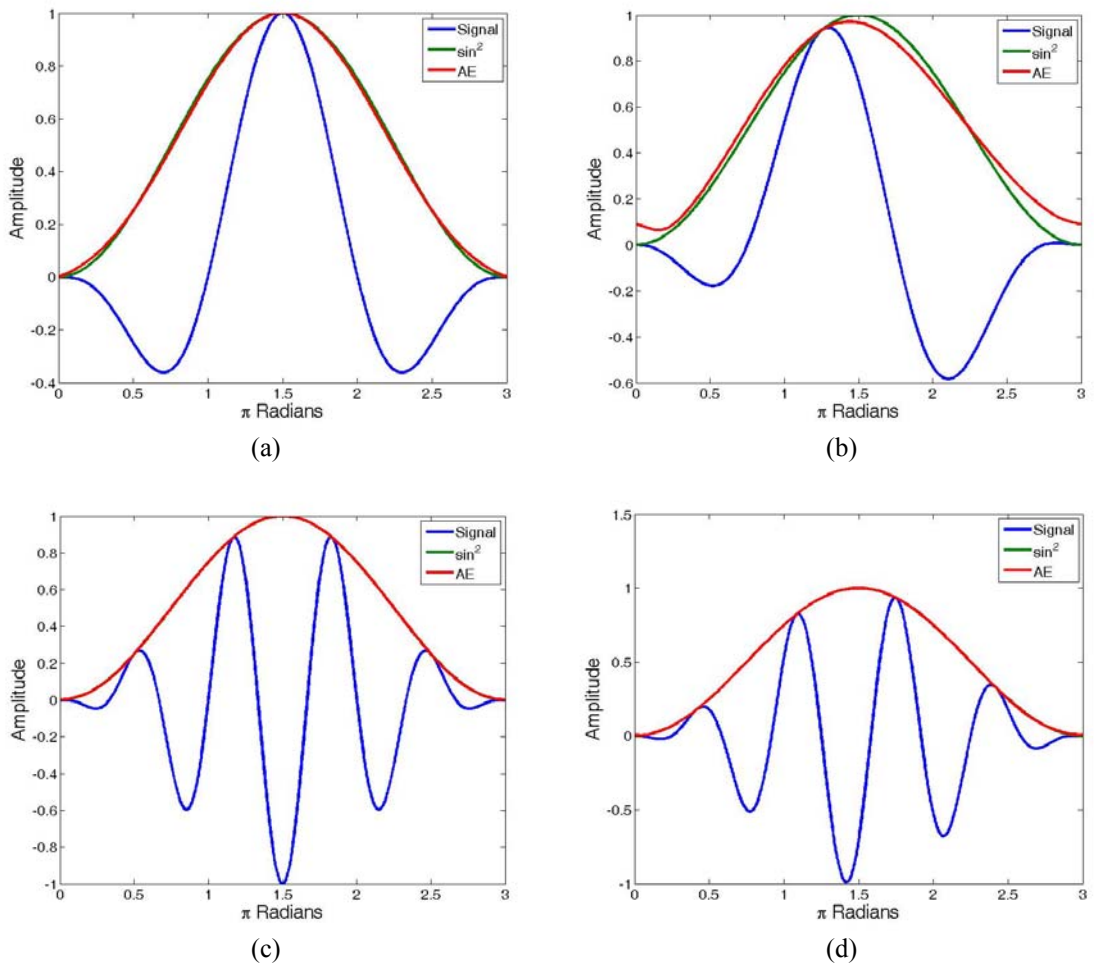

Figure C.7: Analytic envelopes (AE) for a hypothetical signal containing a $\sin^2(x/3)$ envelope function. (a) 1.5 cycle signal with 0° phase shift. (b) 1.5 cycle signal with 22.5° phase shift. (c) 4.5 cycle signal with 0° phase shift. (d) 4.5 cycle signal with 22.5° phase shift. The analytic envelopes derived from the analytic signal show a small deviation from the applied $\sin^2(x/3)$ envelope. Increasing the number of cycles decreases the deviation.

In Figure C.8, increasing the number of cycles under the envelope (from 1.5 to 4.5) reduced the absolute difference between the analytic signal and the prescribed $\sin^{1/2}(x/3)$ envelope. However, the increased number of cycles did not necessarily improve the overall shape of the analytic envelope. As shown in Figure C.8c, the analytic envelope was less "smooth," containing more inflection points compared to Figure C.8a.

Figure C.9 shows the envelopes calculated for hypothetical sinusoidal signals which have the function sin(N*x+φ)*sin(x/3)*(1-N/(3*pi)). The (1-N/(3*pi)) term was add to produce an asymmetric envelope. As before, the φ term allows a phase shift under

the sin(x/3)*(1-N/(3*pi))envelope. For Figures C.9a and C.9b, N=1 was used to obtain 1.5 cycles under the sin(x/3)*(1-N/(3*pi))envelope. For Figure C.9c and C.9d, N=3 was used to obtain 4.5 cycles under the sin(x/3)*(1-N/(3*pi))envelope.

In general, the analytic envelopes shown in Figure C.9 are relatively close to the prescribed sin(x/3)*(1-N/(3*pi)) envelope. However, there was now a small difference in the location of the maximum amplitude found via the analytic envelope for the 0° phase shift cases. The differences in the observed location of the analytic envelope's maximum value are summarized in Table C.1.

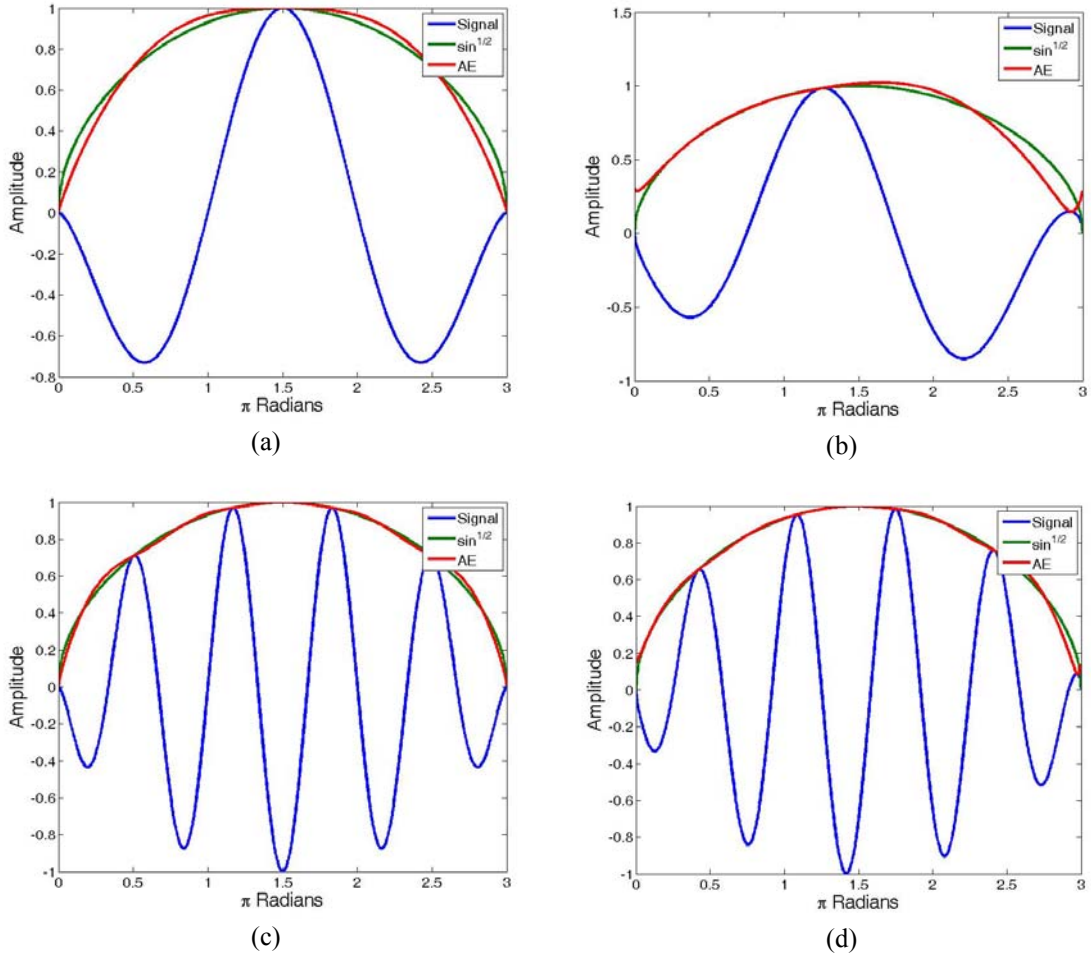

Figure C.8: Analytic envelopes (AE) for a hypothetical signal containing a $\sin^{1/2}(x/3)$ envelope function. (a) 1.5 cycle signal with 0° phase shift. (b) 1.5 cycle signal with 22.5° phase shift. (c) 4.5 cycle signal with 0° phase shift. (d) 4.5 cycle signal with 22.5° phase shift. The analytic envelopes derived from the analytic signal show a small deviation from the applied $\sin^{1/2}(x/3)$ envelope. Increasing the number of cycles decreases the relative difference between the analytic envelope and the $\sin^{1/2}(x/3)$ envelope, but did not necessarily improve the overall shape.

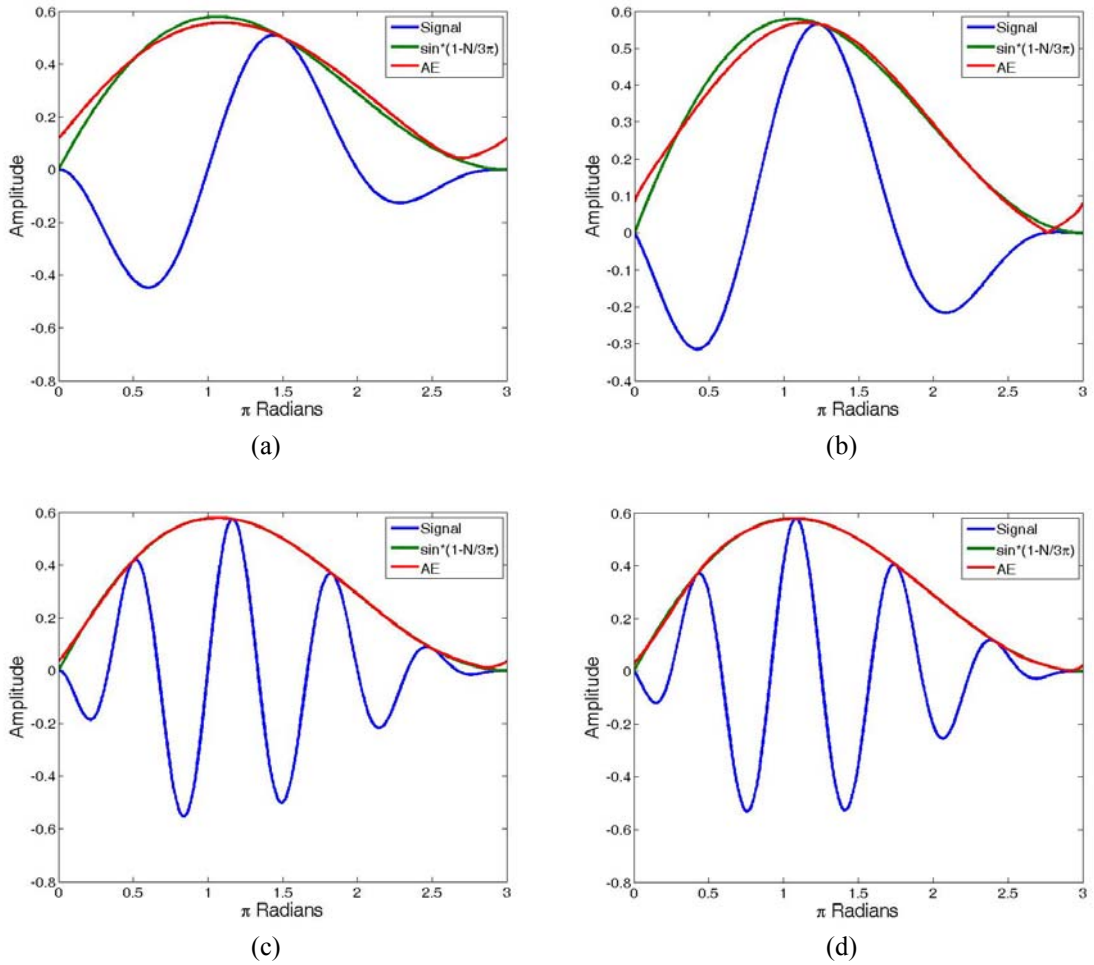

Figure C.9: Analytic envelopes (AE) for a hypothetical signal containing a sin(x/3)*(1-N/(3*pi)) envelope function. (a) 1.5 cycle signal with 0° phase shift. (b) 1.5 cycle signal with 22.5° phase shift. (c) 4.5 cycle signal with 0° phase shift. (d) 4.5 cycle signal with 22.5° phase shift. The analytic envelopes derived from the analytic signal show a small deviation from the applied sin(x/3)*(1-N/(3*pi)) envelope. Increasing the number of cycles decreases the deviation.

Table C.1: Deviation observed between the applied envelope function and the analytic envelope determined via the analytic signal calculation. (1 bin ≈ 0.003*π radians)

	Deviation from applied envelope (bins)			
	1.5 cycle signal		4.5 cycle signal	
	0° phase	22.5° phase	0° phase	22.5° phase
sin(x/3) envelope	0	0	0	0
$\sin^2(x/3)$ envelope	0	20	0	1
$\sin^{1/2}(x/3)$ envelope	0	47	0	10
sin (x/3)*(1-N/(3*pi)) envelope	12	28	3	7

Figures C.10 and C.11 show a few examples of the analytic envelopes calculated for simulated signals containing multiple reflections. The results for Figures C.10b and C.11b indicated that spacing between the simulated reflections did not affect the location of the maximum values in the analytic envelope. In contract, the results for Figures C.10c and C.11c indicated that a phase shift in one of the reflections did produce a small change in the location of the maximum values in the analytic envelope.

Further studies should more closely examine the relationship between the analytic envelope and the envelope of guided wave signals where group and phase velocities are not equal. The results shown here and in Chapter 6, suggest that there may be some deviation between the envelope obtained from the analytic signal and the actual envelope of the data.

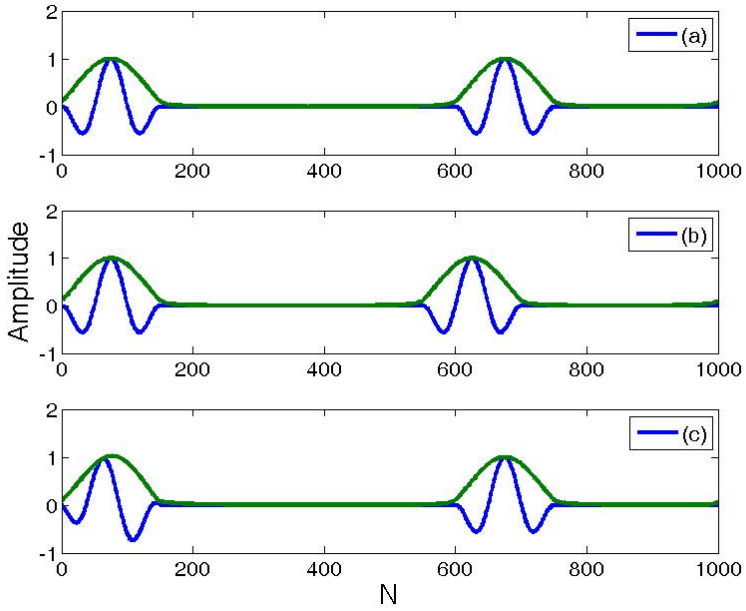

Figure C.10: Analytic envelopes (AE) for a hypothetical signal containing two reflections containing 1.5 cycles. (a) Reference signal with a simulated time-of-flight = 600 'steps' in the discrete signal. (b) Signal with a simulated time-of-flight = 550 'steps in the discrete signal. A pure time-of-flight shift does not appear to affect the analytic envelope in this case. (c) Signal with a simulated time-of-flight = 600 'steps in the discrete signal and a $\pi/4$ phase shift in the first reflection. In this case, there is a 2 bin change in the spacing on the maximum amplitudes in the analytic envelope.

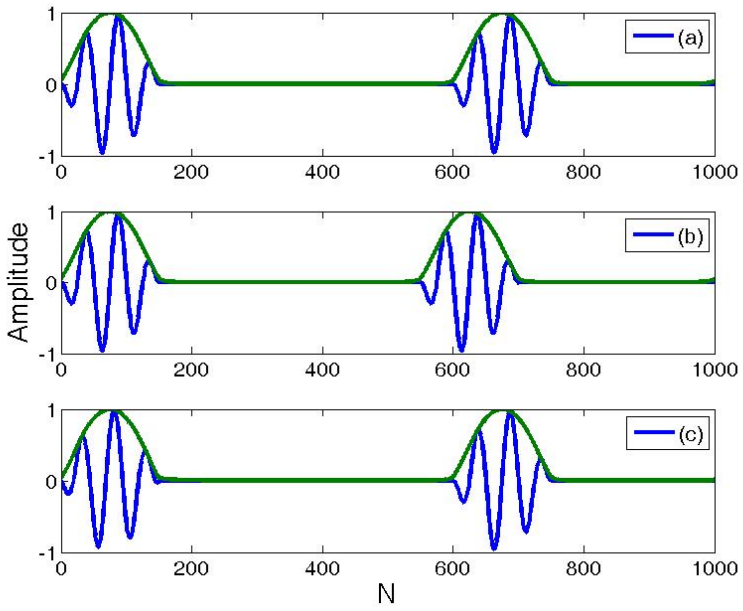

Figure C.11: Analytic envelopes (AE) for a hypothetical signal containing two reflections containing 4.5 cycles. (a) Reference signal with a simulated time-of-flight = 600 'steps' in the discrete signal. (b) Signal with a simulated time-of-flight = 550 'steps in the discrete signal. A pure time-of-flight shift does not appear to affect the analytic envelope in this case. (c) Signal with a simulated time-of-flight = 600 'steps in the discrete signal and a $\pi/4$ phase shift in the first reflection. In this case, there is a 1 bin change in the spacing on the maximum amplitudes in the analytic envelope.

APPENDIX D: TEMPERATURE DEPENDENCE

D.1 Lamb Waves

In Chapter 5, the guided wave propagation in a rectangular bar was discussed. As Figures 5.8 through 5.10 showed, it was theoretically possible to select a guided wave mode and frequency where there was minimal change in the group velocity as a function of temperature. For the sake of comparison, a similar analysis of Lamb wave propagation in a plate is presented in this appendix.

As discussed in Chapter 2, all wave propagation in solids is governed by the Navier-Cauchy equations. For a homogeneous, isotropic medium, Equation D.1 shows the Navier-Cauchy equations in Cartesian coordinates using vector notation, where λ_{Lame} is Lame's constant, E is elastic modulus, G is shear modulus, ρ is density, $\bar{u}$ is the displacement vector, and t is time [34-36].

$$(\lambda_{Lame}+G)\nabla\nabla\bullet\bar{u}+G\nabla^2\bar{u}=\rho\frac{\partial^2\bar{u}}{\partial t^2} \tag{D.1}$$

$$\text{where: } \lambda_{Lame}=\frac{G(2G-E)}{E-3G}$$

For an infinitely wide plate, the boundary conditions are such that the Equation D.1 can be reduced to the form given in the Rayleigh-Lamb equations. Equation D.2 describes the equation for symmetric modes in a plate, and Equation D.3 describes the anti-symmetric modes in a plate. For the Rayleigh-Lamb equations, C_L is bulk longitudinal velocity, C_T is bulk shear velocity, C_p is phase velocity, k is the wave number, h is the half thickness (h=d/2), and ω is angular frequency [34,35]. As long as the plate is much wider than the wavelength of ultrasonic waves, the Rayleigh-Lamb equations are acceptable for describing guided waves in practical plate applications [34].

$$\frac{\tan(qh)}{q}+\frac{4k^2p\cdot\tan(ph)}{(q^2-k^2)^2}=0 \quad \text{symmetric modes} \tag{D.2}$$

$$q\cdot\tan(qh)+\frac{(q^2-k^2)^2\cdot\tan(ph)}{4k^2p}=0 \quad \text{anti-symmetric modes} \tag{D.3}$$

$$\text{where: } p^2=\left(\frac{\omega}{C_L}\right)^2-k^2=\left(\frac{\omega}{C_L}\right)^2-\left(\frac{\omega}{C_p}\right)^2$$

$$\text{and } q^2=\left(\frac{\omega}{C_T}\right)^2-k^2=\left(\frac{\omega}{C_T}\right)^2-\left(\frac{\omega}{C_p}\right)^2$$

Since there is no closed form solution to the Rayleigh-Lamb equations, a numerical root finding technique is typically utilized to determine the phase velocity dispersion curves described by Equations D.2 and D.3. Group velocity (C_g) dispersion curves can then be determined from the phase velocity solution via Equation D.4 where *fd* denotes frequency times thickness [34]. The group velocity determines the time-of-flight observed in experimental measurements.

$$C_g = C_p^2 \left[C_p - (fd) \frac{\partial C_p}{\partial (fd)} \right]^{-1} \tag{D.4}$$

In addition to group velocity, the wave structure for each guided wave mode can be determined from the phase velocity data. Equations D.5 and D.6 describe the in-plane and out-of-plate displacement for symmetric modes, respectively.

$$u_s = u_1 = ik \cdot \cos(p \cdot x_3) + q \cdot \cos(q \cdot x_3) \tag{D.5}$$

$$w_s = u_3 = -p \cdot \sin(p \cdot x_3) - ik \cdot \sin(q \cdot x_3) \tag{D.6}$$

Equations D.7 and D.8 describe the in-plane and out-of-plate displacement for anti-symmetric modes, respectively. In equations D.5 through D.8, x_3 represents a position within the thickness of the plate ($-d/2 \leq x_3 \leq d/2$).

$$u_a = u_1 = ik \cdot \sin(p \cdot x_3) - q \cdot \sin(q \cdot x_3) \tag{D.7}$$

$$w_a = u_3 = p \cdot \cos(p \cdot x_3) - ik \cdot \cos(q \cdot x_3) \tag{D.8}$$

Aluminum Plate Example

In order to validate the numerical solution of the Rayleigh-Lamb equations, a test case was required where there are published results for comparison. Since Aluminum plates are frequently studied in the literature, an Aluminum plate was selected to validate the MATLAB code. Figure D.1 shows phase and group velocity curves for an Aluminum plate. The results shown in Figure D.1 match the dispersion curves for an Aluminum plate published by Rose [34].

Wave structures were also calculated for the Aluminum test case. Selected results for the S0 and A0 modes are shown in Figures D.2 and D.3, respectively. The wave structures from this calculation are also in agreement with the wave structures published by Rose [34].

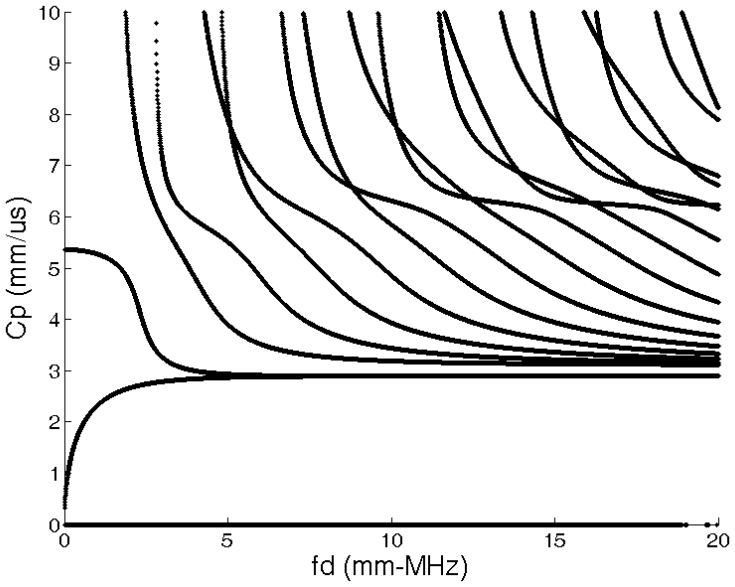

(a)

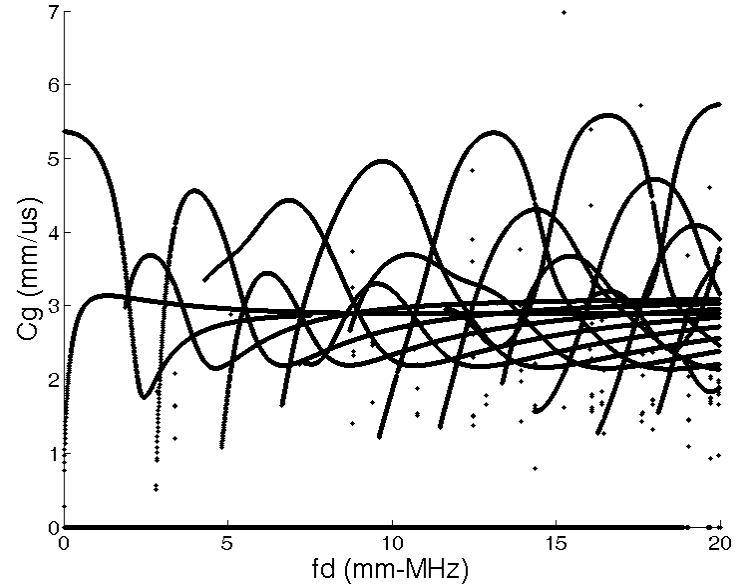

(b)

Figure D.1: Dispersion curves for an Aluminum plate. (a) Phase velocity dispersion curve. (b) Group velocity dispersion curve. Results are in agreement with the dispersion curves published by Rose [34].

Additional dispersion curves where then calculated to examine how the dispersion curves for Aluminum plates varied as a function of temperature. Figure D.4 shows the dispersion curves for an Aluminum plate at 295K, 500K, and 700K. As figure D.4 shows, the dispersion curves shift down and are compressed to the left (lower

frequencies) as temperature increases. Because the material properties of Aluminum are not linear with temperature,[60] the Aluminum curves shift more at higher temperatures (i.e. between 500K and 700K) then at lower temperatures (i.e. between 295K and 500K). Although Aluminum cannot be used to make a direct comparison to the Zircaloy bar results in Chapter 5, the dispersion curves shown in Figure D.4 do not appear to exhibit a point where group velocity is not significantly affected by a change in temperature.

Figure D.5 shows a few selected wave structures at various temperatures. There does not appear to be a large change in wave structure versus temperature at *fd*=0.5.

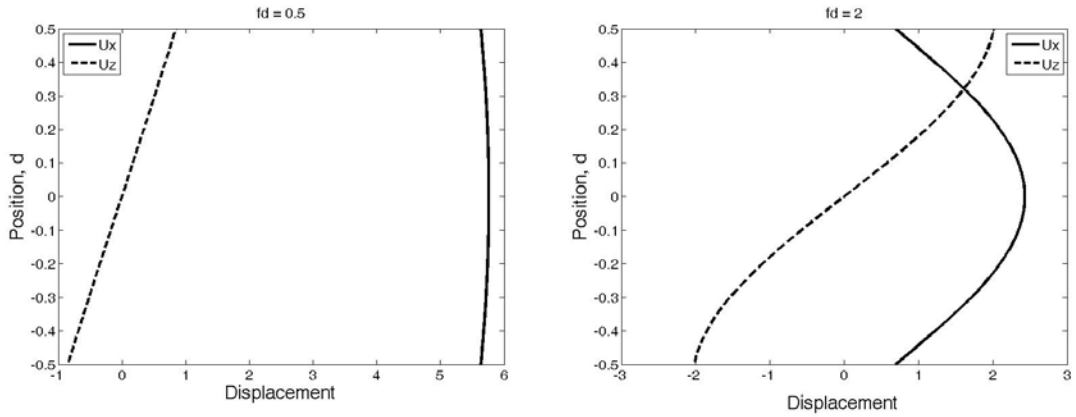

(a) (b)

Figure D.2: Selected wave structures of the S0 mode. (a) Wave structures at *fd*=0.5. (b) Wave structures at *fd*=2.0. Ux is the in-plane displacement, and Uz is the out-of-plane displacement. Results are in agreement with the dispersion curves published by Rose [34].

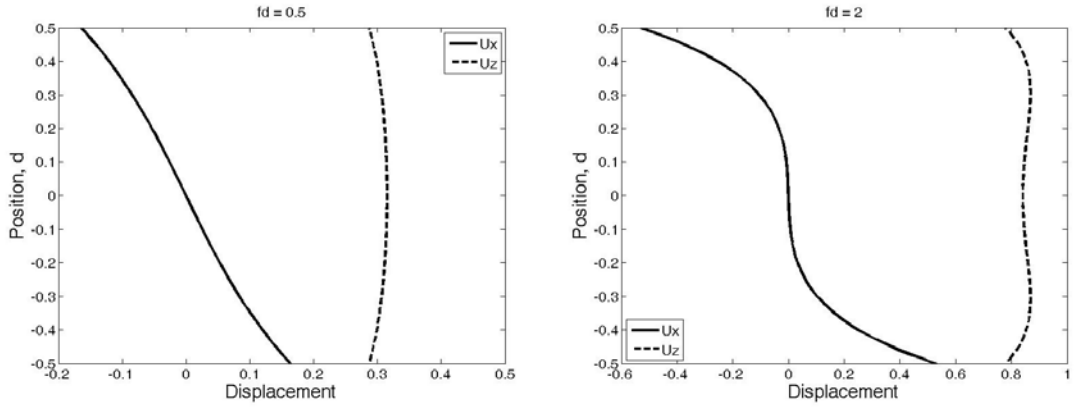

(a) (b)

Figure D.3: Selected wave structures of the A0 mode. (a) Wave structures at *fd*=0.5. (b) Wave structures at *fd*=2.0. Ux is the in-plane displacement, and Uz is the out-of-plane displacement. Results are in agreement with the dispersion curves published by Rose [34].

[60] As discussed in Appendix A.

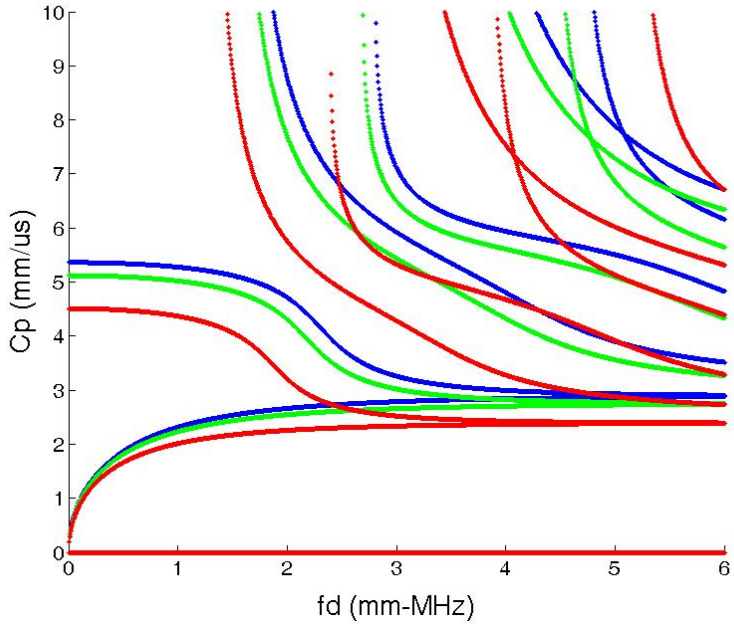

(a)

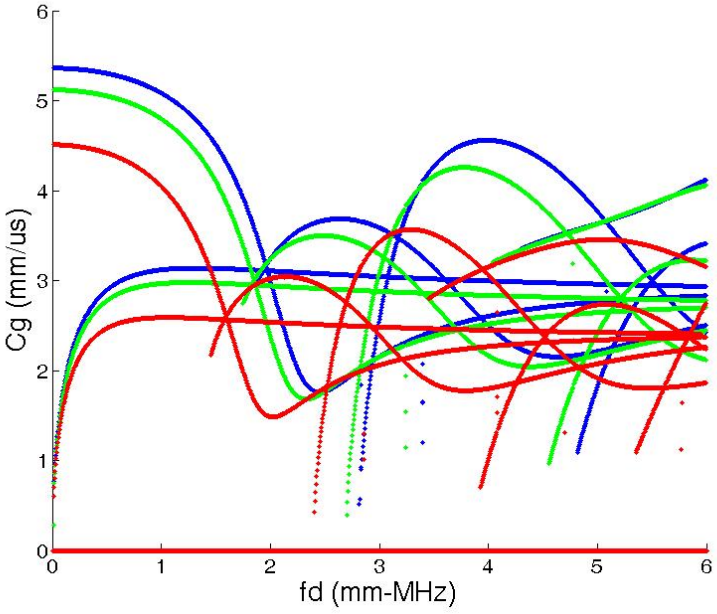

(b)

Figure D.4: Dispersion curves for an Aluminum plate at selected temperatures. (a) Phase velocity dispersion curve. (b) Group velocity dispersion curve. Blue line is at 295K. Green line is at 500K. Red line is at 700K. The spacing between the dispersion curves is not equal because of the nonlinear change in the material properties of Aluminum as a function of temperature.

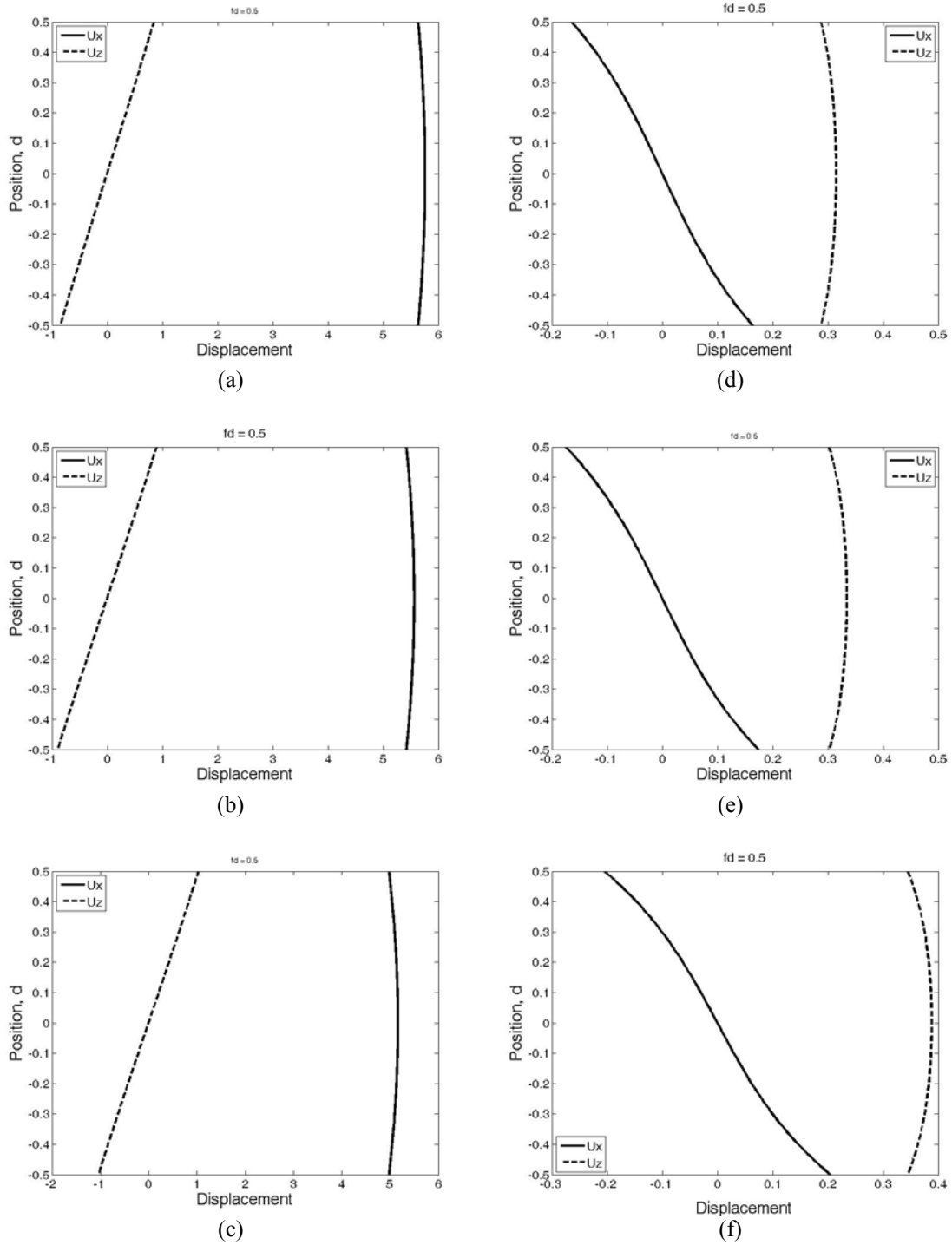

Figure D.5: Comparison of wave structures for an Aluminum plate as a function of temperature at *fd*=0.5. (a) S0 mode at 295K. (b) S0 mode at 500K. (c) S0 mode at 700K. (d) A0 mode at 295K. (e) A0 mode at 500K. (e) A0 mode at 700K. Ux is the in-plane displacement, and Uz is the out-of-plane displacement. The wave structures for both the S0 and A0 modes do not change significantly at *fd*=0.5.

Zircaloy Plate Example

Dispersion curves where then calculated to examine how the dispersion curves for a Zircaloy plate varied as a function of temperature. Figure D.6 shows the dispersion curves for a Zircaloy plate at 295K, 500K, and 700K. As figure D.6 shows, the dispersion curves shift down and are compressed to the left (lower frequencies) as temperature increases. Because the material properties of Zircaloy are relatively linear with temperature,[61] the shift in the dispersion curves is uniform with respect to temperature.

On one-hand, the basic trend of the dispersion curves being shifted down and compressed to the left is consistent with the results for the Zircaloy bar given in Chapter 5. However, the results in Figure D.6b do not show a frequency value where the curves for all three temperatures intersect at the same point.[62] The results shown in Figures 5.8 through 5.10 appear to be inherent to the rectangular cross-section.

[61] As discussed in Appendix A.
[62] When looking at the mode with the highest group velocity at that frequency.

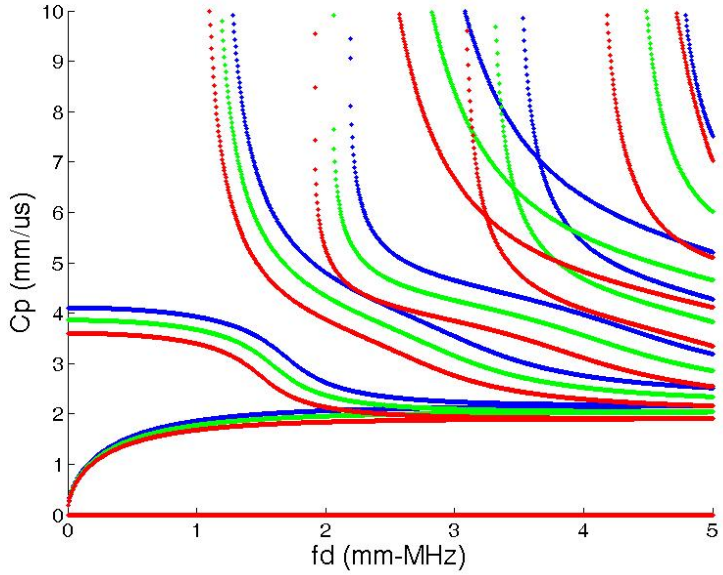

(a)

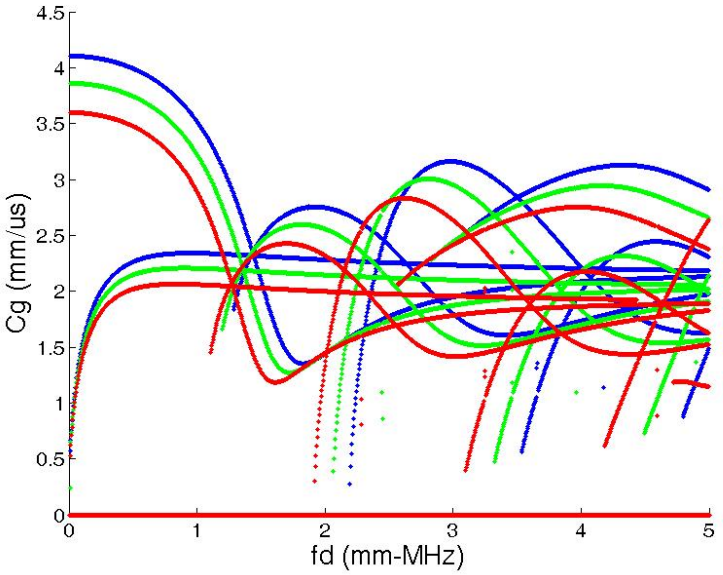

(b)

Figure D.6: Dispersion curves for a Zircaloy plate at selected temperatures. (a) Phase velocity dispersion curve. (b) Group velocity dispersion curve. Blue line is at 295K. Green line is at 500K. Red line is at 700K. Results do not indicate the existence of a frequency when the group velocity does not change significantly with temperature.

APPENDIX E: NON-TECHNICAL ABSTRACT

In nuclear power plants, radiation and high temperatures act to degrade various components over time. With accurate knowledge of how materials behave in a reactor environment, both the design and maintenance of nuclear power plants can be better engineered to improve safety and reliability.

The degradation of materials is typically studied by performing accelerated life testing in a materials and test reactor. Much of the information found through accelerated life testing involves measurements which require the specimen to be removed from the test reactor and transported to a special test facility. This process can be very costly and data collection is limited to the reactor schedule. In addition, data are not obtained under realistic operating condition.

Because of these drawbacks, this work has sought to develop a technique based on ultrasonic waves which would allow some types of data to be collected continuously while the reactor is running. The basic concept is to send "guided" ultrasonic waves down a long wire to the specimen inside the reactor and then determine changes in the specimen based on changes in the ultrasonic signals received.

In this work, a theoretical analysis and experimental tests were performed on two types of specimens commonly used in accelerated life testing. The results for the "dog-bone" shaped creep specimens indicated that changes in length could be measured in real time. The results for the rectangular bar specimens were mixed. However, the proposed technique was sensitive to temperature changes in the bar specimens. Although addition work would be required, the technique could potentially be adapted to monitor critical structures for over heating.

REFERENCES

1. B.A. Ma, *Nuclear Reactor Materials and Applications*. (Van Nostrand Reinhold Co., New York, 1983).

2. S. Glasstone, *Nuclear Reactor Engineering*, 4th ed. (Chapman & Hall, New York, 1994).

3. J. Weisman, *Nuclear Reactors*. (Krieger, Malabar, FL, 1983).

4. J. Wood, *Nuclear Power*. (Inst. of Engr. Tech., London, 2007).

5. H.M. Hashemiam, *Maintenance of Process Instrumentation in Nuclear Power Plants*. (Springer-Verlag, Berlin, 2006).

6. F.M. Marshall, *Advanced test reactor capabilities and future operating plans*, Idaho National Laboratory / National Institute of Standards and Technology, (2005) http://www.ncnr.nist.gov/trtr2005/Proceedings/Marshall%20-%20ATR%20Capabilities%20and%20Plans%20text.pdf

7. R.V. Furstenau and S.B. Grover, *The advanced test reactor irradiation facilities and capabilities*, Idaho National Laboratory, (2007) http://www.inl.gov/technicalpublications/Documents/3634259.pdf

8. *Advanced Test Reactor (ATR) National Scientific User Facility Users' Guide*, Idaho National Laboratory, (2009) https://secure.inl.gov/atrproposal/documents/ATRUsersGuide.pdf

9. *Post Irradiation Examination Capabilities Guide*, Idaho National Laboratory, (2009) https://secure.inl.gov/atrproposal/documents/PIECapabilitiesGuide.pdf

10. R.A. Matzie, "The nuclear renaissance - implications on quantitative nondestructive evaluation," in *Review of Progress in Quantitative Nondestructive Evaluation*, edited by Thompson and Chimenti, AIP, **894**, 3-16 (2007).

11. A. Klein and J. Lance, "Future directions, challenges, and opportunities in nuclear engineering," in *Review of Progress in Quantitative Nondestructive Evaluation*, edited by Thompson and Chimenti, AIP, **894**, 32-38 (2007).

12. D.L. Kundson and J.L. Rempe, "Evaluation of LVDTs for use in ATR irradiation experiments," in *6th American Nuclear Society International Topical Meeting on Nuclear Plant Instrumentation, Control, and Human-Machine Interface Technologies*, **3**, 1783-1794 (2009).

13. D.L. Kundson and J.L. Rempe, "Recommendations for use of LVDTs in ATR high temperature irradiation testing," in *7th International Topical Meeting on Nuclear Plant Instrumentation, Control, and Human-Machine Interface Technologies 2010, NPIC and HMIT*, **2**, 753-763 (2010).

14. APC International, http://www.americanpiezo.com/

15. F. Cegla and P. Cawley, "Ultrasonic crack monitoring using SH waves at high temperatures," in *Review of Progress in Quantitative Nondestructive Evaluation*, edited by Thompson and Chimenti, not published in proceeding (2008).

16. F. Cegla, P. Cawley, J. Allin, and J. Davies, *IEEE Trans. on Ultrasonics, Ferroelectrics, and Frequency Control* **58**, 156-167 (2011).

17. R.J. Grossmann, *IEEE Trans. of Sonics and Ultrasonics* **31**, 25-31 (1984).

18. R. Royer Jr., *Ultrasonic sensor systems for in-situ monitoring of crystal growth*. (The Pennsylvania State University, 2004).

19. R. Royer Jr. and J.L. Rose, *Cryst. Res. Technol.* **40** (8), 761-764 (2005).

20. T. Vogt, M. Lowe, and P. Cawley, *J of Acoust. Soc. Am.* **114** (3), 1303-1313 (2003).

21. B.R. Tittmann and C.E. Yen, *Ultrasonics* **48**, 621-630 (2008).

22. M. Pedrick, M. Heckman, and B.R. Tittmann, "A novel technique with a magnetostrictive transducer for in-situ length monitoring of a distant specimen," in *Ultrasonic Nondestructive Evaluation for Material Science and Evaluation*, ASME PVP Conference Proceedings, **456**, 73-78 (2003).

23. M. Heckman, *A novel application of magnetostrictive sensors and guided ultrasonic waves for structural health monitoring of a remote specimen*. (Masters Thesis - The Pennsylvania State University, 2003).

24. P. Shull, *Nondestructive Evaluation*. (Marcel Dekker, New York, 2002).

25. J. Krautkramer and K. Krautkramer, *Ultrasonic Testing of Materials*, 4th ed. (Springer Verlag, Berlin, 1990).

26. H. Gao, M.J. Guers, and J.L. Rose, "Flexible ultrasonic guided wave sensor development for structural health monitoring," in *NDE and Health Monitoring*, Proceedings of SPIE, **6176**, 61761 (2006).

27. J.L. Rose, A. Pilarski, and J.J. Ditri, "Approach to guided wave mode selection for inspection of laminated plates," in *7th Technical Conference of the American Society of Composites*, 371-379 (1992).

28. Y. Zhu, J.L. Palacios, J.L. Rose, and E.C. Smith, "De-icing of multi-layer composite plates using ultrasonic guided waves," in *49th ASME Structures, Structural Dynamics, and Materials Conference*, 1862 (2008).

29. F. Yan and J.L. Rose, "Guided wave phased array beam steering in composite plates," in *Health Monitoring of Structural and Biological Systems*, Proceedings of SPIE, **6532**, 65320G (2007).

30. J. Mu, L. Zhang, and J.L. Rose, *NDT&E International* **22** (4), 239-253 (2007).

31. J.K. Van Velsor, H. Gao, and J.L. Rose, *Insight* **49** (9), 532-537 (2007).

32. J.L. Rose, M.J. Avioli, P. Mudge, and R. Sanderson, *NDT&E International* **37** (2), 153-161 (2004).

33. J.L. Rose, M.J. Avioli, and W.-J. Song, *Insight* **44** (6), 353-358 (2002).

34. J.L. Rose, *Ultrasonic Waves in Solid Media*. (Cambridge University Press, 1999).

35. B.A. Auld, *Acoustic Fields and Waves in Solids*, 2nd ed. (Krieger Publishing, 1990).

36. H. Kolsky, *Stress Waves in Solids*. (Dover Publications, Ney York, 1963).

37. F. Lanza di Scalea and S. Salamone, *J of Acoust. Soc. Am.* **124** (1), 161-174 (2008).

38. R. Raghavan and C.E.S. Cesnik, "Studies on effects of elevated temperature for guided-wave structural health monitoring," in *Sensors and Smart Structures Technologies*, Proceedings of SPIE, **6529**, 65290A (2007).

39. A.J. Croxford, P.D. Wilcox, G. Konstantindis, and B.W. Drinkwater, "Strategies for overcoming the effect of temperature on guided wave structural health monitoring," in *Health Monitoring of Structural and Biological Systems*, Proceedings of SPIE, **6532** (2007).

40. G. Konstantindis, B.W. Drinkwater, and P.D. Wilcox, *Smart Mater. Struct.* **15**, 967-976 (2006).

41. G. Konstantindis, P.D. Wilcox, and B.W. Drinkwater, *IEEE Sensors* **7** (5), 905 (2007).

42. G.H. Hostetter, M.S. Santina, and P. D'Carpio-Montalvo, *Analytical, Numerical, and Computational Methods for Science and Engineering*. (Prentice Hall, New Jersey, 1991).

43. F. Seco, *PCdisp*, (2009) http://www.iai.csic.es/users/fseco/pcdisp/pcdisp.htm

44. P.M. Morse and H. Feshbach, *Methods of Theoretical Physics (Part 2)*. (McGraw-Hill, New York, 1953).

45. M.V. Peredoi, M. Castaings, B. Hosten, and C. Bacon, *J of Acoust. Soc. Am.* **121** (4), 1935-1944 (2007).

46. T. Hayashi, W.-J. Song, and J.L. Rose, *Ultrasonics* **41**, 175-183 (2003).

47. S. Moaveni, *Finite Element Analysis*, 2nd ed. (Pearson Education, Ney Jersey, 2003).

48. T.R. Chandrupatla and A.D. Belegundu, *Introduction to Finite Elements in Engineering*. (Prentice Hall, New Jersey, 2002).

49. I. Bartoli, F. Lanza di Scalea, M. Fateh, and E. Viola, *NDT&E International* **38**, 325-334 (2005).

50. K. Shivaraj, K. Balasubramaniam, C.V. Krishnamurthy, and R. Wadhawan, *J of Pressure Vessel Technology* **130**, 862-871 (2008).

51. L.C. Lynworth, *Ultrasonic Measurements for Process Control*. (Academic Press, Boston, 1989).

52. A. Puchot, C. Duffer, A. Cobb, and G. Light, "Recent innovations using magnetostrictive sensors for nondestructive evaluation," in *Proceedings of SPIE*, **7295**, 72950K (2009).

53. H. Kwun and K.A. Bartles, *Ultrasonics* **36**, 171-178 (1998).

54. H. Kwun, G.M. Light, S.-Y. Kim, and R.L. Spinks, "Magnetostrictive sensor for active health monitoring in structures," in *Proceedings of SPIE*, **4701**, 282-288 (2002).

55. H. Kwun, "Long-range guided wave inspection of pipe using the magnetostrictive sensor technology - feasibility if defect characterization," in *Proceedings of SPIE*, **3398**, 28-34 (1998).

56. H. Kwun and S.Y. Kim, *J of Pressure Vessel Technology* **127** (3), 284-289 (2005).

57. H. Kwun and A.E. Holt, *NDT&E International* **28** (4), 211-214 (1995).

58. H. Kwun, J.J. Hanley, and A.E. Holt, "Detection of corrosion in pipe using the magnetostrictive sensor technique," in *Proceedings of SPIE*, **2459**, 140-148 (1995).

59. K.A. Bartles, C. Dynes, Y. Lu, and H. Kwun, "Evaluation of concrete sure using magnetostrictive sensor technology," in *Proceedings of SPIE*, **3587**, 210-218 (1999).

60. K.A. Bartles, C. Dynes, and H. Kwun, "Nondestructive evaluation of prestressed strands with magnetostrictive sensors," in *Proceedings of SPIE*, **3400**, 326-337 (1998).

61. K.A. Bartles, H. Kwun, and J.J. Hanley, "Magnetostrictive sensors for the characterization of corrosion in rebars and prestressed strands," **2946**, 40-50 (1996).

62. J.W. Brophy and C.R. Brett, "Guided UT wave inspection on insulated feed water piping using magnetostrictive sensors," in *Proceedings of SPIE*, **2947**, 205-210 (1996).

63. W. Liu, L. Zhou, T. Xia, and H. Yu, *Ultrasonics* **44**, 689-692 (2006).

64. E. Kannan, B. Maxfield, and K. Balasubramaniam, *Smart Mater. Struct.* **16**, 2505-2515 (2007).

65. I.K. Kim, W. Kim, and Y.Y. Kim, *Sensors and Actuators A* **137**, 141-146 (2007).

66. I.K. Kim, S.H. Cho, J.S. Lee, and Y.Y. Kim, "Magnetostrictive grating transducers: effect of grating size and shape," in *IEEE Ultrasonics Symposium*, 2081-2084 (2005).

67. Y.Y. Kim, *Sensors and Actuators A* **133**, 447-456 (2007).

68. W.K. Kulczyk, G.W. Smith, and G.A. Jackson, *Sensors and Actuators A* **21-23**, 663-669 (1990).

69. E. Tremolet, *Magnetostriction*. (CRC, Boca Raton, 1993).

70. H. Chiriac, E. Hristoforou, M. Neagu, F. Barariu, and I. Darie, *Sensors and Actuators A* **81**, 147-149 (2000).

71. H. Chiriac, E. Hristoforou, M. Neagu, F. Barariu, and T.A. Ovari, *J of Applied Physics* **85** (8), 5729-5731 (1999).

72. A.F. Cobeno, A. Zhukov, J.M. Blanco, and J. Gonzalez, *Sensors and Actuators A* **106**, 174-178 (2003).

73. E.P Wohlfarth, *Ferromagnetic Materials, Volume 2*. (North-Holland Publishing Co., Amsterdam, 1980).

74. H. Eriksson and A. Salwen, *IEEE Trans. on Magnetics* **13** (5), 1451-1453 (1977).

75. S.G. Khajutin and I.P. Goliamina, *Material Science Forum* **273-275**, 625-626 (1998).

76. S.G. Khayutin and I.P. Golyamina, *Metal Science and Heat Treatment* **39** (4), 108-110 (1997).

77. E. Klokholm and J.A. Aboaf, *J of Applied Physics* **52** (3), 2474-2476 (1981).

78. Arnold Magnetics, (2011) http://www.arnoldmagnetics.com/Thin_Gauge_Strip_and_Foil_Literature.aspx

79. J.F.W. Bell, *Phil. Mag.* **2** (1113-1120) (1957).

80. S. Taylor, *Personal communication (Idaho National Laboratory).* (2010).

81. M. Kropf and B.R. Tittmann, "Ultrasonic magnetostrictive transducers for guided ultrasonic waves in thin wires," in *Health Monitoring of Structural and Biological Systems*, Proceedings of SPIE, **6532**, 65320L (2007).

82. Y.S. Kim, G.L. Hofman, A.B. Robinson, J.L. Snelgrove, and N. Hanan, *J of Nuclear Materials* **378**, 220-228 (2008).

83. G.K. Miller, D.E. Burkes, and D.M. Wachs, *Materials and Design* **31**, 3234-3243 (2010).

84. I. Ioka, M. Futakawa, A. Naito, Y. Nanjyo, K. Kiuchi, and T. Naoe, *J of Nuclear Materials* **329-333**, 1142-1146 (2004).

85. M. Matsubara and A. Nitta, *Trans. of the Japan Society of Mechanical Engineers, Part A* **59** (565), 2061-2065 (1993).

86. M. Nakashiro, H. Yoneyama, S. Shibata, and A. Ohotomo, *Trans. of the Iron and Steel Institute of Japan* **28** (2) (1987).

87. M. Okazaki, "Nondestructive detection of creep and creep-fatigue damages in welded joints by ultrasonic techniques," in *AMSE PVP Proceedings*, 303 (1995).

88. *Annual Book of ASTM Standards*. (2007).

89. L. Rotherham, *Creep of Metals*. (IOP, London, 1951).

90. E.G. Stanford, *The Creep of Metals and Alloys*. (Temple Press, London, 1949).

91. A.H. Sully, *Metallic Creep*. (Buttersworths Scientific, London, 1949).

92. D.A. Parks and B.R. Tittmann, "High temperature broadband contact BAW transducer," in *Proceedings of the IEEE Ultrasonics Symposium*, IEEE, **2389-2392** (2007).

93. D.A. Parks and B.R. Tittmann, "Stepped ultrasonic array for inspection of submersed plates in a harsh environment," in *Review of Progress in Quantitative Nondestructive Evaluation*, edited by Thompson and Chimenti, AIP, **28**, 1743-1750 (2009).

94. P.J. Stephanou and A.P. Pisano, "GHz contour extensional mode Aluminum Nitride MEMS resonator," in *IEEE Ultrasonics Symposium*, 2401-2404 (2006).

95. B.T. Reinhardt, M.M. Kropf, M.J. Guers, and B.R. Tittmann, "Dislocation detection through harmonic generation," in *Review of Progress in Quantitative Nondestructive Evaluation*, edited by Thompson and Chimenti, AIP, **29**, 1391-1396 (2010).

96. S. Baby, B. Nagaraja Kowmuni, C.M. Omprakash, D.V.V. Satyanarayana, K. Balasubramaniam, and V. Kumar, *Scripta Materialia* **59**, 818-821 (2008).

97. J.-Y. Kim, L.J. Jacobs, J. Qu, and J.W. Littles, *J of Acoust. Soc. Am.* **120** (3), 1266-1273 (2006).

98. C. Bermes, J.-Y. Kim, J. Qu, and L.J. Jacobs, *Mechanical Systems & Signal Processing* **22**, 638-646 (2008).

99. A. Migliori and J.L. Sarrao, *Resonant Ultrasound Spectroscopy*. (John Wiley & Sons, New York, 1997).

100. R. Demirli, *Model Based Estimation of Ultrasonic Echoes: Analysis, Algorithms, and Applications*. (Illinois Institute of Technology, 2001).

101. B. Xu, L. Yu, and V. Giurgiutiu, "Advanced Methods for Time-Of-Flight Estimation with Application to Lamb Wave Structural Health Monitoring," in *The 7th International Workshop on Structural Health Monitoring* (2009).

102. B. Xu, L. Yu, and V. Giurgiutiu, "Lamb wave dispersion compensation in piezoelectric wafer active sensor phased-array applications," in *Proceedings of SPIE Smart Structures/NDE*, **7295** (2009).

103. C.M. Lee and J.L. Rose, *NDT&E International* **42** (3), 174-180 (2009).

104. P. Puthillath, *Ultrasonic Guided Wave Propagation Across Waveguide Transitions Applied to Bonded Joint Inspection*. (The Pennsylvania State University, 2010).

105. *Reactor grade zirconium alloys for nuclear waste disposal*, ATI Wah Chang, http://www.wahchang.com/pages/products/data/pdf/Zr_Alloys%20for%20Nuclear%20Waste%20Dspsl.pdf

106. C. Nam, B.-K. Choi, M.-H. Lee, and Y.-H. Jeong, *J of Nuclear Materials* **305**, 70-76 (2002).

107. J.S. Dubey, S.L. Wadekar, R.N. Singh, T.K. Sinha, and J.K. Chakravartty, *J of Nuclear Materials* **264**, 20-28 (1999).

108. H.E. Rosinger and D.O. Northwood, *J of Nuclear Materials* **79**, 170-179 (1979).

109. D.O. Northwood, I.M. London, and L.E. Bahen, *J of Nuclear Materials* **55**, 299-310 (1975).

110. COMSOL 4.1 Finite Element Software.

111. J.K. Fink, *Zircaloy thermal expansion*, Argonne National Laboratory, (1999) http://www.insc.anl.gov/matprop/zircaloy/zircexp.pdf

112. R. Dutton, *A Layman's Guide to Radiation-Induced Deformation Processes in Zirconium Alloys*. (Atomic Energy of Canada Limited, 1990).

113. G.M.E. Cooke, *Fire Safety Journal* **13**, 45-54 (1988).

114. M.F. Rothman, *High-temperature Property Data: Ferrous Alloys*. (ASM International, 1988).

115. *Matweb Data for 302 Stainless Steel*, http://www.matweb.com

116. *Inconel Alloy 600*. (The International Nickel Co. Inc., 1987).

117. *Inconel Alloy 625*. (The International Nickel Co. Inc., 1966).

118. *Inconel Alloy 718*. (The International Nickel Co. Inc., 1968).

119. *Incoloy Alloy 800*. (The International Nickel Co. Inc., 1961).

120. R.B. McLellan and T. Ishikawa, *J Phys. Chem. Solids* **48** (7), 603-606 (1987).

121. W.J. Arnoult and R.B. McLellan, *Acta Metallurgica* **23**, 51-56 (1975).

122. P.M. Sutton, *Phys. Rev.* **91** (4), 816-821 (1953).

123. F. Augereau, D. Laux, L. Allais, M. Mottot, and C. Caes, *Ultrasonics* **46**, 34-41 (2007).

124. J.L. Tallon and A. Wolfenden, *J Phys. Chem. Solids* **40**, 831-837 (1979).

125. I.N. Prassianakis, in *Non Destructive Testing*, edited by D. Van Hemelrijck and A. Anastassopoulou (A.A. Balkema, Netherlands, 1996), pp. 267-271.

126. W.T. Parry, J.C. Bellows, J.S. Gallagher, and A.H. Harvey, *ASME International Steam Tables for Industrial Use*. (ASME Press, New York, 2000).

127. R. Kazys, A. Voleisis, R. Sliteris, L. Mazeika, R.V. Nieuwenhove, P. Kupschus, and H.A. Abderrahim, *IEEE Trans. on Ultrasonics, Ferroelectrics, and Frequency Control* **52** (4), 525-537 (2005).

128. G.H. Broomefiled, *J of Nuclear Materials* **91**, 23-34 (1980).

129. V.M. Baranov, S.P. Martynenko, and A.I. Sharapa, *Soviet Atomic Energy* **53** (5), 803-804 (1982).

130. W. Primak and T.T. Anderson, *Nuclear Technology* **28** (2), 235-248 (1976).

131. K.E. Hlobert, S. Sankaranarayanan, and S.S. McCready, *IEEE Trans. on Ultrasonics, Ferroelectrics, and Frequency Control* **52** (4), 525-537 (2005).

132. L.I. Berger, *Semiconductor materials*. (CRC Press, 1997).

133. T. Yano, K. Inokucho, M. Shikama, J. Ukai, S. Onose, and T. Maruyama, *J of Nuclear Materials* **329-333**, 1471-1475 (2004).

134. T. Yano and T. Iseki, *j of Nuclear Materials* **203**, 249-253 (2003).

135. T. Yano, K. Ichikawa, M. Akiyoshi, and Y. Tachi, *J of Nuclear Materials* **329-333**, 1471-1475 (2003).

136. K. Atobe, M. Okada, and M. Nakagawa, *Nuclear Instruments and Methods in Physics Research B* **166-167**, 57-63 (2000).

137. D. Akers, *Personal communication (Idaho National Laboratory).* (2010).

138. T. Shikama, T. Yano, J. Ukai, S. Onose, M. Itoh, S.J. Zinkle, L.L. Snead, T. Maruyama, S. Nagata, B. Tsuchiya, and K. Toh, *Fusion science and technology* **44** (495-499) (2003).

139. E.M. Baum, H.D. Knox, and T.R. Miller, *Nuclides and Isotopes: Chart of the Nuclides*, 16th ed. (KAPL / Lockheed Martin, 2002).

140. H. Kim, K. Park, B. Min, J.S. Lee, K. Cho, S. Kim, H.S. Han, S.K. Hong, and T. Yao, *Nuclear Instruments and Methods in Physics Research B* **217**, 429-434 (2004).

141. U. Ozgur, Y.I. Alivov, C. Liu, A. Teke, M.A. Reshchikov, S. Dogan, V. Avrutin, S.J. Cho, and H. Morkoc, *J of Applied Physics* **98**, 041301 (2005).

142. C.T. Searfass, B.R. Tittmann, and D.K. Agrawal, "Sol-gel deposited thick film bismuth titanate based transducer achieves operation over 600C," in *Review of Progress in Quantitative Nondestructive Evaluation*, edited by Thompson and Chimenti, AIP, **28**, 1751-1758 (2010).

143. ANSYS Inc., http://www.ansys.com

144. Wissoft, http://www.wissoft.de/

145. Mallett Technology Inc., http://www.mallett.com/

146. COMSOL Inc., http://www.comsol.com

147. COMSOL Inc., *COMSOL 4.1 Multiphysics User's Guide*. (2010).

148. COMSOL Inc., *COMSOL 4.1 Structural Mechanics Module User's Guide*. (2010).

149. COMSOL Inc., *COMSOL 4.1 Acoustics Module User's Guide*. (2010).

150. *COMSOL technical support case 485523*. (2011).

151. *COMSOL technical support case 491118*. (2011).

152. M. Bezdek, K. Joseph, M.J. Guers, and B.R. Tittmann, "Structural health monitoring and nondestructive evaluation of double wall structures," in *Proceedings of the SPIE: Health Monitoring of Structural and Biological Systems* edited by T. Kundu, **6935**, 693516-693511 (2008).

153. M. Bezdek and B.R. Tittmann, *Acta Acustica* **94** (5), 792-806 (2008).

154. M. Bezdek and B.R. Tittmann, "Fluid-coupled waveguide for leaky guided waves," in *Ultrasonics Symposium* 1169-1172 (2006).

155. A.V. Oppenheim and R.W. Schafer, *Discrete-Time Signal Processing*, 2nd ed. (Prentice Hall, Ney Jersey, 1999).

156. E.W. Weisstein, *"Convolution." From MathWorld--A Wolfram Web Resource*, Wolfram Inc., http://mathworld.wolfram.com/Convolution.html

157. I.I. Hirschman and D.V. Widder, *The Convolution Transform*. (Princeton University Press, New Jersey, 1955).

158. E.W. Weisstein, *"Cross-Correlation." From MathWorld--A Wolfram Web Resource*, Wolfram Inc., http://mathworld.wolfram.com/Cross-Correlation.html

159. MathWorks, http://www.mathworks.com/products/matlab/

160. MATLAB 7.4 Software Help Menu.

161. D. Marioli, C. Narduzzi, C. Offelli, D. Petri, E. Sardini, and A. Taroni, *IEEE Trans. on Instrumentation and Measurement* **41** (1), 93-97 (1992).

162. R. El Guerjouma, A. Mouchtachi, Y. Jayet, and J.C. Baboux, "Nondestructive evaluation of graphite by ultrasonic velocity measurement using cross-correlation and Hilbert transform methods," in *IEEE Ultrasonics Symposium*, IEEE (1992).

163. K. Srinivasan, T. Sundararajan, S. Narayanan, and T.J.S. Jothi, *Applied Acoustics* **70**, 1061-1072 (2009).

164. R. Queiros, F.C. Alegria, P.S. Girao, and A.C. Serra, *IEEE Trans. on Instrumentation and Measurement* **59** (12), 3227-3326 (2010).

165. K. Toiyama and T. Hayashi, "Pulse compression technique considering dispersion of guided waves," in *Review of Quantitative Nondestructive Evaluation*, edited by Thompson and Chimenti, AIP, **27**, 587-593 (2008).

166. C.-C. Tong, J.F. Figueroa, and E. Barbieri, *IEEE Trans. on Instrumentation and Measurement* **50** (5), 1324-1328 (2001).

167. M.G. Duncan, *IEEE Trans. on Instrumentation and Measurement* **39** (6), 1024-1029 (1990).

168. M.G. Duncan, "Real-time analytic signal processor for ultrasonic nondestructive testing," in *IEEE Instrumentation and Measurement Technology Conference* IEEE, 32-37 (1990).

169. C. Fritsch, A. Ibanez, and M. Parrilla, *IEEE Trans. on Instrumentation and Measurement* **48** (6), 1287-1293 (1999).

170. R. Demirli and J. Saniie, "A generic parametric model for ultrasonic signal analysis," in *IEEE International Ultrasonics Symposium*, IEEE, 1522-1525 (2009).

171. A. Reilly, G. Frazer, and B. Boashash, *IEEE Trans. on Signal Processing* **42** (11), 3241-3245 (1994).

VITA

Manton John Guers

EDUCATION

Ph.D. 2011	Engineering Science & Mechanics, The Pennsylvania State University
M.S. 2004	Engineering Science, The Pennsylvania State University
B.S. 2002	Engineering Science, The Pennsylvania State University, Schreyer Honors College (with Honors and Distinction, plus a Minor in Mechanics)

PROFESIONAL EXPERIENCE

2002-2011	Graduate Research/Teaching Assistant, The Pennsylvania State University
2010	Internship at Idaho National Laboratory
2000	Internship at Pennsylvania Technology Assistance Program (PennTAP)

TEACHING EXPERIENCE

EMCH 523	Ultrasonic Nondestructive Evaluation (Teaching Assistant FA 2007)
EMCH 440	Survey of Nondestructive Evaluation Techniques (Teaching Assistant SP 2007, SP 2008)
EMCH 402/506	Experimental Stress Analysis (Teaching Assistant SP 2005)

INVITED TALKS

2010 "Finite Element Analysis and Ultrasonic Inspection" at Southeastern Louisiana University

PUBLICATIONS

M.J. Guers, B.R. Tittmann. *Magnetostrictive sleeve transducer for in-situ monitoring of specimens.* Proceedings of SPIE Smart Structures/NDE. Vol. 7650 (76501O) 2010.

M.J. Guers, B.R. Tittmann. *Modeling of wave propagation and defect detection in rectangular bar specimens.* Review of Progress in Quantitative Nondestructive Evaluation: v29, p97-103, 2010.

B.T. Reinhardt, M.M. Kropf, K. Boudraeu, **M.J. Guers**, B.R. Tittmann. *Dislocation detection through harmonic generation.* Review of Progress in Quantitative Nondestructive Evaluation, v29, p1391-1396, 2010.

M.J. Guers, B.R. Tittmann. *Influence of temperature on in-situ guided wave inspection and health monitoring of a rectangular bar specimen.* Proceedings of SPIE Smart Structures/NDE Vol. 7295 (72950N) 2009.

M.J. Guers, B.R. Tittmann. *Finite element analysis of ultrasonic methods for in-situ monitoring of an ASTM creep specimen*. Review of Progress in Quantitative Nondestructive Evaluation, v28, p1394-1401, 2009.

H. Gao, **M.J. Guers**, J.L. Rose. *Flexible ultrasonic guided wave sensor development for structural health monitoring*. Proceedings of SPIE Smart Structures/NDE Vol. 6176 (61761I) 2006.

H. Gao, **M.J. Guers**, J.L. Rose. *Ultrasonic guided wave annular array transducers for structural health monitoring*. Review of Progress in Quantitative Nondestructive Evaluation, v25, p1680-1686, 2006.

N. Zhang, J. Xie, **M. Guers**, V.K. Varadan. *Chemical bonding of multiwalled carbon nanotubes to SU-8 via ultrasonic irradiation*. Smart Materials and Structures, v 12, n 2, April, 2003, p 260-263.

J. Xie, N. Zhang, **M. Guers**, V.K. Varadan. *Ultraviolet-curable polymers with chemically bonded carbon nanotubes for microelectromechanical system applications*. Smart Materials and Structures, v 11, n 4, August, 2002, p 575-580.